ISSN 2542-1565

Vol. 18 2025 No. 03

GEOGRAPHY ENVIRONMENT SUSTAINABILITY

«The journal GEOGRAPHY, ENVIRONMENT, SUSTAINABILITY was founded in 2008 by Russian Geographical Society, the Lomonosov Moscow State University Geography Department, and the Russian Academy of Sciences Institute of Geography. Since that time the journal publishes **4 issues per year**, containing original research papers and reviews. The journal issues are open source and distributed through subscriptions, library exchanges of leading universities, and via the website through the world»

FOUNDERS OF THE JOURNAL: Russian Geographical Society, Faculty of Geography, Lomonosov Moscow State University and Institute of Geography of the Russian Academy of Sciences

The journal is published with financial support of the Russian Geographical Society.

The journal is registered in Federal service on supervision of observance of the legislation in sphere of mass communications and protection of a cultural heritage. The certificate of registration: ПИ № ФС77-67752, 2016, December 21.

PUBLISHER
Russian Geographical Society
Moscow, 109012 Russia
Novaya ploshchad, 10, korp. 2
Phone 8-800-700-18-45
E-mail: press@rgo.ru
www.rgo.ru/en

EDITORIAL OFFICE
Lomonosov Moscow State University
Moscow 119991 Russia
Leninskie Gory, 1,
Faculty of Geography, 1806a
Phone 7-495-9391552
Fax 7-495-9391552
E-mail: ges-journal@geogr.msu.ru
www.ges.rgo.ru

DESIGN
Layout designer: Tereshkin Anton
Moscow, 115088,
26 Simonovsky Val str., bldg. One
Phone: +7 (903) 108-04-44
E-mail: smile.tai@gmail.com

DOI prefix: 10.24057

Format A4 (210x297mm)

"GEOGRAPHY, ENVIRONMENT, SUSTAINABILITY" is the only original English-language journal in the field of geography and environmental sciences published in Russia. It is supposed to be an outlet from the Russian-speaking countries to Europe and an inlet from Europe to the Russian-speaking countries regarding environmental and Earth sciences, geography and sustainability. The main sections of the journal are the theory of geography and ecology, the theory of sustainable development, use of natural resources, natural resources assessment, global and regional changes of environment and climate, social-economical geography, ecological regional planning, sustainable regional development, applied aspects of geography and ecology, geoinformatics and ecological cartography, ecological problems of oil and gas sector, nature conservations, health and environment, and education for sustainable development.

Date of publication: October 1st 2025.

EDITORIAL BOARD

EDITORIAL OFFICE

CONTENTS

RESEARCH PAPER

WOULD CLIMATE CHANGE POSE A CHALLENGE TO MEETING WIND TARGETS? A GIS-BASED APPROACH TO UNRAVEL IMPACTS AND IDENTIFY SUITABLE SITES IN EGYPT

Azza Ghanem[1]*, Mohamed Abdel Karim Abdrabo[1], Mahmoud Adel Hassaan[1]
[1]Department of Environmental Studies, Institute of Graduate Studies and Research, University of Alexandria, 163 Horreya Avenue, Elshatby, Alexandria, 21526, Egypt
***Corresponding author:** azza.ghanem@alexu.edu.eg
Received: October 10th 2024 / Accepted: July 28th 2025 / Published: October 1st 2025
https://doi.org/10.24057/2071-9388-2025-3669

ABSTRACT. Renewable energy sources are critical choices for achieving long-term energy security while minimizing the effects of climate change. Wind energy in Egypt has received attention, however, wind power potential is dependent on climatic factors such as wind speed and temperature. Therefore, the wind power plan must rely on an in-depth understanding of wind resource sensibility to climate change to guarantee its sustainability, thereby supporting wind plan and climate change strategy. Using GIS analysis, the effect of climate change has been estimated on wind power density by 2065 under the climate change RCP 8.5 scenario. Furthermore, some criteria, such as elevation, slope, road networks, protectorates, archeological sites, touristic sites, and grids, have been used to identify regions that would be suitable for wind projects. The results revealed that wind energy potential is expected to be vulnerable to climate change, reflected in a 1% decrease in regions with high wind power density. Even after considering the effect of climate change, the Suez Gulf region would be the most suitable. Projects can also be expanded to other suitable locations where there are no projects yet, such as the Sinai Peninsula and the Red Sea coast.

KEYWORDS: climate change; renewable energy; wind power potential; Egypt; GIS, site suitability

CITATION: Ghanem A. , Abdrabo M.A. , Hassaan M.A. (2025). Would climate change pose a challenge to meeting wind targets? A GIS-based approach to unravel impacts and identify suitable sites in Egypt. Geography, Environment, Sustainability, 3 (18), 6-18
https://doi.org/10.24057/2071-9388-2025-3669

Conflict of interests: The authors reported no potential conflict of interests.

INTRODUCTION

Climate change is a serious challenge that will confront humanity in the coming years, which will have socio-economic and geopolitical consequences. Economic activities are a major driver behind the current warming trend, as greenhouse gas emissions (GHGs) have been steadily increasing since the mid-twentieth century, at an unprecedented rate over decades (Pachauri et al. 2014). One of the main challenges in addressing climate change is how to balance the growing energy demand with the need to reduce CO_2 emissions. Renewable energy is essential to reaching climate goals because of its crucial role in reducing emissions and meeting rising electricity demand in a more sustainable way, as well as its advantageous strategic and economic benefits (Al-Riffai et al. 2015). In this regard, wind energy is regarded as one of the most successful renewables in the world, owing to its cost-competitiveness and technological maturity (IRENA 2023). Thus, wind energy supports the transition to a green economy, achieving sustainable development goals (SDGs), and international ambitions in terms of climate change mitigation. Climate change, on the other hand, would have an impact on the energy sector, including supply, demand, and infrastructure. Permanently rising global surface temperatures associated with unprecedentedly high levels of GHGs may considerably affect energy demand patterns (Clarke et al. 2022). Climate change is expected to cause spatial and temporal variability in wind resource, which can have a significant impact on extractable power output and production costs. Different parts of the world are likely to experience varying trends and magnitudes of change in wind power potential (Cronin et al. 2018; Fant et al. 2016; Ohba 2019; Pereira et al. 2013). Risks related to climate change, such as extreme weather, storms, hurricanes, temperature increases, and flooding, are anticipated to influence on the resilience of the power system and may harm the infrastructures of wind farms (Clarke et al. 2022). Climatic determinates of wind power potential include wind speed, air pressure, and temperature, hence changes in wind speed and temperature as a result of climate change impacts would have an influence on wind power output (El-Ahmar et al. 2017; Rao 2019).

In Egypt, renewable energy sources have experienced a noteworthy growth during the last decade. The total installed capacity was 6691 MW, which includes hydropower, onshore wind, solar PV, solar CSP, and biomass, accounting for 25.87 TWh of total electricity

generated. This transition to renewable energy is anticipated to save $287.01 billion by 2050 due to decreased emissions (Abbas et al. 2021). Wind power represents one of the most promising sources of renewable energy. The installed wind power capacity has reached 2191 MW, contributing 3% of the country's total electricity generation. With ambitious national strategies aiming to increase this share to 14% in the near future, Egypt is actively positioning itself as a regional leader in wind energy development. Key projects such as Gebel El-Zeit and Zaafrana have demonstrated considerable success, attracting international investment for large-scale wind power deployment. A clear and supportive governmental policy framework underpins its progress in wind power. The government has adopted a long-term Integrated Sustainable Energy Strategy (ISES) targeting 42% renewable energy by 2035, with wind playing a major role in this mix. Policy instruments such as feed-in tariffs, competitive bidding, and public-private partnerships have been crucial in mobilizing both domestic and foreign investment. In addition, streamlined licensing procedures and the availability of land in high-wind zones, such as the Gulf of Suez, have further accelerated project implementation (Ghanem & Elsobki 2024). Moreover, Egypt is fostering local manufacturing capabilities for wind energy components, including towers and related infrastructure. This is supported by competitive advantages such as low labor costs, favorable energy prices for industry, and access to raw materials (Salah et al. 2022). These factors enhance Egypt's competitiveness in the global renewable energy market. Moreover, the development of wind power contributes to national goals of reducing greenhouse gas emissions, diversifying energy sources, and achieving long-term sustainability.

Egypt has a desert climate, with hot and dry summers and mild winters with little rainfall. It is predicted to experience negative climate change consequences as it becomes hotter and drier. Also, climate change may make climate extremes more frequent and severe that are related to renewable energy production in the future (Abbas et al. 2021; Smith et al. 2013). In warmer temperatures, wind power plants, for instance, which are usually designed for conditions of around 25ºC, may become less effective, reducing generation efficiency. Egyptian electricity systems may be better able to deal with the negative effects of rising temperatures and heat waves if adaptation measures are taken, such as incorporating a climate change impact assessment into energy planning with the aim of identifying locations for the construction of future power plant[1].

Most published research on climate change's impact has overlooked several critical sectors, including the energy sector, despite its vital importance (Hassaan 2018). Naturally, numerous research studies were carried out to assess the wind resource at multiple sites (Agwa et al. 2023; Ahmed 2010; Ahmed 2012; Ahmed 2018a; Ahmed 2018b; Hamouda 2012; Lashin & Shata 2012), as well as conducted multi-criteria suitability analysis for installing offshore wind farms (Mahdy & Bahaj 2018). However, these studies presented assessments of wind power potential under current wind speeds, without considering climate change impacts and climate change scenarios. Hence, this study aims to assess the impact of climate change on the potential for wind power generation and determine the most suitable area to install projects by 2065 under the climate change RCP 8.5 scenario. Such research work can support the decision-making and policymaking process in terms of planning wind energy projects.

Materials and Methods

Geographical Information System (GIS) can be used for a wide range of fields as they can assist in organizing, querying, storing, and displaying spatial and non-spatial data. Thus, it can support knowledgeable decisions and policymaking. Power generation from renewable resources depends on numerous spatial determinants, such as wind speed, solar radiation, biomass availability, locations, grids, energy demand …etc. In this regard, several studies have been undertaken in different regions of the world, applying GIS analysis tools to analyze wind power potential (Eshete & Abate 2022; Razeghi et al. 2023; Samak 2023) or perform multi-criteria suitability analysis for siting wind power farms in either inland regions (Atici et al. 2015; Aydin et al. 2010; Elmahmoudi et al. 2020; Pakere et al. 2022), onshore regions (Effat 2014; Sliz-Szkliniarz et al. 2019), or offshore regions (Saleous et al. 2016; Tercan et al. 2020). Meanwhile, some previous research work used GIS to assess the economic impact of the turbines, in the construction and operation phases (Pakere et al. 2022).

The Arab Republic of Egypt is located in the northeastern part of Africa, with the Sinai Peninsula forming a land bridge into western Asia. Egypt is bordered by the Mediterranean Sea to the north, the Red Sea to the east, Libya to the west, Sudan to the south, and the Gaza Strip to the northeast. Geographically, it lies between latitudes 22° and 31° North and longitudes 25° and 35° East. The Nile River flows through the country from south to north, dividing it into distinct eastern and western regions. This strategic location encompasses a variety of climatic and topographic zones relevant to wind energy assessment under different climate change scenarios.

In this study, a four-phase methodology was implemented to assess the potential impacts of the climate change RCP 8.5 scenario on wind power in Egypt and identify suitable sites for future development using a GIS-based approach. The phases include (1) data collection and manipulation, (2) assessing current and projected wind power potential, (3) spatial-temporal profiling of changes in wind power, and (4) multi-criteria suitability analysis. Fig. 1 presents an overview of the workflow, and the following sections describe each phase in detail.

Data Collection and Manipulation

Data on wind energy determinants were obtained from the Coordinated Regional Climate Downscaling Experiment (CORDEX)[2] in February 2022 for the Middle East and North Africa region. Climate models are forecasts of the future state of the climate system and are used to understand how the climate will change (Abbas et al., 2021). The CORDEX provides downscaled climate change scenarios using Regional Climate Models (RCMs) alongside the Intergovernmental Panel on Climate Change (IPCC) Fifth Assessment Report for a variety of global domains. RCMs usually provide climatic data at high spatial and temporal resolution. The data were collected monthly, and had a spatial resolution of 24 km, which was achieved using the RCA4 model (Hassaan et al. 2024; Nabipour et al. 2020). The gathered data included historical data on wind speed, air temperature, and air pressure at 10 m from 1970 to 2005, which represents the historical period, with 1988 being the mid-period year for this reference period. In addition, projected data on the same variables were acquired for the climate change RCP 8.5 scenario for 2050-2080, which represents 2065. The IPCC developed four Representative Concentration Pathways (RCPs) labeled based on possible radiative forcing in W/m^2 by the end of the twenty-

[1]IEA. (2023). Climate Resilience for Energy Transition in Egypt. International Energy Agency (IEA), Paris. https://www.iea.org/countries/egypt. [Accessed 16 August 2023]

[2]CORDEX. (2022). Coordinated Regional Climate Downscaling Experiment. https://esgdn1.nsc.liu.se/search/cordex/. [1 February 2022].

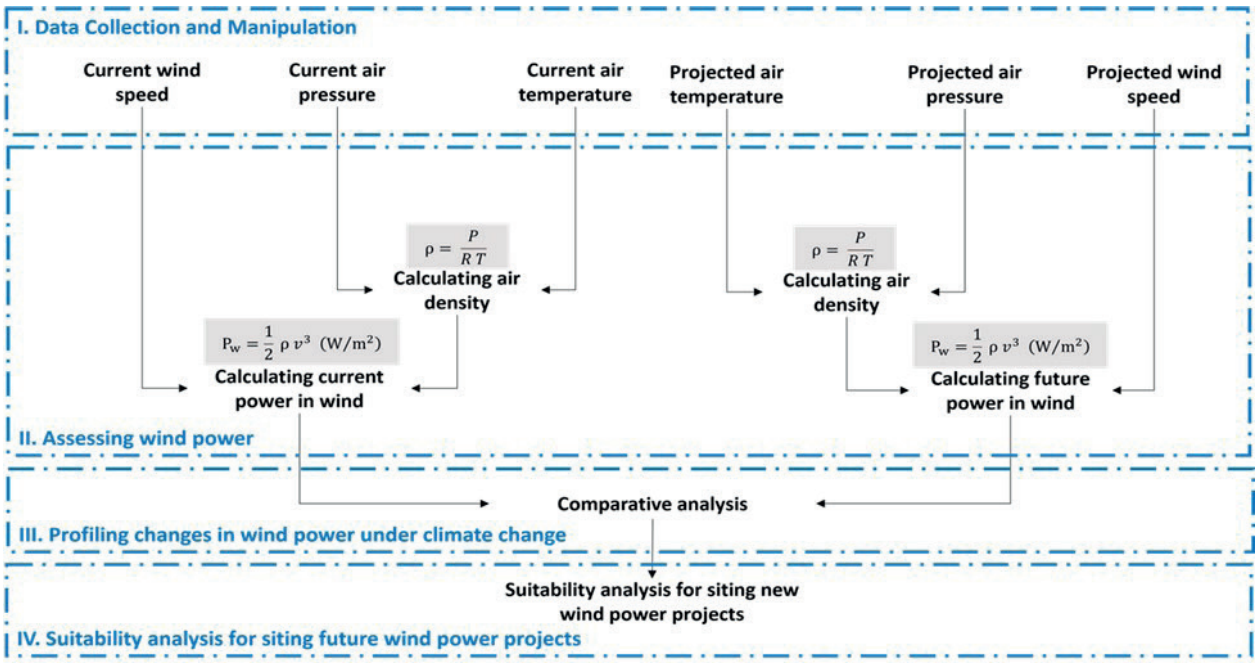

Fig. 1. Proposed methodology of assessment wind power under climate change

first century, relative to the 1986-2005 period. Climate change scenarios represent how anthropogenic GHG concentrations may evolve in the future. RCP8.5 is considered the worst-case scenario, which has a radiative forcing of 8.5 W/m^2, high-level emissions of more than 1000 CO_2-eq, and a 3.7 °C increase in mean temperature by 2100, implying no further climate efforts (Pachauri et al. 2014). The RCP 8.5 scenario is selected, which, despite being the highest emission pathway, provides valuable insights into potential extreme impacts on wind resources. Given Egypt's long-term energy planning and the critical need to assess site robustness under high-risk climate conditions, RCP 8.5 is a useful analytical boundary to explore the upper limits of climatic impact.

Given the absence of direct long-term observational wind speed data across Egypt for the historical period, this study relied on the validation efforts of previous research that assessed the accuracy and performance of CORDEX-RCM outputs (Hassaan et al. 2024; Nabipour et al. 2020). Therefore, no additional bias correction or validation was conducted in this study, and the dataset was used as a reliable source to analyze climate-induced changes in wind power potential.

Furthermore, data on criteria for siting wind power projects such as elevation, roads, high voltage grids, and land use were downloaded from DIVA-GIS[3], which provides geographical open access data for the world's countries. Moreover, data on sensitive land uses such as archeological sites were acquired from (Nagi & Nagi 2002). The collected data were integrated into a geodatabase that included various vector and raster feature classes (Table 1). Using ArcGIS Software version 10.8, the collected data were masked and manipulated to produce raster layers representing monthly and annual averages of wind speed, air pressure, and air temperature over historical and future periods.

To assess whether the observed changes in monthly mean wind speeds between the reference period (1970–2005) and the future period (2050–2080) under the RCP8.5 scenario are statistically significant, a paired sample T-test was conducted. The test compared the same months between the two periods, based on monthly mean values derived from wind speed data that had been spatially processed. The analysis was performed using SPSS software version 26.

Table 1. Geodatabase Structure

Feature Class	Type	Description
Current_Wind_Speed	Raster	Current wind speed for the reference period (1970-2005)
Current_Air_Pressure	Raster	Current air pressure for the reference period (1970-2005)
Current_Air_Temperature	Raster	Current air temperature for the reference period (1970-2005)
Projected_Wind_Speed	Raster	Projected wind speed for the period (2050-2080) under RCP 8.5 scenario
Projected_Air_Pressure	Raster	Projected air pressure for the period (2050-2080) under RCP 8.5 scenario
Projected_Air_Temperature	Raster	Projected air temperature for the period (2050-2080) under RCP 8.5 scenario
Elevation	Raster	Elevation above mean sea level
Slope	Raster	Slope of land
Roads	Vector	Road network
Sensitive land uses	Vector	Protectorates, archaeological sites, and touristic destinations
Grid	Vector	High voltage grids

[3]DIVA-GIS. (2022). DIVA-GIS. Free Spatial Data by Country. Available: https://www.diva-gis.org/gdata. [Accessed 16 November 2022].

Assessing Current and Projected Wind Power Potential

To find wind power potential under current conditions as well as projected climatic conditions in the future, the Eq.1 was employed:

$$P_{wind} = \frac{1}{2}\rho v^3 \quad (1)$$

Where: P_w – Power in wind, ρ – Air density, v – Wind Speed (Sawadogo et al. 2021)

The air density was calculated according to the Eq. 2:

$$\rho = \frac{P}{TR} \quad (2)$$

Where: ρ – Air density, R – The gas constant = 287 J/kg-K for air, P – Air pressure, T – Air temperature in kelvin (Tong 2010)

Profiling Changes in Wind power Under Climate Change

The estimated wind power potential of the reference period (1970–2005) was compared to the estimated future wind power potentials under the RCP8.5 scenario by the year 2065 (2050–2080). It is worth noting that wind turbulence needs to be considered when deciding to locate wind farms, as wind speed fluctuations may cause fluctuations in power output and also damage the turbine. Therefore, probability density functions (PDFs) were produced on an annual basis to determine the variance in wind speed in each area.

Suitability Analysis for Siting Future Utilization of Wind Power

In general, wind power potential is critical but not sufficient for deciding where to locate wind power projects due to the existence of other factors that may raise the cost of the project or restrictions that prevent its construction. This emphasizes the importance of multi-criteria suitability analysis in determining the most suitable locations for wind farms, which are dependent on a variety of factors. Such an analysis involves the use of a set of criteria, including local topography, economic viability, and environmental aspects. Local topography criteria assess appropriateness for wind power farm construction and operation. For example, suitable sites for a wind farm should have a gentle slope to avoid difficulties in the installation and operation of wind turbines. In this respect, it was suggested that the slope of wind farm sites should not exceed 25 or more favorably 15 . In addition, wind farms are usually installed at relatively high altitudes to generate more power. Nevertheless, installation at higher than 2000 m is not preferred because the air density reduces at these levels, resulting in low turbine efficiency. Also, moving the turbine components to extremely high regions is challenging (Feng 2021; Rediske et al. 2021). Economic viability entails identifying sites with the largest wind power potential as well as more accessible sites, allowing for easier and lower-cost wind farm construction and maintenance. Also, installing wind farms as close to the transmission power grid as possible to minimize power loss and grid connection costs. Wind farm construction and operation are usually associated with environmental impacts, for instance, turbine noise that can influence on both human health and animal life. Wind farms should thus be located away from sensitive land uses such as protectorates, archaeological sites, and tourism destinations.

To represent the identified criteria and their relevant indicators, the slope was derived from the elevation digital model. Also, using Spatial Analyst Tools (Euclidean Distance Tool), several raster surfaces were created, representing the distance to road networks, power grids, and sensitive areas. As a result, six raster feature classes were produced, representing various indicators of the criteria considered. Thereafter, each of these raster surfaces was normalized through one of the Eqs. 3-4:

$$N_x = \frac{X - X_{min}}{X_{max} - X_{min}} \quad (3)$$

$$N_x = 1 - \left[\frac{X - X_{min}}{X_{max} - X_{min}}\right] \quad (4)$$

Where: N_x – Normalized pixel value, X – Pixel value, X_{min} – Minimum pixel value in the raster surface, X_{max} – Maximum pixel value in the same raster surface (Hassaan et al. 2021)

It should be noted that the raster surfaces of those indicators that are positively correlated with suitability were normalized according to formula (3), while the raster surfaces of those indicators that are negatively correlated with suitability were normalized according to formula (4). Meanwhile, the raster surface of elevation, whose curvilinear relationship with suitability, was normalized according to the Eq. 5:

$$N_x = 1 - \frac{|X - 2000|}{X_{max} - 2000} \quad (5)$$

Where: N_x – Normalized pixel value, X – Pixel value, X_{min} – Minimum pixel value in the raster surface, X_{max} – Maximum pixel value in the same raster surface

These different formulae of normalization ensured consistent normalized raster surfaces, with pixel values ranging between 0 and 1 representing the least and highest levels of suitability, respectively. This is followed by calculating the composite suitability index through

Table 2. List of criteria and their relevant indicators

Criteria	Indicator	Unit	Relationship
Local topography	Slope	Degree	Negative
	Elevation	Meter	Curvilinear
Cost-effectiveness	Wind power potential	W/m^2	Positive
	Distance to roads network	Meter	Negative
Environmental impact	Distance to Grid	Meter	Negative
	Distance to sensitive land uses	Meter	Positive

aggregating various primary indicators, assuming equal weight of all indicators according to the Eq. 6:

$$S = \sum_{i=1}^{n} \left(N_i \times W_i \right) \quad (6)$$

Where: S – Suitability index, N_i – Normalized pixel value of indicator i, W_i – Weight of indicator N_i

As a result, a new raster surface was generated, representing different levels of suitability according to the considered criteria and their indicators. The resulting raster surface has pixel values ranging between 0 for the least suitable locations and 1 for the most suitable locations.

Results and Discussion

Projected Changes in Wind Speed

Annual mean wind speed in the reference period (1970–2005) ranged from 2.76 to 5.73 m/s at 10 m, whereas under the RCP8.5 scenario, annual mean wind speed would range from 2.74 to 5.91 m/s at 10 m (Fig. 2). This means that the annual mean wind speed is expected to experience a marginal increase. It should be noted in this respect that the annual mean wind speed does not reflect temporal and spatial variations in different locations within the country. Therefore, there would be a need to look more in-depth at temporal and spatial variations in different parts.

Temporally, the monthly mean wind speed in the reference period (1970–2005) ranged between 3.07 and 4.20 m/s at 10 m. Winds exceeding 4 m/s are prevalent in the summer and spring. Higher wind speeds indicate greater potential for electricity generation. It is worth noting that wind speeds are high during the summer, which is Egypt's peak electricity demand season[4]. Monthly mean wind speed is expected to range between 3.20 and 4.22 m/s under the climate change scenario RC8.5. Compared to the reference period, wind speed on average would increase by 10% in September, while wind speed in February is expected to be unchanged. Some months would, meanwhile, experience some decline in wind speed, with August experiencing the largest decline, exceeding 4% (Fig. 3).

A paired sample T-test was applied to the corresponding monthly averages between the two periods, and the results showed that the difference was not statistically significant at the 0.05 level ($p > 0.05$). This minor variation can be attributed to natural variability and may also fall within the margin of error inherent in the climate model used.

Spatially, wind speed varies from one area to another. Different sites have been chosen to evaluate wind potential. In the Gulf of Suez region, there are already some wind power

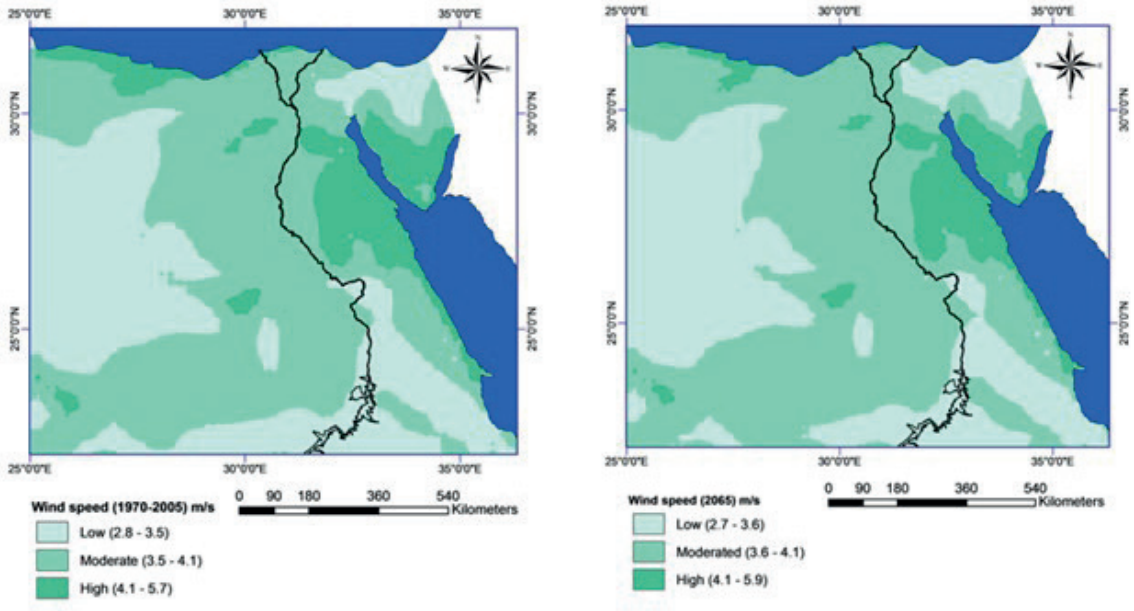

(a) Reference period (1970 - 2005) (b) By 2065, under RCP 8.5 scenario

Fig. 2. Annual wind speed by 2065 under RCP 8.5 scenario compared to the reference period (1970-2005)

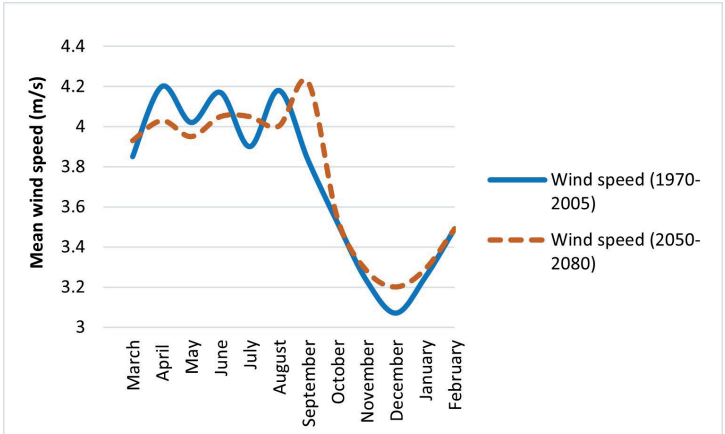

Fig. 3. Predicted change in monthly mean wind speed

[3]CEIC. (2024). Egypt Electricity Consumption. Ceicdata. https://www.ceicdata.com/en/egypt/electricity-consumption/electricity-consumption. [Accessed 11 April 2024].

projects, and more will be added in the future. Egypt intends to grow in the future, including the Red Sea and the West Nile areas. Furthermore, other sites, such as Sinia, Aswan, Sharq El Owainat, the Mediterranean Coast, and Kharga Oasis, have been selected to investigate the possibility of establishing future wind farms for local community development if they are determined to be suitable (Fig. 4).

Climate change is likely to cause different patterns in wind speed (Fig. 5). The Suez Gulf, Red Sea Coast, Sharq El-Owainat, and Aswan areas are expected to have significant increases in annual mean wind speeds ranging between 2.8 -1.1%. Kharga Oasis would experience the largest increase in wind speed with 7.3% compared to the reference period. The West Nile and the Sinai Peninsula areas would be unchanged, while the Mediterranean coast would experience a 2% decrease. The expected decline in wind speed alongside the Mediterranean coast was attributed to a decrease in the temperature difference between the polar regions and the tropics, resulting in a decrease in average wind speeds in the middle latitudes (Ebinger & Vergara 2011).

In order to understand patterns of change in wind speed in different sites under the climate change scenario RCP8.5 compared to the reference period, the wind speed probability density function (PDFs) was estimated. It is obvious that PDFs vary noticeably among different sites, so it is crucial to choose a location with favorable wind conditions for wind power generation (Fig. 6). The findings indicate that (a) Suez Gulf is predicted to be the windiest site, with increased variance with high wind speed values. (b) The annual mean wind speed of the Red Sea Coast is expected to rise, which would increase the likelihood of higher wind speeds at low values and lower wind speeds at high values. Furthermore, no significant variations are expected in this area. (c) In the West Nile region, the variance in wind speed would increase without a rise in its annual mean. This means a lower level of reliability of wind power in this region. (d) In the Sharq El-Qwinat region, the annual mean wind speed is expected to experience a marginal increase with an unchanged variance in wind speed, indicating that there is a probability increase in wind speed toward high values. (e) The annual mean of wind speed in Aswan would increase with a low variance, indicating that there is an increased probability of higher wind speed values. (f) In Kharga, the annual mean wind speed is expected to increase, with an increased probability of higher wind speed values and also low variance that indicates less fluctuation in wind speed. (g) Alongside the Mediterranean Sea coast, annual mean wind speed would decrease with unchanged variance, indicating that there is a decreased probability of higher wind speed values. (h) The variance in wind speed in Sinai would increase slightly without a rise in its annual mean. This generally means unchanged under climate change conditions.

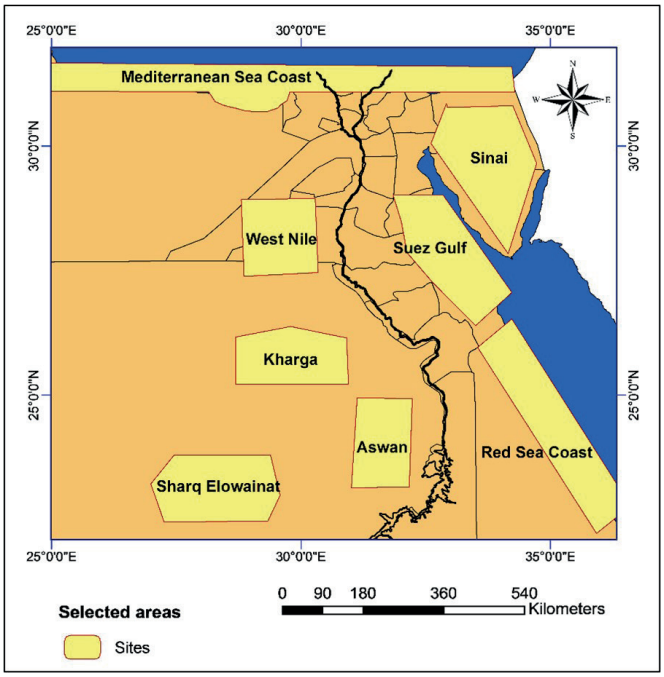

Fig. 4. Geographic location map of the eight selected sites in Egypt

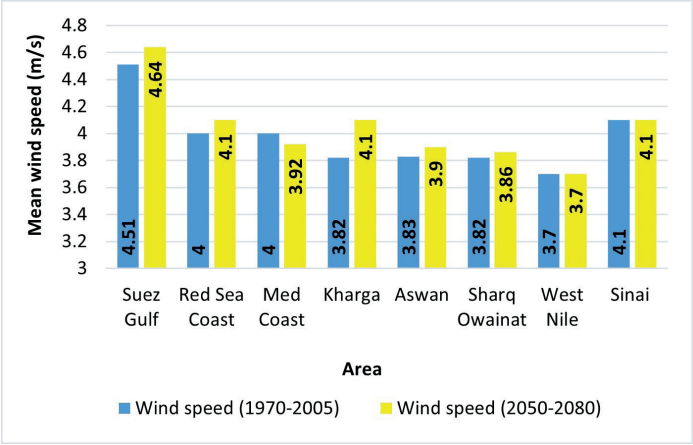

Fig. 5. Changes in annual mean wind speed at the selected areas

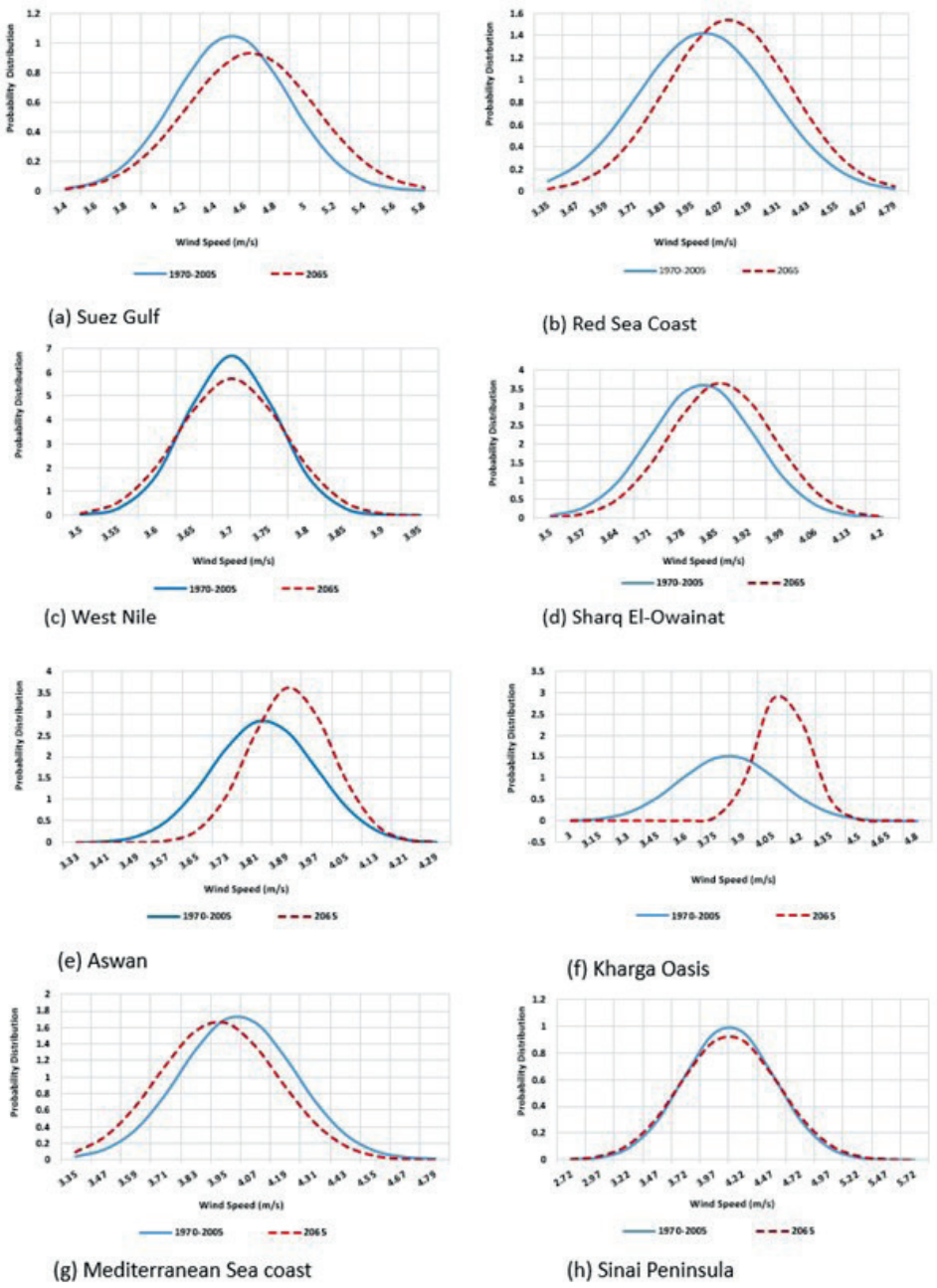

Fig. 6. Probability distribution function (PDFs) of wind speed in the selected areas

Expected Changes in Air Density

Based on temperature and air pressure for the reference period (1970–2005), the annual mean air density was found to be 1.00 – 1.22 kg/m^3. Due to the inverse relationship between temperature and air density, an increase in temperature causes a decrease in air density. Under the RCP8.5 scenario, the annual average temperature is expected to increase by about 3 K on average, while air pressure is expected to experience an approximate decline compared to current levels of air pressure on average. Accordingly, the range of the annual average air density is expected to be 1.21–0.99 kg/m^3, decreasing by about 3% (Fig. 7).

Estimated Changes in Wind Power Potential

Annual wind power density ranged between 12.34 and 112.70 W/m^2 during the reference period (1970–2005), whereas it is anticipated to be 11.99 to 122.33 W/m^2 (Fig. 8). This, consequently, shows that climate change would have a slight negative impact on annual mean wind power density, and this decline is mainly due to a reduction in expected air density.

Wind power potential was classified into three categories based on wind speed in the reference period and under the RCP8.5 climate change scenario (Tables 3 and 4). Land areas with high wind power potential are projected to decrease by 1% because of climate change impacts.

Annual wind power density in different locations of Egypt varied notably during the reference period, ranging between 29.35 and 53.61 W/m^2, and is anticipated to range between 29.95 and 55.40 W/m^2 under climate change (Fig. 9). Except for the Mediterranean Sea coast, all of the selected areas are predicted to increase their annual average wind power density. The Suez Gulf, which has significant potential, is anticipated to increase by 3%. This is consistent with (Gebaly et al. 2023) finding that wind power density in the Gulf of Suez would experience an increase under climate change scenarios. Meanwhile, sites with moderate wind power potential, such as Kharga Oasis, are expected to increase by 18%.

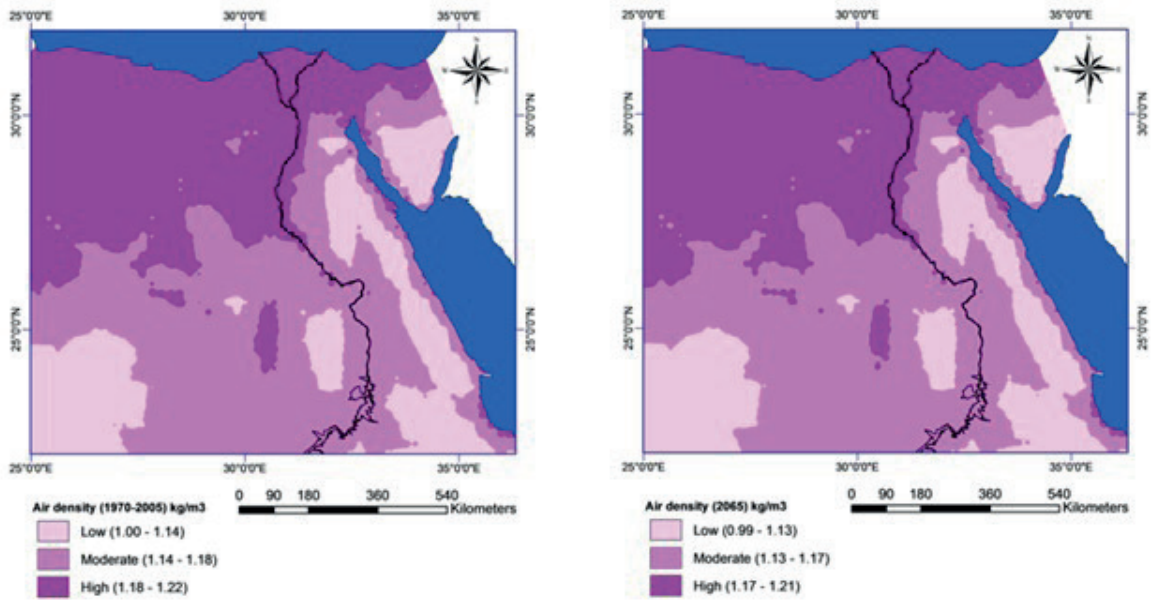

(a) Reference period (1970 - 2005) (b) By 2065, under RCP 8.5 scenario

Fig. 7. Annual air density by 2065 under RCP 8.5 scenario compared to the reference period (1970-2005)

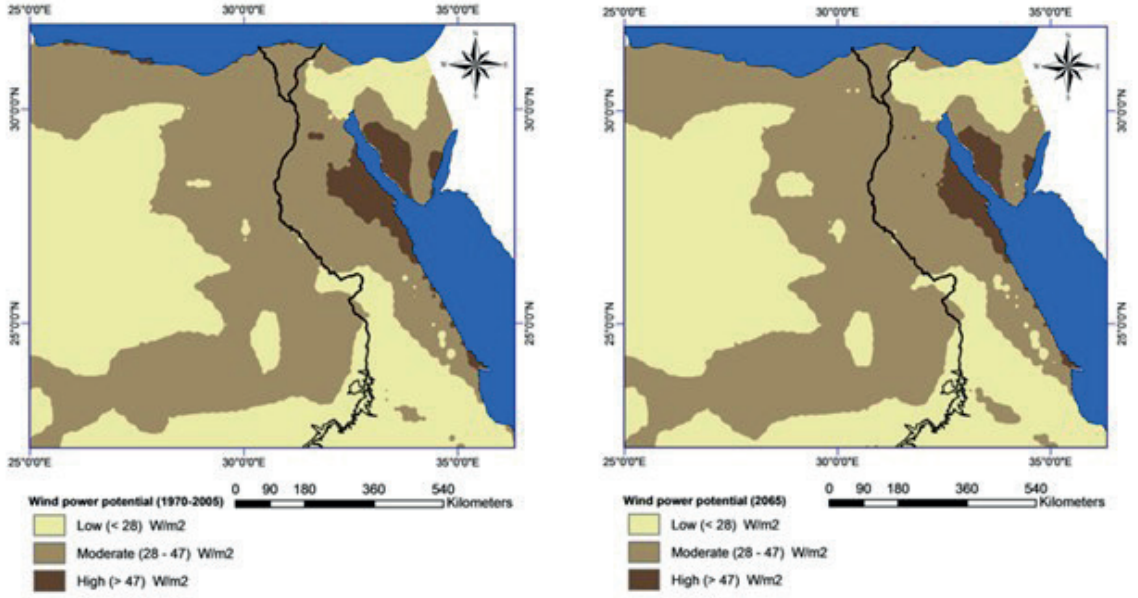

(a) Reference period (1970 - 2005) (b) By 2065, under RCP 8.5 scenario

Fig. 8. Annual wind power density by 2065 under RCP 8.5 scenario compared to the reference period (1970-2005)

Table 3. Classification of wind power density (1970-2005) at 10m

Class	Wind speed (m/s)	Wind power density (W/m^2)	Resource potential	Area (%)
1	2.8 - 3.5	< 28	Low	44
2	3.5 - 4.1	28 - 47	Moderate	52
3	4.1 - 5.7	> 47	High	4

Table 4. Classification of wind power density under RCP 8.5 scenario at 10m

Class	Wind speed (m/s)	Wind power density (W/m^2)	Resource potential	Area (%)
1	2.7 - 3.6	< 28	Low	45
2	3.6 - 4.1	28 - 47	Moderate	52
3	4.1 - 5.9	> 47	High	3

Limited research publications (Gebaly et al. 2023; Hassaan et al. 2024) examined changes in wind resources under climate change scenarios that revealed multiple expected trends in wind power density over Egypt. This research article's findings differed from those of (Gebaly et al. 2023), who found that wind power potential based on the worst scenario (SSP5-8.5) would rise between 2041 and 2100.

Suitable Sites for Future Utilization of Wind Power Projects

This research paper suggested an approach to conducting a suitability analysis to determine the most suitable locations for wind power projects in light of climate change, which aspect has not been discussed in previous studies at all (Gebaly et al. 2023; Hassaan et al. 2024). Indicators revealed various levels of suitability (Fig. 10); for instance, based on slope and the distance to sensitive areas, western parts are more suitable than eastern parts. Meanwhile, the eastern parts have a higher level of suitability based on elevation and distance to the roads. This emphasizes the importance of a composite index, which combines several indicators into a single numerical value that represents the overall compatibility of different parts.

Fig. 11 depicts the composite suitability index that indicates the most suitable regions are predicted to be in the Suez Gulf, a part of Sinai, and southern Egypt, which together encompass around 8.8% of Egypt's entire landmass. In general, depending on the criteria chosen, it is possible to argue that up to 75% of Egypt's land would be suitable for wind power installation in the future under the RCP8.5 climate change scenario.

Expected minimization in the landmass of the most suitable sites, especially in the Gulf of Suez region (Table 5), where wind power projects are highly concentrated, may obstruct the growth of additional wind projects there and necessitate expansion in other sites. There are no plans for installing wind power projects in the Sinai Peninsula, the Red Sea Coast, or Kharga Oasis, for instance, but these areas may be more suitable under climate change, especially since technological progress ensures that integrating remote locations is no longer a barrier to Egypt's renewables development (Elgeziry et al. 2019). There could be a considerable socio-economic improvement for the local community if a wind farm proposal is made there. Furthermore, it presents a chance to export energy

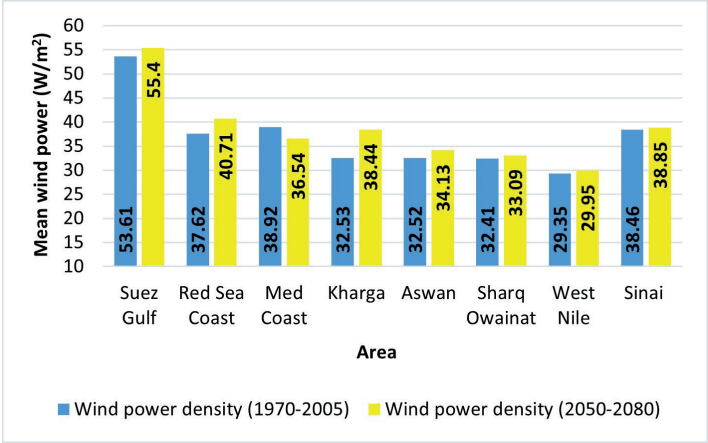

Fig. 9. Predicted change in wind power density in 2065

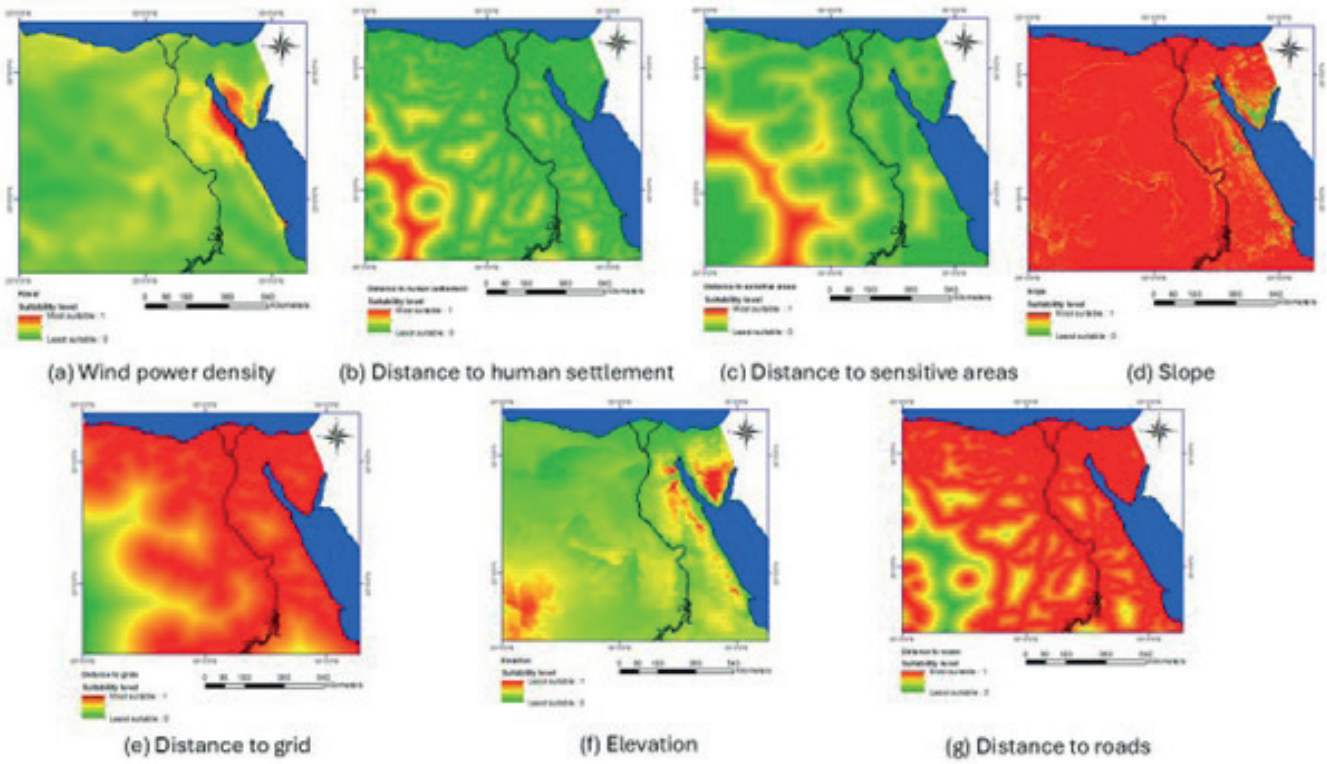

Fig. 10. Normalized raster surfaces of the selected indicators

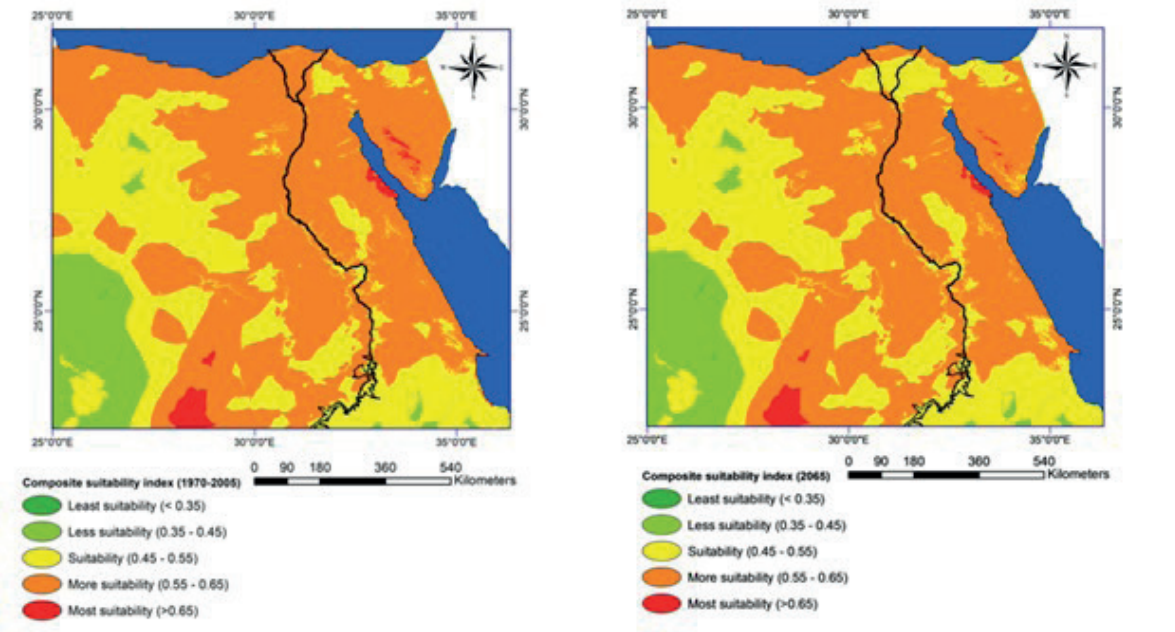

(a) Suitable sites in the reference period (1970 - 2005) (b) Suitable sites under climate change (2050-2080)

Fig. 11. Suitable sites for installing wind power projects

Table 5. Suitability level for future utilization of wind power under RCP8.5 climate change scenario

Suitability level	Reference Period (1970-2005)		Under RCP8.5 scenario (2050-2080)	
	Area (km^2)	(%)	Area (km^2)	(%)
Most suitable areas	95,167.39	9.50	88,837.18	8.85
More suitable areas	461,043.49	45.94	450,372.7	45.15
Moderately Suitable areas	288,279.32	28.72	298,773.12	29.95
Less suitable areas	155,858.11	15.54	156,858.94	15.72
Least suitable areas	2,363.28	0.23	2,458.71	0.24

production to foreign nations. The West Nile region is one of the planned sites for wind farms with towers of up to 120 m for developing this area, which is expected to be suitable for wind project installation under climate change based on the selected criteria. Nevertheless, in general, it is preferable to expand to another much more suitable site with great potential for wind power. In addition, this area would experience significant fluctuations in wind speed, making it unsuitable for the installation of a wind farm since turbulence reduces wind turbine performance.

Conclusions

Climate change has become an issue of concern, with a wide range of impacts already observed in countries all over the world. The objective of this research article is to assess climate change impacts on wind power potential utilizing climatic factors such as wind speed, air pressure, and temperature from 1970 to 2005, as well as expected values under the climate change RCP 8.5 scenario (2050-2080). In addition, some criteria were employed to determine the most suitable regions for wind farm installations, including wind power density, elevation above mean sea level, slope of land, road networks, protectorates, archeological sites, touristic sites, and power grids. Spatial analysis was carried out using GIS, and the results were presented in maps, tables, and figures.

Although the average wind speed did not exhibit a statistically significant change between the reference and future periods under the RCP8.5 climate change scenario, the wind power density demonstrated more spatial and quantitative variability. Specifically, the annual maximum wind power density increased from 112.70 W/m^2 to 122.33 W/m^2, while the minimum slightly decreased from 12.34 W/m^2 to 11.99 W/m^2. However, the overall average wind power density across Egypt declined. This apparent inconsistency is due to the nonlinear relationship between wind speed and wind power density, where even small increases in wind speed at certain locations can produce relatively large increases in power output. At the same time, this decline is mainly due to a decrease in the predicted air density that is greater than the rise in the expected wind speed under the future climate scenario (RCP8.5). This study demonstrates that climate change would have a slight adverse impact on wind power potential. Thus, it may not be able to produce more wind power in the future than it already does in current climate conditions.

Meeting increased power demand in the future can be accomplished by installing more wind farms. The findings revealed that wind power potential in the different sites would not change greatly under climate change, with different patterns in each area, however, the Gulf of Suez, Red Sea Coast, Sinai, and Kharga would have high annual mean wind density. Suitability analysis revealed that different parts have varied levels of suitability for future utilization of wind power. In this respect, the Suez Gulf region is expected to be the most suitable region, which is consistent with the state's plans for wind projects in this region. It can be expanded to other suitable areas, such as the Red Sea Coast and Sinai, for example, to establish more

projects to reach the desired percentage of electricity from wind.

In developing a strategy for wind energy utilization, it is essential to take into account not only the current situation but also predicted conditions under climate change and more viable measures.

It is important to note that the observed changes in wind speed and power density may fall within the typical range of modeling uncertainty. Therefore, the conclusions and recommendations are not only based on these numerical differences, but also on the absence of any substantial decline in wind resource potential, as well as the strategic importance of energy diversification.

Maximum utilization of wind power potential in Egypt under climate change requires:

• Integrating wind power into a diversified energy system can enhance energy security and its resilience. By combining various renewable energy sources including wind and solar power, with energy storage systems, a stable supply of energy can be maintained, especially under climate variability.

• As climate change may cause an increase in the magnitude and frequency of extreme weather events, there is a need to develop and implement comprehensive disaster preparedness and response plans for wind farms to minimize damage due to extreme weather events. For example, wind turbines should be designed and constructed to withstand extreme weather conditions. This includes using materials and engineering techniques that can resist high winds, heavy precipitation, and temperature fluctuations. Regular maintenance and inspection of turbines are also essential to identify and address any wear and tear due to climate impacts.

• Plan new wind farms or expand existing ones by taking into account long-term climate projections. By using climate data and models, developers can choose sites that are less vulnerable to extreme weather events, such as hurricanes, storms, or prolonged heatwaves.

• Implementing adaptive management practices allows for the flexibility to adjust operations in response to changing climate conditions. Regularly reassessing the risks and vulnerabilities associated with climate change can assist in ensuring proper and viable investment concerning renewable energy utilization.

• Promoting policy-relevant research on wind energy potentials under climate change can support generating knowledge and thus more informed policy and decision-making process.

• Encouraging collaboration between climate researchers and renewable energy stakeholders can improve wind power resilience. Research can focus on developing advanced weather forecasting models, understanding climate change impacts on wind patterns, and optimizing wind turbine technologies.

• Adopting a more participatory approach actively engaging different stakeholders including local communities in decision-making processes and encouraging renewable energy adoption can foster community support and enhance the long-term sustainability of wind power projects.

• Increasing awareness of climate change impacts and the importance of renewable energy and promoting renewable energy initiatives can encourage public-private partnerships in the renewable energy sector. This may require developing policies that promote renewable energy adoption by implementing measures such as providing financial incentives for climate-resilient projects.

Limitations and Future Work

This study provides insights into the spatial and temporal variability of wind power potential under projected climate conditions. While the findings lead to a broader understanding of future wind energy resources, several limitations have been identified that may influence the interpretation of the results. Recognizing these limitations is essential for guiding more targeted research in the future. First, the analysis relied on a single regional climate model (RCM) under a single climate change scenario (RCP8.5), which may not fully capture the range of possible climate futures. Therefore, multiple RCMs and climate scenarios such as RCP4.5 or Shared Socioeconomic Pathways (SSPs) should be incorporated in future analyses to improve the robustness and generalizability of the results. Second, the land suitability assessment was limited to proximity constraints such as roads, power grids, protected areas, archaeological sites, and touristic destinations. Certain land use categories were not fully integrated, such as military zones, urban expansion areas, high-value agricultural lands, and airport zones. It is recommended that future studies incorporate these additional constraints to enhance the practical feasibility of the selected sites. Third, all suitability criteria were assigned equal weights, which may not reflect the importance of each criterion. Future studies could apply multi-criteria decision-making techniques, such as the Analytic Hierarchy Process or fuzzy logic, to assign relative weights. Fourth, the reference period (1970–2005) may not fully represent current climatic conditions, particularly given recent trends in climate variability, and the collected data are at a height of 10 meters. It is recommended to use more recent reference periods, such as the 2000–2020 period, higher temporal resolution data, and extrapolate wind speeds to turbine hub heights, such as 50–100 meters, to enhance practical relevance. Fifth, wind speed modeling involves a degree of uncertainty, especially when using data from only one regional climate model and low spatial resolution. These uncertainties can affect how accurately wind power density is estimated. To improve future results, it is recommended to use multiple climate models and apply downscaling techniques to reduce uncertainty and increase confidence in the projections. Finally, although this study evaluated wind power density across Egypt and performed an analysis at eight selected sites using ArcGIS tools, these locations may not fully capture the local variability of wind resources. Future research could benefit from focusing on only a single location using the same methodology with higher-resolution spatial and climate data, possibly combined with ground-based measurements to enhance the local accuracy and provide deeper insights into wind power potential.

REFERENCES

Abbas W., Hassan A., & Ismael H. (2021). Climate Change Impact On Renewable Energy Resources In The Arab World Based On Jacobson's Roadmap Of Renewable Wind, Water, And Sunlight (Wws) 2050. Geography, Environment, Sustainability, 14(2), 92–104.

Ahmed A. S. (2010). Wind energy as a potential generation source at Ras Benas, Egypt. Renewable and Sustainable Energy Reviews, 14(8), 2167–2173.

Ahmed A. S. (2012). Potential wind power generation in South Egypt. Renewable and Sustainable Energy Reviews, 16(3), 1528–1536.

Ahmed A. S. (2018a). Wind energy characteristics and wind park installation in Shark El-Ouinat, Egypt. Renewable and Sustainable Energy Reviews, 82, 734–742.

Ahmed A. S. (2018b). Wind resource assessment and economics of electric generation at four locations in Sinai Peninsula, Egypt. Journal of Cleaner Production, 183, 1170–1183.

Al-Riffai P., Blohmke J., Breisinger C., & Wiebelt M. (2015). Harnessing the sun and wind for economic development? An economy-wide assessment for Egypt. Sustainability, 7(6), 7714–7740.

Atici K. B., Simsek A. B., Ulucan A., & Tosun M. U. (2015). A GIS-based Multiple Criteria Decision Analysis approach for wind power plant site selection. Utilities Policy, 37, 86–96.

Aydin N. Y., Kentel E., & Duzgun S. (2010). GIS-based environmental assessment of wind energy systems for spatial planning: A case study from Western Turkey. Renewable and Sustainable Energy Reviews, 14(1), 364–373.

Clarke L., Wei Y.-M., de la Vega Navarro, A., Garg A., Hahmann A. N., Khennas S., Azevedo I. M. L., Löschel A., Singh A. K., & Steg, L. (2022). Energy systems. In Climate Change 2022: Mitigation of Climate Change. Working Group III Contribution to the IPCC Sixth Assessment Report (pp. 69–77). Cambridge University Press. https://doi.org/10.1017/9781009157926.008

Cronin J., Anandarajah G., & Dessens O. (2018). Climate change impacts on the energy system: a review of trends and gaps. Climatic Change, 151, 79–93. https://doi.org/10.1007/s10584-018-2265-4

Ebinger J., & Vergara W. (2011). Climate impacts on energy systems: key issues for energy sector adaptation. The World Bank. https://doi.org/10.1596/978-0-8213-8697-2

Effat H. A. (2014). Spatial modeling of optimum zones for wind farms using remote sensing and geographic information system, application in the Red Sea, Egypt. Journal of Geographic Information System, 6(4), 358–374.

El-Ahmar M. H., El-Sayed A.-H. M., & Hemeida A. M. (2017). Evaluation of factors affecting wind turbine output power. 2017 Nineteenth International Middle East Power Systems Conference (MEPCON), 1471–1476.

Elgeziry M. Z., Kawady T. A., Elkalashy N. I., Elsadd M. A., Izzularab M. A., El-Khayat M. M., & Taalab A.-M. I. (2019). Integration enhancement of grid-connected wind farms using HVDC systems: Egyptian network case study. 2019 21st International Middle East Power Systems Conference (MEPCON), 502–508.

Elmahmoudi F., El kheir Abra O., Raihani A., Serrar O., & Bahatti L. (2020). GIS based Fuzzy Analytic Hierarchy Process for wind energy sites selection in Tarfaya Morocco. 2020 IEEE International Conference of Moroccan Geomatics (Morgeo), 1–5.

Eshete S., & Abate T. (2022). Wind energy potential assessment in Nifas Mewucha, Amhara Province, Ethiopia. Wind Engineering, 46(1), 23–33.

Fant C., Schlosser C. A., & Strzepek K. (2016). The impact of climate change on wind and solar resources in southern Africa. Applied Energy, 161, 556–564.

Feng J. (2021). Wind farm site selection from the perspective of sustainability: A novel satisfaction degree-based fuzzy axiomatic design approach. International Journal of Energy Research, 45(1), 1097–1127.

Gebaly A. M., Nashwan M. S., Khadr W. M. H., & Shahid S. (2023). Future changes in wind energy resources in Egypt under Paris climate agreements' goals. Regional Environmental Change, 23(2), 1–14.

Ghanem A., & Elsobki M. S. (2024). Wind Power Development in Egypt: Historical Overview, Current Status, and Perspectives. Athens Journal of Mediterranean Studies (AJMS), 11(1), 21–46. https://doi.org/10.30958/ajms.11-1-2

Hamouda Y. A. (2012). Wind energy in Egypt: Economic feasibility for Cairo. Renewable and Sustainable Energy Reviews, 16(5), 3312–3319.

Hassaan M. A. (2018). Using scholarly big data in assessing contribution of national expertise to climate change knowledge; case study: Egypt. Journal of Data Analysis and Information Processing 06: 67-78. 10.4236/jdaip.2018.63005

Hassaan M. A., Hassan A., & Al-Dashti H. (2021). GIS-based suitability analysis for siting solar power plants in Kuwait. The Egyptian Journal of Remote Sensing and Space Science, 24(3), 453–461. https://doi.org/10.1016/j.ejrs.2020.11.004

Hassaan M. A., Abdrabo M. A. K. A., Hussein H. A., Ghanem A., & Abdel-Latif H. (2024). Potential Impacts of Climate Change on Renewable Energy in Egypt. Environmental Monitoring and Assessment, 196(3), 268. https://doi.org/10.1007/s10661-024-12428-1

IRENA. (2023). Renewable Power Generation Costs in 2022. International Renewable Energy Agency (IRENA), Abu Dhabi.

Lashin A., & Shata, A. (2012). An analysis of wind power potential in Port Said, Egypt. Renewable and Sustainable Energy Reviews, 16(9), 6660–6667.

Mahdy M., & Bahaj A. S. (2018). Multi criteria decision analysis for offshore wind energy potential in Egypt. Renewable Energy, 118, 278–289.

Nabipour N., Mosavi A., Hajnal E., Nadai L., Shamshirband S., & Chau K.-W. (2020). Modeling climate change impact on wind power resources using adaptive neuro-fuzzy inference system. Engineering Applications of Computational Fluid Mechanics, 14(1), 491–506. https://doi.org/10.1080/19942060.2020.1722241

Nagi A. A., & Nagi H. A. (2002). Archaeological and tourist attractions in Egypt. Cairo: Dar Nahdat El Sharq.

Ohba M. (2019). The impact of global warming on wind energy resources and ramp events in Japan. Atmosphere, 10(5), 265.

Pachauri R. K., Allen M. R., Barros V. R., Broome J., Cramer W., Christ R., Church J. A., Clarke L., Dahe Q., & Dasgupta P. (2014). Climate change 2014: synthesis report. Contribution of Working Groups I, II and III to the fifth assessment report of the Intergovernmental Panel on Climate Change. IPCC.

Pakere I., Kacare M., Grāvelsiņš A., Freimanis R., & Blumberga A. (2022). Spatial analyses of smart energy system implementation through system dynamics and GIS modelling. Wind power case study in Latvia. Smart Energy, 7, 100081.

Pereira E. B., Martins F. R., Pes M. P., da Cruz Segundo E. I., & Lyra A. de A. (2013). The impacts of global climate changes on the wind power density in Brazil. Renewable Energy, 49, 107–110.

Rao K. R. (2019). Wind Energy: Technical Considerations. In Wind energy for power generation: meeting the challenge of practical implementation. Springer Nature.

Razeghi M., Hajinezhad A., Naseri A., Noorollahi Y., & Moosavian S. F. (2023). Multi-criteria decision for selecting a wind farm location to supply energy to reverse osmosis devices and produce freshwater using GIS in Iran. Energy Strategy Reviews, 45, 101018.

Rediske G., Burin H. P., Rigo P. D., Rosa C. B., Michels L., & Siluk J. C. M. (2021). Wind power plant site selection: A systematic review. Renewable and Sustainable Energy Reviews, 148, 111293.

REN21. (2023). Renewables in Energy Supply. In Renewables 2023 Global Status Report (GSR).Paris

Salah S. I., Eltaweel M., & Abeykoon C. (2022). Towards a sustainable energy future for Egypt: A systematic review of renewable energy sources, technologies, challenges, and recommendations. Cleaner Engineering and Technology, 8, 100497.

Saleous N., Issa S., & Al Mazrouei J. (2016). GIS-based wind farm site selection model offshore Abu Dhabi Emirate, UAE. The International Archives of the Photogrammetry, Remote Sensing and Spatial Information Sciences, 41, 437–441.

Samak Y. A. A. (2023). Geospatial Multi-criteria Analysis for Solar and Wind Power Modelling for Kingdom of Saudi Arabia's Population Using GIS: A Case Study for the Cities of Makkah and Jeddah. American Journal of Geographic Information System, 12(1), 28–42.

Sawadogo W., Reboita M. S., Faye A., da Rocha R. P., Odoulami R. C., Olusegun C. F., Adeniyi M. O., Abiodun B. J., Sylla M. B., & Diallo I. (2021). Current and future potential of solar and wind energy over Africa using the RegCM4 CORDEX-CORE ensemble. Climate Dynamics, 57(5–6), 1647–1672.

Sliz-Szkliniarz B., Eberbach J., Hoffmann B., & Fortin M. (2019). Assessing the cost of onshore wind development scenarios: Modelling of spatial and temporal distribution of wind power for the case of Poland. Renewable and Sustainable Energy Reviews, 109, 514–531.

Smith J., Deck, L., McCarl B., Kirshen P., Malley J., & Abdrabo M. (2013). Potential impacts of climate change on the Egyptian economy. In Report of a study implemented under the UN Climate Change Risk Management Joint Programme funded by the UN MDG Fund and the Finnish Government, prepared for the United Nations Development Programme (UNDP) with the Government of Egypt, UNDP, Cairo, Egypt.

Tercan E., Tapkın S., Latinopoulos D., Dereli M. A., Tsiropoulos A., & Ak M. F. (2020). A GIS-based multi-criteria model for offshore wind energy power plants site selection in both sides of the Aegean Sea. Environmental Monitoring and Assessment, 192, 1–20.

Tong, W. (2010). Fundamentals of wind energy. In Wind Power Generation and Wind Turbine Design (p. 8). WIT Transactions on State of the Art in Science and Engineering, WIT press. https://doi.org/10.2495/978-1-84564- / 205-101

RESEARCH PAPER

STATISTICAL METHOD FOR REDUCING THE NUMBER OF CLIMATIC PREDICTORS IN SPECIES DISTRIBUTION MODELING

Igor O. Popov[1,2*], Elena N. Popova[2]

[1]Yu. A. Israel Institute of Global Climate and Ecology, Glebovskaya str., 20B, Moscow,107258, Russia

[2]Institute of Geography, Russian Academy of Sciences, Staromonetniy pereulok, 29/4, Moscow,119017, Russia

***Corresponding author:** igor_o_popov@mail.ru**

Received: November 16th 2024 / Accepted: July 21st 2025 / Published: October 1st 2025

https://doi.org/10.24057/2071-9388-2025-3734

ABSTRACT. Nineteen bioclimatic parameters from BIOCLIM are widely used in Species Distribution Modeling (SDM). To improve modeling quality, it is essential to reduce the number of parameters. Several approaches have been proposed to solve this challenge, but each has its own limitations. In this study, we aimed to develop an effective statistical method based on identifying correlation groups of parameters and selecting the least correlated ones. Several statistical techniques were used to ensure a reliable parameter selection: simple correlation matrix analysis, cluster analysis (HDBSCAN), and factor analysis (varimax and quartimax). As an example, bioclimatic parameter values for the period 1991–2020 were analyzed for the whole globe. The results obtained using different methods show good consistency. Several correlation groups were identified, ranging from four to five, depending on the interpretation of the negative correlations. One group of two parameters, BIO14 and BIO17, can also be identified based on the results of the varimax factor analysis, although this correlation group was not identified by other methods. Finally, six bioclimatic parameters were selected (BIO2, BIO5, BIO7, BIO14, BIO15, and BIO18), one from each group that demonstrated the minimum average value of the correlation coefficient with parameters from other groups. The average correlation between the selected parameters was significantly lower than in the case of using previously applied methods with the same number of selected parameters.

KEYWORDS: species distribution modeling, data dimension, cluster analysis, factor analysis, HDBSCAN

CITATION: I. O. Popov, E. N. Popova (2025). Statistical Method For Reducing The Number Of Climatic Predictors In Species Distribution Modeling. Geography, Environment, Sustainability, 3 (18), 19-31
https://doi.org/10.24057/2071-9388-2025-3734

ACKNOWLEDGEMENTS: The studies were supported by the grant of the Ministry of Science and Higher Education of Russian Federation (agreement № 075-15-2024-554 of 24.04.2024).

Conflict of interests: The authors reported no potential conflict of interests.

INTRODUCTION

Living organisms, as open systems, are affected by the environment. Climatic factors, particularly ambient temperature, are the most significant abiotic factors determining the existence and reproduction of individuals and populations. For terrestrial organisms, humidity is also an important factor (Bonan 2008; Schimel 2013). Climate change has various effects on land and marine ecosystems, including their structure, species composition, and relationships between components. The most significant issue is the impact of climate and climate change on species distribution, including shifts in their ranges (McCarty 2001; Gilman et al. 2010; Post 2013).

The assessment of potential changes in species distribution, particularly those important for economic activity and human health, presents a significant challenge for modern science. Currently, the main methodological approach to this issue is Species Distribution Modeling (SDM), which is a rapidly evolving field at the intersection of ecology, biogeography, applied climatology, and information technology (Franklin 2009; Peterson et al. 2011; Araújo et al. 2019; Srivastava et al. 2019). Various algorithms are used to construct these models, including general-purpose machine learning techniques such as support vector machines, logistic regression, and neural networks, as well as specialized methods designed for habitat modeling, the most commonly used of which is MaxEnt (Phillips et al. 2004; Phillips et al. 2006).

Although a wide variety of environmental factors, both abiotic and biotic, can be used as predictors of species distribution in these models, climate variables play a major role in almost all models, as they have a fundamental limiting effect on organism ranges (Popova and Popov 2013; Popova and Popov 2019). Obviously, it is possible to design a huge, if not infinite, number of such variables. However, not all variables will correlate well with distribution data or be significant for range formation, and not all will be convenient for projecting models to other regions of the world.

In 1984, BIOCLIM was proposed as one of the first methods for constructing Species Distribution Models (Nix 1986; Busby 1991). This software package included a set of 12 climatic parameters, specifically designed to be

biologically significant for most species and suitable for projecting models across hemispheres. The package was developed by a group of Australian scientists and was initially used to assess the invasive potential of different species. In 1996, a new version of this software package was presented, with the number of bioclimatic parameters increased to 19 (Booth 2018). Their list is given in Table 1. The names of these parameters begin with the prefix BIO, followed by a number from 1 to 19 (BIO1-BIO19).

As shown in Table 1, the first 11 parameters (BIO1-BIO11) are related to temperature, while the remaining 8 (BIO12-BIO19) reflect a precipitation regime. There is no specific mention of a particular month or season. Instead, periods of the year with the highest or lowest temperatures, or the highest or lowest precipitation, are used. This makes it easy to move models between regions with different annual climatic variation, like hemispheres. In addition, four parameters (BIO8, BIO9, BIO18, and BIO19) are "mixed", reflecting the values of climatic factors of one type over a period determined by factors of another type. Such an arrangement can be useful for modeling the ranges of certain species, but it can also cause some problems in certain cases. For instance, they can have a very high gradient of spatial variability in some regions, particularly in equatorial and tropical areas. Some researchers recommend avoiding the use of these parameters or using them with extreme caution (Booth 2022).

The design of the BIOCLIM parameters has been so successful that they are widely used in SDM and other areas of ecological modeling. This set was further popularized with the release of the WorldClim database in 2005 and its second version in 2017[1]. This database contains values for six continents and is interpolated onto a spatial grid with a step of up to 30" (Hijmans et al. 2005; Fick and Hijmans 2017). According to the study (Bradie and Leunig 2017), the BIOCLIM parameters have been used significantly more often than other climate variables in the modeling of nearly 1900 species in about 2000 publications.

However, using a large number of potential predictors has several disadvantages. First, it introduces a challenge known as the "curse of dimensionality" in machine learning. As the number of independent variables increases, so does the distance between samples in feature space. That can result in inaccuracies in the classification of virtual space (Hastie et al. 2009) and lead to overfitting of models, when a model that fits too well to the training data classifies new data with a high error rate. Additionally, a large number of variables can significantly increase the computational load, especially when analyzing large amounts of data.

In addition to the above-mentioned problems, climate variables have a fairly strong correlation between each other, which can also influence the performance of several algorithms (for instance, in the case of MaxEnt). Furthermore, when it is necessary to assess the predictor significance for classification, which in SDM may be linked to their biological significance for a particular species, the presence of strongly correlated variables may lead to an inaccurate assessment of their significance, especially when using ensemble techniques based on decision trees such as "random forest" or gradient boosting.

One possible approach to reducing the number of predictors is to create new variables based on linear or non-linear combinations of the original variables. These new variables should retain as much information as

Table 1. Bioclimatic parameters

BIO1	annual mean temperature
BIO2	mean diurnal range (mean of monthly (max temp - min temp))
BIO3	isothermality (BIO2/BIO7) (×100)
BIO4	temperature seasonality (standard deviation ×100)
BIO5	max temperature of warmest month
BIO6	min temperature of coldest month
BIO7	temperature annual range (BIO5-BIO6)
BIO8	mean temperature of wettest quarter
BIO9	mean temperature of driest quarter
BIO10	mean temperature of warmest quarter
BIO11	mean temperature of coldest quarter
BIO12	annual precipitation
BIO13	precipitation of wettest month
BIO14	precipitation of driest month
BIO15	precipitation seasonality (coefficient of variation)
BIO16	precipitation of wettest quarter
BIO17	precipitation of driest quarter
BIO18	precipitation of warmest quarter
BIO19	precipitation of coldest quarter

[1] *https://www.worldclim.org*

possible while being significantly smaller in number. Common methods for such reduction include various versions of Principal Component Analysis (PCA), Locally-Linear Embedding (LLE) and Multidimensional Scaling (MDS), among others (Roweis and Saul 2000). In particular, the study (Dinnage 2023) used a neural network Variable Autoencoder (VAE) to reduce the set of WorldClim variables to 5 synthetic variables without significant information loss. These synthetic variables are nonlinear combinations of the original 19 parameters. However, the disadvantage of this approach is that the obtained variables are artificial. It complicates a biological interpretation of the results.

An alternative approach is to identify correlation groups of the actual variables, i.e., groups with a higher correlation within than between them. From these groups, we can select variables that either have the lowest correlation with the other groups or are particularly significant for a specific study. Typically, this approach eliminates variables that demonstrate a high level of correlation with each other; for example, if the value of a correlation coefficient is above a certain threshold (Bellard et al. 2013; Petrosyan et al. 2023; Zhang et al. 2023). However, such simultaneous pairwise reduction may result in the loss of several important variables since a variable that is highly correlated with one or more variables may also be weakly correlated with other variables. In addition, the choice of a selection threshold is not always clear.

As an alternative to the strategies described, we propose using statistical methods to identify correlation groups. This approach involves using algorithms that allow for the identification of fine structures and groups in data based on various types of relationships between its elements. For this purpose, we used a modern, highly effective clustering algorithm called HDBSCAN. Two methods of factor analysis, varimax and quartimax, were also used as an alternative approach to verifying the clustering results. These three algorithms were used for the first time to solve this problem.

After identifying the correlation groups, our approach involves selecting one parameter from each group with the least mean correlation to parameters from other groups. The identification of correlation groups allows us to determine the optimal number of selected parameters. This number balances the minimization of the correlation between parameters with their minimum sufficient quantity.

The aim of this study was to evaluate the effectiveness of the proposed approach to reducing the number of SDM predictors using 19 bioclimatic parameters calculated for the entire globe as an example.

MATERIALS AND METHODS

Climate data

The climate data source used in this study was the CRU TS 4.05 database (Harris et al. 2020), which contains the results of meteorological observations with a monthly resolution, interpolated onto a regular spatial grid with a step of 0.5°. This database is widely used in SDM. In particular, it forms the basis for the popular bioclimatic database WorldClim, which was discussed in the introduction. The fact that CRU is based on meteorological observations affords it several advantages over reanalysis, such as ERA5. Many studies have found that reanalysis often produces erroneous results, especially with respect to precipitation data, which is of special importance for SDM (Purnadurga et al. 2019; Bodjrènou et al. 2025; Fatolahzadeh et al. 2024).

In total, this grid contains 67,420 nodes with values, as the nodes over the seas, oceans, and Antarctica do not have climate variables' values. Nineteen bioclimatic parameters were calculated according to their description in Table 1 for the entire globe, using temperature variables and monthly precipitation amounts. These values were averaged over the period 1991-2020 for each node in the spatial grid.

As a result of the calculations, each of the 67,420 spatial nodes was characterized by 19 bioclimatic parameters. Based on this data, linear correlation coefficients were calculated for each pair of parameters to form a correlation matrix with a size of 19×19.

All calculations in this work were performed using the Python 3 programming language. A Python 3 module for the calculation of bioclimatic parameters is available in the repository[2]. Jupyter notebooks containing the calculations and some additional materials are available in the repository[3].

Cluster analysis

To identify correlation groups among bioclimatic parameters, cluster analysis was used. This method allows the identification of groups of objects (in this study, sets of bioclimatic parameter values) that are closer together than other objects. In other words, it helps to detect areas of increased density in the space of objects. Cluster analysis can use different metrics to measure the distance between objects. In this study we used metrics based on the linear correlation coefficient to measure the distance between the values of bioclimatic parameters. This allows us to determine groups of parameters that have a higher correlation with each other than with other parameters.

Currently, there are many methods of cluster analysis (Wierzchoń and Kłopotek 2018). In this work, we used the HDBSCAN (Hierarchical Density-Based Spatial Clustering of Applications with Noise) algorithm, which is an evolution of the DBSCAN and OPTICS methods (Campello et al. 2013; McInnes and Healy 2017). A special feature of this method is that it can independently determine the number of clusters and identify noise points – samples that do not belong to any cluster and can be considered as single-sized clusters. Furthermore, it does not require access to the original data but only a matrix of distances between the analyzed samples.

In its modern form, the HDBSCAN algorithm includes several stages of data processing:

1. Transformation of the original sample space to better select areas of increased density, using the method described and justified in the paper (Eldridge et al. 2015).
2. Construction of a graph where the vertices are the samples, and the edge weights are equal to the distance between the samples. The graph is then transformed into a minimum spanning tree, which is a graph where each vertex has at least one connection to other vertices, and the total weight of all the edges is minimized.
3. Construction of a hierarchical cluster tree based on the obtained minimum connected tree.
4. Transformation of the hierarchical cluster tree into a flat cluster system. At this stage, both user-defined hyperparameters (minimum cluster size and ε – minimum allowable distance between clusters) and several parameters calculated directly from the data are used. This distinguishes the HDBSCAN method from DBSCAN, which only identifies clusters based on the specified hyperparameters.

[2]https://doi.org/10.5281/zenodo.13913422
[3]https://doi.org/10.5281/zenodo.13970876

When analyzing a small number of samples, as in this study, it is recommended to set the minimum cluster size to 2. In this case, ε becomes the only hyperparameter that needs to be optimized to find the optimal value that provides the best quality of cluster selections. (Malzer and Baum 2020).

The distance between bioclimatic parameters was determined using two different metrics. These metrics differ in their assessment of negative correlations. Negative correlation, like positive correlation, implies the presence and duplication of information about one variable in another variable, albeit in a different sense. This type of correlation can also negatively affect the quality of the modeling.

The first metric, d1, considers negative correlation values as an indicator of a greater distance between parameters. It is calculated using the Eq. 1:

$$d_1 = 1 - r \tag{1}$$

where r is the linear correlation coefficient.

This metric ranges from 0 (for parameters with a perfect positive correlation) to 2 (for parameters with a perfect negative correlation).

The second metric, d_2, considers negative correlation as equivalent to positive correlation. It is calculated using the absolute value of the correlation coefficient (Eq. 2):

$$d_2 = 1 - |r| \tag{2}$$

This metric ranges from 0, where the parameters have correlation coefficients of 1 or -1, to 1, where there is a complete lack of correlation between the parameters.

To select the optimal value for the hyperparameter ε, the average value of the silhouette coefficients was used (Rousseeuw 1987). This is one of the most commonly used metrics for evaluating clustering quality. The implementation of the HDBSCAN algorithm from the scikit-learn machine learning library[4] was used in this study.

Factor analysis

Another alternative approach that we used to identify correlation groups is factor analysis. This method is used in conjunction with cluster analysis to increase the reliability and validity of the results.

Factor analysis is based on the assumption that there are a small number of latent variables (called factors) underlying the observed variables. Observed variables can be expressed as linear or non-linear combinations of factors (Mulaik 2009; Gorsuch 2014). The most common model currently used is the linear model for the relationship between factors and observed variables. It can be expressed mathematically as (Eq. 3):

$$X = AP + U + E \tag{3}$$

where X is a matrix of observed values with m rows and n columns, corresponding to n observed variables and m samples. P is a matrix of factor scores. It has a size of $k \times m$ ($k << n$) and contains columns with the coordinates of the observed variables in the new space of k factors. U is a matrix of deviations from the mean of the observed values, and E is an error matrix. A is called a factor matrix of size $n \times k$. Its elements are called factor loadings, which are the coordinates of the factor space basis and reflect the influence of the factors on the observed variables (Reyment and Jöreskog 1996).

Before conducting factor analysis, it is common to standardize the values of the observed variables. This process leads to the matrix U becoming a zero matrix. This simplifies further analysis.

The goal of further calculations is to determine a matrix A in which the factor loadings of each variable for different factors are as distinct as possible, while minimizing the number of factors and the values of the elements in the error matrix E. The most common approach to solving this problem is the so-called "rotation". It involves rotating the initial basis or its subset in the space of observed variables by a certain angle. This operation is done to satisfy the criteria mentioned above. The resulting factors can be either orthogonal or non-orthogonal, depending on the specific rotation method used.

These methods are based on a specific criterion for optimally choosing the factor matrix. Historically, the first criterion was the quartimax method proposed in the work (Ferguson 1954). This criterion corresponds to the maximization of the criterion q_4, which is the sum of the factor loadings aij in the fourth power (Eq. 4):

$$q_4 = \sum a_{ij}^4 \rightarrow maximum \tag{4}$$

A feature of this method is that it tends to produce factors that are too general. The number of factors produced is too small, and each of these factors has too great an influence on several observed variables simultaneously. Nevertheless, this criterion is still in use today.

As a development of the quartimax method, the varimax method was proposed in the work (Kaiser 1958). According to it, the criterion to be maximized is

$$V_{varimax} = \sum_i \left[\sum_j \left(\frac{a_{ij}}{\sqrt{\sum_j aij^2}} \right)^4 - \frac{\left(\sum_j \left(\frac{a_{ij}}{\sqrt{\sum_j a_{ij}^2}} \right)^2 \right)^2}{n} \right] \rightarrow maximum \tag{5}$$

where a_{ij} are the elements of the factor matrix A and n is the number of observed variables.

There are several other rotation methods available, both orthogonal (such as oblimax, equimax, and parsimax) and non-orthogonal (including promax and quartimin). Each of these methods has its set of benefits and drawbacks. However, varimax and quartimin, which are both orthogonal, are currently the most commonly used in factor analysis.

As can be seen, the search for a factor matrix is reduced to solving an optimization problem of the corresponding criterion. Currently, several methods are used for this purpose, the most effective of which is recognized as the Gradient Projection Algorithm (GPA) (Jennrich 2001; Jennrich 2004).

In this study, two rotation methods were used to identify correlation groups among bioclimatic parameters: quartimax and varimax. Their implementation in the scikit-learn package was used. Before the analysis, the values of the bioclimatic parameters were standardized.

[4] *https://scikit-learn.org/stable*

According to the accepted approach, it was considered that the identified factor could be defined as the main factor for a certain parameter (in other words, the parameter could be attributed to a certain correlation group) if its loading value was maximum (since loadings can have negative values, we will talk hereinafter about their absolute values) and exceeded the values of the loadings of other factors by at least 30%. If there were one or more factors with a lower loading value and the difference in loadings did not exceed 30% of the maximum value, then a conclusion was drawn about the influence of several main factors on the bioclimatic parameter (Mulaik 2009).

RESULTS

Correlation matrix analysis

Fig. 1 shows a heatmap of the correlation matrix for all 19 bioclimatic parameters. This matrix contains Pearson linear correlation coefficients *r*. As can be seen, all bioclimatic parameters can be divided into several groups.

Firstly, two groups of parameters are distinguished, containing temperature (BIO1-BIO11, excluding BIO4 and BIO7) and humidity (BIO12-BIO19, excluding BIO15) factors. Within these groups, the correlations are significantly higher than those between parameters from different groups. Within the first group, the correlation coefficients ranged from 0.53 to 0.99, with an average of 0.829. In the second group, they ranged from 0.45 to 0.99, averaging 0.712. The correlation coefficients between the groups ranged from -0.05 to 0.63, with an average of 0.32.

Secondly, two factors stand out among the temperature parameters: BIO4 and BIO7. These factors characterize the annual temperature range and have a fairly strong negative correlation with most other parameters, except for BIO7 and BIO2. There is also a strong positive correlation between BIO4 and BIO7 ($r = 0.97$).

The BIO2 parameter also stands out, having a fairly weak positive correlation with the temperature parameters (ranging from 0.08 to 0.29), and a weak negative correlation with the humidity parameters (ranging from -0.14 to -0.3), except for BIO15 ($r = 0.38$).

The parameter BIO15, in turn, also stands out among the other humidity parameters. It has a negative or very weak positive (with BIO13) correlation with other humidity parameters and a low positive correlation (from 0.17 to 0.38) with most temperature parameters, except for the above-described BIO4 and BIO7, with which it has *r* values equal to -0.12 and -0.03, respectively.

Thus, five correlation groups can be distinguished already at the stage of simple analysis of the correlation matrix of bioclimatic parameters:

1. BIO1, BIO3, BIO5, BIO6, BIO8-BIO11
2. BIO12-BIO14, BIO16-BIO19
3. BIO4, BIO7
4. BIO2
5. BIO15.

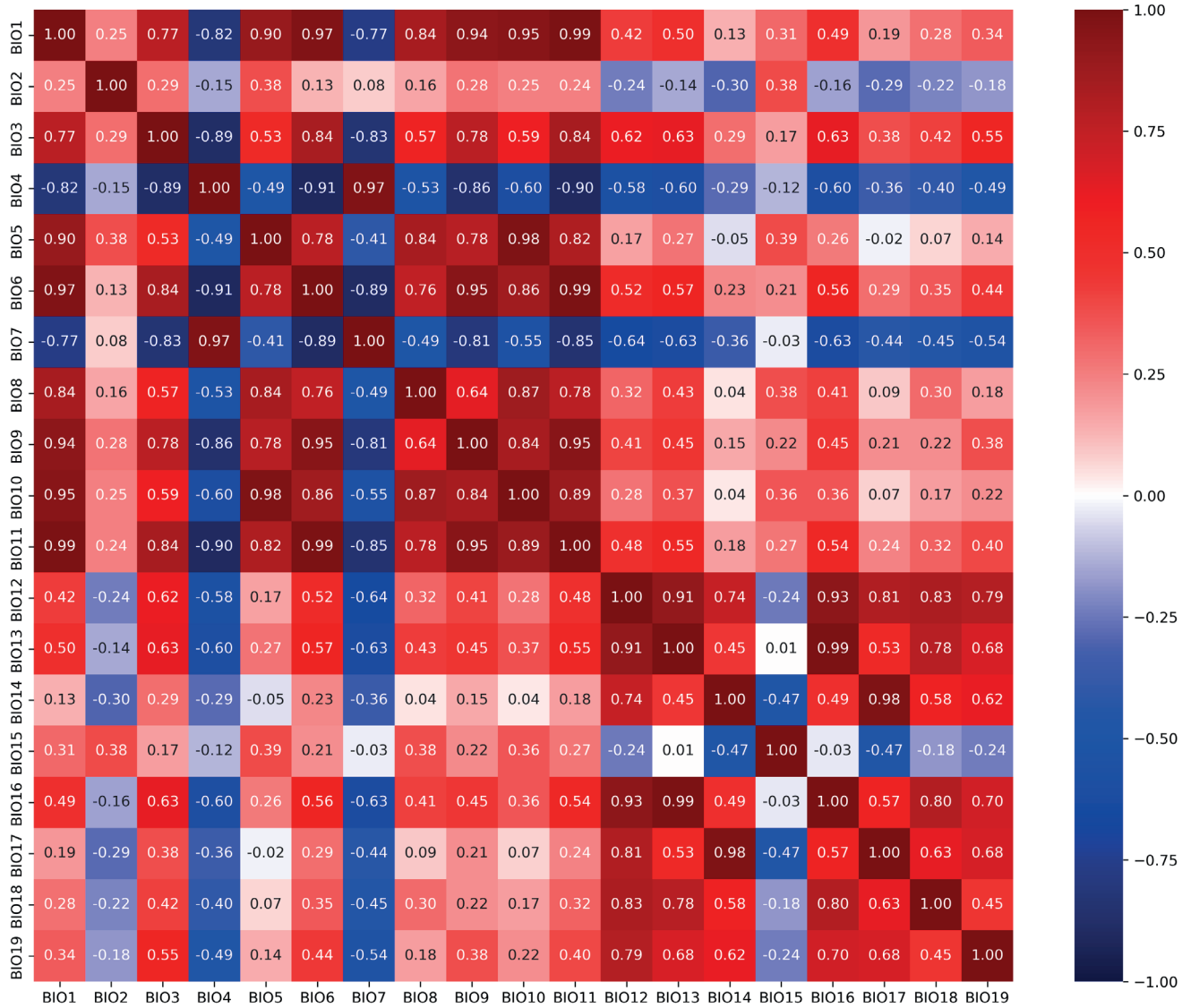

Fig. 1. Heatmap of the correlation matrix of bioclimatic parameters

Results of the cluster analysis

The optimal value of the hyperparameter ε for the HDBSCAN algorithm was found by simply enumerating its possible values in the range from 0.01 to 0.5, with a step size of 0.01. For the metric d_1, the optimal ε value was found to be in the range of 0.19-0.36, giving an average silhouette coefficient of 0.6336. For the metric d_2, the same range of values (0.19-0.36) was found to provide the optimal ε, with an average silhouette coefficient of 0.5531.

Table 2 shows the obtained distribution of bioclimatic parameters by clusters for the two distance metrics used. The noise points are marked with a value of -1. As can be seen, when using the d_1 metric, the HDBSCAN algorithm identified three clusters and two noise points. In the case of the d_2 metric, two clusters and two noise points were identified. In both cases, the BIO2 and BIO15 parameters were identified as noise points. Cluster 1 was completely the same for both metrics. Cluster 0, obtained for the d_2 metric, when using the d_1 metric, was divided into two clusters: 0 and 2. In this case, cluster 2 contained the parameters BIO4 and BIO7.

As can be seen, the results of the cluster analysis coincide completely with the results of a simple analysis of the correlation matrix. The noise points (BIO2 and BIO15 parameters) were previously assigned to groups 4 and 5, respectively. Cluster 1 corresponds to group 2, and cluster 0 (d_2 metric) includes groups 1 and 3. When the d_1 metric is used, clusters 0 and 2 coincide completely with these groups.

Results of the factor analysis

Table 3 shows the results of the factor analysis (factor matrix and identified main factors) conducted using the varimax method. As can be seen, varimax identifies 5 factors. Meanwhile, for most bioclimatic parameters, it can be concluded that there is only one main factor.

The temperature parameters BIO1 and BIO3-BIO11 are influenced by the main factor 1, which is consistent with the results of the correlation matrix analysis and cluster analysis.

The parameters BIO4 and BIO7 are also influenced by the main factor 3. This conclusion is consistent with the results of the cluster analysis, which allocated them to cluster 2 when using the metric d_1 and combined them with cluster 0, corresponding to factor 1 when using the metric d_2. In this case, the loadings of factor 1 for these parameters are positive, unlike the loadings of the other temperature parameters, for which they are negative. This means a different nature of the influence of factor 1 on these parameters, and corresponds to the negative correlation of the parameters BIO4 and BIO7 with the other temperature parameters (except BIO2). These circumstances allow us to allocate the parameters BIO4 and BIO7 to a separate group, if we take into account the nature of their correlation with other temperature parameters, or to combine them if the sign of the correlation coefficient is considered to be unimportant.

The BIO2 parameter has one main factor, 5, which is not the main factor for any other parameter. This corresponds to the allocation of this factor to a separate group 4 and to a separate noise point.

Table 2. Belonging of the studied bioclimatic parameters to the selected clusters according to two metrics

Bioclimatic parameter	Cluster number	
	metric d_1	metric d_2
BIO1	0	0
BIO2	-1	-1
BIO3	0	0
BIO4	2	0
BIO5	0	0
BIO6	0	0
BIO7	2	0
BIO8	0	0
BIO9	0	0
BIO10	0	0
BIO11	0	0
BIO12	1	1
BIO13	1	1
BIO14	1	1
BIO15	-1	-1
BIO16	1	1
BIO17	1	1
BIO18	1	1
BIO19	1	1

Table 3. Factor matrix of the bioclimatic parameters obtained using the varimax method (loadings of the main factors are highlighted)

Parameter	Factor loadings					Main factor
	1	2	3	4	5	
BIO1	**-0.9393**	0.2066	-0.2091	0.0183	-0.0338	1
BIO2	-0.2896	-0.2246	-0.0365	-0.2483	**-0.5180**	5
BIO3	**-0.6146**	0.4194	-0.4777	0.0983	-0.1950	1
BIO4	**0.6481**	-0.3408	**0.6066**	-0.1174	0.0304	1.3
BIO5	**-0.9362**	0.0151	0.1118	-0.0779	-0.0902	1
BIO6	**-0.8679**	0.2764	-0.3608	0.0902	0.0142	1
BIO7	**0.5878**	-0.3902	**0.6036**	-0.1867	-0.0852	1.3
BIO8	**-0.8371**	0.2314	0.1058	-0.0916	0.0079	1
BIO9	**-0.8548**	0.1491	-0.3749	0.0748	-0.0605	1
BIO10	**-0.9579**	0.0986	0.0285	-0.0312	-0.0168	1
BIO11	**-0.8915**	0.2533	-0.3324	0.0422	-0.0432	1
BIO12	-0.2235	**0.8269**	-0.1694	0.4163	0.0242	2
BIO13	-0.3051	**0.8701**	-0.1482	0.1011	0.0163	2
BIO14	-0.0141	0.4509	-0.0585	**0.7711**	0.0280	4
BIO15	-0.3547	-0.0657	0.0470	**-0.5679**	-0.1909	4
BIO16	-0.2923	**0.8753**	-0.1525	0.1422	0.0178	2
BIO17	-0.0488	0.5216	-0.1043	**0.7473**	0.0183	4
BIO18	-0.1147	**0.7889**	-0.0327	0.2531	0.0673	2
BIO19	-0.1780	**0.5949**	-0.2218	0.4326	-0.0451	2

The humidity parameters BIO12, BIO13, BIO16, BIO18, and BIO19 have one main factor, 2, which corresponds to their assignment to cluster 1 and correlation group 2.

The parameters BIO14, BIO15, and BIO17 are influenced by one main factor, 4, which distinguishes them from the other parameters. At first glance, they could be combined into one group on this basis. However, the values of the loadings of factor 4 for these parameters have a peculiarity: the loading of the parameter BIO15 is negative, and that of BIO14 and BIO17 is positive. This distinction means that this factor determines these parameters in different senses: it has a negative relationship with BIO15 and a positive relationship with BIO14 and BIO17. This difference can also be seen in the correlation matrix: BIO14 and BIO17 have a strong positive correlation with each other (r = 0.98) and a moderate negative correlation with BIO15 (r = -0.47 for both parameters). In addition, BIO14 and BIO17 have quite large positive loadings for factor 2. The loadings of the other humidity bioclimatic parameters, for which this factor is the main one, are also positive. At the same time, the loading of factor 2 for BIO15 is very low. These results allow us to single out the parameter BIO15 as a separate group, as well as the parameters BIO14 and BIO17, but this group has a relative proximity to the parameters that are influenced by factor 2, as by the main one.

Table 4 shows the factor matrix obtained as a result of applying the quartimax method.

All temperature parameters, except BIO2, are influenced by factor 1. Simultaneously, the parameters BIO4 and BIO7 have loadings of the main factor with signs opposite to the signs of loadings for the other parameters. This finding is consistent with the negative correlation between these groups of parameters. A similar situation was observed when using the varimax method, as well as cluster analysis, which, when using the d_1 metric, singled out these parameters into a separate group, and when using the d_2 metric, combined them with other temperature parameters.

The parameter BIO2 is influenced by one main factor, 4, for which it is the only parameter with a significant load value.

All the humidity parameters are influenced by the main factor 2. At the same time, the parameters BIO14 and BIO17 do not differ from other parameters, as was the case with the varimax method. But the parameter BIO15 is determined not only by the factor 2 but also by the main factor 3, which does not influence any other parameter. The loading value of factor 2 for BIO15 also has a different sign from the sign of the loadings of this factor for other humidity parameters. These results obtained on the basis of the quartimax method allow us to single out the parameter BIO15 into a separate group and to combine the other humidity parameters. This data is consistent with the results of the correlation matrix analysis, cluster analysis, and partly with the results of using the varimax method.

In general, it is possible to note the consistency of the results obtained from all applied methods for identifying correlation groups. At the same time, factor analysis is

Table 4. Factor matrix of bioclimatic parameters obtained using the quartimax method (loadings of the main factors are highlighted)

Parameter	Factor loadings				Main factor
	1	2	3	4	
BIO1	**-0.9782**	0.0875	0.0013	0.0039	1
BIO2	-0.2851	-0.3667	-0.0766	**-0.4936**	4
BIO3	**-0.7772**	0.3583	-0.0554	-0.1790	1
BIO4	**0.8274**	-0.3108	-0.0107	0.0122	1
BIO5	**-0.8659**	-0.1456	0.0005	-0.0456	1
BIO6	**-0.9579**	0.2029	0.0282	0.0449	1
BIO7	**0.7688**	-0.3988	-0.0406	-0.0978	1
BIO8	**-0.7973**	0.0454	-0.1254	0.0440	1
BIO9	**-0.9367**	0.0872	0.0772	-0.0274	1
BIO10	**-0.9161**	-0.0458	0.0047	0.0257	1
BIO11	**-0.9731**	0.1523	-0.0006	-0.0096	1
BIO12	-0.3533	**0.9003**	-0.0335	0.0069	2
BIO13	-0.4409	**0.7659**	-0.3197	0.0093	2
BIO14	-0.0623	**0.7781**	0.4386	0.0009	2
BIO15	-0.3410	**-0.3957**	**-0.4259**	-0.1593	2, 3
BIO16	-0.4294	**0.7930**	-0.2879	0.0092	2
BIO17	-0.1186	**0.8247**	0.3872	-0.0083	2
BIO18	-0.2088	**0.7885**	-0.1648	0.0506	2
BIO19	-0.2984	**0.7201**	0.0901	-0.0608	2

distinguished by greater complexity in interpreting the results, although it allows the detection of some subtle properties of the data not revealed by other methods.

Selection of parameters from the identified correlation groups

On the basis of the above results, it is possible to identify five groups of bioclimatic parameters, the correlation within which is higher than the correlation with parameters from other groups. The composition of these groups is presented in Table 5.

In case it is assumed that the negative correlation has the same value as the positive one, it is possible to combine groups 5 and 1. Also, from the results of the factor analysis using the varimax method, it follows that the parameters BIO14 and BIO17 can be separated, if necessary, from group 2 into a separate group 6 (for example, if it is known that they are of particular importance for modeling the distribution of the species under study).

Next, a final selection of parameters was carried out, one from each identified group that demonstrated minimal correlation with parameters from other groups. For this purpose, the average values of the corresponding linear correlation coefficients and their absolute values were calculated (Table 6).

Based on the results presented in Tables 5 and 6, a list of selected bioclimatic parameters can be proposed as follows:

1. BIO2 (mean diurnal range (mean of monthly (max temp - min temp)))
2. BIO5 (max temperature of warmest month)
3. BIO7 (temperature annual range BIO5-BIO6)
4. BIO14 (precipitation of driest month)

Table 5. Identified correlation groups of bioclimatic parameters

Group	Bioclimatic parameters
1	BIO1, BIO3, BIO5, BIO6, BIO8-BIO11
2	BIO12-BIO14, BIO16-BIO19
3	BIO2
4	BIO15
5	BIO4, BIO7

Table 6. Average values of correlation coefficients *r* and average absolute values of correlation coefficients |*r*| between bioclimatic parameters and parameters from other groups (the minimum values in each group are highlighted)

Bioclimatic parameter	Average value	
	r	| *r* |
Group 1		
BIO1	0.121	0.409
BIO3	0.206	0.519
BIO5	**0.064**	**0.242**
BIO6	0.136	0.464
BIO8	0.117	0.303
BIO9	0.100	0.405
BIO10	0.087	0.296
BIO11	0.134	0.452
Group 1 (including BIO4 and BIO7)		
BIO1	0.324	0.324
BIO3	0.443	0.443
BIO4	-0.396	0.396
BIO5	0.179	**0.194**
BIO6	0.367	0.367
BIO7	**-0.404**	0.422
BIO8	0.256	0.256
BIO9	0.308	0.308
BIO10	0.234	0.234
BIO11	0.358	0.358
Group 2		
BIO12	0.127	0.409
BIO13	0.201	0.429
BIO14	**-0.034**	**0.211**
BIO16	0.190	0.427
BIO17	-0.008	0.253
BIO18	0.073	0.282
BIO19	0.100	0.342
Group 2 (without BIO14 and BIO17)		
BIO12	0.219	0.462
BIO13	0.242	0.438
BIO16	0.239	0.442
BIO18	**0.149**	**0.328**
BIO19	0.179	0.386

Group 5		
BIO4	-0.544	**0.554**
BIO7	**-0.563**	0.563
Group 6		
BIO14	**0.145**	**0.389**
BIO17	0.184	0.434

5. BIO15 (precipitation seasonality (coefficient of variation))

6. If it is necessary to separate group 6 from group 2, BIO18 (precipitation of the warmest quarter) can be added to this list, but this should be done with caution due to the mixed nature of this parameter and the possible negative effects associated with it when constructing species distribution models (see Introduction).

If the same meaning of positive and negative correlations is accepted, the parameter BIO7 can be removed from the list due to the merging of groups 2 and 5. Scatter plots of the mutual dispersion of these six parameters and the values of their correlation coefficients r are presented in Fig. 2.

As can be seen in Fig. 2, the maximum value of the correlation coefficient between the selected parameters is 0.389 (BIO5 and BIO15). In absolute value, it is -0.582 (BIO14 and BIO18). Generally, the correlation between these selected parameters is quite low.

To compare the results obtained, we selected parameters using a method based on pairwise correlation threshold. Only those parameters were selected that had values of the linear correlation coefficient *r* below a certain value. As a result, only two parameters were selected at the threshold of 0.7 (BIO2 and BIO15), three parameters were selected at the threshold of 0.8 (BIO2, BIO15 and BIO19), five parameters at the threshold of 0.85 (BIO2, BIO3, BIO15, BIO18, and BIO19) and six parameters at the threshold of 0.9 (BIO 2, BIO 3, BIO8, BIO15, BIO18 and BIO19). Different

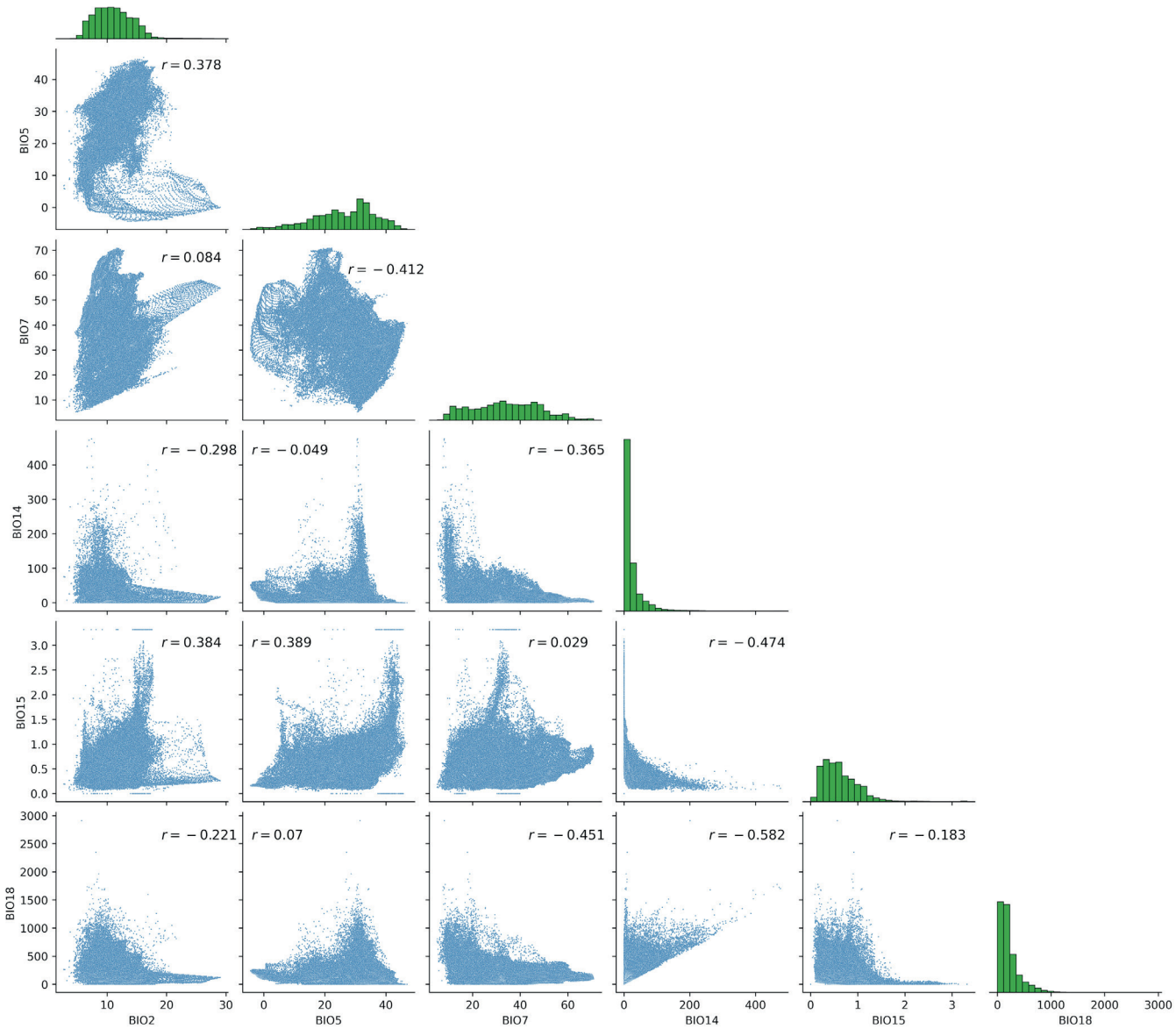

Fig. 2. Scatter plots, linear correlation coefficients r and histograms of distributions (on the diagonal) for six selected bioclimatic parameters

threshold values lead to different numbers of selected parameters. What threshold must be used is unclear. At threshold 0.85 maximum value of the linear correlation coefficient is 0.575 (BIO3 and BIO8), which is significantly higher than the maximum value for the method we used (0.389). The number of parameters with low correlation coefficients with other selected parameters were lost. As can be seen, this comparative study indicates that the approach we used for the analyzed data is more effective than the commonly used method based on selection by correlation threshold.

DISCUSSION

As noted in the introduction, the problem of reducing the number of predictors in SDM, as in any classification problem, is an important step in reducing the overfitting of the constructed models. The resource for this reduction is the presence of redundant information in the initial set of predictors, expressed in a high level of correlation between them.

As can be seen in the results of this study, the statistical approach we proposed made it possible to reduce the pairwise correlation to a low level. At the same time, the number of selected predictors (5 or 6), as experience shows, is sufficient to build effective species distribution models. It can be noted that the number of main correlation groups of bioclimatic parameters identified in this study coincides with the number of synthetic variables obtained as a result of using a neural network of the Variable Autoencoder type in the paper (Dinnage 2023), which was mentioned in the introduction.

The use of the HDBSCAN cluster analysis algorithm to identify correlation groups in our study showed its effectiveness. With its help, a fairly large number of clusters with a good level of difference between them were identified. At the same time, the technology of its application and, importantly, the interpretation of the obtained results are easy to use and can be applied routinely.

The results of factor analysis, in general, with the exception of some nuances, corresponded to the results of the cluster analysis. This fact confirms the reliability of the results of the cluster analysis. The assignment of a number of parameters to several main factors is quite consistent with the presence of a high negative correlation between the parameters. When using factor analysis, it is important to pay attention to the sign of the loading. However, it should be noted that the sufficient complexity and ambiguity of the interpretation of the factor analysis results make it less preferable for routine use in SDM practice compared to cluster analysis.

Our proposed approach to the final selection of parameters from correlation groups is not the only possible one. Firstly, it is possible to select them based on the special significance of any parameter for the vital activity of the organism, known in advance from physiological or ecological studies. Secondly, it is possible to make a selection based on the results of a preliminary distribution modeling using an unreduced set of predictors, followed by analysis of their importance for model construction. Approaches based on the jackknife principle, with successive elimination of parameters or modeling using only one parameter, can be applied. Thirdly, the approach used in our work can also estimate the correlation in the final set of predictors in another way. For example, we can use multiple correlation metrics, such as the variance inflation factor (VIF).

In this study, the values of 19 bioclimatic parameters were analyzed across the globe for the period of 1991–2020. Obviously, even when analyzing this set of parameters for a narrower geographic area or for a different time period, different results can be obtained. The degree and nature of the correlation between these variables vary in time and space, and also depend on the spatial scale of their calculation (Dormann et al. 2012).

Reducing the number of predictors while preserving the information they contain as much as possible is a common problem in machine learning and predictive systems, as noted in the introduction. The approach proposed in this work can be applied to a wide variety of areas related to modeling and forecasting, including both classification and regression. First of all, it can be useful for climatological and meteorological studies, since meteorological and climatological parameters tend to strongly correlate with each other.

CONCLUSIONS

In the course of the conducted studies, using several methods, it was shown that, for the period 1991-2020, for the entire territory of the Earth, it is possible to identify 4-6 correlation groups of bioclimatic parameters, depending on the interpretation of the negative correlation. From these groups, it is possible to select six bioclimatic parameters that demonstrate a minimum average correlation with parameters from other groups. The obtained results are an illustration of the proposed method for reducing bioclimatic parameters and focusing on the selected time period and geographical area. They are of a recommendatory nature. The developed approach to reduce the number of predictors can be used in various areas of statistical modeling and forecasting, both in classification and in regression analysis.

REFERENCES

Araújo M.B., Anderson R.P., Barbosa M.A., Beale C.M., Dormann C.F., Early R., Garcia R.A., Guisan A., Maiorano L., Naimi B., O'Hara R.B., Zimmermann N.E., and Rahbek C. (2019). Standards for distribution models in biodiversity assessments. Science advances, 5(1), DOI: 10.1126/sciadv.aat4858.

Bellard C., Thuiller W., Leroy B., Genovesi P., Bakkenes M., and Courchamp F. (2013). Will climate change promote future invasions? Global Change Biology, 12(19), 3740–3748, DOI: 10.1111/gcb.12344.

Bodjrènou R., Sintondji L., N'Tcha Y., Germain D., Azonwade F., Sohindji F., Hounnou G., Amouzouvi E., Kpognin A., and Comandan F. (2025). Assessment of Hydrologic Data Estimates From ERA5 Reanalyses in Benin, West Africa. Geoscience Data Journal, 12(1), 1-16, DOI: 10.1002/gdj3.288

Bonan G.B. (2008). Ecological Climatology. 2nd ed. Cambrige: Cambrige University Press, DOI: 10.1017/CBO9780511805530.

Booth T.H. (2018). Why understanding the pioneering and continuing contributions of BIOCLIM to species distribution modelling is important. Austral Ecology, 43(8), 852-860, DOI: 10.1111/aec.12628.

Booth T.H. (2022). Checking bioclimatic variables that combine temperature and precipitation data before their use in species distribution models. Austral Ecology, 47(7), 1506-1514, DOI: 10.1111/aec.13234.

Bradie J. and Leunig B. (2017). A quantitative synthesis of the importance of variables used in MaxEnt species distribution models. Journal of Biogeograhy, 44(6), 1344–1361, DOI: 10.1111/jbi.12894.

Busby J. R. (1991). BIOCLIM – A bioclimate analysis and prediction system. Plant Protection Quarterly, 6(1), 8–9.

Campello R.J.G.B., Moulavi D., and Sander J. (2013). Density-Based Clustering Based on Hierarchical Density Estimates. In: J. Pei, V.S. Tseng, L. Cao, H. Motoda, and G. Xu, eds., Advances in Knowledge Discovery and Data Mining. PAKDD 2013. Lecture Notes in Computer Science, 7819. Berlin, Heidelberg: Springer, 160-172, DOI: 10.1007/978-3-642-37456-2_14.

Dinnage R. (2023). How many variables does Wordclim have, really? Generative A.I. unravels the intrinsic dimension of bioclimatic variables. bioRxiv preprint, DOI: 10.1101/2023.06.12.544623.

Dormann C.F., Elith J., Bacher S., Buchmann C., Carré G., Marquéz J.R.G., Gruber B., Lafourcade B., Leitão P.J., Münkemüller T., McClean C., Osborne P.E., Reineking B., Schröder B., Skidmore A.K., Zurell D., and Lautenbach, S. (2012). Collinearity: a review of methods to deal with it and a simulation study evaluating their performance. Ecography, 36(1), 27–46, DOI: 10.1111/j.1600-0587.2012.07348.x.

Eldridge J., Belkin M., and Wang Y. (2015). Beyond Hartigan Consistency: Merge Distortion Metric for Hierarchical Clustering. Proceedings of The 28th Conference on Learning Theory. Proceedings of Machine Learning Research, 40, 588-606.

Fatolahzadeh G. A., Maghoul P., Ojo E.R., and Shalaby A. (2024). Reliability of ERA5 and ERA5-Land reanalysis data in the Canadian Prairies. Theoretical and Applied Climatology, 155(4), 3087-3098, DOI: 10.1007/s00704-023-04771-z.

Ferguson G. A. (1954). The concept of parsimony in factor analysis. Psychometrika, 19, 281–290, DOI: 0.1007/BF02289228.

Fick S.E. and Hijmans R.J. (2017). WorldClim 2: new 1km spatial resolution climate surfaces for global land areas. International Journal of Climatology, 37(12), 4302-4315, DOI: 10.1002/joc.5086.

Franklin J. (2009). Mapping species distributions. Spatial inference and prediction. Cambridge: Cambridge University Press. DOI: 10.1017/CBO9780511810602.

Gilman S.E., Urban M.C., Tewksbury J., Gilchrist G.W., and Holt R. D. (2010). A framework for community interactions under climate change. Trends in Ecology and Evolution, 25(6), 325-331, DOI: 10.1016/j.tree.2010.03.002.

Gorsuch R.L. (2014). Factor Analysis. New York: Routledge. DOI: /10.4324/9781315735740

Harris I., Osborn T.J., Jones P., and Lister D. (2020). Version 4 of the CRU TS Monthly High-Resolution Gridded Multivariate Climate Dataset. Scientific Data, 7(109), DOI: 10.1038/s41597-020-0453-3.

Hastie T., Tibshirani R., and Friedman J. (2009). The Elements of Statistical Learning. Data Mining, Inference, and Prediction. Second Edition. New York: Springer. DOI: 10.1007/978-0-387-84858-7.

Hijmans R. J., Cameron S. E., Parra J. L., Jones P. G., and Jarvis A. (2005). Very high resolution interpolated climate surfaces for global land areas. International Journal of Climatology, 25(15), 1965–1978, DOI: 10.1002/joc.1276.

Jennrich R.I. (2001). A simple general procedure for orthogonal rotation. Psychometrika, 66(2), 289-306, DOI: 10.1007/BF02294840.

Jennrich R.I. (2004). Derivative free gradient projection algorithms for rotation. Psychometrika, 69(3), 475-480, DOI: 10.1007/BF02295647.

Kaiser H.F. (1958). The varimax criterion for analytic rotation in factor analysis. Psychometrika, 23(3), 187-200, DOI: 10.1007/BF02289233.

Malzer C. and Baum M. (2020). A Hybrid Approach To Hierarchical Density-based Cluster Selection. 2020 IEEE International Conference on Multisensor Fusion and Integration for Intelligent Systems (MFI), Karlsruhe, Germany, 2020, 223-228, DOI: 10.1109/MFI49285.2020.9235263.

McCarty J.P. (2001). Ecological Consequences of Recent Climate Change. Conservation Biology, 15(2), 320–331, DOI: 10.1046/j.1523-1739.2001.015002320.x.

McInnes L. and Healy J. (2017). Accelerated Hierarchical Density Based Clustering. IEEE International Conference on Data Mining Workshops (ICDMW), New Orleans, LA, USA, 2017, 33-42, DOI: 10.1109/ICDMW.2017.12.

Mulaik S.A. (2009). Foundations of Factor Analysis. 2nd ed. New York: Chapman and Hall/CRC, DOI: 10.1201/b15851.

Nix H.A. (1986). A biogeographic analysis of Australian elapid snakes. In: R. Longmore, ed., Atlas of Elapid Snakes of Australia. Australian Flora and Fauna Series No. 7. Canberra: Australian Government Publishing Service, 4-15.

Peterson A.T., Soberón J., Pearson R.G., Anderson R.P., Martínez-Meyer E., Nakamura M., and Araújo M.B. (2011). Ecological niches and geographic distributions. Princeton and Oxford: Princeton University Press, DOI: 10.1515/9781400840670.

Petrosyan V., Osipov F., Feniova I., Dergunova N., Warshavsky A., Khlyap L., and Dzialowski A. (2023). The TOP-100 most dangerous invasive alien species in Northern Eurasia: invasion trends and species distribution modelling. NeoBiota, 82, 23–56, DOI: 10.3897/neobiota.82.96282.

Phillips S., Dudík M., and Schapire R.E. (2004). A Maximum Entropy Approach to Species Distribution Modeling. In R. Greiner and D. Schuurmans, eds., Proceedings, Twenty-First International Conference on Machine Learning, ICML 2004, 655-662, DOI: 10.1145/1015330.1015412.

Phillips S.J., Anderson R.P., and Schapire R.E. (2006). Maximum entropy modeling of species geographic distributions. Ecological Modelling, 190(3), 231-259, DOI: 10.1016/j.ecolmodel.2005.03.026.

Popova E.N. and Popov I.O. (2013). Climatic factors determining ranges of agricultural pests and agents of plant diseases and model methodology for assessment of change in ranges. Problems of Ecological Monitoring and Ecosystem Modelling, 25, 177–206 (in Russian with English summary).

Popova E.N. and Popov I.O. (2019). Modeling of potential climatic ranges of biological species and their climate-driven changes. Fundamental and Applied Climatology, 1, 58-75, DOI: 10.21513/2410-8758-2019-1-58-75 (In Russian with English summary).

Post E. (2013). Ecology of Climate Change. The Importance of Biotic Interactions. Princenton and Oxford: Princenton Unversity Press. DOI: 10.2307/j.ctt2jc8jj.

Purnadurga G., Kumar T., Kundeti K., Barbosa H., and Mall R. (2019). Evaluation of evapotranspiration estimates from observed and reanalysis data sets over Indian region. International Journal of Climatology, 39(15), DOI: 10.1002/joc.6189.

Reyment R.A. and Jöreskog K. G. (1996). Applied Factor Analysis in the Natural Sciences. Cambridge: Cambridge University Press.

Rousseeuw P. J. (1987). Silhouettes: A graphical aid to the interpretation and validation of cluster analysis. Journal of Computational and Applied Mathematics, 20, 53-65, DOI: 10.1016/0377-0427(87)90125-7.

Roweis S.T. and Saul L.K. (2000). Nonlinear Dimensionality Reduction by Locally Linear Embedding. Science, 290(5500), 2323-2326, DOI: 10.1126/science.290.5500.2323.

Schimel D. (2013). Climate and ecosystems. Princenton and Oxford: Princenton Unversity Press.

Srivastava V., Lafond V., and Griess V.C. (2019). Species distribution models (SDM): Applications, benefits and challenges in invasive species management. CAB Reviews: Perspectives in Agriculture, Veterinary Science, Nutrition and Natural Resources, 14(20), 1-13, DOI: 10.1079/PAVSNNR201914020.

Wierzchoń S. and Kłopotek M. (2018). Modern Algorithms of Cluster Analysis. Studies in Big Data, 34. Cham: Springer, DOI: 10.1007/978-3-319-69308-8.

Zhang H., Zheng S., Huang T., Liu J., and Yue J. (2023). Estimation of potential suitable habitats for the relict plant Euptelea pleiosperma in China via comparison of three niche models. Sustainability, 15(14), 1-23, DOI: 10.3390/su151411035.

RESEARCH PAPER

RADIATION PARAMETERS OF THE PEAT BOG DUE TO PERMAFROST CONDITIONS VARIATIONS: A CASE STUDY OF THE OMA RIVER BASIN OF THE NENETS AUTONOMOUS OKRUG, NORTHWEST OF RUSSIA

Andrey V. Puchkov[1*], Evgeny Yu. Yakovlev[1]

[1]N. Laverov Federal Centre for Integrated Arctic Research of the Ural Branch of Russian Academy of Sciences, 109 Severnoj Dviny Emb., Arkhangelsk, 163000, Russia

***Corresponding author:** andrey.puchkov@fciarctic.ru**

Received: December 12nd 2024 / Accepted: June 19th 2025 / Published: October 1st 2025

https://doi.org/10.24057/2071-9388-2025-3762

ABSTRACT. The purpose of this article is to examine the distribution of natural radionuclides as well as the gamma radiation flux due to the variations of soil seasonal thawing depth. The study was conducted at a lumpy peat bog located within the catchment area of the Oma River, located within the Nenets Autonomous Okrug of Russia. The site was selected due to the presence of an active layer (AL) with varying depths of thawing, as well as the warming effect of the river. This feature enabled an initial assessment of the impact of thawing depth on radon flux, gamma radiation, and the distribution of other natural radionuclides along the peat profile. Field observations revealed that permafrost deposits act as a barrier to the intake of ^{222}Rn from geological layers. The relationship between alterations in radiation parameters (gamma radiation flux, radon flux density (RFD), radionuclide composition of peat) and the thickness of the AL has been established. An increase in gamma radiation levels and RFD has been observed in areas exhibiting maximum seasonal thawing of the seasonally thawed layer. The correlation coefficients were found to be 0.70 and 0.83, respectively. The analysis of peat profiles in diverse permafrost settings revealed that in regions exhibiting deeper thawing of soil, there is an abundance of 210Pb relative to the concentration of its progenitor radionuclide, ^{226}Ra. The observed excess of ^{210}Pb may be attributed to radon flux from deeper geological layers.

KEYWORDS: radon, permafrost, Arctic, climate warming, natural radioactivity, frozen soil, peat bog

CITATION: Puchkov A. V., Yakovlev E. Yu. (2025). Radiation Parameters Of The Peat Bog Due To Permafrost Conditions Variations: A Case Study Of The Oma River Basin Of The Nenets Autonomous Okrug, Northwest Of Russia. Geography, Environment, Sustainability, 3 (18), 32-42

https://doi.org/10.24057/2071-9388-2025-3762

ACKNOWLEDGEMENTS: This work was supported by the Ministry of Science and Higher Education of the Russian Federation (FUUW-2025-0011, project No. 125022002727-2).

Conflict of interests: The authors reported no potential conflict of interests.

INTRODUCTION

Permafrost plays an integral role in the Arctic natural environment, exerting a considerable influence on global change and human activity (Streletskiy et al. 2023). An increase in air temperature and snow cover parameters, particularly a reduction in snow depth, results in permafrost degradation, which is manifested as an expansion of the permafrost roof depth in both Arctic and mountainous regions (Streletskiy et al. 2023). It is observed that alterations in the boundaries of permafrost are occurring (Zhang et al. 2021). The consequences of permafrost degradation are already evident in several significant incidents, including the formation of extensive sinkholes in the Yamalo-Nenets Autonomous Okrug (Buldovicz et al. 2018) and the collapse of industrial facilities in Norilsk (Koptev 2020). Furthermore, permafrost can exert a considerable influence on the distribution of chemical elements in the environment. Consequently, the degradation of permafrost may result in alterations to the chemical composition of the elements present, including radioactive elements, within soils and rocks (Shirokova et al. 2021; Pokrovsky et al. 2021; Puchkov et al. 2021).

Radon (^{222}Rn) is a member of the radioactive 238U family and is ubiquitous in environmental components on Earth. 222Rn is continuously formed in all geological environments. The ^{222}Rn decay sequence results in the emission of short-lived radioactive products, including ^{218}Po, ^{214}Pb, and ^{214}Bi, and long-lived ^{210}Pb and ^{210}Po, which are characterized by alpha and beta decay. The physical and chemical properties of ^{222}Rn and its decay products permit its utilization as a tracer for the investigation of a multitude of geological and atmospheric processes (Sabbarese et al. 2021; Giustini et al. 2019; Miklyaev et al. 2010; Baskaran et al. 2016; Daraktchieva et al. 2021; Selvam et al. 2021). Concurrently, ^{222}Rn and its decay products represent a

significant health risk, particularly in contexts where high concentrations are present, such as residential dwellings (Lorenzo-Gonzalez et al. 2020; Maier et al. 2021; Petrova et al. 2020; Rodríguez-Martínez et al. 2018; Rosenberger et al. 2018).

To date, there has been a paucity of scientific literature devoted to the behavior of ^{222}Rn and its decay products in frozen rocks and permafros, while simultaneously observing the thawing and alteration of phase boundaries, which in turn modifies the pathways for ^{222}Rn migration to the surface. The majority of these studies are of a theoretical nature (Puchkov et al. 2021). The results of the theoretical synthesis presented in Zhang et al. (2024) highlight the dearth of relevant studies on ^{222}Rn migration and its relationship in permafrost regions, underscoring the urgent need for further research in this area. As the authors observe, priority research areas include the study of ^{222}Rn migration mechanisms in freezing and thawing soils/rocks; the response to permafrost degradation due to the release of ^{222}Rn absorbed in permafrost soils; and ^{222}Rn migration in groundwater systems, among others. Scientists have published numerous articles on the experimental evaluation of ^{222}Rn migration under conditions of varying temperatures (Puchkov 2022; Ye 2024). It has been demonstrated in existing scientific literature that permafrost serves as an effective barrier to the upward migration of ^{222}Rn from the ground (Glover et al. 2022). This study highlights the necessity to extend these findings to other locations, given the heterogeneous and geographically distinctive nature of permafrost conditions. This prompts our investigation into the migration and flow of radioactive gases to the Earth's surface in the event of permafrost thawing.

The objective of this scientific article is to evaluate the flux of gamma radiation and RFD at the peat bog surface, as well as the distribution of natural radionuclides along the peat profile, under varying conditions of AL formation.

MATERIALS AND METHODS

Study area

The experimental site is situated in the Kanin tundra territory within the Nenets Autonomous Okrug in northwestern Russia (Fig. 2). The experimental site is the lumpy peat bog situated within the Oma River basin. Throughout the river basin, permafrost peat soils are prevalent. Soils of the alluvial soddy-gley and alluvial-boggy types are present along the riverbanks. Alluvial solonchak soils are found at the river mouth. In the Kanin tundra territory (Chizha, Nes, Vizhas and Omariver basins), the average AL depth is up to 0.4 m, according to Iglovsky (2010). Average annual soil temperatures in the study area can range from +1.5 to -1.3°C in the AL and down to -3.5°C in the upper permafrost layers (Iglovsky 2010). The peat deposit is characterized by an uneven degree of decomposition. The upper layers (10–15 cm deep) contain highly decomposed peat (over 40%) mixed with the remains of shrubs, herbaceous plants, and lichens. The middle layer (10–30 cm) consists of poorly decomposed (5–10%) sphagnum peat. The lower layer consists of medium-decomposed (20–25%) sedge-sphagnum peat. The weight moisture content of peat can vary widely, from tens of percent in the upper, highly decomposed layers to 1000–2000% in the lower, weakly decomposed layers of the peat deposit (Prokhorenko 2013). Hillock peat ash content can range from 1.5 to 10%, peaking in the lower part of the AL. Closer to the mineral layer, the peat's ash content can increase to several tens of percent (Prokhorenko 2013).

The choice of the experimental site is conditioned by the varying thawing levels of AL, including the warming effect of the river. This peculiarity allows for an initial approximation of the influence of thawing depth on the ^{222}Rn flux, gamma radiation, and the distribution of other natural radionuclides along the peat profile.

The methodology employed in the survey, along with the principal findings pertaining to the AL thaw depth, gamma radiation flux, and RFD estimation, are illustrated in Fig. 2. A total of 76 points were measured in the bog area, and two peat profile cuts were investigated. For gamma-spectrometric measurements, peat and soil samples from two peat profile cuts were taken by shovel in a 20×20 cm plot at 5 cm horizons. Peat and soils in frozen condition were cut with a battery-powered electric saw. Sample preparation and measurements were carried out at the Environmental Radiology Laboratory of the Northern Laverov Federal Center for Integrated Arctic Research of the Ural Branch of the Russian Academy of Sciences (Russia, Arkhangelsk). The selected samples were allowed to dry in a BINDER E28 desiccator at 105°C. After drying, soil and peat samples were ashed at a temperature not exceeding 400°C to avoid loss of radionuclides. Ashing the soil and peat samples is necessary to improve the radionuclide detection efficiency of the semiconductor detector. This is done by reducing the volume and weight of the sample and the distance between the sample and the detector. The radionuclide activity presented in this paper is on a dry weight.

Radiometric measurement method

The measurement of the RFD utilizes the radon radiometer «Alpharad plus» (manufacturer: NTM Protection, Moscow city, Russia) (Fig. 1). The measurements were conducted in accordance with the prescribed algorithms and in compliance with the instructions set forth in the operational manuals. The equipment employs a semiconductor detector in which electrostatically charged ^{218}Po ions are deposited. The radiation parameters of ^{222}Rn, including activity concentration and flux density, are determined by the number of registered alpha particles resulting from the decay of ^{218}Po atoms that fall on the detector (Afonin 2013).

Prior to the installation of the samplers, the soil surface was leveled and a 1 cm deepening was prepared. The sampler was left *in situ* for a period of 30 minutes, after which the air was pumped out of it into the measuring chamber of the radonometer. The measurements were conducted for a period of 20 minutes. In light of the necessity to perform a considerable number of RFD measurements, it was deemed appropriate to utilize two radon radiometers with identical technical specifications.

Gamma Spectrometry Measurements

Gamma spectrometry is a widely used method to measure gamma radiation from radionuclides of natural origin, including ^{226}Ra. It is a universal, non-destructive and easy-to-use method, especially at the stage of sample preparation and in the measurement process (Syam et al. 2020). The radionuclides ^{226}Ra, ^{232}Th, ^{210}Pb, and 40K were determined using a low-background semiconductor gamma spectrometer manufactured by ORTEC (USA). The instrument is based on a coaxial detector, the GMX25, which is made of high-purity germanium (HPGe). The spectrometer is equipped with SpectraLine software. The relative efficiency of the gamma-ray spectrometer is 25%.

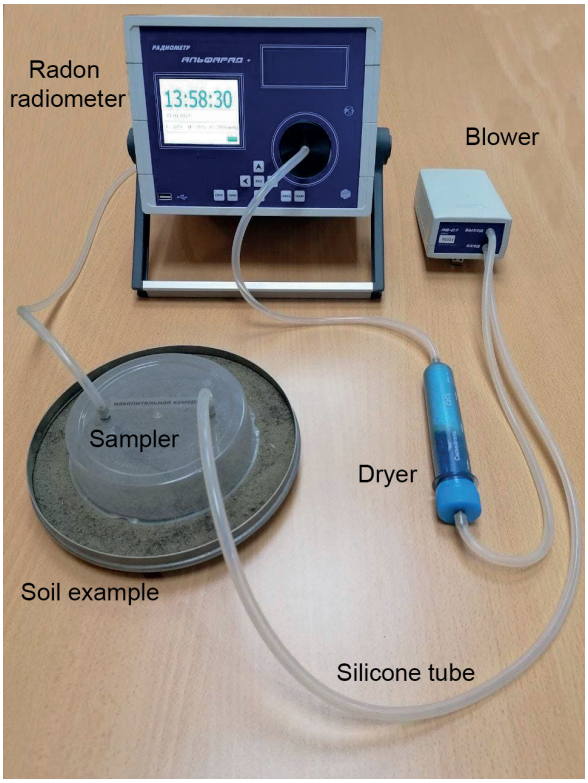

Fig. 1. The radon radiometer "Alpharad plus"

The calibration and quality control of gamma-spectrometric measurements were conducted using disc-type sources (OSGI-P) and special measures of volumetric activity, namely Marinelli beakers of varying density (RITWERZ, Russia-Germany). A plastic Petri dish with a diameter of 60 mm and a counting sample volume of 5 to 25 ml was chosen as the geometry for peat soil measurements. For clay bedrock samples, a 1-liter Marinelli vessel was used.

To achieve an equilibrium state of ^{226}Ra decay products, the counting sample was sealed for a period of approximately three weeks. The Petri dishes were sealed using a sealant and duct tape. The samples were measured for a minimum of 12,000 seconds. The primary gamma-ray energies of ^{214}Pb (351.93 keV) and ^{214}Bi (609.32 keV, 1120.29 keV, 1764.49 keV) were employed to detect ^{226}Ra and ascertain its activity concentration. The primary gamma-ray energies of ^{212}Pb (238.63 keV), ^{228}Ac (911.20 keV) and ^{208}Tl (583.19 keV, 2614.51 keV) were employed to identify ^{232}Th and quantify its activity concentration. In this study, it was assumed that the decay products of ^{232}Th and the parent radionuclide itself are in a state of radioactive equilibrium. The activity concentration of the radionuclide ^{210}Pb was determined from the 46.50 keV gamma ray line, while the activity concentration of radionuclide 40K was determined using the energy of 1460.82 keV.

Dosimetry measurements

To measure gamma radiation flux, the scintillation geological exploration radiometer SRP-88n was employed. The measurements were conducted in accordance with the prescribed algorithms and in compliance with the instructions set forth in the operational manuals. The height of the measurements at each point was 10 cm.

AL thaw level measurements

AL thawing level measurements were carried out using a contact thermometer TK-5.04 with a submersible probe of length L=500 mm. At each control point, the probe was immersed into the ground as far as it would go in at least 3 locations 10 cm apart. This method was used to exclude the probe stop in hard material (stone, wood). The parameter that indicated the level of ice in the ground was the probe temperature = 0 degrees Celsius. The level of ground thawing was measured by the depth of probe immersion. The average value of at least 3 immersions into the ground up to the ice stop was taken as the result.

Quality control of measurements

The determination of ^{222}Rn, ^{226}Ra, ^{232}Th, 40K, ^{210}Pb, and gamma ray flux was conducted utilizing the instrumentation of the Environmental Radiology Laboratory of the N. Laverov Federal Center for Integrated Arctic Research of the Ural Branch of the Russian Academy of Sciences (Russia, Arkhangelsk), which is in compliance with the accreditation criteria for testing laboratories as outlined in ISO/IEC 17025. The laboratory is equipped with an extensive range of reference radionuclide sources, which are employed for the calibration of equipment and the monitoring of measurement quality.

If the measurement result was beyond the sensitivity of the measuring instrument, parallel measurements were made at such points. The result was accepted if the following condition was fulfilled (Eq. 1):

$$\left|A_1 - A_2\right| < \sqrt{\delta A_1^2 + \delta A_2^2} \quad (1)$$

where A_1 and A_2 – measurement results; $\delta A_{1,2}$ – uncertainties of measurement results A_1 and A_2.

If the condition was not fulfilled, the measurement was repeated again.

Statistical analysis

Statistical analysis was performed using licensed software packages OriginPro and Microsoft Office. Mapping was carried out using Surfer software by Golden Software, Inc. (Golden, Colorado, USA).

RESULTS

The study scheme and the main results of AL thaw depth, gamma ray flux, and RFD are summarized in Fig. 2.

During the study period (July 2023), the greatest depth of AL thawing was observed along the edge of the bog (band width not exceeding 1-2 m), reaching 50-60 cm (bedrock level). From the edge of the bog, the thawing depth decreased markedly, with a range of 5 to 15 cm.

The gamma radiation flux within the area under study exhibits a range of 14.4 to 30.4 impulses per second, with an average value of 21.7 impulses per second. The results of the measurements indicated a slight increase in gamma ray flux in areas of maximum AL thawing within the peat strata. A comparable distribution pattern is evident for RFD in the area under study. The parameter in question exhibits a range of 6.0 to 44.0 mBq·m^{-2}·s^{-1}, with an average value of 16.4 mBq·m^{-2}·s^{-1}. The highest RFD values are observed along the edge of the peat bog, within a band with a width of no more than 1-2 m.

Two peat profile cuts were conducted within the bog, one at the edge (Profile 1) and one at a distance of 100 meters (Profile 2) (Fig. 3). The results of the assessment of the natural radionuclide content in samples from peat profile cuts are presented in Tables 1 and 2.

For the purposes of clarity and informative content, the results presented in Tables 1 and 2 are plotted in Fig. 4. As evidenced in Tables 1 and 2, the distribution of radionuclides ^{226}Ra, ^{210}Pb, ^{232}Th, and 40K exhibits a comparable pattern across the depth of peat profile cuts. In general, the values of these radionuclides are consistent with the available data for the Northwest region, as reported by Kriauciunas (2018), Yakovlev (2022, 2023).

The ^{210}Pb activity concentration ranges from the lowest measured values (2.3±1.1 Bq·kg^{-1} for the 20-25 cm horizon) to 330.0±60.0 Bq·kg^{-1} for peat profile 1 and from the lowest measured values (4.1±1.9 Bq·kg^{-1} for the 15-20 cm horizon) to 270.0±60.0 Bq·kg^{-1} for peat profile 2. The maximum activity concentration of ^{210}Pb (330.0±60.0 Bq·kg^{-1}) falls on the uppermost horizon (0-5 cm), which is a natural phenomenon given that the

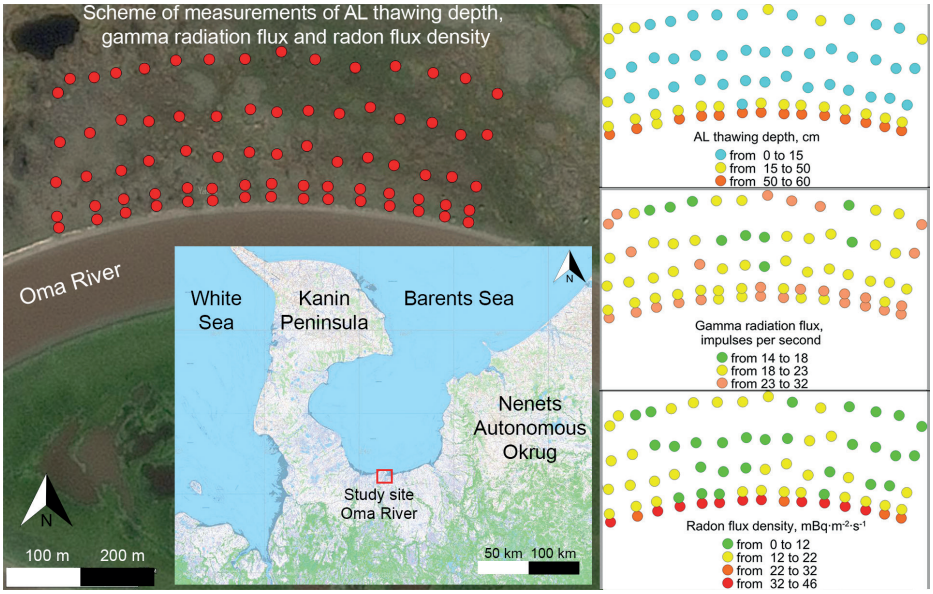

Fig. 2. Distribution of gamma ray flux, RFD over peat bog surface, and AL thawing depth in the Oma River basin

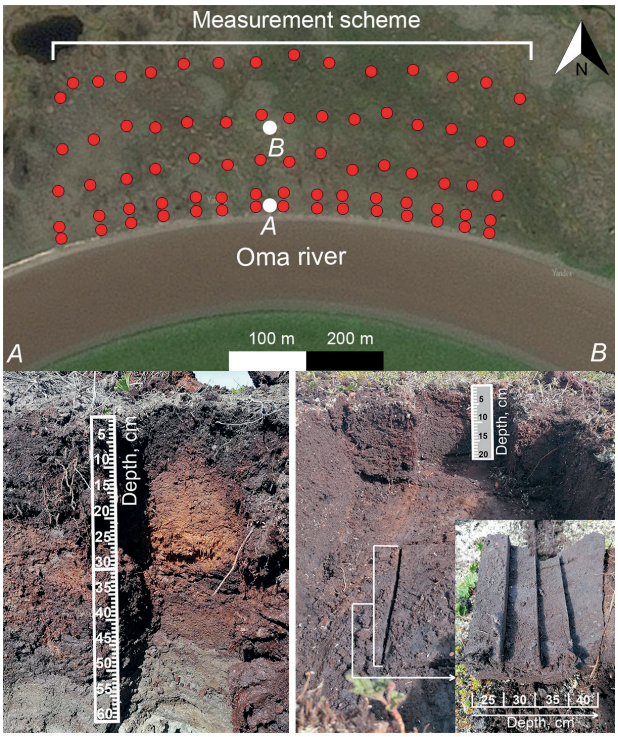

Fig. 3. Peat profile cuts at the edge of the bog (A, profile 1) and 100 m from the edge of the bog (B, profile 2)

Table 1. Variation of natural radionuclide content with depth in profile 1

Layer, cm	Activity concentration, Bq·kg^{-1}				Isotopic ratio ^{226}Ra/^{210}Pb
	^{226}Ra	^{210}Pb	^{232}Th	40K	
0-5	< MDA	330.0±60.0	3.1±1.0	60.0±18.0	-
5-10	< MDA	65.0±18.2	2.5±1.0	51.0±19.0	-
10-15	< MDA	10.0±2.5	2.0±0.8	45.0±18.0	-
15-20	< MDA	< MDA	< MDA	35.0±14.0	-
20-25	0.3±0.2	2.3±1.1	1.3±0.8	23.0±9.2	0.13
25-30	1.1±0.4	8.1±3.2	4.8±0.6	78.0±12.5	0.14
30-35	2.8±0.8	7.3±2.9	4.5±0.6	62.0±11.8	0.38
35-40	2.3±0.7	12.0±5.0	5.1±0.7	155.0±21.7	0.19
40-45	10.5±1.6	16.0±6.4	20.1±1.8	330.0±29.7	0.66
45-50	14.2±2.6	21.0±8.4	25.0±2.3	370.0±33.3	0.68
50-55	16.3±2.5	17.0±6.8	25.9±2.2	530.0±47.7	0.96

Table 2. Variation of natural radionuclide content with depth in profile 2

Layer, cm	Activity concentration, Bq·kg^{-1}				Isotopic ratio ^{226}Ra/^{210}Pb
	^{226}Ra	^{210}Pb	^{232}Th	40K	
0-5	< MDA	270.0±60.0	< MDA	51.0±18.0	-
5-10	< MDA	22.0±18.2	< MDA	45.0±19.0	-
10-15	< MDA	< MDA	< MDA	35.0±18.0	-
15-20	< MDA	4.1±1.9	4.8±2.3	78.0±14.0	-
20-25	3.6±0.2	9.0±1.1	8.6±0.8	155.0±9.2	0.40
25-30	3.3±0.4	6.5±3.2	8.4±0.6	183.0±12.5	0.51
30-35	4.5±0.8	11.0±2.9	9.6±0.6	167.0±11.8	0.41
35-40	5.8±0.7	8.0±5.0	9.7±0.7	190.0±21.7	0.73

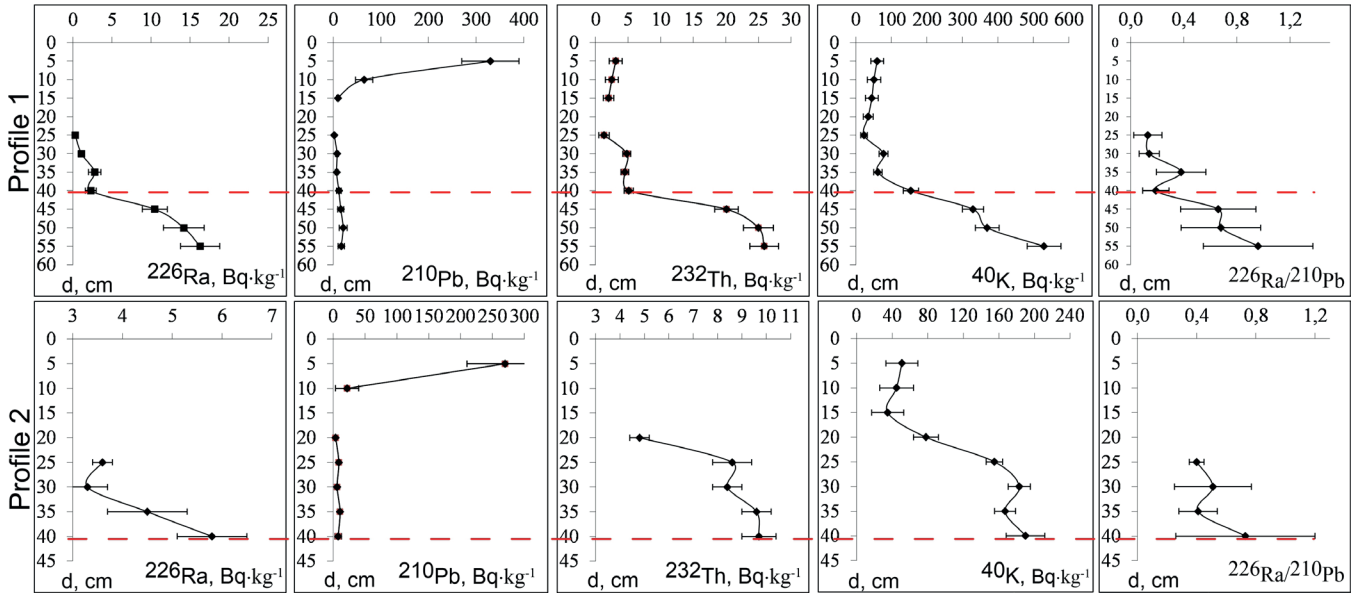

Fig. 4. Plots of radionuclide activity concentration distribution and isotopic ratios along profiles 1 and 2 (red dashed line shows average AL level according to (Iglovsky 2010))

only way ^{210}Pb enters the peatland is atmospheric fallout (Yakovlev et al. 2022). The concentration of ^{210}Pb at a depth of 15-20 cm in profile 1 and 10-15 cm in profile 2 is below the minimum detectable activity concentration. In general, the ^{210}Pb activity concentration in the studied profiles is comparable to other regions of Northwest Russia. For instance, the maximum ^{210}Pb activity concentration recorded in the Ilassky peatland in the Arkhangelsk region was 310.8 Bq·kg^{-1} (Yakovlev et al. 2022). However, there are cases where the vertical distribution of ^{210}Pb differs from the above. Cwanek and Łokas (2022) demonstrated that the highest activity concentration was not confined to the uppermost layer but occurred within intermediate depths. Additionally, there were significant deviations from the simple monotonic decrease of atmospheric components, which often fluctuated downward, presumably reflecting episodic variations in recent peat growth or decomposition rates.

The vertical distribution of ^{226}Ra, ^{232}Th, and 40K differs from the vertical distribution of ^{210}Pb for our study area. The maximum values of these radionuclides are observed in the underlying horizons. This effect is especially noticeable for peat profile 1, where samples were taken including the bedrock, with increased sorption properties of clay minerals.

DISCUSSION

The obtained data sets of AL, RFD and gamma flux density differ from the normal distribution, so we used the nonparametric Spearman's rank criterion to evaluate correlation dependencies. A correlation coefficient of 0.70 (significant at the 0.05 p-value) was observed between gamma ray flux and AL thawing depth. It is likely that the elevated gamma ray flux is attributable to the flux of natural radioactive gases, including ^{222}Rn and its decay products, given the absence of a permafrost barrier. Conversely, the observed increase in gamma radiation flux may be attributed to intrinsic properties of gamma radiation. The ability of gamma radiation to penetrate an object is contingent upon the energy of the gamma quantum and the density of the substance absorbing it. The thickness of the water layer at 24 cm (which, in the present study, is equated with the thickness of the frozen ground) attenuates the gamma radiation flux with an energy of 0.5 MeV by a factor of 10. Given the considerable range of gamma-radiation energies exhibited by natural radionuclides (Levin 1973), spanning from the X-ray zone to energies exceeding 2.5 MeV, ice or frozen ground can serve as a substantial barrier to the passage of gamma-quanta. This phenomenon may be reflected in the findings of studies examining the distribution of gamma-ray flux in peat bogs within the Oma River basin.

I n contrast to gamma radiation, there is a very strong correlation between RFD and the AL thaw level of 0.83 (significant at the 0.05 *p-value*). Concurrently, a comparison of RFD and gamma radiation flux reveals a relatively weak correlation between these parameters – 0.59 (significant at the 0.05 *p-value*)). It can be reasonably assumed that the greatest contribution to the gamma-quantum flux is made by gamma-emitting radionuclides, including ^{222}Rn decay products present in the soil. ^{40}K, a radionuclide found in abundance in natural environments, also emits gamma radiation. In the present study, its activity concentration exceeds that of other radionuclides, especially in the underlying horizons. Furthermore, the gamma-ray energy of ^{40}K is notably high at 1460 keV. However, it is important to note that the beta decay of ^{40}K is accompanied by gamma-quantum yield in only 10.6% of cases (Levin 1973). Consequently, the contribution of ^{40}K to the total gamma radiation flux is likely to be approximately equivalent to that of other radionuclides.

The surface distribution of radiation parameters can be directly related to the vertical distribution of radionuclides in different frozen conditions. As previously mentioned, the concentration of ^{210}Pb at a depth of 15-20 cm in profile 1 and 10-15 cm in profile 2 is below the minimum detectable activity concentration. This lower concentration is likely attributable to the absence of vertical migration of ^{210}Pb, which entered via atmospheric deposition due to the shallow depth of the AL and its brief melt period. Conversely, in horizons deeper than 15-20 cm, both profiles demonstrate an increase in the content of ^{210}Pb, as well as its parent isotope ^{226}Ra. The results of the calculation of the ^{226}Ra/^{210}Pb isotopic ratio for depths between 20 and 40 cm demonstrated that in profile 1, this parameter exhibited a range of 0.13 to 0.38, while in profile 2, it varied between 0.40 and 0.73. The low value of the isotopic ratio in profile 1 may be indicative of an excess of ^{210}Pb (in comparison to the ^{226}Ra content), which is likely due to the ^{222}Rn flux from the underlying horizons. The application of the ^{226}Ra/^{210}Pb isotope ratio method is discussed in detail by Tsapalov (2013). The authors demonstrate that the ^{210}Pb content is excessive in conditions of active geodynamics due to the inflow of «deep» ^{222}Rn. In the present study, it is hypothesized that in permafrost conditions, the activities of ^{226}Ra and ^{210}Pb are in radioactive equilibrium, whereby their ratio is assumed to be 1 (one). This assumption is founded upon a series of indirect indications, as direct evidence for this phenomenon is not available within the scientific literature. For instance, in 1990, research was conducted to assess the distribution of permafrost by measuring the activity concentration of ^{222}Rn as a tracer (Sellmann et al. 1990). The results of the studies demonstrated a strong correlation between the ^{222}Rn activity concentration and frozen areas in the permafrost distribution, with varying levels of permafrost roof occurrence. The necessity to take into account the factors such as surface ice and permafrost presence when assessing ^{222}Rn distribution was pointed out in Evangelista et al. (2002). It has been hypothesised that surface ice and permafrost act as significant barriers to the ^{222}Rn flux reaching the Earth's surface. Theoretical studies on this contentious issue were initiated in 2006-2008 (Glover 2022). Conclusions have been drawn by Russian scientists (Klimshin et al. 2010) regarding the significant influence of the level of seasonal ground freezing (up to 1 m) in wintertime on ^{222}Rn emanation to the Earth's surface. The evidence suggests that ^{222}Rn may be sealed within the permafrost. The absence of ^{222}Rn migration can be interpreted as an absence of both ^{222}Rn itself and its decay products. However, when permafrost conditions are disrupted, ^{222}Rn will begin to migrate through the geological environment (Puchkov et al. 2021), leaving behind radioactive decay products, which may potentially result in a reduction in the value of the ^{226}Ra/^{210}Pb ratio.

In terms of the ongoing discussion of ^{226}Ra/^{210}Pb ratio violations, there is a further potential cause of the ^{210}Pb excess: the compression of pore waters and gases (including gas hydrates) containing ^{222}Rn because of cryogenic concentration from the permafrost zone to the freezing zone (Chuvilin et al. 2000). The ^{222}Rn does not form gas hydrate crystals with water independently, as it lacks the requisite partial pressure for hydrate formation. However, its atoms are actively embedded in the nodes of hydrate crystals of the auxiliary gas, thereby forming a mixed hydrate (Portman 2014).

It is important to note that the discussions presented above do not conclusively address the issues of increased ^{222}Rn fluxes resulting from permafrost degradation and the deterioration of the radiological situation in areas with an unfavorable radiochemical background. These issues remain open for further debate and investigation. The results of the observed increase in ^{222}Rn and gamma radiation fluxes can be interpreted not only in the context of permafrost conditions but also in relation to other factors. The measured RFD values indicate that the concentration of ^{222}Rn decay daughter products in the air and on the soil surface is likely insufficient to significantly impact gamma radiation flux values. To this end, it would be advisable to conduct a further study in territories with an unfavorable radiogeochemical background. The excess of ^{210}Pb compared to ^{226}Ra may be related to the increased concentration of ^{210}Pb in this layer. This level is probably formed in autumn and early winter during freezing of the AL from above. In this process, soil ^{222}Rn cannot escape to the atmosphere and appears 'sealed' in the melted area between permafrost rocks and the freezing layer. For example, Klimshin et al. (2010) demonstrate that the freezing of the surface soil layer can reduce the ^{222}Rn flux by up to 10 times compared to the period preceding freezing.

CONCLUSIONS

This paper presents the findings of field studies investigating the distribution of ^{226}Ra, ^{222}Rn, its decay products, and gamma radiation flux in relation to varying levels of AL occurrence. The studies were conducted on the territory of a hillocky peat bog situated within the Oma River basin, which is located in the Nenets Autonomous Okrug in Russia. A total of 76 points were sampled across the bog territory, and two peat profile cuts were investigated.

A significant correlation has been revealed between the gamma radiation flux and AL, which may be related, on the one hand, to the flux of natural radioactive gases and accumulation of their decay products in the absence of a frozen barrier. This hypothesis is further substantiated by the substantial correlation between RFD and AL ($R = 0.83$). Conversely, the association between gamma radiation and AL may be attributable to inherent characteristics of gamma radiation itself.

The vertical migration of natural radionuclides ^{210}Pb, ^{226}Ra, ^{232}Th, and ^{40}K was studied in two selected peat profile cuts. The highest activity concentration of ^{210}Pb is observed in the upper peat horizon (330.0±60.0 Bq·kg^{-1} for profile 1 and 270.0±60.0 Bq·kg^{-1} for profile 2), which is associated with atmospheric deposition. The ^{210}Pb activity concentration sharply decreases to the minimum detectable values in the 10-20 cm horizon, which may be related to the absence of vertical migration of atmospheric ^{210}Pb as a result of permafrost spreading and short AL thawing periods. In the underlying horizons of profile 1, where the AL thawing level is the highest, a violation of the ^{226}Ra/^{210}Pb isotopic ratio is noted in favor of a ^{210}Pb increase. We attribute this fact to the increased flux of ^{222}Rn from the underlying horizons in the absence of a permafrost barrier. However, we do not exclude other possible factors of ^{210}Pb excess in the underlying horizons under permafrost thawing conditions, such as the compression of pore waters and gases (including gas hydrates) containing ^{222}Rn because of cryogenic concentration from the permafrost zone to the freezing zone.

REFERENCES

Afonin A. and Korchunov A. (2013). Optimizing block parameters measurements for monitoring radon, thoron and their daughter products in various environments. ANRI, 1, 9-11. (in Russian).

Baskaran M. (2016). Radon: A tracer for geological, geophysical and geochemical studies. Basel: Springer, DOI: 10.1007/978-3-319-21329-3.

Buldovicz S. N., Khilimonyuk V. Z., Bychkov A. Y., Ospennikov E. N., Vorobyev S. A., Gunar A. Y., Gorshkov E. I., Chuvilin E. M., Cherbunina M. Y., Kotov P. I., Lubnina N. V., Motenko R. G. and Amanzhurov R. M. (2018). Cryovolcanism on the Earth: Origin of a Spectacular Crater in the Yamal Peninsula (Russia). Scientific Reports, 8(1), DOI: 10.1038/s41598-018-31858-9.

Chuvilin E.M., Yakushev V.Sand Perlova E.V. (2000). Gas and gas hydrates in the permafrost of Bovanenkovo gas fi eld, Yamal Peninsula, West Siberia. Polarforschung, 68, 215-219.

Cwanek A. and Łokas E. (2022). Deposition chronologies in a peat bog from Spitsbergen (High Arctic) using the 210Pb dating method. Polish Polar Research, 43(4), DOI: 10.24425/ppr.2022.143310.

Daraktchieva Z., Wasikiewicz J. M., Howarth C. B. and Miller C. A. (2021). Study of baseline radon levels in the context of a shale gas development. Science of The Total Environment, 753, 141952, DOI: 10.1016/j.scitotenv.2020.141952.

Evangelista H. and Pereira, E. B. (2002). Radon flux at King George Island, Antarctic Peninsula. Journal of Environmental Radioactivity, 61(3), DOI: 10.1016/S0265-931X(01)00137-0.

Giustini F., Ciotoli G., Rinaldini A., Ruggiero L. and Voltaggio M. (2019). Mapping the geogenic radon potential and radon risk by using Empirical Bayesian Kriging regression: A case study from a volcanic area of central Italy. Science of the Total Environment, 661, 449-464, DOI: 10.1016/j.scitotenv.2019.01.146.

Glover P. W. J. and Blouin, M. (2022). Increased Radon Exposure From Thawing of Permafrost Due To Climate Change. Earth's Future, 10(2), DOI: 10.1029/2021EF002598.

Iglovsky S. A., Shvartsman Y. G. and Bolotov I. N. (2010). Cryolithozone of the Dvinsko-Mezenskaya Plain and Kanin Peninsula. Ekaterinburg: FCIARCTIC UrB RAS (in Russian).

Klimshin A.V., Kozlova I.A., Rybakov E.N. and Lukovskoy M.Yu. (2010). Effect of freezing the surface layer of soil on the radon transport. KRAUNTS Bulletin. Series: Earth Sciences, 16(2), 146-151 (in Russian with English summary).

Koptev D.P. (2020). Norilsk spill: lessons and consequences. Drilling and Oil, (7-8), 3-9. (in Russian with English summary).

Kriauciunas V. V., Iglovsky S. A., Kuznetsova I. A., Shakhova E. V., Bazhenov A. V. and Mironenko K. A. (2018). Spatial distribution of natural and anthropogenic radionuclides in the soils of Naryan–Mar. Arctic Environmental Research, 18 (3), 82-89, DOI: 10.3897/issn2541–8416.2018.18.3.82.

Levin V. E. and Khamyanov L. P. (1973). Registration of ionising radiation. Moscow: Atomizdat. (in Russian).

Lorenzo-Gonzalez M., Ruano-Ravina A., Torres-Duran M., Kelsey K. T., Provencio M., Parente-Lamelas I., Piñeiro-Lamas M., Varela-Lema L., Perez-Rios M., Fernandez-Villar A. and Barros-Dios J. M. (2020). Lung cancer risk and residential radon exposure: A pooling of case-control studies in northwestern Spain. Environmental Research, 189, DOI: 10.1016/j.envres.2020.109968.

Maier A., Wiedemann J., Rapp F., Papenfuß F., Rödel F., Hehlgans S., Gaipl U. S., Kraft G., Fournier C. and Frey B. (2021). Radon exposure-therapeutic effect and cancer risk. International Journal of Molecular Sciences, 22(1), DOI: 10.3390/ijms22010316.

Miklyaev P. S. and Petrova T. B. (2010). The study of radon emanation in clay. Geoecology. Engineering geology, hydrogeology, geocryology, (1), 13-22, (in Russian).

Petrova T. and Miklyaev P. (2020). Variations of indoor radon concentration in traditional russian rural wooden houses. Radiation Protection Dosimetry, 191(2), DOI: 10.1093/rpd/ncaa156.

Pokrovsky O. S., Manasypov R. M., Pavlova O. A., Shirokova, L. S. and Vorobyev S. N. (2022). Carbon, nutrient and metal controls on phytoplankton concentration and biodiversity in thermokarst lakes of latitudinal gradient from isolated to continuous permafrost. Science of the Total Environment, 806, DOI: 10.1016/j.scitotenv.2021.151250.

Portman A. I. and Potemkin A. M. (2014). Gas-hydrate method of radon immobilisation ANRI, 4(79), 61-64 (in Russian).

Prokhorenko N. B. (2013). Classification and composition of peat. Kazan: Kazan (Volga Region) Federal University (in Russian).

Puchkov A. V., Berezina E. V., Yakovlev E. Y., Hasson N. R., Druzhinin S. V., Tyshov A. S., Ushakova E. V., Koshelev L. S. and Lapikov P. I. (2022). Radon Flux Density In Conditions Of Permafrost Thawing: Simulation Experiment. Geography, Environment, Sustainability, 15(3), DOI: 10.24057/2071-9388-2022-023.

Puchkov A. V., Yakovlev E. Y., Hasson N., Sobrinho G. A. N., Tsykareva Y. V., Tyshov A. S., Lapikov P. I. and Ushakova E. V. (2021). Radon Hazard In Permafrost Conditions: Current State Of Research. Geography, Environment, Sustainability, 14(4), DOI: 10.24057/2071-9388-2021-037.

Rodríguez-Martínez Á., Torres-Durán M., Barros-Dios J. M. and Ruano-Ravina, A. (2018). Residential radon and small cell lung cancer. A systematic review. In Cancer Letters, 426, DOI: 10.1016/j.canlet.2018.04.003

Rosenberger A., Hung R. J., Christiani D. C., Caporaso N. E., Liu G., Bojesen S. E., le Marchand L., Haiman C. A., Albanes D., Aldrich M. C., Tardon A., Fernández-Tardón G., Rennert G., Field J. K., Kiemeney B., Lazarus P., Haugen A., Zienolddiny S., Lam S. and Gomolka M. (2018). Genetic modifiers of radon-induced lung cancer risk: a genome-wide interaction study in former uranium miners. International Archives of Occupational and Environmental Health, 91(8), DOI: 10.1007/s00420-018-1334-3.

Sabbarese C., Ambrosino F., D'Onofrio A., Pugliese M., La Verde G., D'Avino V. and Roca V. (2021). The first radon potential map of the Campania region (southern Italy). Applied Geochemistry, 126, 104890, DOI:10.1016/j.apgeochem.2021.104890.

Sellmann P. V. and Delaney A. J. (1990). Radon measurements as indicators of permafrost distribution. Cold Regions Science and Technology, 18(3), DOI: 10.1016/0165-232X(90)90029-V.

Selvam S., Muthukumar P., Sajeev S., Venkatramanan S., Chung S. Y., Brindha K. and Murugan R. (2021). Quantification of submarine groundwater discharge (SGD) using radon, radium tracers and nutrient inputs in Punnakayal, south coast of India. Geoscience Frontiers, 12(1), 29-38, DOI: 10.1016/j.gsf.2020.06.012.

Shirokova L. S., Chupakov A. V., Ivanova I. S., Moreva O. Y., Zabelina S. A., Shutskiy N. A., Loiko S. V. and Pokrovsky O. S. (2021). Lichen, moss and peat control of C, nutrient and trace metal regime in lakes of permafrost peatlands. Science of the Total Environment, 782, DOI: 10.1016/j.scitotenv.2021.146737

Streletskiy D. A., Clemens S., Lanckman J. P. and Shiklomanov N. I. (2023). The costs of Arctic infrastructure damages due to permafrost degradation. Environmental Research Letters, 18(1), DOI: 10.1088/1748-9326/acab18.

Syam N. S., Lim S., Lee H. Y. and Lee, S. H. (2020). Determination of radon leakage from sample container for gamma spectrometry measurement of 226Ra. Journal of environmental radioactivity, 220, 106275, DOI: 10.1016/j.jenvrad.2020.106275

Tsapalov A. A., Miklyaev P. S. and Petrova T. B. (2013). The principle of detection of sites with active geodynamics based on the analysis of the ratio of Pb-210/Ra-226 activities in soil samples. ANRI, 1(72).

Yakovlev E., Orlov A., Kudryavtseva A. and Zykov S. (2022). Estimation of Physicochemical Parameters and Vertical Migration of Atmospheric Radionuclides in a Raised Peat Bog in the Arctic Zone of Russia. Applied Sciences (Switzerland), 12(21), DOI: 10.3390/app122110870.

Yakovlev E., Orlov A., Kudryavtseva A., Zykov S. and Zubov I. (2023). Assessment of the Impact of Anthropogenic Drainage of Raised Peat-Bog on Changing the Physicochemical Parameters and Migration of Atmospheric Fallout Radioisotopes in Russia's Subarctic Zone (Subarctic Zone of Russia). Applied Sciences (Switzerland), 13(9), DOI: 10.3390/app13095778.

Ye Y., Wang H., Li M. and Chen M. (2024). Experimental study of radon migration parameters in uranium tailings under frozen and non-frozen conditions. Journal of Radioanalytical and Nuclear Chemistry, 334, 439-447, DOI: 10.1007/s10967-024-09842-7.

Zhang S., Jin D., Jin H., Li C., Zhang H., Jin X. and Cui J. (2024). Potential radon risk in permafrost regions of the Northern Hemisphere under climate change: A review. In Earth-Science Reviews, 250, DOI: 10.1016/j.earscirev.2024.104684.

Zhang Z. Q., Wu Q. B., Hou M. T., Tai B. W. and An Y. K. (2021). Permafrost change in Northeast China in the 1950s–2010s. Advances in Climate Change Research, 12(1), DOI: 10.1016/j.accre.2021.01.006.

APPENDIX A

Table A1. RFD, AL, and gamma radiation flux at the peat bog surface

ID point	RFD*, mBq·m^{-2}·s^{-1}	AL, cm	Gamma radiation flux*, impulses per second
1	30	53	25.9
2	25	52	25.8
3	29	49	29.7
4	36	50	27.9
5	32	55	23.7
6	31	50	21.9
7	35	51	22.1
8	29	54	23.8
9	28	59	26.2
10	31	50	18.3
11	36	51	20.3
12	37	54	25.9
13	32	53	24.7
14	25	55	30.4
15	26	56	28.6
16	18	14	19.9
17	10	7	18.3
18	11	8	19.6
19	12	8	22.0
20	11	10	18.4
21	15	9	21.8
22	14	9	18.5
23	16	8	16.0
24	9	10	18.0
25	9	12	18.3
26	10	12	16.3
27	12	8	22.7
28	12	9	20.1
29	14	13	18.1
30	15	15	20.3
31	14	12	22.1
32	13	11	23.7
33	10	12	22.3
34	6	11	21.4
35	7	9	20.6

36	9	9	15.9
37	10	8	17.7
38	8	9	17.9
39	6	10	18.4
40	15	12	20.6
41	16	12	21.9
42	11	11	16.3
43	6	12	20.4
44	8	10	18.1
45	7	13	23.9
46	19	44	25.7
47	8	12	21.6
48	10	13	19.7
49	11	10	16.8
50	14	33	23.4
51	11	14	23.6
52	19	39	25.3
53	16	12	22.7
54	15	12	18.5
55	12	11	14.6
56	13	10	16.2
57	9	10	14.4
58	10	28	20.3
59	21	47	23.9
60	21	48	24.3
61	18	24	19.0
62	24	30	21.9
63	18	29	26.3
64	19	28	22.7
65	20	32	22.1
66	20	49	32.1
67	24	20	18.2
68	23	41	23.0
69	24	39	26.5
70	23	42	23.0
71	19	37	18.6
72	20	45	22.3
73	21	44	26.8

74	20	29	22.1
75	23	26	24.9

*Notes: According to the technical documentation, the uncertainty of measurements with the scintillation geological exploration radiometer SRP-88n is 10%. According to the technical documentation, the uncertainty of measurements with the radon radiometer «Alpharad plus» is 30%.

RESEARCH PAPER

BIOMASS PREDICTION USING MACHINE LEARNING TECHNIQUES IN GOOGLE EARTH ENGINE: A CASE STUDY OF THE AZROU FOREST IN THE MIDDLE ATLAS MOUNTAINS, MOROCCO

Said Laaribya [1*], Assmaa Alaoui[2]

[1]Ibn Tofail University/Laboratory of Territory planning Geo-Environment and Development, B.P 242, Kenitra, Morocco

[2]Ibn Tofail University/Laboratory of Plant and Animal Production and Agro-Industry, B.P 242 Kenitra, Morocco

***Corresponding author:** said.laaribya1@uit.ac.ma

Received: February 6th 2025 / Accepted: July 11th 2025 / Published: October 1st 2025

https://doi.org/10.24057/2071-9388-2025-3876

ABSTRACT. In the context of climate change, forests are a vital source of ecosystem services for humankind, acting primarily as carbon sinks. The aim of this study is to use the machine learning algorithms available in the Google Earth Engine (GEE) to predict the above-ground biomass of the Azrou forest in the Middle Atlas Mountains of Morocco. After a literature review, the work consisted of characterizing the natural features through Land Use Land Cover analysis (LULC) and forest stand types. The accuracy of the forest stand type classification was assessed at 81.55% using the kappa index. Analysis of vegetation cover time series data, derived from NASA imagery and MODIS, was carried out, focusing on four key indices: NDVI (Normalized Difference Vegetation Index), EVI (Enhanced Vegetation Index), LAI (Leaf Area Index), and FPAR (Fraction of Photo synthetically Active Radiation). The study predicted biomass using the Random Forest machine-learning model, implemented in GEE with JavaScript. NASA/ORNL biomass data for 2010 served as the dependent variable, while LULC, elevation, and the four indices were used (selected summer period) as independent explanatory variables. In addition, forest stand types were integrated to calculate total biomass for specific stand types and for the study area as a whole for the years 2015, 2020 and 2024. In 2024, the predicted biomass is 461,587 tons, compared with 501,172 tons in 2010. The biomass median values by species were 29 tons/ha for pure Atlas cedar (Cedrus atlantica Manetti), 24 tons/ha for pure holm oak (Quercus ilex) and 31 tons/ha for a mixture of Atlas cedar and holm oak. The results highlight challenging conditions for the Azrou forest, with a notable decline in biomass over the study period. These results will serve as a basis for future forestry planning in the context of climate change.

KEYWORDS: carbon sinks, LULC, machine learning, vegetation indices, climate change

CITATION: Laaribya S., Alaoui A. (2025). Biomass Prediction Using Machine Learning Techniques In Google Earth Engine: A Case Study Of The Azrou Forest In The Middle Atlas Mountains, Morocco. Geography, Environment, Sustainability, 3 (18), 43-58 https://doi.org/10.24057/2071-9388-2025-3876

ACKNOWLEDGEMENTS: The authors gratefully acknowledge the support of the entire staff at the Provincial Forest Directorate of Ifrane (Morocco).

Conflict of interests: The authors reported no potential conflict of interests.

INTRODUCTION

In the 21st century, global climate change becomes more severe which is due to greenhouse gas emissions, which are recognized as one of the key drivers of ecosystem degradation and climate disruption (Scott et al. 2020). This phenomenon has had serious consequences, including global warming, ocean acidification, accelerated glacier melt, and an increase in the frequency and intensity of extreme weather events (Calvin et al., 2023).

In the context of climate change, the uptake of carbon dioxide by forest ecosystems is precarious for regulating it (Friedlingstein et al., 2022). They play a key role since maintaining and increasing the sink capacity of forests is essential to reduce growing greenhouse gas emissions into the atmosphere (Friedlingstein et al., 2022; R. B. Myneni et al., 2001; Pan et al., 2024; Schilling et al., 2012). In December 2015, the COP 21 in Paris led to an agreement within the United Nations Convention on Climate Change with the purpose of keeping the increase in global surface temperature well under 2°C, while pursuing efforts to limit the rise to 1.5°C. In this concern, each party involved in the agreement has to establish a national goal to limit greenhouse gas emissions (Erickson & Brase, 2020; Ourbak & Magnan, 2018). Biomass carbon pools act as a sink for atmospheric CO_2 and, in the Mediterranean region, carbon sequestration by forests ranges between 0.01 and 1.08 t C ha^{-1} annually (Merlo & Croitoru, 2005). The ability to quantify forest carbon stock at the regional and local levels is expected to support compliance with the treaty and its goals.

Forests are a vital source of ecosystem services for humans and mainly act as carbon sinks (FAO, 2020). Nonetheless, forest

improvement activities and changes in land and forest use emanate directly from forests and account for all emissions from agriculture and other related uses (Laaribya et al., 2024; Nourelbait et al., 2016; Rudel et al., 2005). In addition, activities linked to deforestation, reforestation, and forest conservation are important. Combined with the effects of deforestation and acceptable sustainable harvesting, forests can also act as a source of carbon long before the agreement. In this context, the reduction of greenhouse gas emissions from deforestation and increased forest degradation is part of a sustainable development approach and enhances carbon storage (Alaoui et al., 2021; Forsell et al., 2016; García et al., 2010; Laaribya et al., 2021; Sinha, 2022).

Although much research has been carried out on the Atlas cedar forest to assess its state of conservation, much remains to be discovered about its capacity to store carbon in biomass and the long-term sustainability of this emblematic Moroccan ecosystem (Boulmane et al., 2015; El Mderssa, 2022; El Mderssa et al., 2019; Laaribya, 2024; Laaribya et al., 2024; Linares et al., 2011; Terrab et al., 2006; Zaher et al., 2020a). This work has highlighted the need to improve conservation strategies to preserve this ecosystem, as its ability to act as a carbon sink is highly dependent on its sustainability and maintenance. Indeed, this remarkable ecosystem plays an essential role in carbon sequestration, helping to mitigate climate change.

The aim of this study is to use the available machine learning techniques, adapted inside the GEE environment, to assess the cover dynamic and to predict the above-ground biomass of the Azrou Cedar Atlas forest in the Middle Atlas Mountains in Morocco.

Satellite imagery, coupled with the power of Artificial Intelligence (AI) and cloud-based platforms like GEE, has revolutionized the way environmental monitoring is conducted, making it possible to analyze vast forest landscapes over extended periods efficiently (Laaribya & Alaoui, 2025; Mutanga & Kumar, 2019; Zhao et al., 2021). Indeed, given that traditional methods are difficult to meet the requirements in this field due to the long period of experimentation in the field, the availability of timber cuttings, and the high cost. Nowadays, machine learning (ML) is emerging as a new research paradigm to facilitate research in the field of machine learning for forest biomass prediction.

MATERIALS AND METHODS

Study area

The Azrou forest is located on the northern edge of the Middle Atlas plateau (Morocco) and covers an area of 17,807 ha. Contrasting relief characterizes it, with altitudes ranging from 1,100 m to 2,100 m. Precipitation is relatively high and comes in the form of rain or snow. Annual rainfall varies between 563 mm and 1122 mm, while maximum temperatures range from 30.3°C to 43°C, with July and August being the hottest months (Laaribya, 2024).

The bioclimate is humid Mediterranean with a cold variant and subhumid with a temperate variant. Atlas Cedar (*Cedrus atlantica* Manetti) is the main species in this forest, and depending on the nature of the substrate, it forms pure stands or a mixture with holm oak (*Quercus ilex)* (Laaribya, 2024). The topographic characteristics of the study area are shown in Fig. 2.

Referring to the International Soil Classification System (WRB 2014), the study area offers three main soil groups (Fig. 3).

In our study area, analysis of the Gaussen Index (Bagnouls & Gaussen, 1953) (Fig. 4) reveals a dry period lasting approximately four months, from June to September (1985-2022). This prolonged aridity significantly affects vegetation cover and tree growth in the Azrou forest.

Data collection

To achieve our objectives, we used a dual approach to analyze environmental changes and biomass evolution over time (Fig. 5). This study relies on various data from reliable and verified sources. All thematic maps were produced using software tools ArcGIS 10.8.

Forest stand types mapping and accuracy assessment

The accuracy of the forest stand types classification is assessed using a confusion matrix, which compares the stand type results to a set of reference data (ground truth or other high-quality datasets).

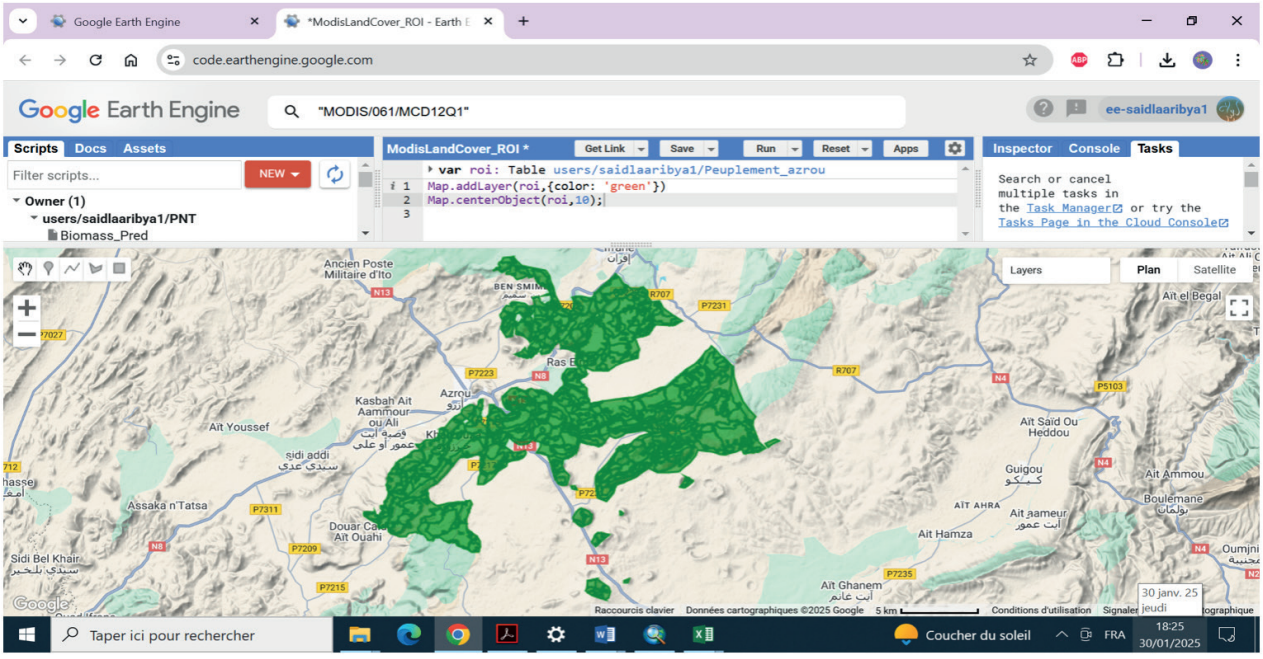

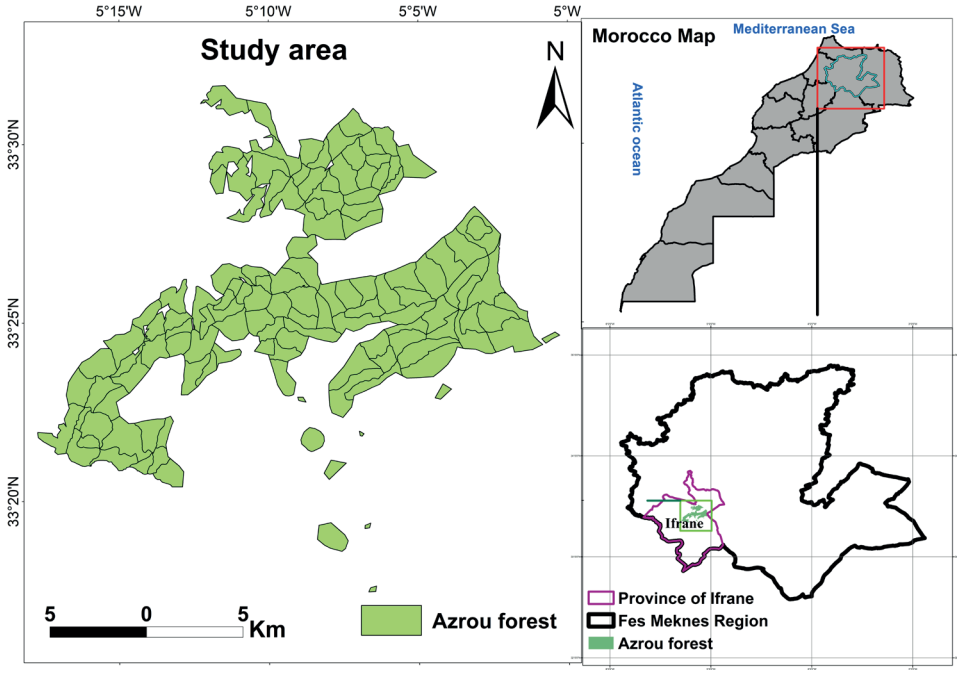

Fig. 1. Study area (the Azrou forest)

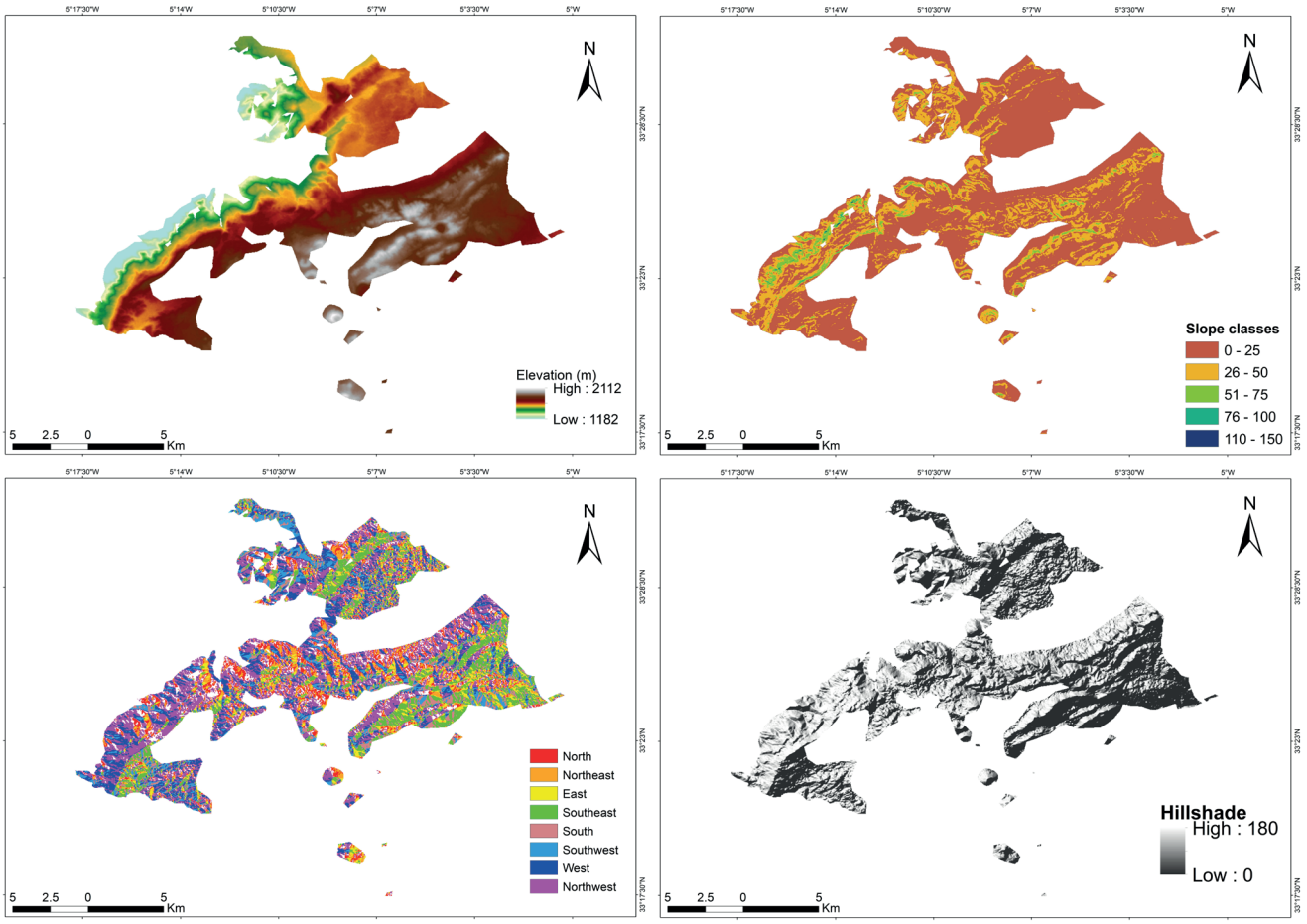

Fig. 2. Topographic maps of the study area

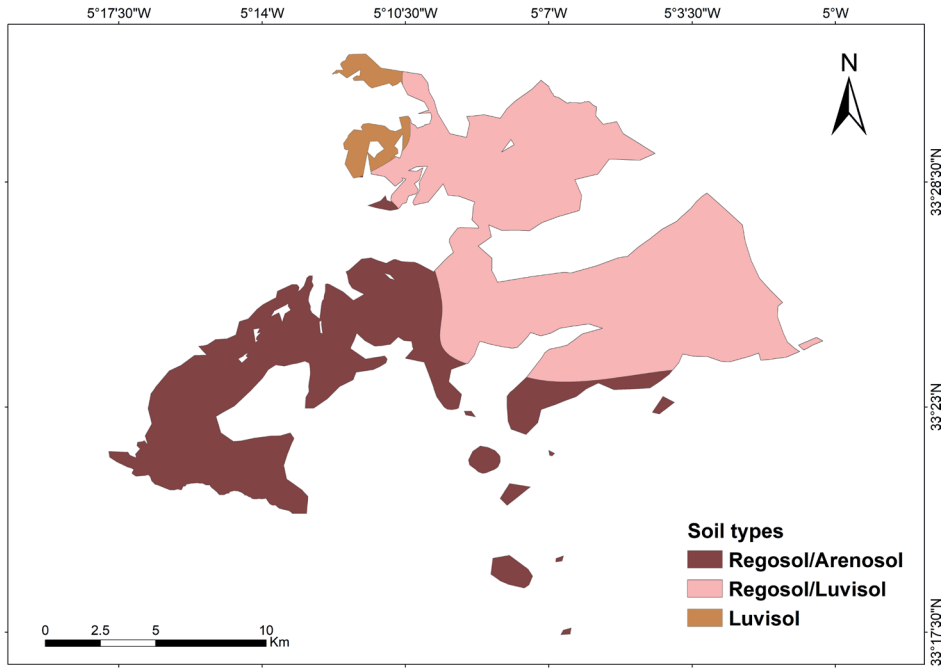

Fig. 3. Soil type in the study area (map based on the soil maps (INRA 2000) not published)

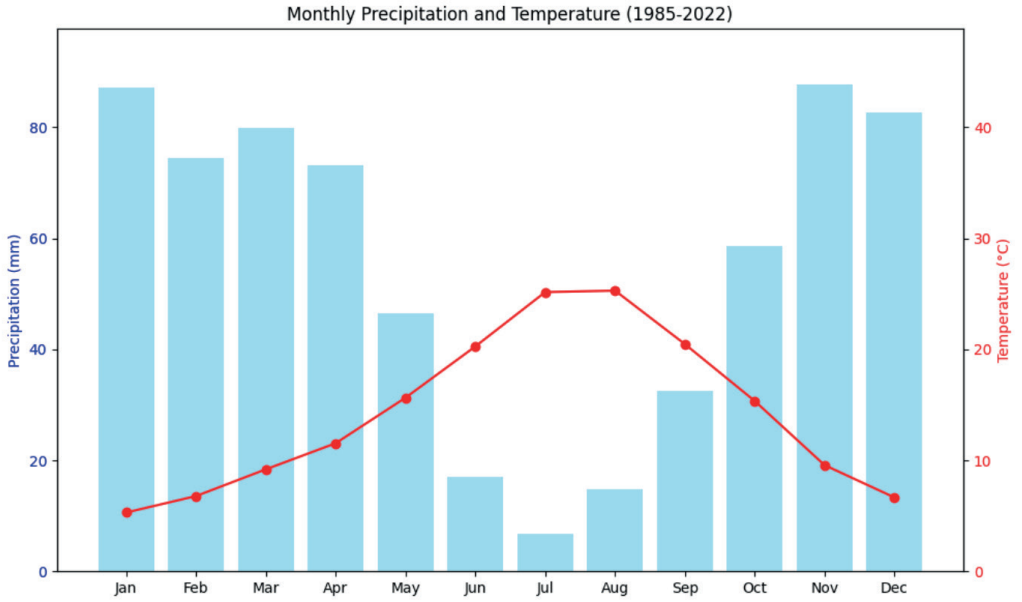

Fig. 4. Bagnouls and Gaussen climate diagrams (1985-2022)

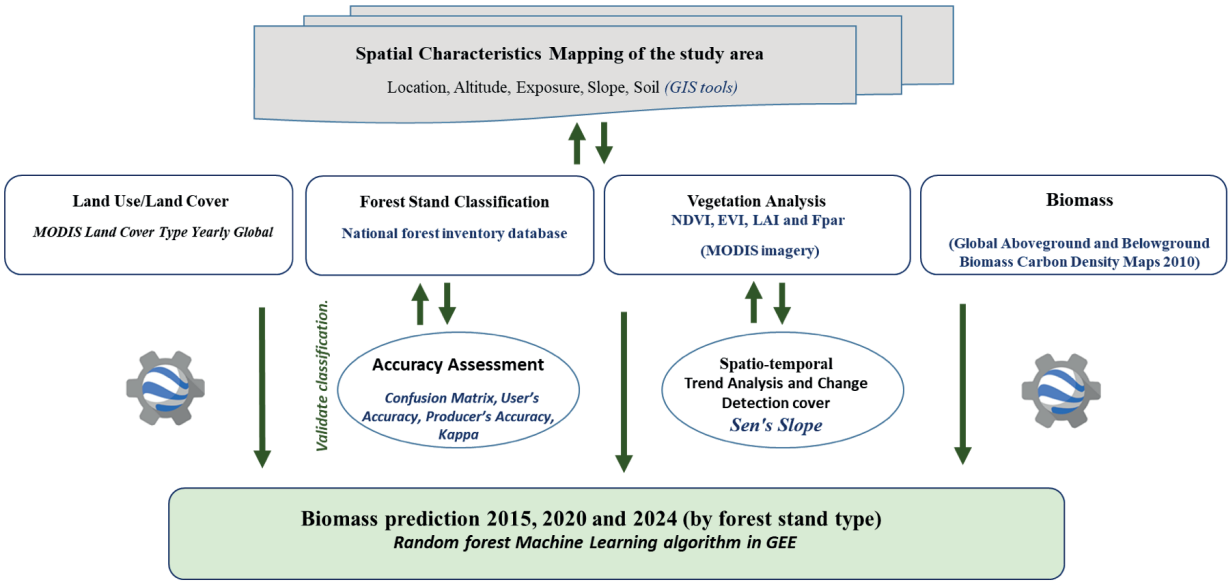

Fig. 5. Methodological Framework

User's accuracy: Measures the accuracy of classification from the user's perspective (correctly classified instances out of all instances predicted for a given class) (Eq. 1).

$$\frac{(Number\ of\ Correctly\ Classified\ Pixels\ in\ each\ Category)}{(Total\ number\ of\ Classified\ Pixels\ in\ that\ Category\ (The\ Row\ Total))} \times 100 \quad (1)$$

Producer's accuracy: Evaluates the accuracy of the classification from the producer's perspective (correctly classified instances out of all instances belonging to a given class) (Eq. 2).

$$\frac{Number\ of\ Correctly\ Classified\ Pixels\ in\ each\ Category}{Total\ number\ of\ Reference\ Pixels\ in\ that\ Category\ (The\ Column\ Total)} \times 100 \quad (2)$$

Kappa coefficient (K): A statistical measure that assesses the overall accuracy of the classification, accounting for random chance (Eq. 3).

$$\frac{\left((TS \times TCS) - \left(\sum\ (Column\ Total \times Row\ Total)\right)\right)}{(TS \times TS) - \left(\sum\ (Column\ Total \times Row\ Total)\right)} \times 100 \quad (3)$$

Spatio-temporal comparisons of vegetation conditions (2001-2024)

Monitoring and change detection for indices used throughout the year (mean for 4 seasons) all over the 2001-2024 period.

For analyzing the vegetation conditions across time, global MODIS vegetation indices (NDVI, EVI, LAI and FPAR) were used (Table 1). The two indices provide insights into vegetation health and productivity:

Normalized Difference Vegetation Index (NDVI): Used to assess vegetation density and health, where higher values correspond to denser vegetation.

The Normalized Difference Vegetation Index (NDVI) (Tucker, 1979) is the most commonly used vegetation index for observe greenery globally (Eq. 4):

$$NDVI = \frac{NIR - R}{NIR + R} \quad (4)$$

where *NIR* - Near-Infrared reflectance, *R* - Red reflectance

Enhanced Vegetation Index (EVI): Similar to NDVI but includes corrections for atmospheric and soil variations, making it particularly useful in areas with dense vegetation. The Enhanced Vegetation Index (Huete, 1997) is an improved version of the NDVI, designed to minimize the influence of atmospheric conditions and soil reflectance, particularly in areas with dense vegetation (Eq. 5):

$$EVI = G\frac{NIR - R}{NIR + C1R - C2Blue + L} \quad (5)$$

where: *NIR:* Near-Infrared reflectance, *R:* Red reflectance, *Blue:* Blue reflectance, *G:* Gain factor, *C1:* Coefficient for the red band, *C2:* Coefficient for the blue band, *L:* Canopy background adjustment

Leaf Area Index (LAI) : LAI (Eq. 6) is broadly defined as the amount of leaf area (m^2) in a canopy per unit ground area (m^2) (Watson, 1958). Leaf area index (LAI) is one of the most frequently used parameters for the analysis of canopy structure and is an important structural characteristic of crop monitoring and crop productivity (Behera et al., 2010).

$$LAI = LA / P \quad (6)$$

Variables: *LA:* Leaf area m^2), P: Ground area (m^2)

Note also that if LAI is the mean leaf area per plant, and n is the plant density, then also (Eq. 7)

$$LAI = LA \times n \quad (7)$$

Variables: *LA:* Leaf area of a single plant (in m^2 or cm^2), *n:* Plant density the number of plants per unit ground area (e.g., plants/m^2)

Fraction of photosynthetic active radiation (FPAR): Photosynthetic active radiation used by plants in the photosynthesis process. PAR knowledge can provide key inputs for modeling biomass and forestry production (Aguiar et al., 2012; García-Rodríguez et al., 2021).

The two indices LAI and FPAR were used from the MOD15A2H V6.1 (MODIS product) combining leaf area index (LAI) and fraction of photosynthetically active radiation (FPAR) in an 8-day composite dataset at 500 m resolution (R. Myneni et al., 2021).

Trend analysis and change detection for NDVI and EVI

To detect trends and changes in vegetation conditions, the following statistical methods were applied especially to NDVI and EVI indices:

Sen's slope estimator: A non-parametric method for estimating the slope of a trend in time series data. It is widely used for trend analysis when dealing with datasets that may contain non-linear trends or outliers (Sen, 1968).

Random forest machine learning algorithm in GEE

To to apply biomass prediction over 3 years (2015, 2020 and 2024), we have used the summer period (month 5 to month 9) to calculate the biomass explanatory indices NDVI, EVI, LAI, and FPAR. The median was used to perform all those parameters. Indeed, the summer period is generally the best time to calculate the values of these indices, making it easier to identify patterns, assess vegetation health, and monitor changes.

Given the model's robustness in prediction, we have used the Random Forest Machin Learning algorithm. The dependent variable is biomass 2010 (ee. ImageCollection('NASA/ORNL/biomass_carbon_density/v1'). This is the carbon stock density of the above-ground living biomass of the combined woodland and herbaceous cover in 2010. This includes carbon stored in living plant tissues above the earth's surface (stems, bark, branches, and twigs) (Spawn et al., 2020).

The random forest is an ensemble learning method mainly used for modeling. Its principle is to build a multitude of decision trees during training and merge their results to improve overall accuracy and control overfitting (Schonlau & Zou, 2020). Random forests are a combination of tree predictors such that each tree depends on the values of a random vector sampled independently and with the same distribution for all trees in the forest (Breiman, 2001). The model parameters and their characteristics are presented in Table 1 below. Other parameters (excluding indices) are also included in the Random Forest model as independent variables.

Biomass = f (NDVI, EVI, LAI, FPAR, LULC, Elevation)
Var dataset = ee.Image.cat([NDVI, EVI, LAI, FPAR, LULC, Elevation])

RESULTS

Lund Use Land Cover

Analysis of the LULC map shows that our study area is marked by a diversity of vegetation cover, mainly grassland, which accounts for more than half the surface area (57%). Forest cover appears to be open and in a state of degradation all over the study area (Fig. 6 and Table 2).

Table 1. Parameters and data collection

Parameters	Collection Snippet	Resolution (m)	Date
Biomass ('agb' Band)	NASA/ORNL/biomass_carbon_density/v1 (Global Aboveground and Belowground Biomass Carbon Density Maps)	300	2010
NDVI	MOD13Q1.061 (Terra Vegetation Indices 16-Day Global 250m)	250	2001-2024
EVI	MOD13Q1.061 (Terra Vegetation Indices 16-Day Global 250m)	250	2001-2024
LAI (Leaf Area Index) FPAR (Fraction of Photosynthetically Active Radiation)	MOD15A2H.061 (Terra Leaf Area Index/FPAR 8-Day Global 500m)	500	2001-2024
Elevation	USGS/GTOPO30	30 arc seconds (equiv 1 km)	1996
LULC	MODIS/061/MCD12Q1 Land Cover Type Yearly Global	500	2010/2022

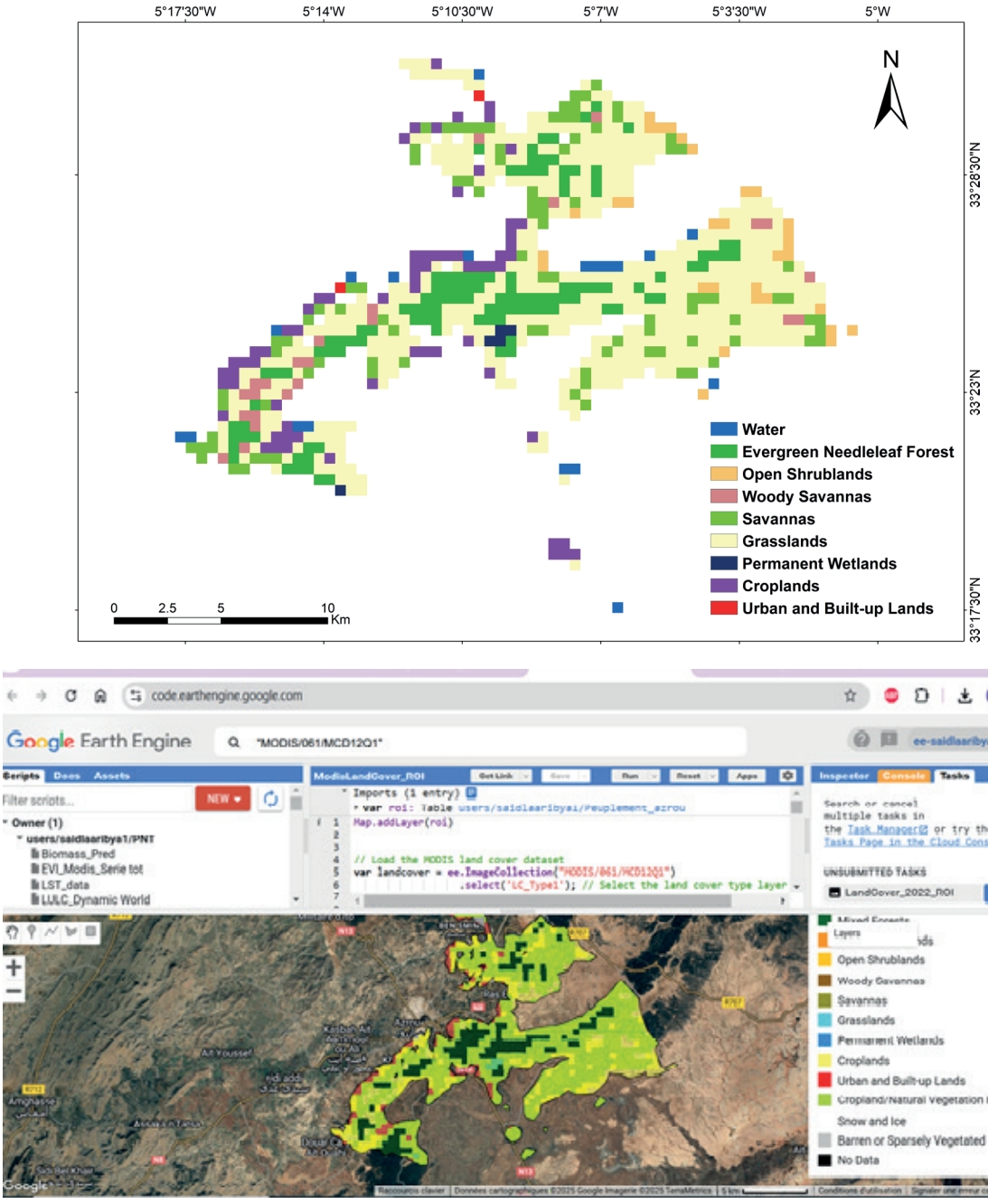

Fig. 6. Landover map 2022

Table 2. LULC 2022 area (ha)

LULC	Area (Ha)	%
Water	404	2.3%
Evergreen Needleleaf Forest	2,468	13.9%
Open Shrublands	660	3.7%
Woody Savannas	511	2.9%
Savannas	2,064	11.6%
Grasslands	10,148	57%
Permanent Wetlands	106	0.6%
Croplands	1,404	7.9%
Urban and Built-up Lands	43	0.2%
Total	17,807	100%

To deepen the analysis and prepare data for the prediction of forest biomass, we prepared a map of forest stand types based on data from the National Forest Inventory. An accuracy assessment was carried out to determine the validity of the classification of the results of this inventory in the field.

The composition of the forest species in our study area includes pure stands of Atlas cedar (*Cedrus atlantica*) (8.4%), Atlas cedar mixed mainly with holm oak (*Quercus ilex*) (40.3%), pure holm oak stands (24.8%) and other areas (24.7%) (Secondary species and non-wooded areas) (Fig. 7 and Table 3).

The Atlas cedar is a noble Moroccan species with a much more majestic and imposing appearance than other species.

The higher Kappa (81.55%) coefficient obtained in our analysis (Table 4) is a strong validation of the classification accuracy, allowing us to confidently focus our study on Forest stand. This robust classification framework forms the basis for assessing spatio-temporal trends in the main indices and corresponding land cover classes, in particular trees, crops, and pasture, over the selected study period (2001-2024).

Time series analysis during 2001-2024

The vegetation assessment parameters NDVI and EVI are widely used to analyze the condition of forest areas. According to the results obtained for the period 2001-2024, NDVI values are generally higher than EVI values over time in the study area (Figs. 9 and 10). In addition to the NDVI index, the use of the EVI index offers additional benefits by mitigating the effects of saturation and correcting for soil and atmospheric influences. The two vegetation indices complement each other and improve the detection of changes in vegetation.

Analysis of the descriptive statistics for the two series (2001-2024) confirms the results of the LULC classification, where vegetation cover is generally sparse and in a degraded state. The coefficient of variation varies by 13 and 15% for NDVI and EVI, respectively (relatively low variability), with relatively low mean values of 0.53 and 0.27 (Table 5).

The coefficient of variation varies from 32% to 17% for LAI and FPAR indices, respectively, with relatively low mean values of 0.99 and 4.13 (Table 5).These results show that the LAI index is the most variable, reflecting direct changes in leaf area over time or space. FPAR is slightly more variable than NDVI and EVI but less than LAI, representing small fluctuations in vegetation productivity (Figs. 11 and 12).
In conclusion, overall vegetation cover and greenness in the study area remain relatively low and stable in space and time in the period 2001-2024.

The differences in dynamics between the two indices (NDVI and LAI) are normal, as they are sensitive to different vegetation characteristics. NDVI reflects chlorophyll content and greenness, but it reaches saturation in dense or mature vegetation. However, LAI continues to increase with leaf growth and vegetation cover stratification, linking it more directly to leaf areas and biomass. NDVI reacts more quickly to greening at the beginning of the season, while LAI shows more gradual and sustained growth. During senescence, NDVI decreases more rapidly, while LAI continues to increase until significant leaf loss occurs.

Spatio-temporal analysis / change detection

For further statistical evaluation, we applied Sen's slope spatio-temporal trend analysis to both the NDVI and EVI series (2001-2024). This method was chosen for its robustness in detecting monotonic trends, making it particularly suitable for analyzing vegetation dynamics over time. The results of this analysis, detailed below, offer an explanation for the spatial evolution of vegetation over the study period.. A summary of results is presented in the following Table 6.

Spatio-temporal analysis carried out over the entire study area reveals both positive and negative trends in vegetation dynamics (NDVI and EVI) (Figs. 13 and 14). These trends vary and cover the entire study area. The decreasing values of Sen's slope in the study area confirm the findings of forest degradation and the impact of climate change in the area. The two vegetation indices complement each other and improve the detection of changes in the study area.
Degradation is occurring mainly in forest ecosystems conquered by Atlas cedar (Cedrus atlantica), as well as in mixed stands of Atlas cedar and holm oak (Quercus ilex). These forest ecosystems are predominantly vulnerable due to a combination of natural and anthropogenic pressures.

Spatio-temporal analysis carried out over the entire study area reveals both positive and negative trends in vegetation dynamics (NDVI and EVI) (Figs. 13 and 14). These

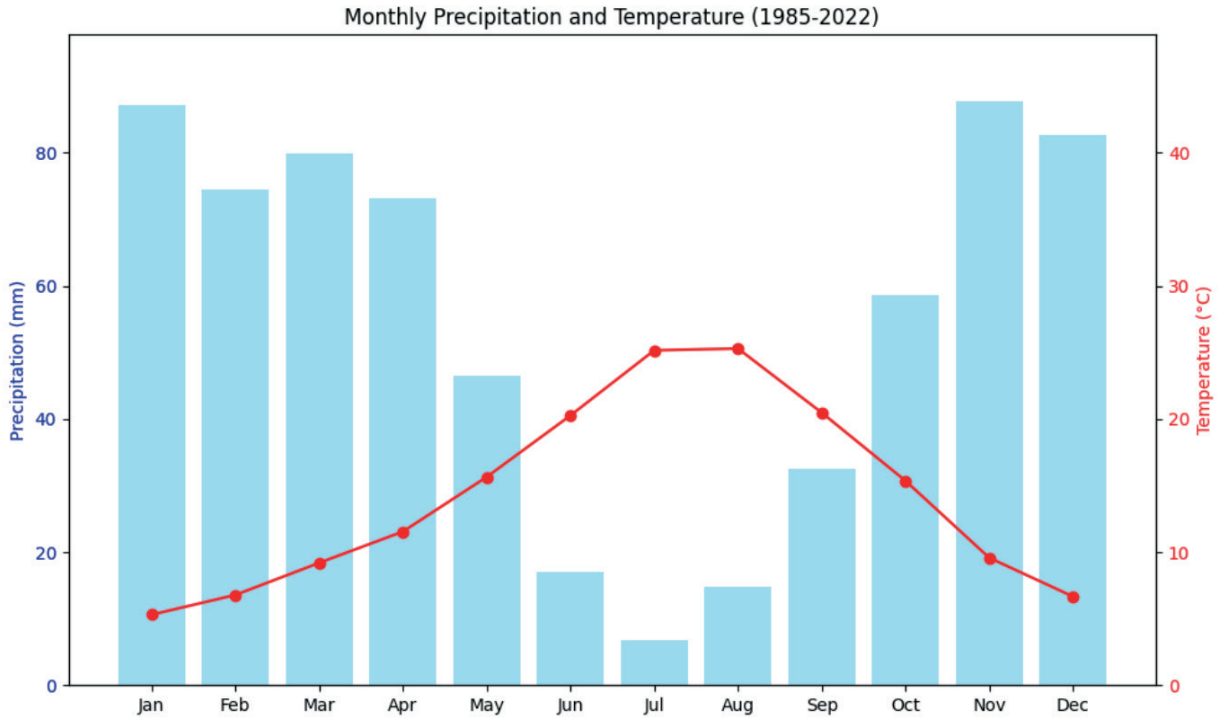

Fig. 7. Classification of the forest stand types in the study area

Table 3. Classification of the forest stand types in the study area

Stand type	Area (ha)	%
Pure Atlas cedar (*Cedrus atlantica*)	1497	8.4
Pure holm oak (*Quercus ilex*)	4420	24.8
Cedar mixed with holm oak	7182	40.3
Others	4708	24.7
Total	17,807	100

Table 4. Forest stand Accuracy assessment

Landuse	Pure Atlas cedar (*Cedrus atlantica*)	Pure holm oak (*Quercus ilex*)	Cedar mixed with holm oak	Others	Total (user)	User accuracy (%)
Pure Atlas cedar (*Cedrus atlantica*)	23	0	3	0	26	88%
Pure holm oak (*Quercus ilex*)	3	9	1	0	13	69%
Cedar mixed with holm oak	1	2	17	1	21	81%
Others	0	0	0	21	21	100%
Total (producer)	27	11	21	22	81	
Producer accuracy (%)	85%	82%	81%	95%		Overall Accuracy = 86.44%
					Kappa = 81.55%	

Table 5. Descriptive statistics for the time series indices (2001-2024)

Indices	Min	Max	Mean	Median	St dev	Coefficient of variation (%)
NDVI	0.196	0.65	0.53	0.54	0.07	13
EVI	0.11	0.37	0.27	0.27	0.04	15
LAI	0.04	1.84	0.99	1.02	0.32	32
FPAR	0.25	5.59	4.13	4.23	0.72	17

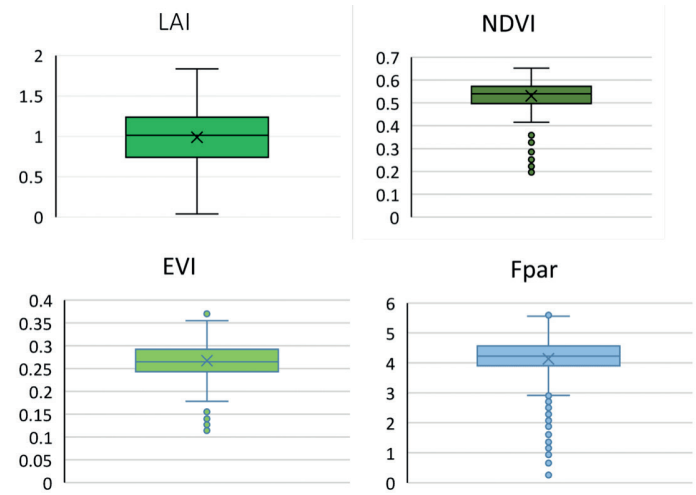

Fig. 8. Box plot for studied vegetation parameters (2001-2024)

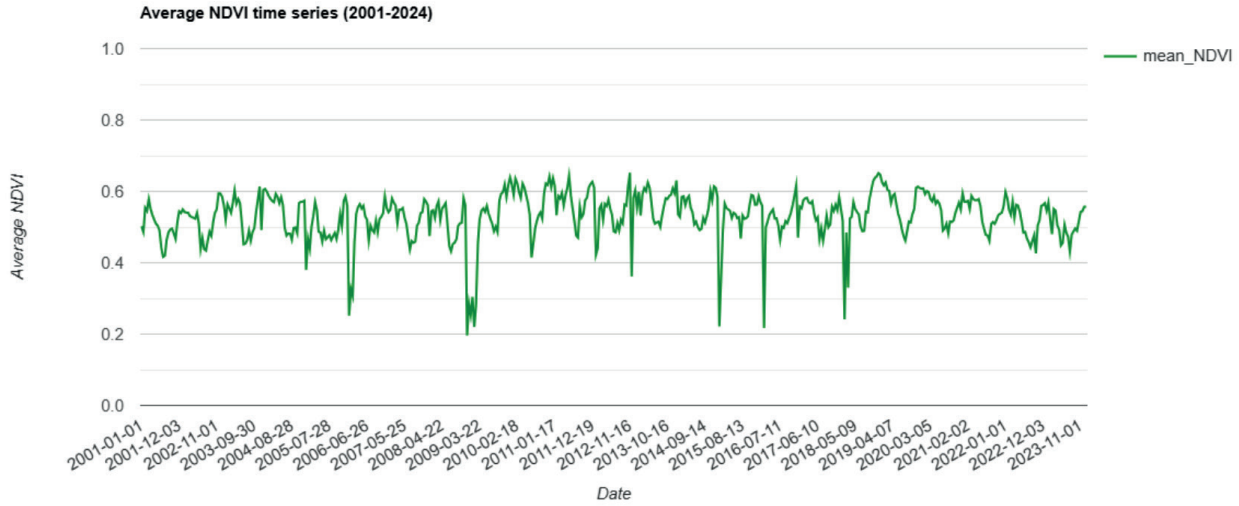

Fig. 9. NDVI time series (2001-2024)

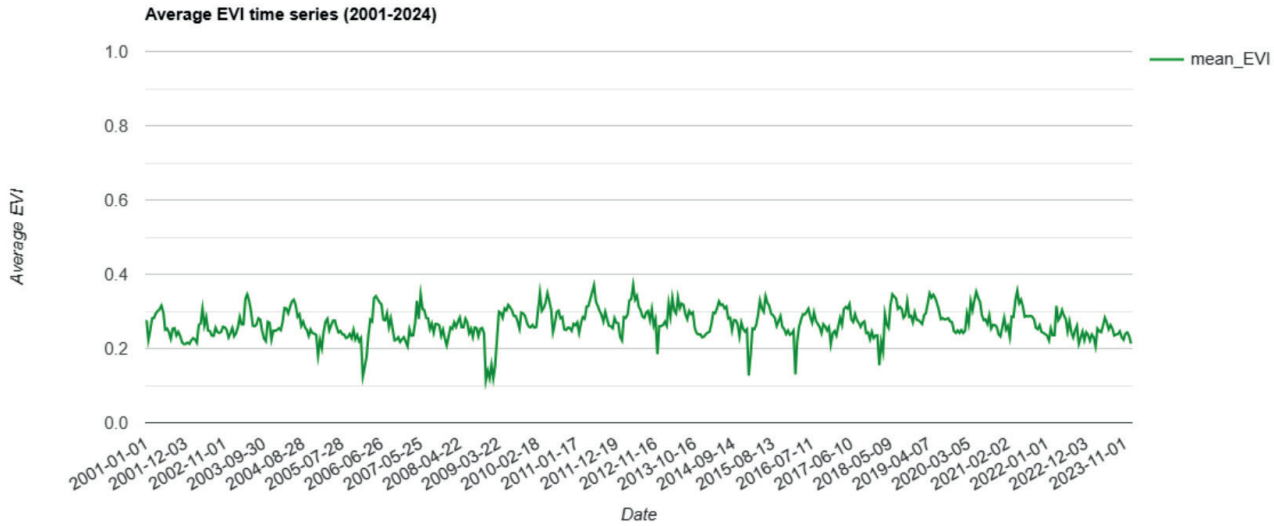

Fig. 10. EVI time series (2001-2024)

trends vary and cover the entire study area. The decreasing values of Sen's slope in the study area confirm the findings of forest degradation and the impact of climate change in the area. The two vegetation indices complement each other and improve the detection of changes in the study area.

Degradation is occurring mainly in forest ecosystems conquered by Atlas cedar (*Cedrus atlantica*), as well as in mixed stands of Atlas cedar and holm oak (*Quercus ilex*). These forest ecosystems are predominantly vulnerable due to a combination of natural and anthropogenic pressures.

Biomass prediction using Machine Learning in GEE

Biomass estimation models based on remote sensing data (NDVI, EVI, LAI, FPAR) are sensitive to changes in vegetation structure and vigor, which can decrease without any visible change in land cover type. Biomass modelling provided an assessment of the mass in the forest area studied, expressed in dry weight, of the woody parts (stem, bark, branches and twigs) of all living trees, excluding stumps and roots (Spawn et al., 2020). The Random Forest model designed for our prediction (correlation = 0, 7 with a

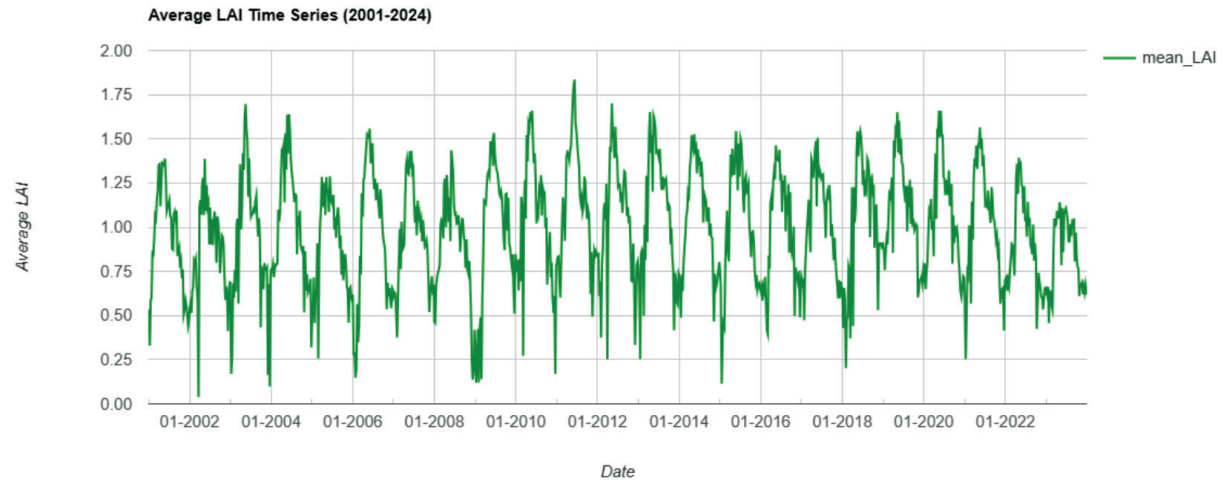

Fig. 11. LAI time series (2001-2024)

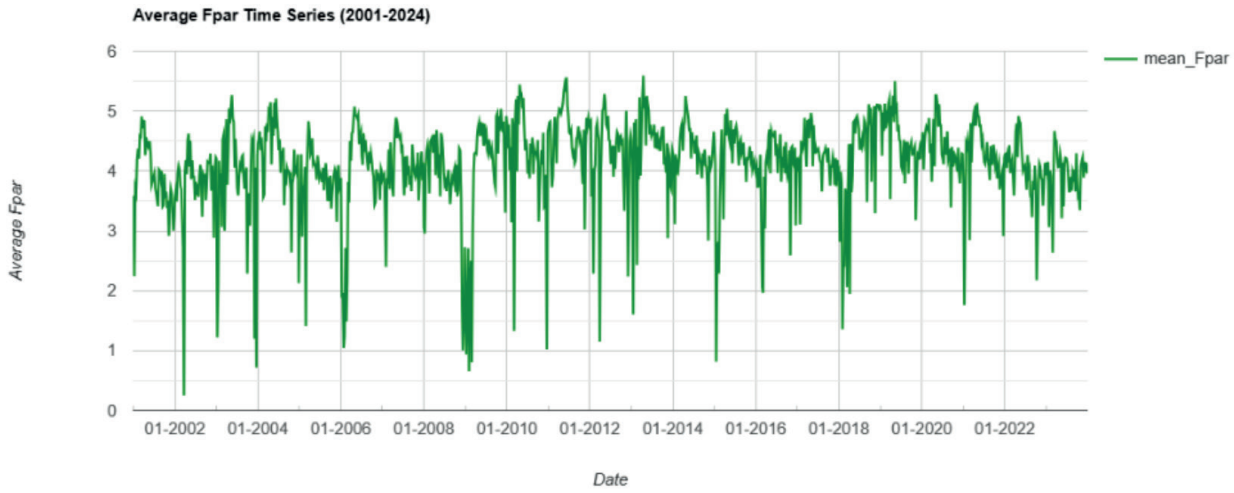

Fig. 12. FPAR time series (2001-2024)

Table 6. Sen's slope class for NDVI and EVI

Indices/Sen's slope	Decreasing	Stable	Increasing
NDVI	-2.23 to 0	0-1	1 to 3.6
EVI	-1.4 to 0	0-1	1 to 3.4

p-value < 0, 05) has enabled us to obtain the first results by period (2010, 2015, 2020 and 2024) in the forest study area for data based on the satellite dataset (Fig. 15).

The results obtained showed a decrease in value (-8%) between 2010 and 2024, with a biomass of 501,172 tons/ha in 2010 versus 461,587 tons/ha predicted by our model for 2024.

In 2024, the biomass median values by species were 29 tons/ha for pure Atlas cedar, 24 tons/ha for pure holm oak, and 31 tons/ha for a mixture of Atlas cedar and holm oak (Table 7, Figs. 16 and 17).

Generally, between holm oak (*Quercus ilex*) and Atlas cedar (*Cedrus atlantica*), above-ground biomass potential depends on several factors such as region, ecological conditions (soil type, climate, elevation), stand density and tree age.

These results further confirm that Atlas cedar produces a higher above-ground biomass than holm oak, particularly under favorable conditions. These results provide a comprehensive approach to mapping biomass estimation in forestry and suggest guidelines for forest planning.

DISCUSSION

In addition to vegetation condition over time and space, this research work examines the assessment of forest biomass by machine learning algorithms in GEE. This innovative approach replaces the use of costly field investigations. The biomass values obtained are reference values for the main forest species in the area, namely Atlas cedar and holm oak.

A negative evolution was highlighted, in biomass values, between 2010 and 2024, materializing the negative trend in vegetation parameters studied in the area. In 2024, the predicted biomass is 461,587 tons, compared with 501,172 tons in 2010. This measurement is the carbon stock density of the above-ground living biomass of the combined woodland and herbaceous cover. The biomass median values by species were 29 tons/ha for pure Atlas cedar, 24 tons/ha for pure holm oak, and 31 tons/ha for a mixture of Atlas cedar and holm oak. According to the FAO (2006) in (Oubrahim et al., 2016), carbon stocks in forests

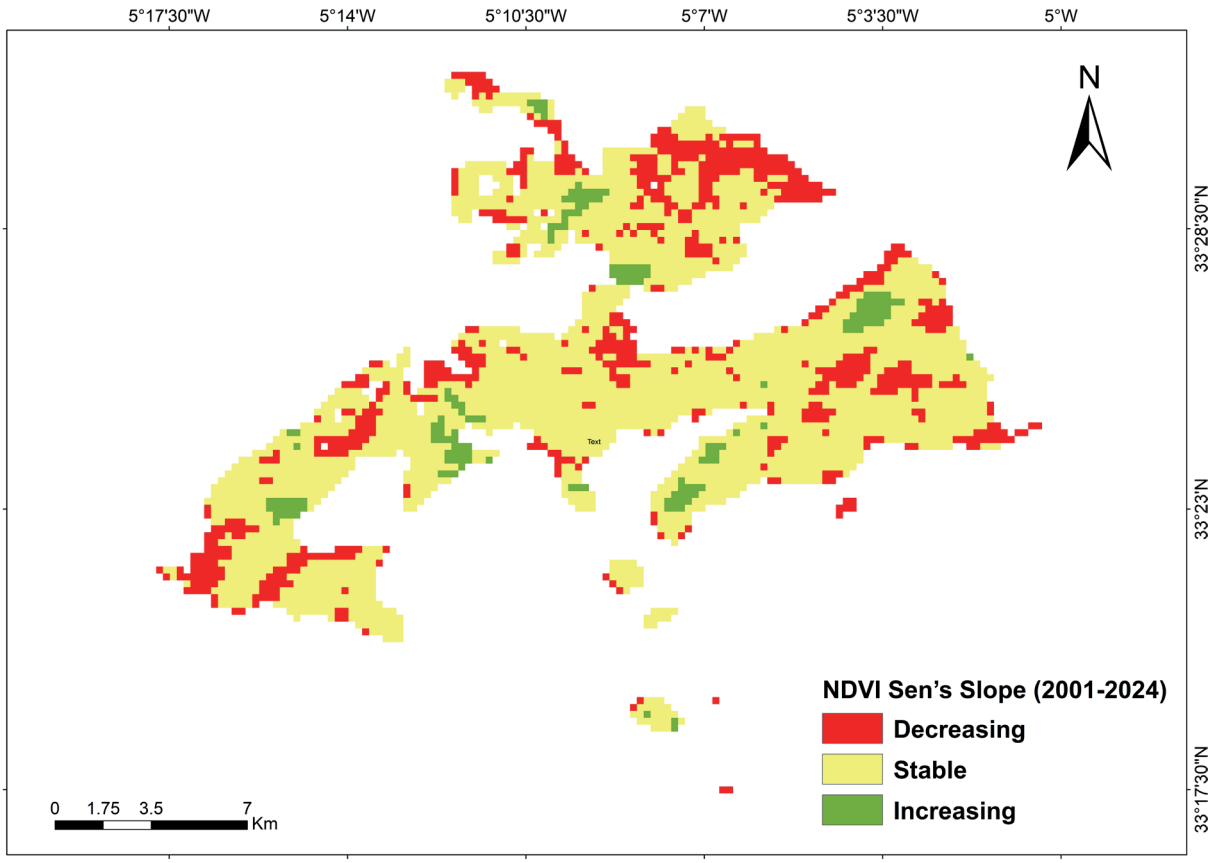

Fig. 13. NDVI Sen's slope (2001-2024)

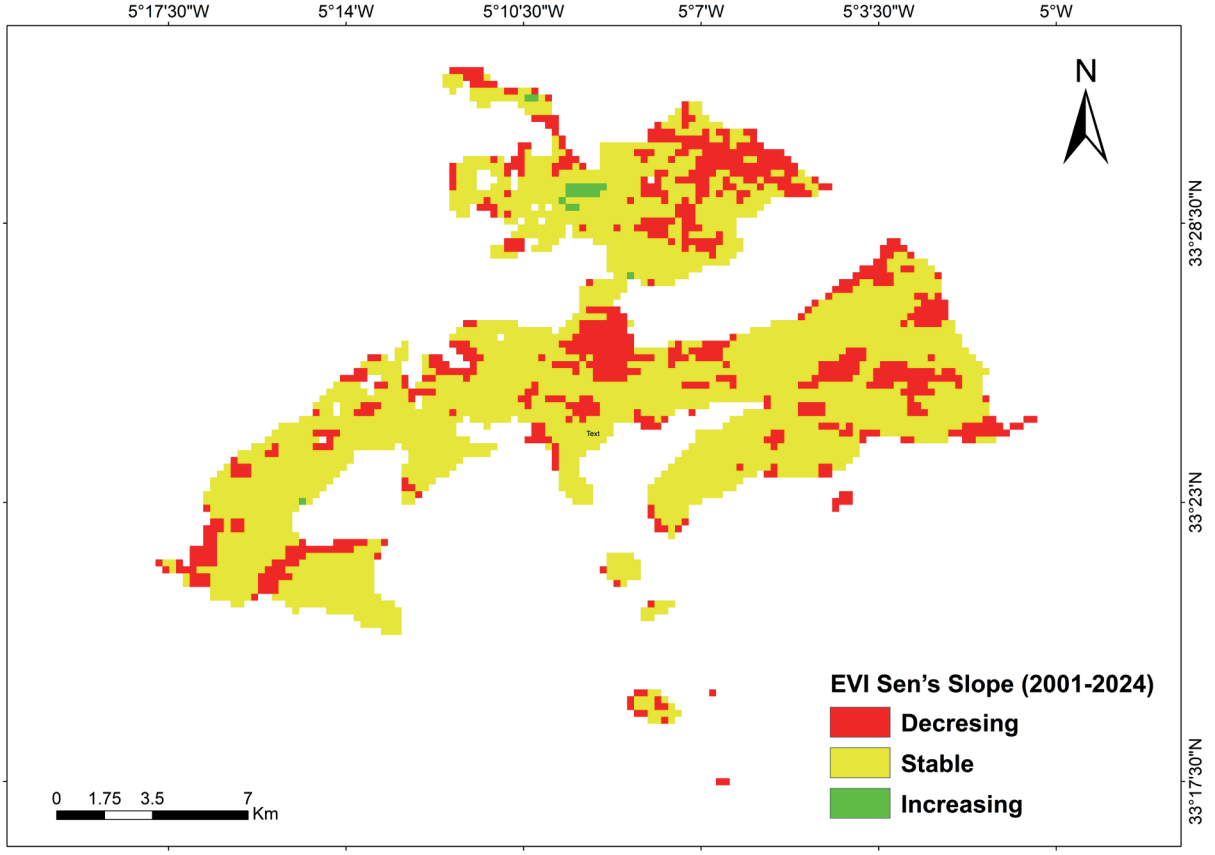

Fig. 14. EVI Sen's slope (2001-2024)

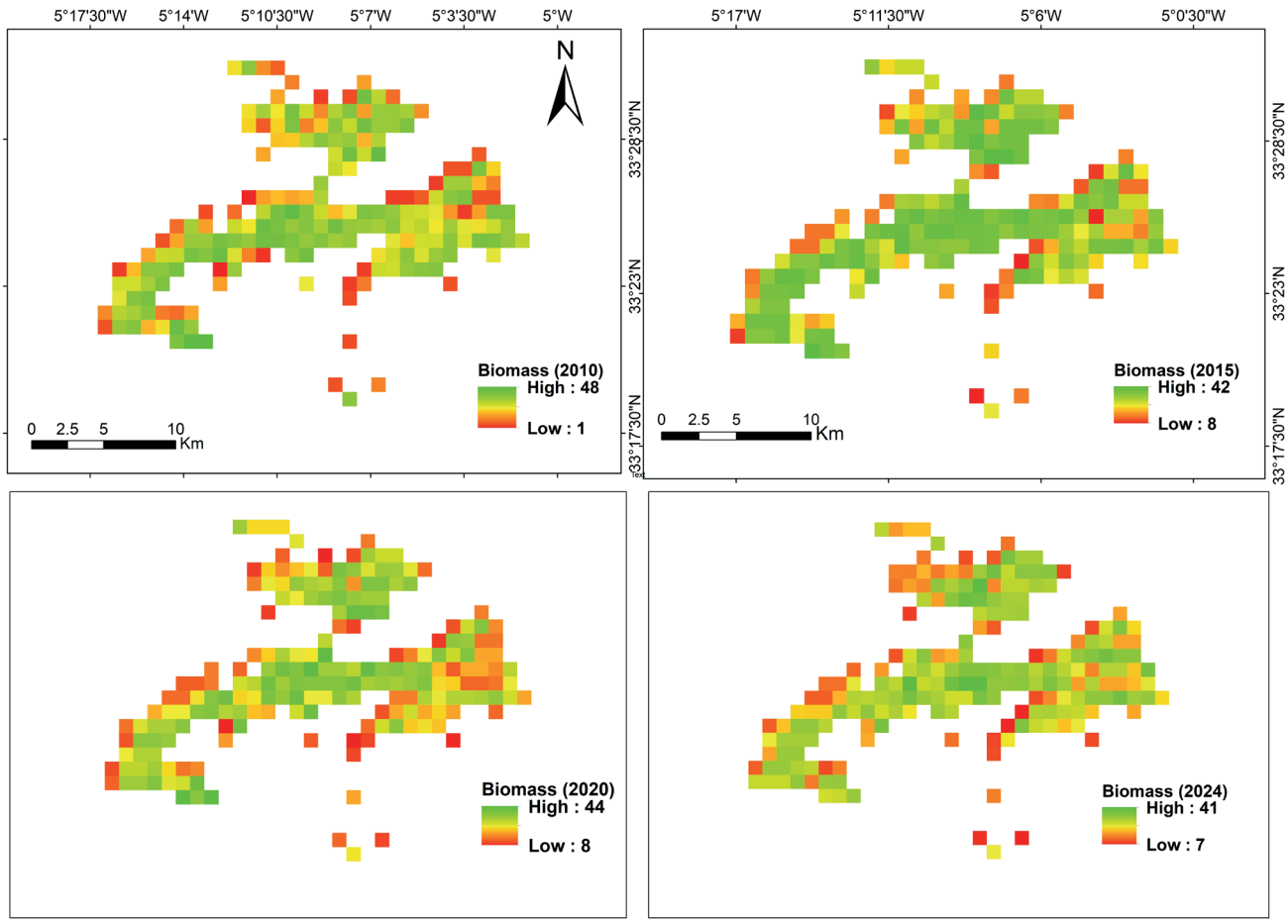

Fig. 15. Biomass 2010 and biomass prediction 2015, 2020 and 2024 (Megagrams (Mg) per hectare)

Table 7. Biomass predicted by period in the study area

Biomass	Stand type	Atlas cedar (Cedrus atlantica)	Holm oak (Quercus ilex)	Atlas Cedar mixed with holm oak	Others	Total
	Area (ha)	1,497	4,420	7,182	4,708	17,807
Biomass 2010	Median (Mg/ha)	32	26	34	20	----
	Total (Mg)	47,904	114,920	244,188	94,160	501,172
Biomass predicted 2015	Median (Mg/ha)	31	26	33	20	----
	Total (Mg/ha)	46,407	114,920	237,006	94,160	492,493
Biomass predicted 2020	Median (Mg/ha)	30	24	32	19	----
	Total (Mg)	44,910	106,080	229,824	89,452	470,266
Biomass predicted 2024	Median (Mg/ha)	29	24	31	19	----
	Total (Mg)	43,413	106,080	222,642	89,452	461,587

(Units of measurement are expressed in megagrams (Mg) per hectare. 1 Mg = 1 metric ton)

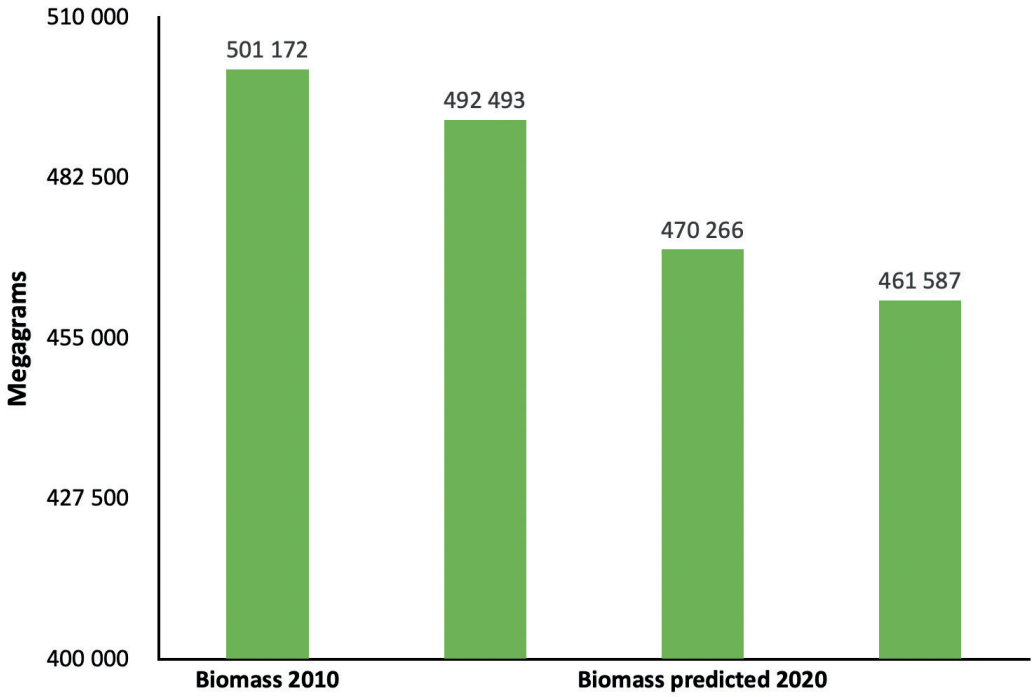

Fig. 16. Biomass (Mg) predicted by period

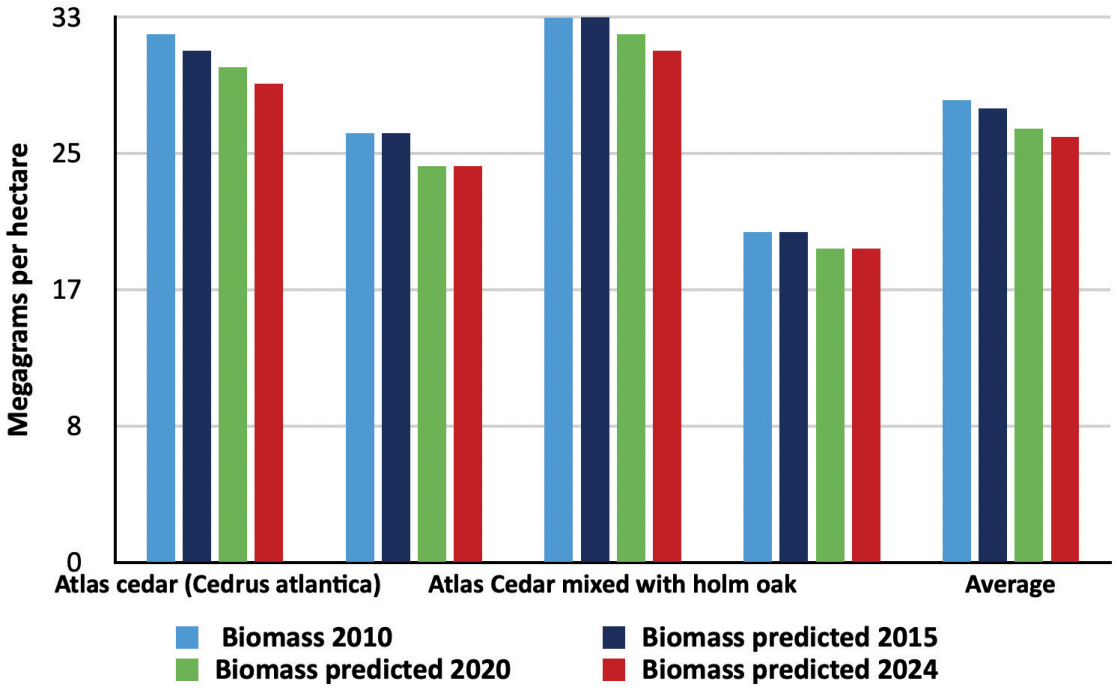

Fig. 17. Median biomass predicted by period

in North Africa (the total carbon in biomass, dead wood, forest floor and the first 30 cm of the soil profile) were on average 64.9 tons/ha.

In the Middle Atlas cedar area, in four reservoirs, i.e., aboveground biomass, belowground biomass (roots), necromass (litter and deadwood) and the soil, carbon stocks were esteemed at 395.37 Mg/ha for the natural cedar Atlas and 76.05 Mg/ha for the cleared area. Analysis of the carbon stock distribution in the ecosystem discovered that soil was the largest reservoir. Indeed, the soil carbon stock varies from 46.4% to 93.5%, that of the biomass (aboveground and belowground) fluctuates between 4.3% and 52.7% and in the necromass, it is between 0.8 and 2.2% (Zaher et al., 2020b).

The highest carbon stocks are found in the most densely wooded areas (dense forests). This finding is confirmed by other studies on the subject (Le Clec'h et al., 2013; Oubrahim et al., 2016). In addition to aboveground biomass, assessing the contribution of forest soils makes it possible to estimate the total biomass level of the ecosystem. Forest soils are a significant reservoir of carbon; more than 40% of the total organic carbon in terrestrial ecosystems is stored in forest soils (Wei et al., 2014; Weston & Whittaker, 2004). In the banj oak forests (*Quercus leucotrichophora*) of the Central Himalaya, tree biomass declined by 62% from undisturbed to degraded forests, the carbon sequestration rate decreased by 73%, peaking in moderately disturbed-A forests, while total soil carbon fell by 79% (Pandey et al., 2020).

The decline in biomass values in our increasingly fragile ecosystem is attributed to several interdependent processes and factors that do not necessarily involve a change in LULC classification. Firstly, we can note the degradation of forest areas, such as the excessive logging of precious Atlas cedar wood and overgrazing that exceeds the carrying capacity, which can significantly reduce

biomass even though the overall forest cover appears unchanged. Secondly, reduced tree density and stress can also lead to lower biomass estimates. Known climatic stress factors in recent decades (droughts and rising temperatures, etc.) have limited tree growth and health, thereby reducing biomass accumulation.

The increased stress on vegetation in the area was highlighted by analyzing spatial and temporal variations in vegetation indices (NDVI, EVI, LAI and FPAR). These indices are reliable indicators of vegetation health and are sensitive to changes in vegetation cover and structural properties (González-Alonso et al., 2006; Shammi & Meng, 2021).

The negative trends observed for NDVI and EVI indices reflect a reduction in photosynthetic activity and vegetation density in the forest study area. Shortened vegetation affects carbon sequestration, biodiversity, and ecosystem services in the study area.

Models based on remote sensing and machine-learning techniques have made it possible to detect subtle changes in biomass, even in areas where LULC cover does not appear to have changed visibly. We can therefore conclude that these tools are powerful for monitoring and assessing the state of forest ecosystems beyond simple changes in land use.

The downward trends observed in biomass, particularly in cedar forests and mixed oak and cedar forests, reflect both local degradation processes and regional environmental pressures. In our area, carbon stocks vary considerably depending on the type of forest. The ecosystem is vulnerable to degradation, which reduces its carbon sequestration potential. Overgrazing and deforestation not only reduce above-ground biomass but also lead to soil erosion and loss of organic matter, contributing to a decrease in soil carbon stocks. In a regional context marked by human pressures and climate change (Del Río et al., 2017; Gómez et al., 2012; Vayreda et al., 2012), intensified land use, and difficulties in natural regeneration, similar trends in biomass decline and carbon loss are observed, suggesting that these trends may be regional. Globally, these findings are consistent with broader concerns about the declining carbon storage capacity of dry Mediterranean forests, pointing to the importance of sustainable management strategies.

It would be interesting to take into account local data validation (forest inventories or biomass measurements in the field) for a more accurate comparison. Assessment of biomass by species would be more interesting if we focused on results by station type, taking into account the main ecological (soil, climate, stand age, elevation) and local socio-economic factors. In fact, human and pastoral pressure on the environment would have a negative impact on the forest ecosystem in question.

CONCLUSIONS

Today, the adoption of innovative approaches offered by Google Earth Engine (GEE) combined with GIS and remote sensing tools is playing an increasingly central role in the analysis, monitoring, and management of forest ecosystems. Indeed, the use of these platforms in our work has provided very useful results for assessing the evolution of canopy dynamics and the prediction of aerial biomass in the study area.

This study reveals that between 2010 and 2024, biomass values in the Azrou forest studied showed a decline over time and space. This negative trend reflects a more general deterioration in vegetation vigor and health indicators. The main vegetation indices studied in the model, notably NDVI, EVI, LAI, and FPAR, followed descending trends. These trends are due to natural and human factors that have caused environmental stress. Overall, the results confirm a marked degradation of the ecosystem during the study period.

Significant spatio-temporal negative trends in vegetation indices and biomass levels underline the need for adaptive management strategies in the context of climate change. Future research should focus more on field investigations and the integration of socio-economic data to better understand the interactions of the studied forest ecosystem. Assessment of canopy and biomass dynamics would benefit from the integration of other environmental factors related to local sites (soil type and physico-chemical characteristics, stand structure, age, density).

Future research should also focus on integrating local socioeconomic data to better understand human-environment interactions and develop predictive models that promote effective mitigation and adaptation measures.

REFERENCES

Aguiar, L. J. G., Fischer, G. R., Ladle, R. J., Malhado, A. C. M., Justino, F. B., Aguiar, R. G., & Da Costa, J. M. N. (2012). Modeling the photosynthetically active radiation in South West Amazonia under all sky conditions. Theoretical and Applied Climatology, 108(3–4), 631–640. https://doi.org/10.1007/s00704-011-0556-z

Alaoui, A., Laaribya, S., Sezgin, A., Ghallab, A., & López-Tirado, J. (2021). Modelling spatial distribution of endemic Moroccan fir (Abies marocana Trabut) in Talassemtane National Park, Morocco. 138(2), 73–94.

Bagnouls, F., & Gaussen, H. (1953). Dry season and xerothermic index. 193–239.

Behera, S. K., Srivastava, P., Pathre, U. V., & Tuli, R. (2010). An indirect method of estimating leaf area index in Jatropha curcas L. using LAI-2000 Plant Canopy Analyzer. Agricultural and Forest Meteorology, 150(2), 307–311. https://doi.org/10.1016/j.agrformet.2009.11.009

Boulmane, M., Santa-Regina, M. D. C., Halim, M., Khia, A., Oubrahim, H., Abbassi, H., & Santa-Regina, I. (2015). Organic Carbon Storage in Evergreen Oak Forest Ecosystems of the Middle and High Moroccan Atlas Areas. Open Journal of Forestry, 05(03), 260–273. https://doi.org/10.4236/ojf.2015.53023

Breiman, L. (2001). Random Forests. Machine Learning. Machine Learning, 45(1), 5–32. https://doi.org/10.1023/A:1010933404324

Calvin, K., Dasgupta, D., Krinner, G., Mukherji, A., Thorne, P. W., Trisos, C., Romero, J., Aldunce, P., Barrett, K., Blanco, G., Cheung, W. W. L., Connors, S., Denton, F., Diongue-Niang, A., Dodman, D., Garschagen, M., Geden, O., Hayward, B., Jones, C., … Péan, C. (2023). IPCC, 2023: Climate Change 2023: Synthesis Report. Contribution of Working Groups I, II and III to the Sixth Assessment Report of the Intergovernmental Panel on Climate Change [Core Writing Team, H. Lee and J. Romero (eds.)]. IPCC, Geneva, Switzerland. (First). Intergovernmental Panel on Climate Change (IPCC). https://doi.org/10.59327/IPCC/AR6-9789291691647

Del Río, M., Barbeito, I., Bravo-Oviedo, A., Calama, R., Cañellas, I., Herrero, C., Montero, G., Moreno-Fernández, D., Ruiz-Peinado, R., & Bravo, F. (2017). Mediterranean Pine Forests: Management Effects on Carbon Stocks. In F. Bravo, V. LeMay, & R. Jandl (Eds.), Managing Forest Ecosystems: The Challenge of Climate Change (Vol. 34, pp. 301–327). Springer International Publishing. https://doi.org/10.1007/978-3-319-28250-3_15

El Mderssa, M. (2022). Détermination des paramètres d'évaluation du stock de carbone dans les écosystèmes forestiers (Cedrus atlantica Manetti, cèdre de l'Atlas au Maroc): Méthodes spécifiques et génériques. BOIS & FORETS DES TROPIQUES, 351, 67–77. https://doi.org/10.19182/bft2022.351.a36330

El Mderssa, M., Belghazi, B., Benjelloun, H., Zennouhi, O., Nassiri, L., & Ibijbijen, J. (2019). Estimation of Carbon Sequestration; Using Allometric Equations; in Azrou Cedar Forests (Cedrus atlantica Manetti) in the Central Middle Atlas of Morocco under Climate Change. Open Journal of Forestry, 09(03), 214–225. https://doi.org/10.4236/ojf.2019.93011

Erickson, L. E., & Brase, G. (2020). Reducing Greenhouse Gas Emissions and Improving Air Quality: Two Interrelated Global Challenges. Taylor & Francis.

FAO. (2020). Global Forest Resources Assessment 2020. FAO. https://doi.org/10.4060/ca9825en

Forsell, N., Turkovska, O., Gusti, M., Obersteiner, M., Elzen, M. D., & Havlik, P. (2016). Assessing the INDCs' land use, land use change, and forest emission projections. Carbon Balance and Management, 11(1), 26. https://doi.org/10.1186/s13021-016-0068-3

Friedlingstein, P., Jones, M. W., O'Sullivan, M., Andrew, R. M., Bakker, D. C. E., Hauck, J., Le Quéré, C., Peters, G. P., Peters, W., Pongratz, J., Sitch, S., Canadell, J. G., Ciais, P., Jackson, R. B., Alin, S. R., Anthoni, P., Bates, N. R., Becker, M., Bellouin, N., … Zeng, J. (2022). Global Carbon Budget 2021. Earth System Science Data, 14(4), 1917–2005. https://doi.org/10.5194/essd-14-1917-2022

García, M., Riaño, D., Chuvieco, E., & Danson, F. M. (2010). Estimating biomass carbon stocks for a Mediterranean forest in central Spain using LiDAR height and intensity data. Remote Sensing of Environment, 114(4), 816–830. https://doi.org/10.1016/j.rse.2009.11.021

García-Rodríguez, A., Granados-López, D., García-Rodríguez, S., Díez-Mediavilla, M., & Alonso-Tristán, C. (2021). Modelling Photosynthetic Active Radiation (PAR) through meteorological indices under all sky conditions. Agricultural and Forest Meteorology, 310, 108627. https://doi.org/10.1016/j.agrformet.2021.108627

Gómez, C., Wulder, M. A., White, J. C., Montes, F., & Delgado, J. A. (2012). Characterizing 25 years of change in the area, distribution, and carbon stock of Mediterranean pines in Central Spain. International Journal of Remote Sensing, 33(17), 5546–5573. https://doi.org/10.1080/01431161.2012.663115

González-Alonso, F., Merino-De-Miguel, S., Roldán-Zamarrón, A., García-Gigorro, S., & Cuevas, J. M. (2006). Forest biomass estimation through NDVI composites. The role of remotely sensed data to assess Spanish forests as carbon sinks. International Journal of Remote Sensing, 27(24), 5409–5415. https://doi.org/10.1080/01431160600830748

Huete, A. (1997). A comparison of vegetation indices over a global set of TM images for EOS-MODIS. Remote Sensing of Environment, 59(3), 440–451. https://doi.org/10.1016/S0034-4257(96)00112-5

Laaribya, S. (2024). Analysis of the determinants of the regeneration and growth of Cedar Atlas (Cedrus atlantica (Endl.) Manetti ex Carrière), an endangered endemic taxon in Morocco-Case of the Middle Atlas forests. IOP Conference Series: Earth and Environmental Science, 1398(1), 012002. https://doi.org/10.1088/1755-1315/1398/1/012002

Laaribya, S., & Alaoui, A. (2025). Spatio-Temporal Trends and Climate Change Impacts on Land Cover Dynamics in Talassemtane National Park (Morocco) Using Artificial Intelligence and Google Earth Engine. Journal of Sustainable Forestry, 1–30. https://doi.org/10.1080/10549811.2025.2516072

Laaribya, S., Alaoui, A., Ayan, S., Benabou, A., Labbaci, A., Ouhaddou, H., & Bijou, M. (2021). Prediction by maximum entropy of potential habitat of the cork oak (Quercus suber L.) in Maamora Forest, Morocco. Forestist, 71(2), 63–69. https://doi.org/10.5152/forestist.2021.20059

Laaribya, S., Alaoui, A., Ayan, S., & Dindaroglu, T. (2024). Changes in the Potential Distribution of Atlas Cedar in Morocco in the Twenty-First Century According to the Emission Scenarios of RCP 4,5 and RCP 8,5. Forestist. https://doi.org/10.5152/forestist.2023.0004

Le Clec'h, S., Oszwald, J., Jégou, N., Dufour, S., Cornillon, P. A., Miranda, I. D. S., Gonzaga, L., Grimaldi, M., Gond, V., & Arnauld De Sartre, X. (2013). Cartographier le carbone stocké dans la végétation: Perspectives pour la spatialisation d¿un service écosystémique. BOIS & FORETS DES TROPIQUES, 316(316), 35. https://doi.org/10.19182/bft2013.316.a20529

Linares, J. C., Taïqui, L., & Camarero, J. J. (2011). Increasing Drought Sensitivity and Decline of Atlas Cedar (Cedrus atlantica) in the Moroccan Middle Atlas Forests. Forests, 2(3), 777–796. https://doi.org/10.3390/f2030777

Merlo, M., & Croitoru, L. (Eds.). (2005). Valuing mediterranean forests: Towards total economic value (1st ed.). CABI Publishing. https://doi.org/10.1079/9780851999975.0000

Mutanga, O., & Kumar, L. (2019). Google Earth Engine Applications. Remote Sensing, 11(5), 591. https://doi.org/10.3390/rs11050591

Myneni, R. B., Dong, J., Tucker, C. J., Kaufmann, R. K., Kauppi, P. E., Liski, J., Zhou, L., Alexeyev, V., & Hughes, M. K. (2001). A large carbon sink in the woody biomass of Northern forests. Proceedings of the National Academy of Sciences, 98(26), 14784–14789. https://doi.org/10.1073/pnas.261555198

Myneni, R., Knyazikhin, Y., & Park, T. (2021). MODIS/Terra Leaf Area Index/FPAR 8-Day L4 Global 500m SIN Grid V061 [Dataset]. NASA EOSDIS Land Processes Distributed Active Archive Center. https://doi.org/10.5067/MODIS/MOD15A2H.061

Nourelbait, M., Rhoujjati, A., Benkaddour, A., Carré, M., Eynaud, F., Martinez, P., & Cheddadi, R. (2016). Climate change and ecosystems dynamics over the last 6000 years in the Middle Atlas, Morocco. Climate of the Past, 12(4), 1029–1042. https://doi.org/10.5194/cp-12-1029-2016

Oubrahim, H., Boulmane, M., Bakker, M., Augusto, L., & Halim, M. (2016). Carbon storage in degraded cork oak (Quercus suber) forests on flat lowlands in Morocco. iForest - Biogeosciences and Forestry, 9(1), 125–137. https://doi.org/10.3832/ifor1364-008

Ourbak, T., & Magnan, A. K. (2018). The Paris Agreement and climate change negotiations: Small Islands, big players. Regional Environmental Change, 18(8), 2201–2207. https://doi.org/10.1007/s10113-017-1247-9

Pan, Y., Birdsey, R. A., Phillips, O. L., Houghton, R. A., Fang, J., Kauppi, P. E., Keith, H., Kurz, W. A., Ito, A., Lewis, S. L., Nabuurs, G.-J., Shvidenko, A., Hashimoto, S., Lerink, B., Schepaschenko, D., Castanho, A., & Murdiyarso, D. (2024). The enduring world forest carbon sink. Nature, 631(8021), 563–569. https://doi.org/10.1038/s41586-024-07602-x

Pandey, A., Arunachalam, K., Thadani, R., & Singh, V. (2020). Forest degradation impacts on carbon stocks, tree density and regeneration status in banj oak forests of Central Himalaya. Ecological Research, 35(1), 208–218. https://doi.org/10.1111/1440-1703.12078

Rudel, T. K., Coomes, O. T., Moran, E., Achard, F., Angelsen, A., Xu, J., & Lambin, E. (2005). Forest transitions: Towards a global understanding of land use change. Global Environmental Change, 15(1), 23–31. https://doi.org/10.1016/j.gloenvcha.2004.11.001

Schilling, J., Freier, K. P., Hertig, E., & Scheffran, J. (2012). Climate change, vulnerability and adaptation in North Africa with focus on Morocco. Agriculture, Ecosystems & Environment, 156, 12–26. https://doi.org/10.1016/j.agee.2012.04.021

Schonlau, M., & Zou, R. Y. (2020). The random forest algorithm for statistical learning. The Stata Journal: Promoting Communications on Statistics and Stata, 20(1), 3–29. https://doi.org/10.1177/1536867X20909688

Scott, M., Lennon, M., Tubridy, F., Marchman, P., Siders, A. R., Main, K. L., Herrmann, V., Butler, D., Frank, K., Bosomworth, K., Blanchi, R., & Johnson, C. (2020). Climate Disruption and Planning: Resistance or Retreat? Planning Theory & Practice, 21(1), 125–154. https://doi.org/10.1080/14649357.2020.1704130

Sen, P. K. (1968). Estimates of the Regression Coefficient Based on Kendall's Tau. Journal of the American Statistical Association, 63(324), 1379–1389. https://doi.org/10.1080/01621459.1968.10480934

Shammi, S. A., & Meng, Q. (2021). Use time series NDVI and EVI to develop dynamic crop growth metrics for yield modeling. Ecological Indicators, 121, 107124. https://doi.org/10.1016/j.ecolind.2020.107124

Sinha, S. (2022). H/A/α Polarimetric Decomposition Of Dual Polarized Alos Palsar For Efficient Land Feature Detection And Biomass Estimation Over Tropical Deciduous Forest. GEOGRAPHY, ENVIRONMENT, SUSTAINABILITY, 15(3), 37–46. https://doi.org/10.24057/2071-9388-2021-095

Spawn, S. A., Sullivan, C. C., Lark, T. J., & Gibbs, H. K. (2020). Harmonized global maps of above and belowground biomass carbon density in the year 2010. Scientific Data, 7(1), 112. https://doi.org/10.1038/s41597-020-0444-4

Terrab, A., Paun, O., Talavera, S., Tremetsberger, K., Arista, M., & Stuessy, T. F. (2006). Genetic diversity and population structure in natural populations of Moroccan Atlas cedar (Cedrus atlantica ; Pinaceae) determined with cpSSR markers. American Journal of Botany, 93(9), 1274–1280. https://doi.org/10.3732/ajb.93.9.1274

Tucker, C. J. (1979). Red and photographic infrared linear combinations for monitoring vegetation. Remote Sensing of Environment, 8(2), 127–150. https://doi.org/10.1016/0034-4257(79)90013-0

Vayreda, J., Gracia, M., Canadell, J. G., & Retana, J. (2012). Spatial Patterns and Predictors of Forest Carbon Stocks in Western Mediterranean. Ecosystems, 15(8), 1258–1270. https://doi.org/10.1007/s10021-012-9582-7

Watson, D. J. (1958). The Dependence of Net Assimilation Rate on Leaf-area Index. Annals of Botany, 22(1), 37–54. https://doi.org/10.1093/oxfordjournals.aob.a083596

Wei, X., Shao, M., Gale, W., & Li, L. (2014). Global pattern of soil carbon losses due to the conversion of forests to agricultural land. Scientific Reports, 4(1), 4062. https://doi.org/10.1038/srep04062

Weston, C. J., & Whittaker, K. L. (2004). SOIL BIOLOGY AND TREE GROWTH | Soil Biology. In Encyclopedia of Forest Sciences (pp. 1183–1189). Elsevier. https://doi.org/10.1016/B0-12-145160-7/00248-9

Zaher, H., Sabir, M., Benjelloun, H., & Paul-Igor, H. (2020a). Effect of forest land use change on carbohydrates, physical soil quality and carbon stocks in Moroccan cedar area. Journal of Environmental Management, 254, 109544. https://doi.org/10.1016/j.jenvman.2019.109544

Zaher, H., Sabir, M., Benjelloun, H., & Paul-Igor, H. (2020b). Effect of forest land use change on carbohydrates, physical soil quality and carbon stocks in Moroccan cedar area. Journal of Environmental Management, 254, 109544. https://doi.org/10.1016/j.jenvman.2019.109544

Zhao, M., Cheng, C., Zhou, Y., Li, X., Shen, S., & Song, C. (2021). A global dataset of annual urban extents (1992-2020) from harmonized nighttime lights (p. 358204912 Bytes) [Dataset]. figshare. https://doi.org/10.6084/M9.FIGSHARE.16602224.V1

RESEARCH PAPER

GEOCHEMICAL INDICATION OF SEDIMENT FLUXES USING CHERNOBYL-DERIVED ^{137}CS: THE CASE STUDY OF A SMALL AGRICULTURAL CATCHMENT IN THE TULA REGION, CENTRAL RUSSIA

Maksim M. Ivanov [1,2], Valentin N. Golosov[1,2], Nadezhda N. Ivanova[1], Polina I. Fominykh[1,2]
[1]Faculty of Geography, Lomonosov Moscow State University, Leninskie Gory 1, Moscow 119991, Russia
[2]Institute of Geography of Russian Academy of Science, Staromonetniy lane. 29, Moscow, 119017, Russia
***Corresponding author:** ivanovm@bk.ru
Received: February 26th 2025 / Accepted: July 18th 2025 / Published: October 1st 2025
https://doi.org/10.24057/2071-9388-2025-3910

ABSTRACT. This paper explores the use of ^{137}Cs derived from Chernobyl as an indicator of sediment supply and transport within small agricultural catchments by analyzing the depth distribution of radionuclides, with a focus on post-Chernobyl changes in the activity concentration of radionuclides. To this end, depth-incremental sampling was carried out along routes of sediment transport within a small agricultural catchment subject to intense radioactive contamination in the Tula region. Some points were set to repeat the position of those made 27 years earlier and to understand the dynamics of deposition and the ^{137}Cs content in the sediment load. It has been suggested that a decrease in the activity concentration of ^{137}Cs can be used as an indicator of the relative age of deposits. Assuming this, the pattern of erosion product deposition on the sides and bottom of the dry valley was determined. This pattern was found to be stable and consistent with the observed geomorphic features and climate trends: the rate of accumulation in the valley bottom over the past 27 years has dropped almost twice, coinciding with a decrease in snowmelt runoff during springtime and no increase in intense rainfall. Grain-size analysis of the collected samples showed that selective transfer of clay particles may occur, but over a short delivery distance, it is unlikely that the sorting process will significantly alter the downward trend of ^{137}Cs concentrations. The proposed approach has the potential to significantly improve the accuracy of sediment budget estimations and environmental quality assessments.

KEYWORDS: erosion, sediment delivery, ^{137}Cs, Chernobyl contamination, sedimentation

CITATION: Ivanov M. M., Golosov V. N., Ivanova N. N., Fominykh P. I. (2025). Geochemical Indication Of Sediment Fluxes Using Chernobyl-Derived ^{137}Cs: The Case Study Of A Small Agricultural Catchment In The Tula Region, Central Russia. Geography, Environment, Sustainability, 3 (18), 59-67
https://doi.org/10.24057/2071-9388-2025-3910

ACKNOWLEDGEMENTS: The work was conducted with financial support from the ongoing Russian Science Foundation project No. 23-77-10045: "Current accumulation of sediments in conjuncted element of erosion network within small river basin under high anthropogenic impact".

Conflict of interests: The authors reported no potential conflict of interests.

INTRODUCTION

Due to anthropogenic impact, which results in disturbances of the natural canopy, accelerated erosion on the interfluve slopes plays a major role in the sediment budget (Vanwalleghem et al. 2017). Yet, the products of erosion are mostly re-deposited along pathways from cultivated slopes to the river channels (Sidorchuk 2018). Emerging sediment fluxes are discontinuous; they begin with single events of short erosion periods on the slopes, continue along the thalwegs of hollows and valleys toward permanent watercourses, and extend beyond the outlets of river catchments, where they partly mix with products of riverbed deformations and become trapped by floodplains and reservoirs. Exploration of accumulated deposits using high-resolution chronomarkers and tracers along the routes of sediment transport may help understand the transformation of sediment budgets due to changes in the intensity of erosion and sediment delivery processes (Owens 2020).

Several artificial compounds that are brought into the environment are successfully used to investigate erosion and sedimentation, including heavy metals (Dai et al. 2013; Wang et al. 2019; Elbaz-Poulichet et al. 2020;), fly ash (Olson et al. 2008; Davis & Fox 2009; Gennadiev et al. 2010), and radioactive isotopes (Zapata 2003; Alewell et al. 2017). The latter is closely linked to regular and occasional discharges from nuclear facilities (UNSCEAR report 2000) and nuclear weapons tests (Aoyama et al. 2006). Among other anthropogenic fallout radionuclides ^{137}Cs is most often used as a tracer (Zapata 2002).

The highest ^{137}Cs activity concentration usually occurs during the ^{137}Cs fallout from the atmosphere, unless the soil has been affected by perturbations and

erosion, intense migration of radionuclides (Jagercikova et al. 2015), and material from a more contaminated area has been transported and deposited at the sediment sinks. Considering the pointed limitations, precise dating of sediments becomes possible by using ^{137}Cs depth distribution (Foucher et al. 2020).

The distribution of radionuclides above the layer associated with massive fallout, such as that from the Chernobyl accident, can be seen as a record of changes in activity concentrations in sediments carried and deposited after the event. These variations are determined by activity concentration in the material from a specific sediment source, the proportion of sources contributing to the sediment flux, and the possible sorting of particles and aggregates during transportation. If the long-term trend in the behavior of ^{137}Cs in mobilized sediment for a selected location is predictable, then it is possible to link activity concentrations with the age of the accumulated sediment.

The aim of this research is to assess the potential use of the Chernobyl-derived ^{137}Cs depth distribution not only as an accurate chronomarker but also as a geochemical indicator of sediment fluxes in a small agricultural catchment affected by intense Chernobyl fallout in Central Russia. To this end, the following questions were raised:

1. How did the ^{137}Cs activity concentration change in sediments that reached the lower boundary of the cultivated fields and then entered a dry valley bottom over the post-Chernobyl period?

2. Is there a significant difference in the grain-size composition of material deposited in different geomorphic units, indicating the potential influence of sorting during transport on the radionuclide content?

3. What is the sedimentation rate in the dry valley along different sediment transfer routes, and can it be related to the activity concentration values of sediment believed to be older than 1986?

4. How long does it take for sediment to move from the arable slope to the catchment outlet, considering changes in erosion and sediment load from the slopes?

Materials and methods

The study area is located in the southern part of the Tula region near Plavsk town in the central part of a zone heavily contaminated with ^{137}Cs following the Chernobyl accident in 1986 (Fig. 1A). The chosen catchment has been studied over the past few decades using Chernobyl-derived ^{137}Cs as a soil erosion tracer (Golosov et al. 1999a,b; Golosov et al. 2000; Ivanova et al. 2000; Panin et al. 2001; Ivanov 2017; Ivanov, Ivanova 2023; Ivanov et al. 2023, 2024a). Despite this, the catchment still has high potential for in-depth exploration of erosion and sediment transport processes. Surveys from different years allow us to observe the long-term transformation of sediment and contaminant fluxes.

The area of the study site is 0.25 km^2, and the elevation difference is 52 m: from 187 m asl near its mouth (see Fig. 1B) to almost 236 m on the watershed surface. A major part of the drainage area is occupied with arable interfluve slopes of 1°–7°. The rest of the catchment area is represented by steep (up to 25°) sides and a gently sloping bottom of a dry valley (Fig. 1B).

The bedrock represented by Carboniferous limestone is covered by a loess-like loam (Ratnikov 1960) that serves as a soil-forming deposit for leached (Luvic Chernic Phaeozems) and podzolized (Luvic Greyzemic Chernic Phaeozems) according to the WRB-22 classification. According to the Plavsk weather station, the average annual precipitation is approximately 650 millimeters. Since the early 1990s, there has been a clear trend towards an increase in average winter air temperatures and a decrease in snowmelt runoff, up to its complete disappearance in some years (Barabanov et al. 2018), due to the lower depth of soil freezing and the higher infiltration capacity of the soil during the snowmelt season.

The lower boundary of arable slopes is usually outlined with lynchets: a ramparts emerged due to ploughing. Therefore, the transfer of mobilized sediments outside the slope occurs mainly through slope hollows, where slope runoff is concentrated (Panin et al. 2001). Before plowing ramparts (lynchets), erosion products accumulate at the foot of arable slopes. Accumulation in this zone plays a significant role in the sediment budget, comparable to the sediment load entering receiving watercourses (Ivanov et al. 2024b). The material that is carried outside the slope is deposited in the form of slopewash fans and covers on the sides of the valley. The rest of the sediments are transferred along the fluvial network and mainly deposited inside valleys.

As far as water flow is predominantly controlled by local topographic features, the specific routes of sediment transfer can be identified and studied separately. In our study, three routes were investigated with depth incremental sampling points (Fig. 1D., Table 1).

The first route is located in the western part of the catchment. The slope runoff from the neighboring slopes is concentrated along the lynchet, so its transfer to the valley bottom is observed in the corner of the cultivated field. Two sampling points were selected here: one at the foot of the slope before the fulfilled lynchet (LF-1) and one on the side of the dry valley (LS-1), where conveyance of mobilized material was expected. The second route passes through the central part of the study area and includes three sampling points: on the slope of the fulfilled lynchet (LF-2), on the side of the dry valley (LS-2), and in the upper reaches of the valley's bottom (LB-1). The third route starts at the lower reach of the bottom of a large slope hollow (LF-3), passes through a well-defined slopewash fan on the side of the valley (LS-3), and continues along the bottom dry valley bottom, where two sampling points were selected: in the upper reaches (LB-2) and near the mouth (LB-3). In the central part of the valley bottom, there is a local area with bottom gully incision. The position of the gully head has not changed significantly since it was first observed in 1997. The locations of LB-2 and LB-3 were selected to be close to the soil sections examined in 1997 by Golosov et al. (1999a) for comparison purposes within the 1997-2024 time window (see Fig. 1C).

The depth incremental sampling was conducted in two ways. Soil cores were collected using a hand auger at points LF-1, LF-2, LS-2, LF-3, and LS-3. At points LS-1, LB-1,

Table 1. The routes of sediment delivery reaching the foot of arable slope

Route	Sampling points	Soil losses 1986-2022, t*
1	LF-1–LS-1	483.4
2	LF-2–LS-2–LB-1	358.3
3	LF-3–LS-3–LB-2–LB-3	7379.2

*after Ivanov et al. 2024b

LB-2, and LB-3, we dug pits to describe the soil profile and collect samples from the walls of the soil sections. Sampling was performed at 3-5 centimeter intervals: either from the wall of the soil section or by cutting a core directly with the hand auger. All samples were delivered to the laboratory and dried out. They were then weighed and ground before being placed in petri dishes for further examination of ^{137}Cs activity, using a gamma spectrometer with a high-purity germanium (HPG) detector manufactured by ORTEC (USA) with an error not exceeding 10%. All activity values were recalculated for 1986, taking into account radioactive decay. For the samples of Route 3 (LF-3, LS-3, LB-2 and LB-3) the grain-size composition was determined using a Malvern Mastersizer 3000 particle size analyzer to figure out any sorting during transport.

Results

After examining samples from set points along the first route, it was learned that some of the material was accumulated at the foot of the slope during the post-Chernobyl period, while the rest was deposited downstream in the valleys. The depth distribution of ^{137}Cs from LS-1 demonstrates heavily contaminated strata, whose thickness is several times greater than the depth of ploughing. Due to the intensive deposition, the sampling depth at this site was insufficient to collect all the soil material containing Chernobyl ^{137}Cs (Fig. 2A). On the valley`s side, accumulation also occurred. The layer with highest activity concentration corresponding to the fallout was identified at depth of 25-30 cm. The upper 25 cm strata is argued to be deposited later (Fig. 2B).

Obviously, the concentration of activity in the accumulated material shows a downward trend. As can be seen from LF-1 (Fig. 2A), despite repeated cultivation resulting in mixing of the upper layer of soil, values dropped from 2124±34 to 1386±27 Bq kg^{-1}. Given no disturbance after the accumulation in point LS-1, the activity concentration dropped by almost two times, from 2564±101 to 1324±30 Bq kg^{-1}. Assuming that the sediments redeposited at the studied points have the same origin, the activity concentration can be used as a parameter to correlate the ^{137}Cs depth distributions. Thereby the almost equal range of concentration indicates that accumulation in LF-1 and LS-2 took place simultaneously. Even if the lynchet had been morphologically pronounced sometime after the Chernobyl fallout, the concentration of runoff was enough to deliver sediment beyond the cultivated field.

For the second route, the situation is quite different. At the point LF-2, activity concentrations of ^{137}Cs exceeding 1500 Bq kg^{-1} are only seen in the upper 30 centimeters and are distributed almost evenly. Downwards in the soil profile, ^{137}Cs content starts to drop (Fig. 3A). Therefore, it can be concluded that there has been no significant accumulation before the cultivated field boundary. On the adjacent side of the valley (point LS-2), the accumulation during the post-Chernobyl period has been no more than 9 cm (Fig. 3B). In addition, the concentration of ^{137}Cs in the upper 6 cm of sediment, which can be linked to post-Chernobyl accumulation, turned out to be higher than in the material deposited at the foot of the slope: 2392±132–2752±168 Bq kg^{-1} versus 1791±167–1940±173 Bq kg^{-1} (Fig. 3B). It may indicate that sediment deposition on the valley side occurred when the activity concentration of ^{137}Cs in the sediment runoff was higher. Currently, no accumulation is detected. Down by the route in the valley`s bottom examination of sediments at the point LB-1 showed that a maximum of ^{137}Cs activity lies almost on the surface (Fig. 3C). The only upper 3 cm layer which can be argued to have accumulated after 1986 has a very high concentration of 3352±72 Bq kg^{-1}. This is much higher than the concentrations in sediments that were accumulated nearby at the LS-2 point. Considering that

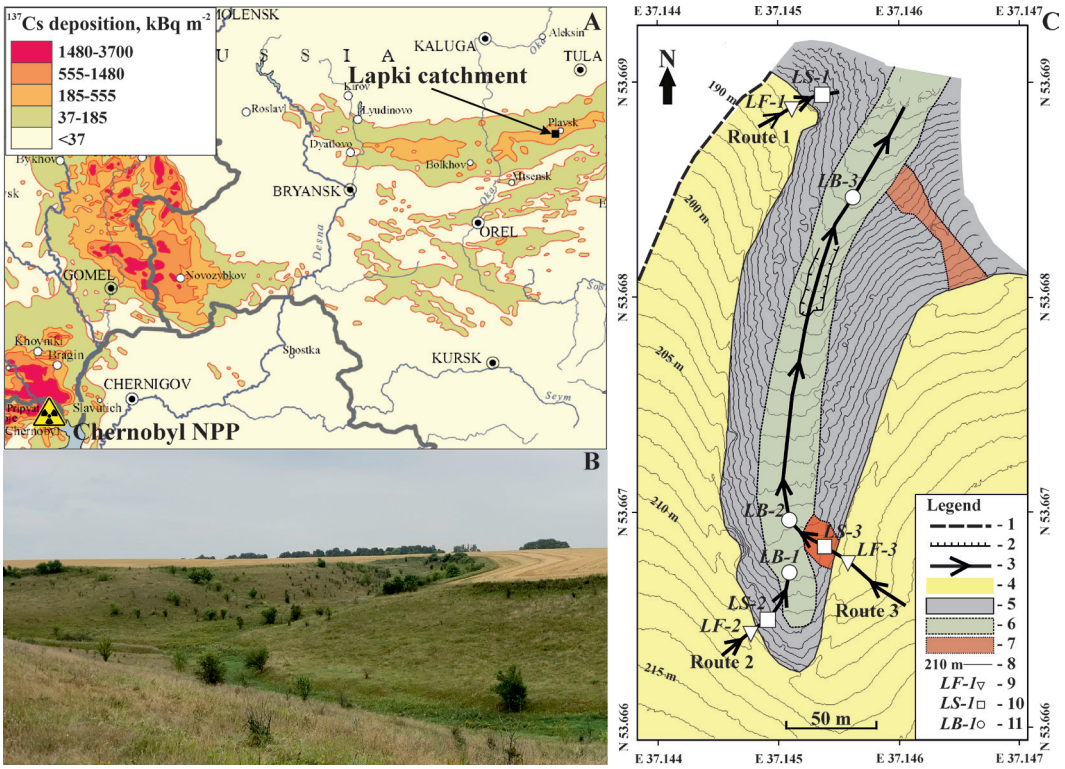

Fig. 1. The map of ^{137}Cs Chernobyl fallout (after Izrael et l., 1996) and location of the study area (A). The photo of the mouth of the Lapki catchment was made in 2021 (B). Observed routes of sediment transport (D): 1 – catchment boundary; 2 – steep eroded slopes; 3 – observed routes of sediment transport; 4 – arable slopes; 5 – dry valley`s sides; 6 – dry valley`s bottom; 7 –slopewash fans and covers; 8 – counter lines, a.s.l.; sampling points with depth incremental sampling on different geomorphic units: 9 – foot of arable slopes, 10 – dry valley sides and slopewash fans, 11 – dry valley bottom

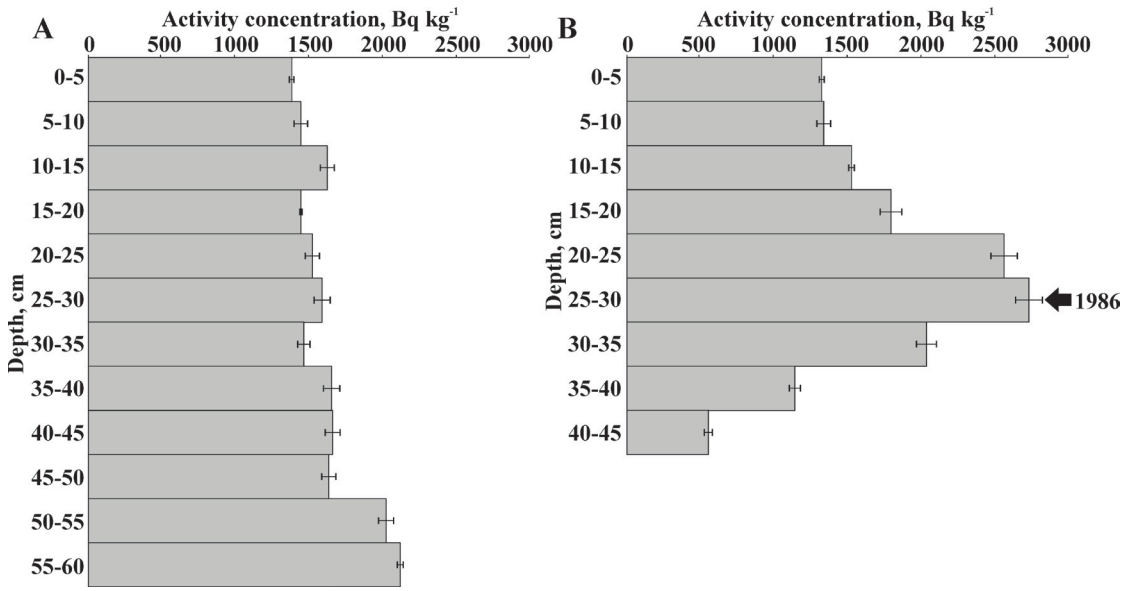

Fig. 2. The depth distribution of ^{137}Cs at points LF-1 (A) and LS-1 (B)

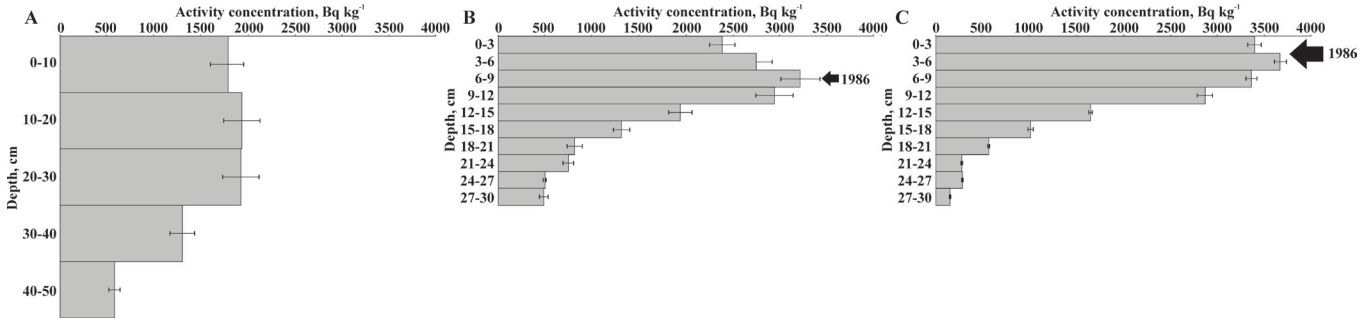

Fig. 3. The depth distribution of 137Cs at points LF-2 (A), LS-2 (B) and LB-1 (C)

samples near the surface are subject to vertical migration of radionuclides, including that along plant roots, it is more likely that there was no accumulation in this location.

At the foot of the slope, at point LF-3, the distribution is similar to that seen in the previously described example at LF-1 (Fig. 2A), indicating intensive accumulation due to high values of slope runoff delivered through the slope hollow (see Table 1). The activity concentration varies between 1263±118 and 1484±114 Bq kg-1, and there is no obvious decreasing trend observed (Fig. 4A).

High accumulation is also seen on the surface of the slopewash fan at point LS-3, with more than 39 centimeters accumulated between 1986 and 2022 (Fig. 4B). The upper 24 cm of the sediment are characterized by a gradual increase in ^{137}Cs concentration moving down, with values that lie close to those observed in LF-3, ranging from 1188±77 to 1437±98 Bq kg^{-1}. In the deeper part (24-39 cm), this growth becomes more intense: from 1580±112 to 2651±172 Bq kg^{-1} and indicates older material than observed at the point LF-3.

In upper reach of the valley bottom (LB-2), the thickness of post-Chernobyl accumulation drops to 27 cm. Here, there is a clear increase in ^{137}Cs concentration, starting at the surface. It is likely that most of the accumulation occurred during a short period after the fallout, when the concentration did not decrease to levels observed in LS-3 and the upper part of LF-3: from 3469±173 to 1380±76 Bq kg^{-1} (Fig. 4C).

Along the valley bottom, the rate of accumulation continues to decline, and near the mouth of the valley (LB-3), the accumulation is less than 18 cm over the period 1986-2024. The concentration of activity in the accumulated sediments ranges from 1664±98 to 3416±159 Bq kg^{-1} (Fig. 4D). This range is almost like that observed at the upper reach (LB-2), indicating the same age of the deposited material. It turns out that modern products of soil erosion are hardly represented here.

Grain-size analysis of the collected samples suggests that there has been a selective transfer of clay particles. The percentage of particles smaller than 2 microns gradually decreases from 12.48% at the foot of the arable slope to 9.66% near the dry valley's mouth. At the same time, the proportion of particles thicker than coarse silty (16 microns) shows an increase as they move downstream (Fig. 5).

The grain-size composition shows no clear trend in the vertical distribution. At the observed points, each fraction has random fluctuations which show (Fig. 6).

Comparison of ^{137}Cs depth distributions obtained in 1997 (Golosov et al., 1999a) and in 2024 showed that the depth of the peak of activity concentration has changed: in LB-2 from 12-15 cm in 1997 (Fig. 7A) to 27-30 cm in 2024 (Fig. 7B) and in LB-3 from 7-9 cm (Fig. 7C) to 15-18 in 2024 (Fig. 7D). Accordingly, in both locations, the rate of accumulation over 27 years decreased almost twice: from 1.1–1.4 cm year^{-1} to 0.7–0.8 cm year^{-1} in LB-2, and from 0.6–0.8 cm year^{-1} to 0.4–0.5 cm year^{-1} in LB-3. The deposition was still much higher in the valley's upper part (LB-2 compared to LB-3), but the ratio of the accumulation rates of LB-2 to LB-3 was stable, at 1.4–2.3 in 1997 and 1.4–2.0 in 2024. Also, the mean activity concentration in the upper samples, 1798 Bq kg^{-1} in LB-2 versus 2358 Bq kg $^{-1}$ in LB-3, indicates a different age of sediment (Fig. 7 A, C).

DISCUSSION

Summarizing the results presented, the following points can be made. The transport of sediment and radioactive isotopes from agricultural slopes is primarily determined by the concentration of slope runoff. This, in turn, is influenced by both the topography of the slope and the microrelief at its foot. It is clearly indicated by the depth

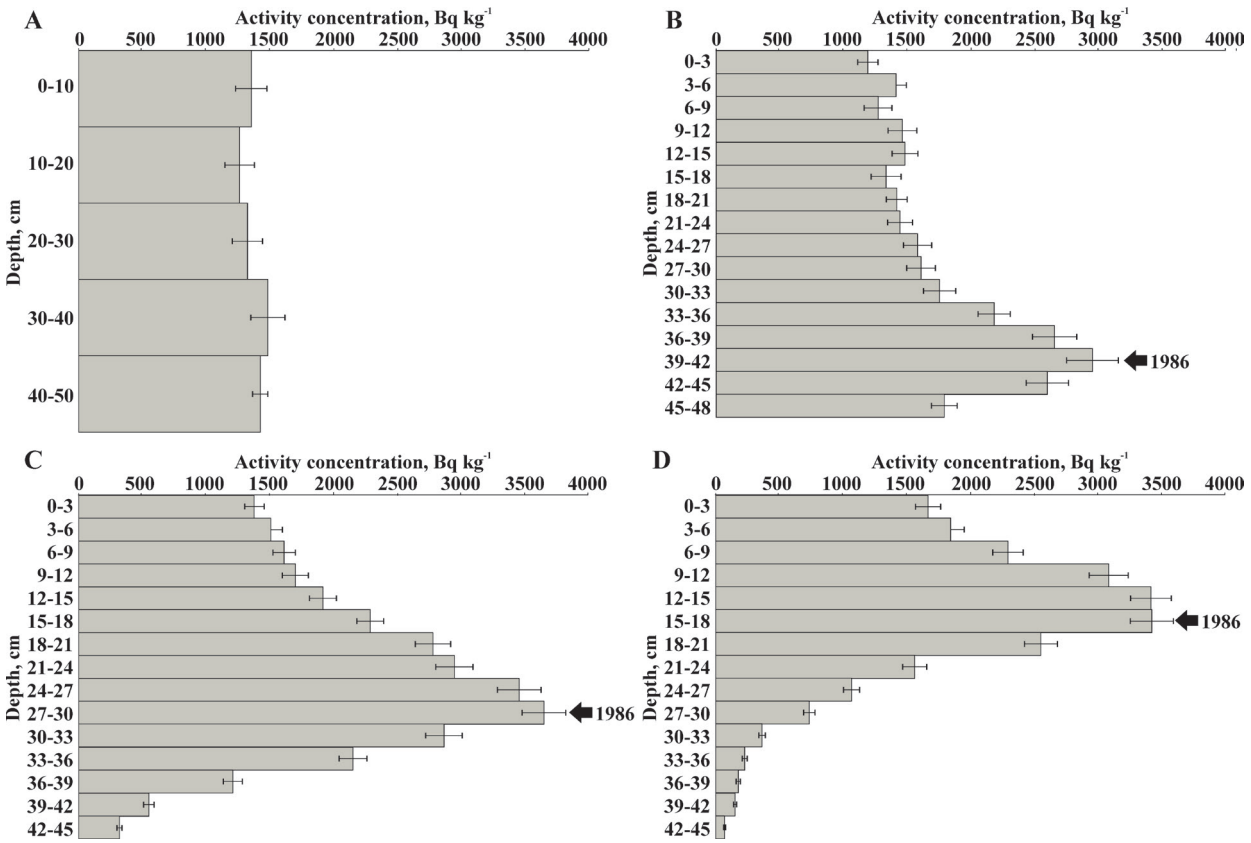

Fig. 4. The depth distribution of ^{137}Cs at points LF-3 (A), LS-3 (B), LB-2 (C) and LB-3 (D)

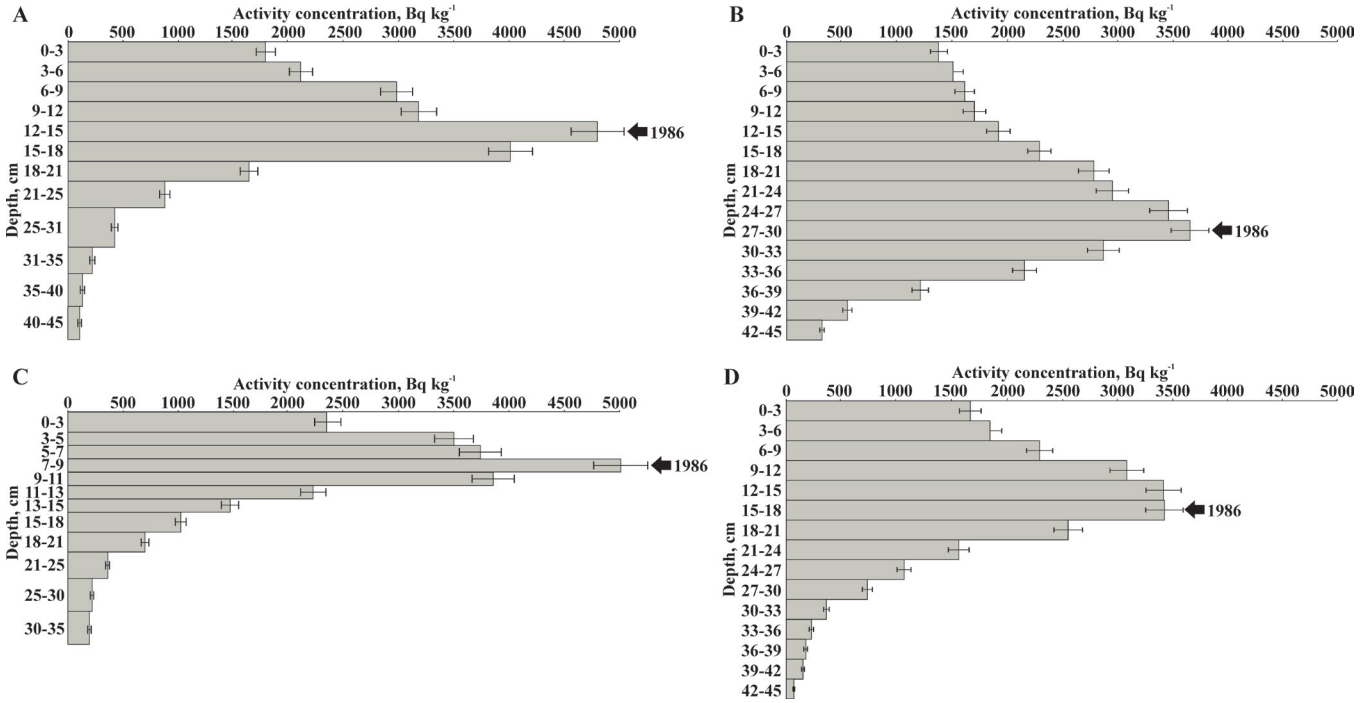

Fig. 5. Mean grain-size composition of sediments from Route 3: 1 – LF-3; 2 – LS-3; 3 – LB-2; 4 – LB-3

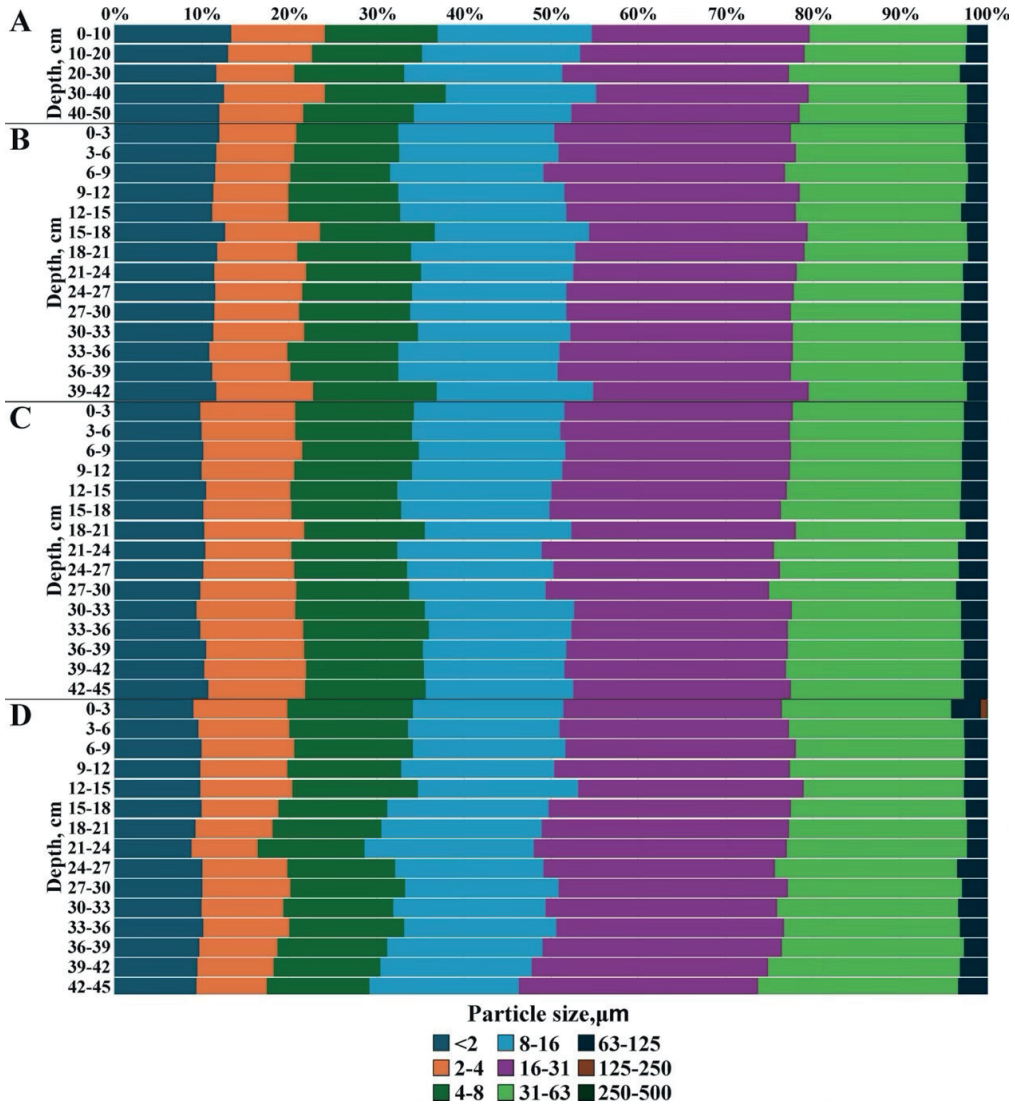

Fig. 6. Depth distribution of grain-size composition of sediments from Route 3: A – LF-3; B – LS-3; C – LB-2; D – LB-3

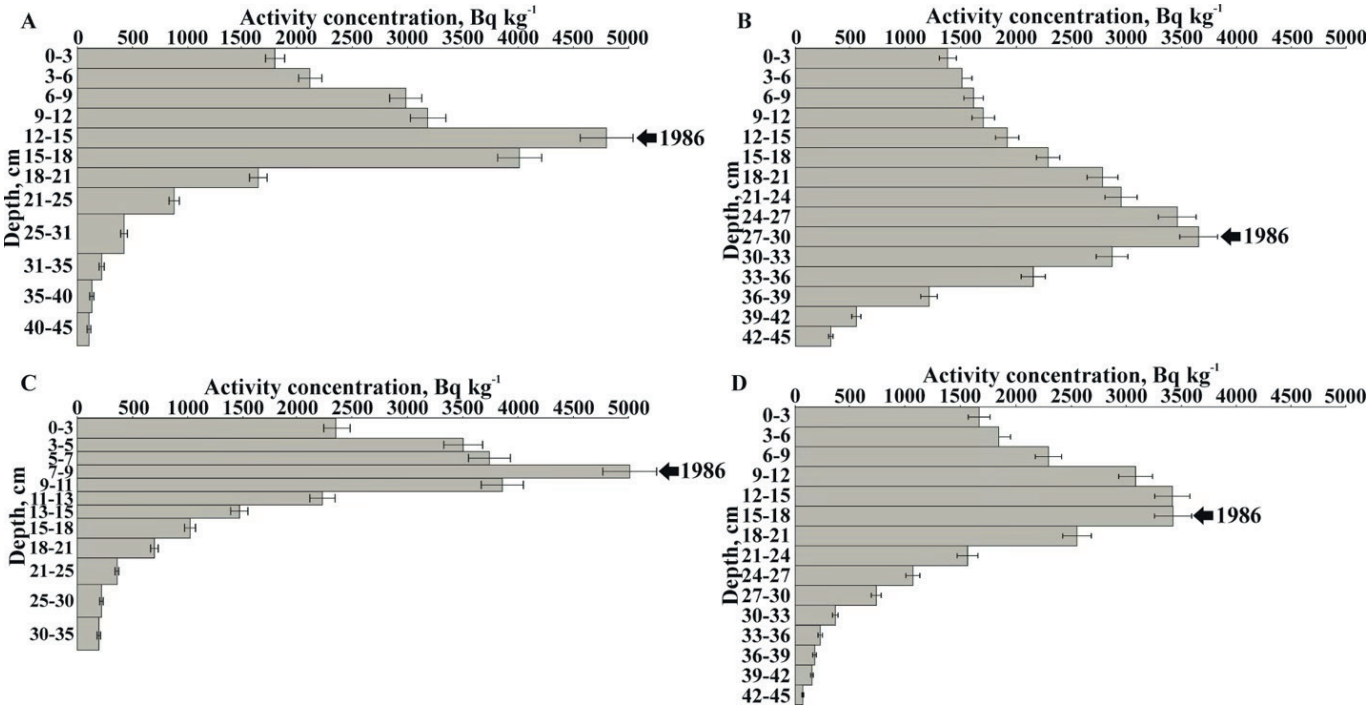

Fig. 7. The depth distribution of ^{137}Cs at points LB-2: in 1997 (A) (after Golosov et al., 1999a), in 2024 (B), and LB-3: in 1997 (C) (after Golosov et al., 1999a), in 2024 (D)

distribution of ^{137}Cs in sediments on both sides of the lower boundary of the cultivated field. The decrease in ^{137}Cs activity concentrations in sediments mobilized on arable slopes and redeposited downstream is typical for all cases observed. This decrease was not linear, with a rapid decline shortly after fallout, becoming smoother over decades until relatively stable values recently. The selective transport of clay particles could affect activity concentration during transportation. The depth distribution of ^{137}Cs suggests an increase in accumulation in the buffer zone on the slopes of the dry valley and in the upper reach of the dry valley. This pattern is consistent with observed climate trends: decreasing snowmelt runoff and no increase in intense rainfall.

The obtained picture is consistent with the current understanding of the lateral migration of particulate ^{137}Cs in areas with intense fallout. The Chernobyl incident was followed by a sharp increase in the contamination of the subsurface soil layer. Within the arable slopes, activity concentration dropped shortly after plowing, which depth was recommended to increase for remediation purposes (Alexakhin et al. 1992). A similar situation was observed in the affected areas of Fukushima, where the activity concentration of ^{137}Cs in terrestrial environments decreased rapidly relative to expectations due to active land use and decontamination efforts (Onda et al., 2020). Afterwards, it was expected that concentration would decrease due to a number of factors.

There would be a loss of upper, highly contaminated soil layers due to erosion and harvesting, which would result in the involvement of deeper and cleaner material during plowing. Freeze-thaw processes can lead to unstable soil surfaces and the development of intense rill erosion in springtime, which in turn causes a decrease in activity concentrations in mobilized sediment (Wakiyama et al. 2019; Igarashi et al. 2021). However, given the increasing average temperature and the reduction of snowmelt runoff in the beginning of the XXI century (Baranov et al. 2018), this factor does not seem to play a significant role. Also, activity concentration values would decline as a result of the complex migration of radionuclides primarily down through the soil profile. However, the latter effect was expected to be negligible (Golosov et al. 2013).

The sorting of material occurs along the entire transportation pathway and can potentially affect the concentration of ^{137}Cs in sediments. Shamshurina et al. (2011) found that activity concentration correlates with the share of soil aggregates. In the soils of the upper and middle slopes, approximately 50% of the total ^{137}Cs inventory is associated with aggregates larger than 2 mm. In the lower part of slopes, this share rises to about 70%. As the material moves and aggregates break down, sorting occurs primarily based on the size of individual particles. The selective deposition of larger particles leads to the enrichment of the sediment load with clay and fine silt (Golosov et. 2000). In turn, the selective transport of clay and silt particles may lead to the intensive migration of bound radionuclides (Evrard et al. 2015; Konoplev et al. 2016). However, over a short delivery distance, it is unlikely that the sorting process will significantly alter the downward trend of ^{137}Cs concentrations. Given a single sediment source, the activity concentration of ^{137}Cs can be used as an indicator for the relative age of the deposited sediment.

As the number of sediment sources increases, the picture of contamination is likely to become more complicated, but changes in activity concentrations may be used for fingerprinting tasks (Schuller et al. 2013; Evrard et al. 2020). If the radiocesium content from different sources is varying, it is possible to understand their contributions by comparing the ^{137}Cs depth distribution in deposits before and after the confluence of sediment fluxes.

Panin et al. (2001) reported that the long profile of the valley gradually decreases from its upper reaches to its mouth but has some slight convexities along the way, indicating separate episodes during the period of cultivation. As it has been declared, for the valley that receives sediment load from the explored catchment, the main way that deposits can be mobilized is through the incision of bottom gullies. Otherwise, the valley bottom provides long-term storage for eroded sediment and radionuclides. This statement may be supported by the fact that the activity concentrations in the upper samples in soil sections along the slope and at the bottom of the selected valley have different values, and consequently, sediments are of different ages. Sediments downstream are found to be older than those upstream, as can be seen in the example of LB-2 and LB-3 (Fig. 4C, D). This pattern has been consistent over decades (Fig. 5). Thus, distribution of the ^{137}Cs activity concentration may act as a geochemical indicator of geomorphic disconnectivity.

Using the distribution of activity concentration as a proxy for the age of sediment mobilization may help us to better understand sediment accumulation by correlating it with specific time periods. Sediment budget studies on small catchments are a useful way to validate estimations of soil erosion and sediment delivery from cultivated slopes to dry valleys and further along fluvial networks (Walling et al. 2002; Reid and Dunne 2016; Zhidkin et al. 2023) obtained results may be used to calibrate existing models. As accelerated erosion is a major source of sediment-associated contaminants, including radioactive ones (Lal 1994; Quinton and Catt 2007; Konoplev et al. 2021; Rashmi et al. 2022), the rate at which eroded material is delivered to watercourses is critical for assessing current environmental quality and forecasting future scenarios.

CONCLUSION

Since intrabasin sediment deposition constitutes a significant part of the sediment budget in river catchments with intensive anthropogenic influence, any additional time markers to explore sedimentation would be instrumental and should be included in the toolbox. The study conducted has shown that the pattern of Chernobyl-derived ^{137}Cs contamination has a close relationship to sediment redistribution in almost all decades after the fallout. The decrease of activity concentration during the post-Chernobyl period demonstrates high potential as a surrogate of relative age. This finding is consistent with previous research and sheds light on the potential use of ^{137}Cs depth distribution as a proxy of the sediment age during post-Chernobyl accumulation. However, the proposed approach requires a clear understanding of the long-term variation in the radionuclide content in material eroded from slopes and transported into the fluvial system.

REFERENCES

Aoyama, M., Hirose, K., Igarashi, Y. (2006). Re-construction and updating our understanding on the global weapons tests 137Cs fallout. Journal of Environmental Monitoring, 8(4), 431-438, https://doi.org/10.1039/B512601K

Alewell C., Pitois A., Meusburger K., Ketterer M., Mabit L. (2017). 239+240Pu from "contaminant" to soil erosion tracer: Where do we stand? Earth-Science Reviews, 172, 107-123. https://doi.org/10.1016/j.earscirev.2017.07.009

Alexakhin P.M., Vasiliev A.V., Dikarev V.G. et al., (1992) Sel'skohozjajstvennaja radiojekologija [Agricultural radioecology]. Ecologiya, Moscow (In Russian)

Barabanov A.T., Dolgov S.V., Koronkevich N.I., Panov V.I., Petel'ko A.I. (2018) Surface runoff and snowmelt infiltration into the soil on plowlands in the forest-steppe and steppe zones of the East European Plain. Eurasian Soil Science. 51 (1), 66–72, https://doi.org/10.1134/S1064229318010039

Dai Z., Feng X., Zhang C., Shang L., Qiu G. (2013). Assessment of mercury erosion by surface water in Wanshan mercury mining area. Environmental research, 125, 2-11, https://doi.org/10.1016/j.envres.2013.03.014

Davis C.M. and Fox J.F. (2009). Sediment fingerprinting: review of the method and future improvements for allocating nonpoint source pollution. Journal of Environmental Engineering, 135(7), 490-504. https://doi.org/10.1061/(ASCE)0733-9372(2009)135:7(490)

Elbaz-Poulichet F., Guédron S., Anne-Lise D., Freydier R., Perrot V., Rossi M., Piot C., Delproux S., Sabatier, P. (2020). A 10,000-year record of trace metal and metalloid (Cu, Hg, Sb, Pb) deposition in a western Alpine lake (Lake Robert, France): Deciphering local and regional mining contamination. Quaternary Science Reviews, 228, 106076. https://doi.org/10.1016/j.quascirev.2019.106076

Evrard O., Laceby J. P., Lepage H., Onda Y., Cerdan O., Ayrault S. (2015). Radiocesium transfer from hillslopes to the Pacific Ocean after the Fukushima Nuclear Power Plant accident: A review. Journal of environmental radioactivity, 148, 92-110. https://doi.org/10.1016/j.jenvrad.2015.06.018

Evrard O., Chaboche P. A., Ramon R., Foucher A., Laceby J. P. (2020). A global review of sediment source fingerprinting research incorporating fallout radiocesium (137Cs). Geomorphology, 362, 107103. https://doi.org/10.1016/j.geomorph.2020.107103

Foucher A., Chaboche P.A., Sabatier P., Evrard O. (2021). A worldwide meta-analysis (1977–2020) of sediment core dating using fallout radionuclides including 137Cs and 210Pbxs. Earth System Science Data Discussions, 13(10), 1-61. https://doi.org/10.5194/essd-13-4951-2021

Gennadiev A.N., Zhidkin, A.P., Olson K.R., Kachinskii V.L. (2010). Soil erosion under different land uses: assessment by the magnetic tracer method. Eurasian soil science, 43, 1047-1054. https://doi.org/10.1134/S1064229310090127

Golosov V.N., Panin A.V., Markelov M.V., (1999a). Chernobyl 137Cs redistribution in the small basin of the Lokna river, Central Russia. Phys. and Chem. of the Earth, Part A: Sol. Earth and Geodesy, 24(10), 881–885 https://doi.org/10.1016/S1464-1895(99)00130-1

Golosov V.N., Walling D.E., Panin A.V., Stukin E.D., Kvasnikova E.V., Ivanova N.N. (1999b) The spatial variability of Chernobyl-derived 137Cs inventories in a small agricultural drainage basin in central Russia. Applied Radiation and Isotopes, 51(3), 341–352. https://doi.org/10.1016/S0969-8043(99)00050-0

Golosov V.N., Walling D.E., Kvasnikova E.V., Stukin E.D., Nikolaev A.N., Panin A.V. (2000). Application of a field-portable scintillation detector for studying the distribution of 137Cs inventories in a small basin in Central Russia. Journal of Environmental Radioactivity, 48(1), 79-94.

Golosov V.N., Belyaev V.R., Markelov M.V. (2013). Application of Chernobyl-derived 137Cs fallout for sediment redistribution studies: lessons from European Russia. Hydrological processes, 27(6), 781-794. https://doi.org/10.1002/hyp.9470

Jagercikova M., Cornu S., Le Bas C., Evrard O. (2015) Vertical distributions of 137Cs in soils: a meta-analysis. Journal of Soils and Sediments, 15, 81–95 https://doi.org/10.1007/s11368-014-0982-5

Igarashi Y., Onda Y., Wakiyama Y., Yoshimura K., Kato H., Kozuka S., Manome R. (2021) Impacts of freeze-thaw processes and subsequent runoff on 137Cs washoff from bare land in Fukushima. Science of Total Environment, 769, 144706. https://doi.org/10.1016/j.scitotenv.2020.144706

Ivanov M.M. (2017) A geomorphological approach to the assessment of radioactive contamination in small lowland agricultural catchments. Geomorfologiya, 1, 30-45 (in Russian) https://doi.org/10.15356/0435-4281-2017-1-30-45

Ivanov M.M., Golosov V.N., Ivanova N.N. (2023) The sediment budget and migration of 137Cs in Chernobyl affected area: 30 years of investigations in the Plava River basin, Tula region. Geomorfologiya i Paleogeografiya, 54(1), 55,73 (in Russian). https://doi.org/10.31857/S0435428123010054

Ivanov M.M. and Ivanova N.N. Express analysis of vertical distribution of 137Cs to assess the rates of erosion and accumulation processes in the zone of intense radioactive contamination. Eurasian Soil Science, 56(4):524–533, 2023. http://dx.doi.org/10.1134/S1064229322602591

Ivanov M.M., Ivanova N.N., Golosov V.N., Usacheva A.A., Smolina G.A., Fomicheva D.V., (2024a) Assessment of Changes in Chernobyl Contamination and Erosion Rates for Arable Soils Using Resampling Method. Eurasian Soil Science , 57(9), 1499-1508 https://doi.org/10.1134/S1064229324601112

Ivanov M.M., Ivanova N.N., Krasnov S.F. (2024b) The role of lynchets in the redistribution of products of anthropogenic soil erosion. Moscow University Soil Science Bulletin, 79(3), 298-305 http://dx.doi.org/10.3103/s0147687424700212

Ivanova N.N., Golosov V.N., Markelov M.V. (2000) Sopostavlenie metodov ocenki intensivnosti jerozionno-akkumuljativnyh processov na obrabatyvaemyh sklonah [Comparison of methods for estimating the intensity of erosion-accumulation processes on cultivated slopes]. Pochvovedenie, 7, 876–887 (In Russian).

Izrael Y.A., De Cort M., Jones A.R., Nazarov I.M., Fridman S.D., Kvasnikova E.V., Stukin E.D., Matveenko I.I., Pokumeiko Yu.M., Tabatchyi K., Tsaturov Y. (1996). The atlas of cesium-137 contamination of Europe after the Chernobyl accident.

Konoplev A., Golosov V., Laptev G., Nanba K., Onda Y., Takase T., Wakiyama Y., Yoshimura K. (2016). Behavior of accidentally released radiocesium in soil–water environment: looking at Fukushima from a Chernobyl perspective. Journal of environmental radioactivity, 151, 568-578. https://doi.org/10.1016/j.jenvrad.2015.06.019

Lal R. (1994). Global overview of soil erosion. Soil and Water Science: Key to understanding our Global environment, 41, 39-51. https://doi.org/10.1007/978-981-16-9310-6_14

Konoplev A., Kanivets V., Zhukova O., Germenchuk M., Derkach H. (2021) Mid-to long-term radiocesium wash-off from contaminated catchments at Chernobyl and Fukushima. Water Research, 188, 116514. https://doi.org/10.1016/j.watres.2020.116514

Olson K.R., Gennadiyev A. N., Golosov V.N. (2008). Comparison of fly-ash and radio-cesium tracer methods to assess soil erosion and deposition in Illinois landscapes (USA). Soil science, 173(8), 575-586. DOI: 10.1097/SS.0b013e318182b094

Onda Y., Taniguchi K., Yoshimura K., Kato H., Takahashi J., Wakiyama Y., Coppin F., Smith H. (2020). Radionuclides from the Fukushima Daiichi nuclear power plant in terrestrial systems. Nature Reviews Earth & Environment, 1(12), 644-660. https://doi.org/10.1038/s43017-020-0099-x

Owens P.N. (2020). Soil erosion and sediment dynamics in the Anthropocene: a review of human impacts during a period of rapid global environmental change. Journal of Soils and Sediments, 20, 4115-4143. https://doi.org/10.1007/s11368-020-02815-9

Panin A.V., Walling D.E., Golosov V.N. (2001) The role of soil erosion and fluvial processes in the post-fallout redistribution of Chernobyl-derived caesium-137: a case study of the Lapki catchment, Central Russia. Geomorphology, 40(3-4), 185-204 https://doi.org/10.1016/S0169-555X(01)00043-5

Quinton J.N. and Catt J.A. (2007). Enrichment of heavy metals in sediment resulting from soil erosion on agricultural fields. Environmental Science & Technology, 41(10), 3495–3500 https://doi.org/10.1021/es062147h

Rashmi I., Karthika K.S., Roy T., Shinoji K.C., Kumawat A., Kala S., Pal R. (2022). Soil Erosion and sediments: a source of contamination and impact on agriculture productivity. In Agrochemicals in Soil and Environment: Impacts and Remediation(pp. 313-345). Singapore: Springer Nature Singapore. https://doi.org/10.1007/978-981-16-9310-6_14

Ratnikov A.I. (1960) "Geomorphological and agro-soil districts of Tula oblast," in Soil Zoning of the USSR (Mosk. Univ., Moscow), 92-115 (in Russian)

Shamshurina E.N., Paramonova T.A., Golosov V.N. (2011) Vlijanie jerozionno-akkumuljativnyh processov na radiacionnuju obstanovku agrolandshaftov Kurskoj oblasti [The influence of erosion-accumulative processes on the radiation situation of agricultural landscapes of the Kursk region] Geografija i prirodnye resursy, (4), 40–45. (in Russsian)

Sidorchuk A.Y. (2018). The fluvial system on the East European plain: Sediment source and sink. Geography, Environment, Sustainability, 11(3), 5-20. https://doi.org/10.24057/2071-9388-2018-11-3-05-20

United Nations Scientific Committee on the Effects of Atomic Radiation, 2000. Sources and Effects of Ionizing Radiation, United Nations Scientific Committee on the Effects of Atomic Radiation (UNSCEAR) 2000 Report, Volume I: Report to the General Assembly, with Scientific Annexes-Sources. United Nations. https://doi.org/10.18356/49c437f9-en

Reid L.M., and Dunne T. (2016). Sediment budgets as an organizing framework in fluvial geomorphology. Tools in fluvial geomorphology, 357-380. https://doi.org/10.1002/9781118648551.ch16

Schuller P., Walling D.E., Iroumé A., Quilodrán C., Castillo A., Navas, A. (2013). Using 137Cs and 210Pbex and other sediment source fingerprints to document suspended sediment sources in small forested catchments in south-central Chile. Journal of environmental radioactivity, 124, 147-159. https://doi.org/10.1016/j.jenvrad.2013.05.002

Vanwalleghem, T., Gómez, J. A., Amate, J. I., De Molina, M. G., Vanderlinden, K., Guzmán, G., Laguna A., Giráldez, J. V. (2017). Impact of historical land use and soil management change on soil erosion and agricultural sustainability during the Anthropocene. Anthropocene, 17, 13-29. https://doi.org/10.1016/j.ancene.2017.01.002

Wakiyama Y., Onda Y., Yoshimura K., Igarashi Y., Kato H. (2019). Land use types control solid wash-off rate and entrainment coefficient of Fukushima-derived 137Cs, and their time dependence. Journal of environmental radioactivity, 210, 105990. https://doi.org/10.1016/j.jenvrad.2019.105990

Walling D.E., Golosov V.N., Panin A.V., He Q. (2000) Use of radiocaesium to investigate erosion and sedimentation in areas with high levels of Chernobyl fallout. Tracers in geomorphology, 183-200

Walling D.E., Russell M.A., Hodgkinson R.A., Zhang,Y. (2002). Establishing sediment budgets for two small lowland agricultural catchments in the UK. Catena, 47(4), 323-353. https://doi.org/10.1016/S0341-8162(01)00187-4Get rights and content

Wang L., Chen G., Liu Y., Li R., Kong L., Huang L., Wang J., Kimpe L.E., Blais J.M. (2019). Environmental legacy and catchment erosion modulate sediment records of trace metals in alpine lakes of southwest China. Environmental Pollution, 254, 113090. https://doi.org/10.1016/j.envpol.2019.113090

Zapata F. (Ed.). (2002). Handbook for the assessment of soil erosion and sedimentation using environmental radionuclides (Vol. 219, pp. 9348054-9). Dordrecht: Kluwer Academic Publishers. https://doi.org/10.1007/0-306-48054-9

Zapata F. (2003). The use of environmental radionuclides as tracers in soil erosion and sedimentation investigations: recent advances and future developments. Soil and Tillage Research, 69(1-2), 3-13. https://doi.org/10.1016/S0167-1987(02)00124-1

Zhidkin A., Gennadiev A., Fomicheva D., Shamshurina E., Golosov, V. (2023). Soil erosion models verification in a small catchment for different time windows with changing cropland boundary. Geoderma, 430, 116322. https://doi.org/10.1016/j.geoderma.2022.116322

RESEARCH PAPER

LARGE-EDDY SIMULATION OF AEROSOL TRANSPORT OVER DIFFERENT URBAN LOCAL CLIMATE ZONES

Alexander I. Varentsov[1,2,3,4*], Evgeny V. Mortikov[1,4,5], Andrey V. Glazunov[5,1], Andrey V. Debolskiy[1,3,4], Mariya A. Kuzmicheva[6], Victor M. Stepanenko[1,2]

[1]Research Computing Center, Lomonosov Moscow State University, Leninskie Gory 1, b. 4, 119234, Moscow, Russia
[2]Faculty of Geography, Lomonosov Moscow State University, Leninskie Gory 1, 119991, Moscow, Russia
[3]Obukhov Institute of Atmospheric Physics, Russian Academy of Sciences, Pyzhevskiy Pereulok 3, 119017, Moscow, Russia
[4]Moscow Center for Fundamental and Applied Mathematics, Leninskie Gory 1, 119991, Moscow, Russia
[5]Marchuk Institute of Numerical Mathematics, Russian Academy of Sciences, Gubkina 8, 119333, Moscow, Russia
[6]Faculty of Mechanics and Mathematics, Lomonosov Moscow State University, Leninskie Gory 1, 119991, Moscow, Russia
***Corresponding author:** aivarentsov98@gmail.com
Received: March 7th 2025 / Accepted: June 5th 2025 / Published: October 1st 2025
https://doi.org/10.24057/2071-9388-2025-3925

ABSTRACT. As urban areas grow, understanding the impact of built environments on aerosol distribution is crucial for accurate monitoring and forecasting of urban air quality and for the development of mitigation strategies. This study uses Large Eddy Simulation approach combined with Local Climate Zones (LCZ) classification to simulate the transport of Lagrangian aerosol particles in different urban configurations. The study simulates several urban configurations based on LCZ classification, specifically LCZ 4 (open high-rise), LCZ 5 (open mid-rise), and LCZ 6 (open low-rise), varying in building height and density. Both regular and randomized urban development configurations were examined to understand the impact of building geometry on particle dispersion. The study reveals that building orientation significantly influences particle distribution, with structures parallel to the wind adding horizontal dispersion and those perpendicular promoting vertical mixing. In randomized configurations, variations in particle concentrations highlight the role of architectural heterogeneity in turbulence development and aerosol dispersion. The findings suggest that aggregated block- or district-scale building geometry properties strongly influence aerosol transport. For randomized urban configurations, without idealized regular structures, the difference in the large-scale morphometric characteristics of specified LCZ types has a significantly greater impact on the particle dispersion process than the local geometric differences between configurations of the same LCZ type. Future research taking into account diverse meteorological conditions and more LCZ types is recommended to enhance the accuracy and applicability of this approach.

KEYWORDS: urban air quality, large eddy simulation, local climate zones, aerosol dispersion, Lagrangian particle transport, urban morphology

CITATION: Varentsov A. I., Mortikov E. V., Glazunov A.V., Debolskiy A. V., Kuzmicheva M. A., Stepanenko V. M. (2025). Large-Eddy Simulation Of Aerosol Transport Over Different Urban Local Climate Zones. Geography, Environment, Sustainability, 3 (18), 68-79
https://doi.org/10.24057/2071-9388-2025-3925

ACKNOWLEDGEMENTS: LES model and LCZ generator development was supported by FSTP project «Research in geophysical boundary layers and the development of new modelling approaches for Earth system models» within the program «Improvement of the global world-level Earth system model for research purposes and scenarios forecasting of climate change». Numerical experiments and data analysis were supported by RNF grant 24-17-00155. Stochastic Lagrangian particles model development was supported by the Russian Ministry of Science and Higher Education, agreement No. 075-15-2025-345.

Numerical experiments were carried out using the equipment of the shared research facilities of HPC computing resources at Lomonosov Moscow State University and computing resources of the Data Center of the Far Eastern Branch of the Russian Academy of Sciences.

Conflict of interests: The authors reported no potential conflict of interests.

INTRODUCTION

With the rise of urbanization, the problem of aerosol air pollution in cities has become more challenging, which has required the use of advanced modeling techniques to assess the dispersion of particulate matter in the urban environment. Understanding and being able to forecast this process is crucial for estimating health risks and developing mitigation strategies, as urban air pollution is associated with serious health consequences, including respiratory and cardiovascular diseases (Pope and Dockery 2006; Kampa and Castanas 2008; Kasimov et al. 2024). The impact of PM2.5 concentrations on mortality has a global effect and is especially evident in low- and middle-income countries (Cohen et al. 2017), where urbanization is usually very active.

The complexity of urban landscapes, characterized by a variety of architectural forms and types of land use, requires models with high spatial resolution to ensure effective analysis and forecasting (Baklanov et al. 2007). At the same time, processes of a wide range of scales are important for the physics of atmospheric processes in urban areas, from an individual building to a meteorological mesoscale, necessitating the use of models with different depths of process description and resolution depending on the task (Blocken 2015). Currently, there is a trend towards multi-scale modeling of meteorological processes and air pollution, as this approach allows for a more comprehensive analysis of processes and more efficient decision-making; however, it requires more complex verification of models and the development of new recommendations and standards for modeling (Kadaverugu et al. 2019; Baklanov and Zhang 2020).

Historically, aerosol dispersion modeling has relied on a Gaussian or plume approach (Berlyand 1991), which is computationally simple but does not allow for detailed consideration of the features of urban development and the underlying surface (Britter and Hanna 2003; Holmes and Morawska 2006). The development of computing technologies and computational fluid dynamics (CFD) models, primarily RANS (Reynolds-Averaged Navier-Stokes) and LES (Large Eddy Simulation) approaches, has allowed us to move to a qualitatively new level for simulation of atmospheric processes in cities. Such models reproduce the complex structure of an airflow and turbulent eddies inside urban areas (Blocken et al. 2012). The influence of urban development on microclimate and thermal comfort has been actively studied for a long time using CFD (Chatzidimitriou and Axarli 2017; Lee and Mayer 2018), but air quality is not ignored either. It has been shown that taking into account the geometry of buildings and streets has a pronounced effect on particle dispersion and allows us to obtain results that differ significantly from simulations using plume models (Oke et al. 2017). At the same time, building geometry exerts complex nonlinear effects on particle concentrations (Starchenko et al. 2023) and provides notable impact on other components of the urban environment, including the air quality, e.g., via greening of roofs (Wu and Liu 2023; Venter et al. 2024).

One of the methods to tackle the issues listed above is the use of LES models, since with sufficient computing resources they can provide a more accurate representation of air flows and turbulence in urban areas than the more popular RANS models (Zheng and Yang 2021). This approach is already used for real urban development on the scale of an entire city and allows us to draw conclusions about the influence of street orientation on the dispersion of pollutants (Zhang et al. 2021). In addition, LES models are used to verify simpler models or parameterizations used for operational forecasting of air quality and atmospheric composition (Grylls et al. 2019). Of particular interest are studies using LES models with Lagrangian tracking of pollutants as individual particles (Glazunov 2018), which accounts for the interaction of solid particles with the urban atmosphere and buildings in a more explicit way compared to Eulerian models; e.g., this approach was used to assess the impact of building development and atmospheric stratification on particle dispersion in Helsinki (Kurppa et al. 2018).

An important achievement in the field of urban meteorology is the creation of the concept of local climate zones (LCZ) and its use in hydrodynamic models of various scales. LCZ classifies urban areas based on building and street parameters, vegetation cover, and surface properties - these variables strongly affect the local microclimate and the structure of air flows (Stewart and Oke 2012). Studies using the LCZ classification are primarily focused on quantifying urban morphology impact on air or surface temperature (Varentsov and Samsonov 2020; Aslam and Rana 2022), however, there are more and more works on the topic of air quality, which demonstrate that the characteristics of urban development strongly affect the concentrations and surface deposition of pollutants (Kosheleva et al. 2018), and many classifications of the underlying surface are not relevant to urban morphology, which is presented in the LCZ (Jiang et al. 2023). It has been repeatedly shown that there is a relationship between the LCZ types and the concentration patterns of solid particles (Shi et al. 2019; Lin et al. 2024; Nourani et al. 2024), however, conclusions about the specific nature of this relationship vary depending on the city and research methods.

The aim of this study is to apply a novel approach combining Large Eddy Simulation with Local Climate Zones classification to analyze the impact of urban development geometry on air pollution at various scales, from district level to individual buildings. This approach not only deepens our understanding of atmospheric environment dynamics in urban settings but also paves the way towards projecting more resilient urban infrastructures and healthier living environments.

MATERIALS AND METHODS

Large Eddy Simulation

As the main tool, we used the model developed at the RCC MSU (Lomonosov Moscow State University Research Computing Center) and the INM RAS (G.I. Marchuk Institute of Numerical Mathematics of the Russian Academy of Sciences) based on a unified hydrodynamic code combining LES (Large Eddy Simulation), DNS (Direct Numerical Simulation) and RANS (Reynolds Averaged Navier-Stokes) approaches for modeling geophysical turbulent flows with high spatial resolution (Mortikov et al. 2019; Kadantsev et al. 2021; Tkachenko et al. 2022; Debolskiy et al. 2023, Suiazova et al. 2024). In this work, the LES configuration of the model was used, which allows for a detailed reproduction of turbulent airflows in the presence of complex urban geometry.

This model calculates the dynamics of a thermally stratified fluid defined using filtered Navier-Stokes equations in the Boussinesq approximation. To parameterize the subgrid stress tensor, the Smagorinsky eddy viscosity model is used, in which the Smagorinsky constant and the subgrid Prandtl number (which depend on time and spatial coordinates) are determined using a dynamical procedure (Germano et al. 1991). The numerical

model utilizes conservative finite-difference schemes of second-order accuracy for spatial approximation on rectangular meshes. A fractional step method is used to integrate the equations of motion and continuity over time and to ensure the incompressibility condition, and an explicit third-order Adams-Bashforth scheme is used to approximate the momentum and heat equations.

An important feature of this model is explicit representation of the buildings (Tarasova et al. 2024). The surface of buildings can be given its roughness and temperature, which allows us to make simulations including complex scenarios when different buildings have different properties.

Lagrangian particle model

To model particulate matter transport in the urban atmosphere, a Lagrangian particle transport module was introduced to the LES model. The main advantage of the Lagrangian approach is its ability to track the trajectories of individual particles in detail, which allows explicitly describing their interaction with the diverse elements of the urban environment. In complex urban environments where buildings, streets, and green spaces create heterogeneous airflow patterns, the Lagrangian method can account for the effects of turbulence, particle sedimentation on buildings surfaces, and changing atmospheric conditions near surfaces, resulting in more accurate predictions of local concentrations compared to the Eulerian framework.

In this paper, the Lagrangian approach is used for numerical modeling of aerosol transport. Each particle is tracked through its entire trajectory, as well as the particle's velocity and other state variables. This approach is used to track a limited number of particles but allows us to explicitly consider the forces acting on the particle. Using the Lagrangian approach, the change in position of each individual particle is described by the Eq. (1) (Thomson and Wilson 2012):

$$dx_p = u_p dt \tag{1}$$

where $\boldsymbol{x}_p$ – particle position, $\boldsymbol{u}_p$ – its velocity, t – time. The developed model allows to consider inertial ("heavy") particles, whose velocity may not coincide with the velocity of the ambient air at particle position. Therefore, changes of both particle's position and its velocity have to be calculated – Eq. (1) is supplemented with Eq. (2) for velocity based on Newton's second law:

$$\frac{du_p}{dt} = \frac{g\left(\rho_p - \rho\right)}{\rho_p} + F_D\left(u - u_p\right) \tag{2}$$

where $\boldsymbol{g}=(0,0,-g)$ – gravitational acceleration ($g>0$) in Cartesian coordinates, ρ_p – particle density, ρ – air (medium) density, $\boldsymbol{u}=(u_1,u_2,u_3)$ – ambient flow (medium) velocity, F_D – drag coefficient.

To account for the interaction with buildings, parameterization of collisions with hard (impermeable) surfaces has been implemented, in which both reflection of a particle from the surface of a building and deposition on it are possible. It is implemented by representing buildings as impenetrable surfaces of the computational grid.

The Lagrangian transport module also takes into account the effect on particle motion of the turbulent eddies which are subgrid for LES model. The total flow velocity from Eq. (2) is represented as the sum of the averaged and subgrid components (Eq. 3):

$$u = \overline{u} + u' \tag{3}$$

where $\overline{\boldsymbol{u}}$ – velocity explicitly resolved at the numerical grid of LES model, $\boldsymbol{u}'$ – subgrid velocity fluctuation which is evaluated using the Lagrangian stochastic model (LSM). The 1st order LSM is used in this work, for which the change of fluctuation component along the trajectory of a fluid parcel (coinciding with the particle path for light particles) can be calculated as Eq. (4) (Reynolds and Cohen 2002):

$$du'_i = -\frac{1}{2}b^2\frac{u'_i}{\sigma^2_{u_i}}dt + b\xi_i \tag{4}$$

where i=1,2,3 is the Cartesian coordinate index, $b^2 = C_0\varepsilon$, $\sigma^2_{u_i}$ – subgrid velocity variance, C_0=6.0 – Kolmogorov's constant, ε – the rate of dissipation of turbulent kinetic energy, diagnosed by LES model, ξ_i – independent delta-correlated (in time) Gaussian random variables with standard deviation $\sigma_{\xi_i} = \sqrt{dt}$.

The developed Lagrangian transport module was previously verified on analytical solutions for light and heavy particles (Varentsov et al. 2020; Varentsov et al. 2023).

Urban configurations

Since a limited number of numerical experiments cannot cover the entirety of urban geometry variability, to select urban geometry configurations for LES experiments, it was necessary to choose building development types that are both idealized enough to be described by a small set of properties and easily reproduced in other studies and relevant to the real urban settings so that they could describe urban areas in different cities of Russia and the world. The classification of Local Climate Zones (LCZ), proposed in (Stewart and Oke 2012), is increasingly used as such a universal tool for identifying characteristic types of homogeneous (in terms of mean morphological characteristics) urban development within a city.

We restrict our study to 3 types of LCZ – the selected configurations are LCZ 4, LCZ 5, and LCZ 6. The parameters defining each type are shown in Table 1. These types of LCZ are widespread both in Russia and in the world, as evidenced by the global LCZ map (Demuzere et al. 2022). Configurations LCZ 1, LCZ 2, LCZ 3, and LCZ 7 require calculations with more detailed resolution and higher computational cost due to the very high density of buildings, and LCZ 8, LCZ 9, and LCZ 10 are not so common in residential areas of Russian cities – so these types are planned to be considered not now, but in further studies.

LCZ 4 is an open high-rise building zone. In Russian cities, a common example of such development is Soviet-era housing, which typically consists of tower blocks with 8 to 12 floors in park-like surroundings. LCZ 5 is an open medium–rise building zone. The typical example is the neighborhoods of Soviet five–storey apartment buildings (e.g., so-called "khrushevka"), typical of almost any Russian city. LCZ 6 is an open low–rise building zone, and it can include areas with both individual private houses and low-rise apartment buildings. Common examples in Russia are suburbs with private houses and city districts built up with two-storey communal housing.

To generate building geometry so that the whole domain corresponds to one of the selected LCZs, two methods were used: manual specification of the geometry with a regular pattern and automatic generation of the geometry with a randomized pattern using specially developed generator software. Hereafter, the

Table 1. LCZ parameters used to generate the building geometries for numerical experiments

LCZ	Buildings height	Building areal fraction	Aspect ratio (the ratio of building height to street width)
LCZ 4	> 25 m	20-40 %	0.75-1.25
LCZ 5	10-25 m	20-40 %	0.3-0.75
LCZ 6	3-10 m	20-40 %	0.3-0.75

configurations of these two types are called "regular" and "randomized", respectively.

As a result of the manual generation of regular geometry, 9 configurations were prepared (Fig. 1), with 3 variants for each of the selected LCZ. The only differences between the LCZs in these configurations were building height and aspect ratio, while the shape and orientation of the buildings differed between LCZ variants. The first two options (LCZ 4 (a-b), LCZ 5 (a-b), LCZ 6 (a-b)) are regular patterns with long buildings forming urban canyons stretching from South to North or from West to East, such scenarios mimic areas of Soviet residential districts, newly built according to the cities' master plans (Engel 2022). The third option (LCZ 4 (c), LCZ 5 (c), LCZ 6 (c)) is the regular pattern of square buildings, typical for some urban areas of the 21st century in Russia and for many cities around the world, especially in developing countries.

Urban development rarely has a perfectly periodic structure, so the regular geometry of identical buildings and streets presented above is an idealized option. A pseudorandom pattern of buildings of similar scale can be found in almost any city. To consider more realistic scenarios, we have created randomized building geometries in which the structure of streets, blocks, and buildings is present, but their location and parameters are random within acceptable values for a particular LCZ.

The approach of generating building geometry based on specified characteristics is used both in atmospheric flow simulations in general (Sutzl et al. 2020) and specifically for LCZ classification (Zhou et al. 2023). However, the available generation methods are usually limited in setting or selecting parameters. Therefore, to generate a randomized building geometry, we developed a generator tool that takes as input the area size and the morphological characteristics of the selected LCZ, including parameters from Table 1 and manually selected restrictions on building sizes. Next, the fractal geometry of urban development is generated in several stages.

At the first stage, the minimum and maximum sizes of streets and blocks and their number are calculated based on the LCZ parameters. The area is randomly divided into a corresponding number of streets (along the X and Y axes) and rectangular blocks; all random values have a uniform distribution within the minimum and maximum sizes mentioned above. A block refers to an area with a width of 1 to 3 buildings and a length of at least 1 building. At the second stage, rectangular building objects are generated in each of the obtained blocks, taking into account the LCZ parameters and the selected building size restrictions. The third stage of the generation is to check the correspondence of the generated geometry and the selected LCZ. The morphological characteristics (height and area of buildings, aspect ratio) are checked separately for each block. If any of the parameters deviate by more than 5% from the required value, the buildings in this block are generated again. If in a certain quarter it is not possible to achieve the required values in several generation attempts, or all blocks are approved, but a deviation of more than 5%

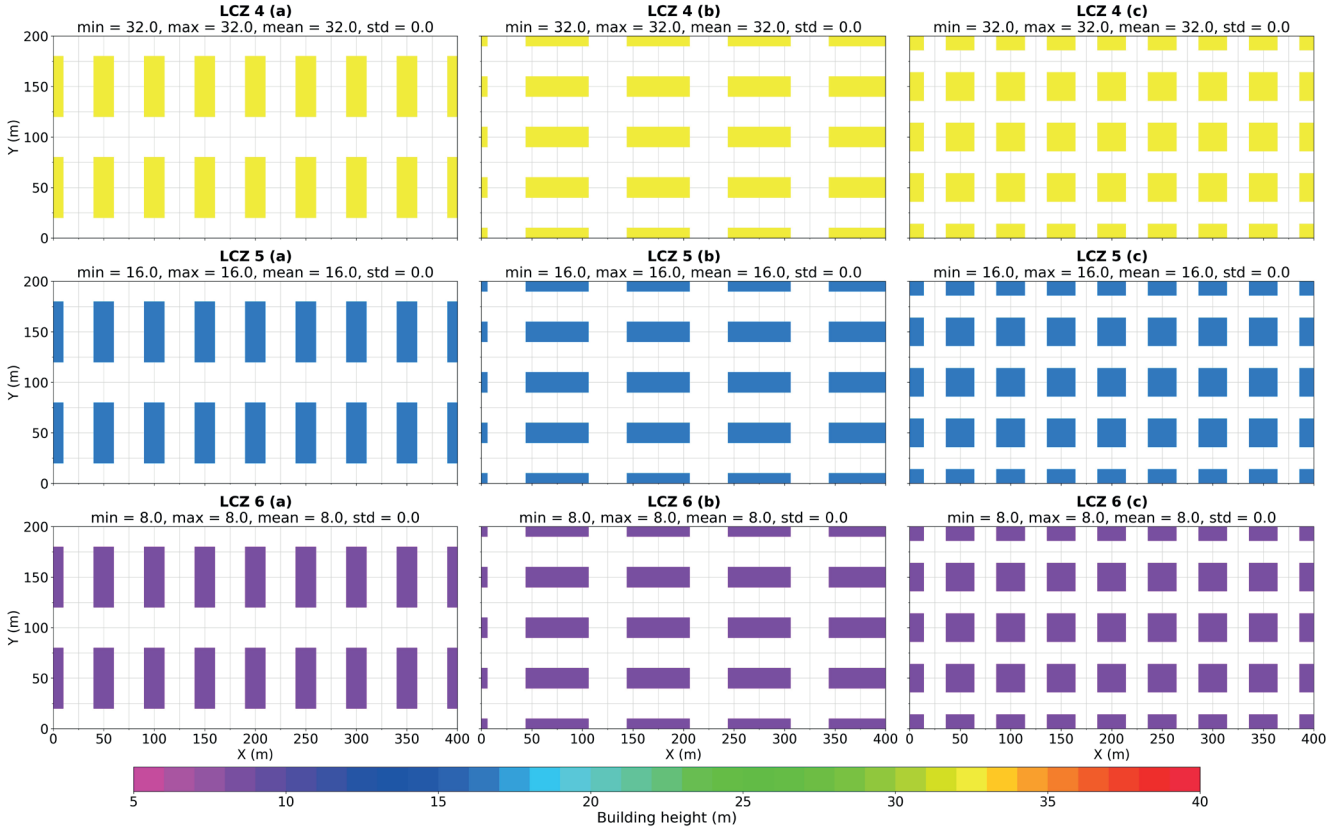

Fig. 1. Elevation maps for manually created regular building configurations corresponding to Local Climate Zones LCZ 4, LCZ 5, and LCZ 6

is obtained for the entire region, then the entire region is being regenerated, that is, streets and blocks.

In this way, 12 building configurations were generated, 4 for each LCZ (Fig. 2). The main differences between randomized and regular configurations are the variation in building sizes and heights, the different shape and orientation of buildings within even one block, the lack of a regular structure, and the different number and width of streets. The building sizes for LCZ 4 and LCZ 5 are quite similar for both generation methods. However, the randomized LCZ 6 configurations have significantly more buildings, and their size is smaller than in the regular LCZ 6 configurations, which is caused by the limitations of the generation method.

Although such a random building pattern may not have exact real-world analogues, it can be called more realistic, since perfectly regular geometry is extremely rare in cities (even cities built according to master plans usually have a heterogeneous structure), and randomized buildings of the same scale can be found in almost any city.

Numerical experiments setup

For each building configuration (for 9 regular and 12 randomized ones), a numerical experiment was conducted to compute aerosol transport. The experiments simulated the spread of atmospheric pollutants emitted from the street in the form of vehicle emissions and fine road dust. The spread of such pollutants within urban areas was assessed under common meteorological conditions: low wind and neutral atmospheric stratification, which together provide ventilation of the city and vertical mixing, but with low intensity.

The characteristic meteorological conditions of the experiments included the wind speed and direction at the upper boundary, as well as the vertical temperature gradient. The wind boundary conditions were set to 4 m/s at an altitude of 120 m and above, and the wind direction was westerly (along X-axis). For temperature, the boundary conditions were set to +15 °C at an altitude of 120 m and +16 °C on the surface of the earth and buildings, which ensured neutral temperature stratification of the atmosphere when vertical air mixing, unlike stable stratification, is significant but not as active as with unstable stratification. The lateral boundaries were set with periodic conditions for atmospheric parameters, allowing the airflow to be adapted to the geometry of urban development as if a similar pattern of buildings surrounded the entire domain area. The graphical representation of the experiment setup is shown in Fig. 3.

Spherical solid particles with a diameter of 1 μm and a material density of 1000 kg/m^3 were defined as

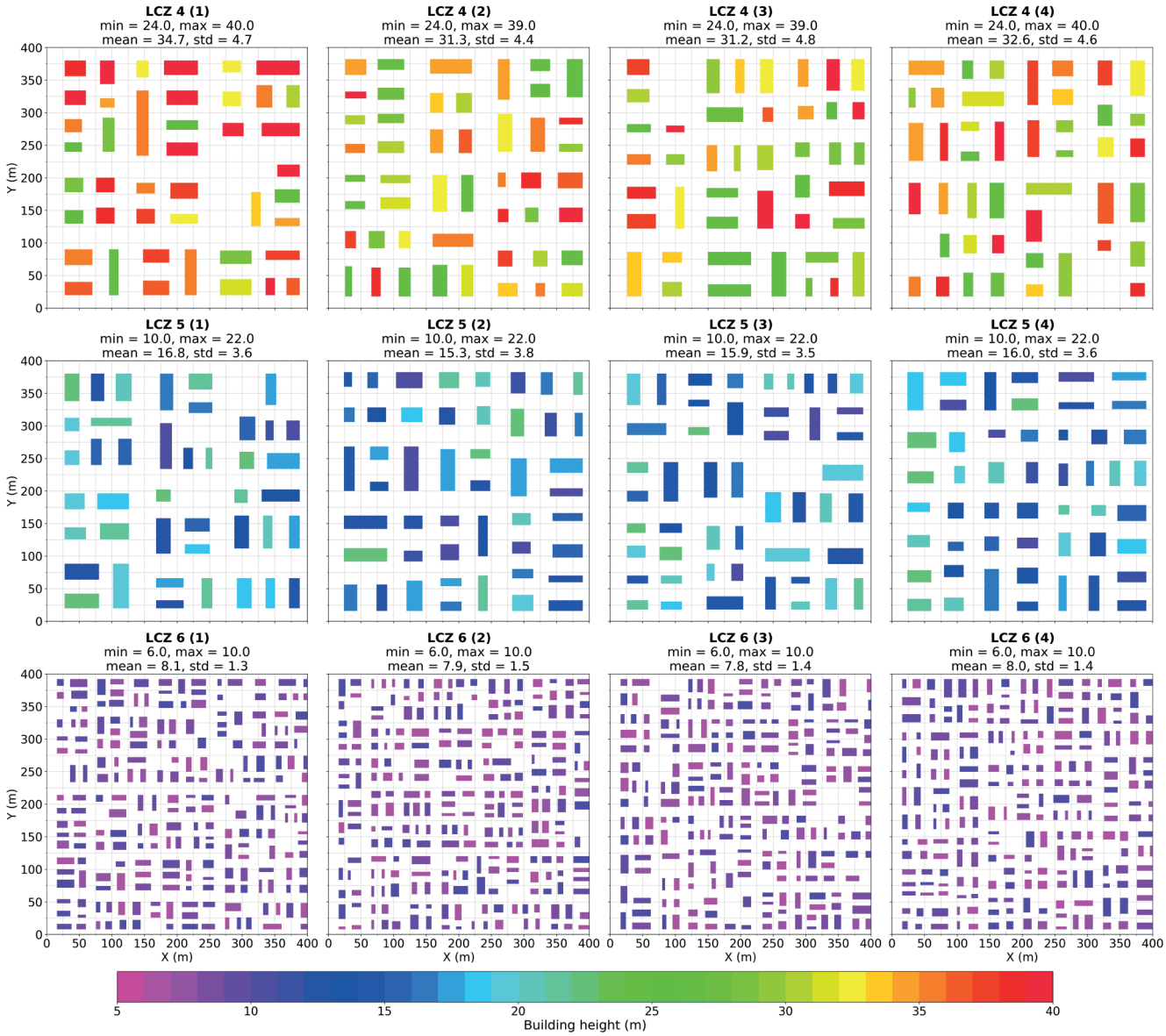

Fig. 2. Elevation maps for randomized building configurations corresponding to Local Climate Zones LCZ 4, LCZ 5, and LCZ 6

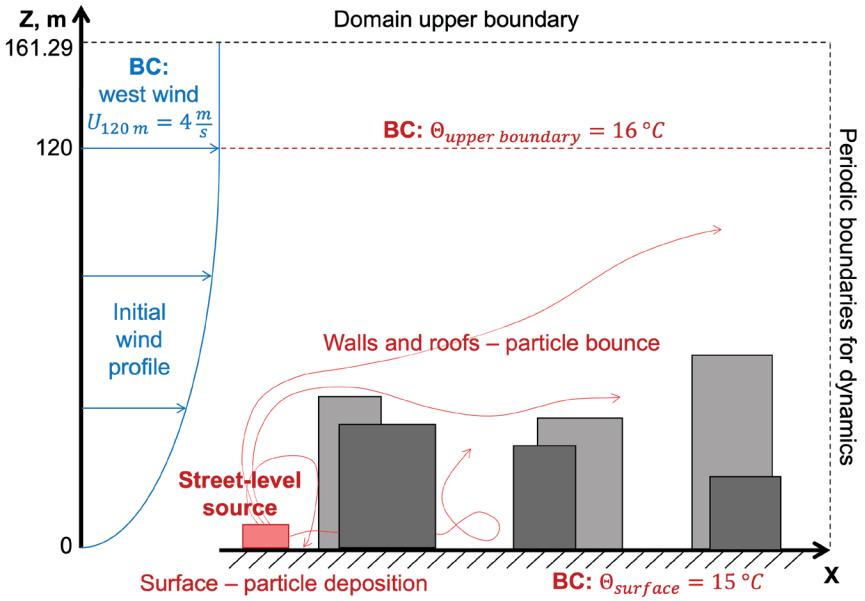

Fig. 3. Schematic of the experiment setup

aerosols, which correspond to the widely used aerosol category PM2.5 (Zwozdziak et al. 2017). The particles we are considering are relatively light and weakly affected by inertia and gravitational subsidence. Heavier and larger particles (PM10 and larger) are planned to be considered in future studies. The source of particles in all experiments was a volumetric source having a width of 8 meters (along X) and a height of 4 meters (from 0 to 4 m along Z) and elongated through the entire Y axis, that is, simulating emissions from a long street perpendicular to the wind direction. In configurations with regular geometry, the source was located at coordinates from X=21.0 to X=29.0 meters from the western border of the domain; that is, it was located in the first left canyon. In configurations with randomly generated geometry, the source occupied the south-north strip at coordinates from X=4.0 to X=12.0 meters, i.e., it was also located in the first left canyon. Particles escaped domain on the western, eastern, and upper borders of the computational domain, periodic conditions were set on the southern and northern borders (particles appear at the southern margin while crossing the northern, and vice versa), and deposited on the earth's surface.

The dimensions of the computational domain were 400 (X) m by 200 (Y) m by 161.29 (Z) m for regular configurations and 400 (X) m by 400 (Y) m by 161.29 (Z) m for randomized ones. The horizontal grid spacing along the X and Y axes was 2 m, the vertical resolution was 2 m inside bottom 80-meter layer, and above it the cell size increased by 4% with each grid step up to 5.12 m. In total, the vertical domain extent was divided into 64 cells. The experiments were carried out for a period of 12 hours, sufficient for the flow to achieve a quasi-stationary equilibrium state and gather statistics (mean and fluxes) in the last 4 hours of the simulation. The time step of the LES model was fixed in all cases and equal to 0.04 seconds.

RESULTS AND DISCUSSION

Regular configurations

Based on the results of numerical experiments, the distribution of particle concentrations and the characteristics of their propagation were analyzed. For regular building configurations, Fig. 4 shows the average concentrations at the ground level (0-4 m above surface), demonstrating the removal of particles from the source through the streets. In the plots of time-averaged near-surface concentrations, plumes of higher concentrations can be clearly traced along the streets through which the particles are carried horizontally. The maximum average concentrations are observed in LCZ 4 (a-c), which can be explained by the highest height of buildings among the selected LCZs and, as a result, the greatest resistance to airflow, which negatively affects the street ventilation. At the same time, there is no significant difference in average concentrations and standard deviation (SD) of concentrations between LCZ 5 (a-c) and LCZ 6 (a-c), despite the twofold difference in the height of buildings.

Significant differences are noticeable among the various building configurations that belong to the same LCZ (between (a), (b) and (c) configurations of each same LCZ). For each of the LCZs, it can be seen that the lowest concentrations were obtained in configuration (a), elongated buildings perpendicular to the wind, which is associated with the formation of vertical vortices (Glazunov 2018) inside the canyons and the active removal of particles into the layer above the buildings. At the same time, configurations (b) show average concentrations that are 10-15% higher, which is associated with a lower vertical mixing effect and a more active removal of particles along the streets at the same height near the surface. The highest average concentrations and SD are observed in configurations (c) – these are the variants with the highest building density, which affects the weakening of vertical mixing and a decrease in wind speed inside the urban canopy.

Randomized configurations

For randomly generated configurations, the average concentrations at the ground level (0-4 m in height) are shown in Fig. 5. Due to the random nature of the building patterns, there are much more significant differences between LCZs and, as before, noticeable differences between realizations of a single LCZ. The most noticeable difference from the experiments with regular configurations (Fig. 4) is that the highest average concentrations were obtained for LCZ 6 with the lowest building height, while the values for LCZ 4 and LCZ 5 are similar. Such a drastic difference can be explained by the fact that in the case of randomized geometry, the airflow becomes more turbulent, and the role of vertical mixing

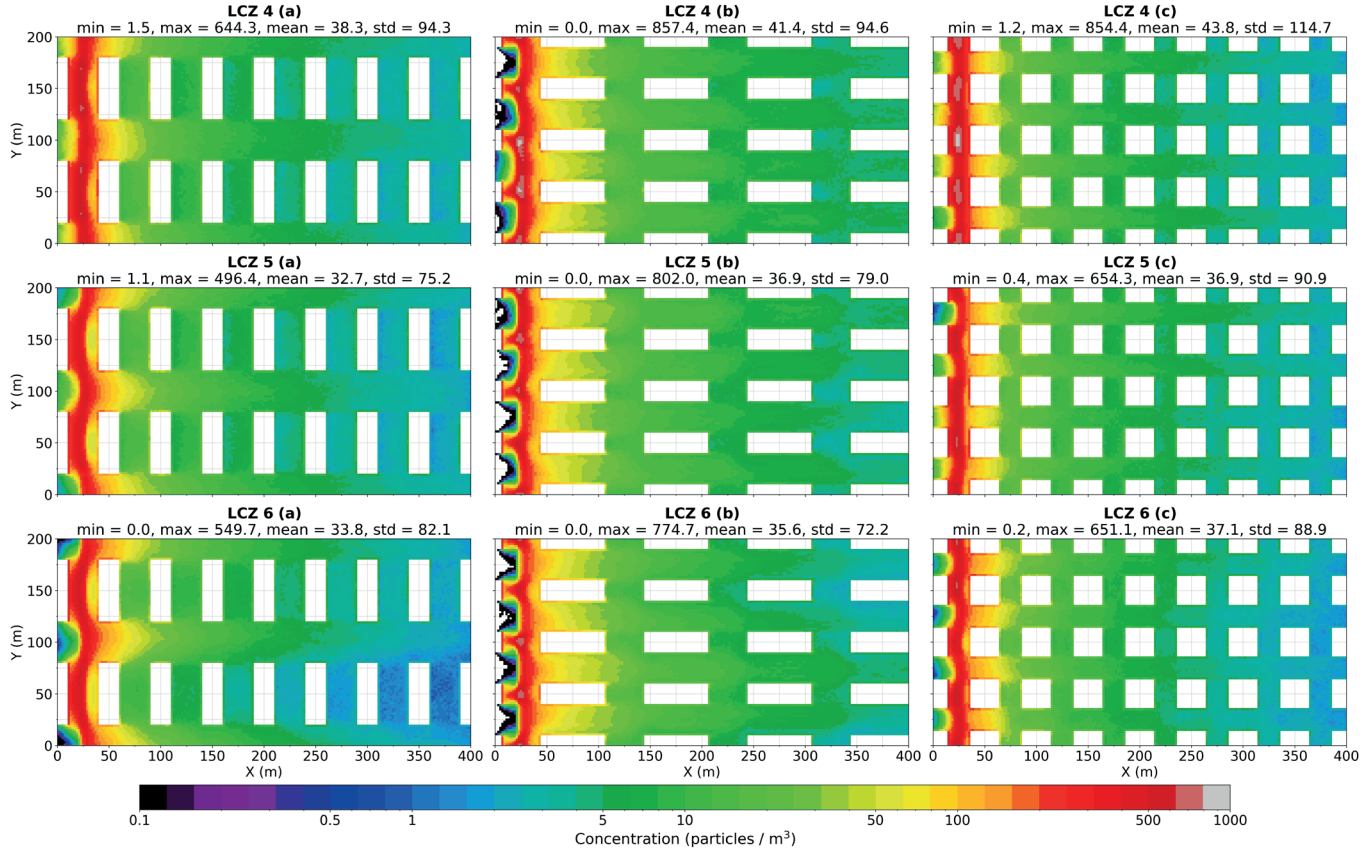

Fig. 4. Simulated surface (altitude 0-4 m) particle concentrations for regular building configurations corresponding to Local Climate Zones LCZ 4, LCZ 5, LCZ 6

and removal of particles into the air layer above buildings increases. At the same time, in the case of LCZ 6, the urban environment is lower and denser than in LCZ 4 and LCZ 5. This, in turn, reduces the exchange between the air layers inside it and above the buildings.

If we compare different configurations within the same LCZ, then there is a very strong influence of geometry near the source – concentrations at different points at the same distance from the source may differ by an order of magnitude, but at large enough distances, this is smoothed out due to the random nature of the urban development.

From the above results, it can be concluded that buildings parallel to the wind (regular configurations (b), Fig. 4) contribute to the horizontal removal of particles without active vertical mixing, while perpendicular buildings (regular configurations (a), Fig. 4) contribute to the vertical removal of air into the layer above buildings. However, these effects have been tested under conditions of neutral stratification. In cities with frequent stable stratification, i.e., at high latitudes and in winter (Varentsov et al. 2023), the removal of aerosols requires the presence of well-ventilated streets and courtyards. With frequent daytime unstable stratification, particle removal will also be accelerated by wind-obstructing structures that activate vertical mixing. However, from the point of view of aerosol removal, randomized building configurations have been proven to be the best, in which streets parallel to the wind and buildings perpendicular to the wind are combined, but low building density remains – in total, all this leads to increased turbulence and active horizontal and vertical mixing.

Configurations intercomparison

To assess the LCZ classification relevance to pollution dispersion in urban environments, we determined how large the differences in concentration and particle transport patterns are between variations in geometry within a single LCZ type.

Fig. 6 shows vertical profiles of particle concentrations averaged over the eastern half of the region (coordinates [200:400 m, 0:400 m] on the X and Y axis respectively), that is, over the part of the building as far away from the sources as possible, where the concentration field is already significantly mixed by buildings and less dependent on the position of buildings compared to the latter located directly next to the source. The general shape of the profiles is similar for most configurations. The maximum concentrations are observed at a height close to the average building height, since inside the urban canopy, vertical mixing lifts particles up, but above the roofs, it is not so active, and particles are carried away by horizontal flows. At the same time, particles sediment on the ground, so surface concentrations are not high at a distance from the source. For some configurations, high concentrations are observed not only at the roof level but also up to the upper boundary of the domain. This effect can be caused by the severe turbulence that occurs over tall and highly heterogeneous urban development.

For regular geometries (Fig. 6a, 6c, 6e), the profiles and the spread between them are very similar – the standard deviation of concentration ranges from 0.23 to 0.27 (in dimensionless units relative to the maximum concentration among the profiles), and the shape of the profiles for the same buildings' configurations but for different LCZs is the same (with profiles normalized by building heights), e.g., for (c) configurations of all LCZs. For each of the LCZs, there is a large variation in concentrations between different versions of its geometry, which suggests that the LCZ cannot be approximated by any single geometry configuration – it is necessary to consider various options and take into account the influence of the shape and orientation of buildings.

For randomized geometries, similar conclusions were obtained for LCZ 4 and LCZ 5 (Fig. 6b, 6d) – the profiles for different configurations of the same LCZ differ significantly from each other. However, for LCZ 6 (Fig. 6f), extremely low variability was obtained between the geometry variants – due

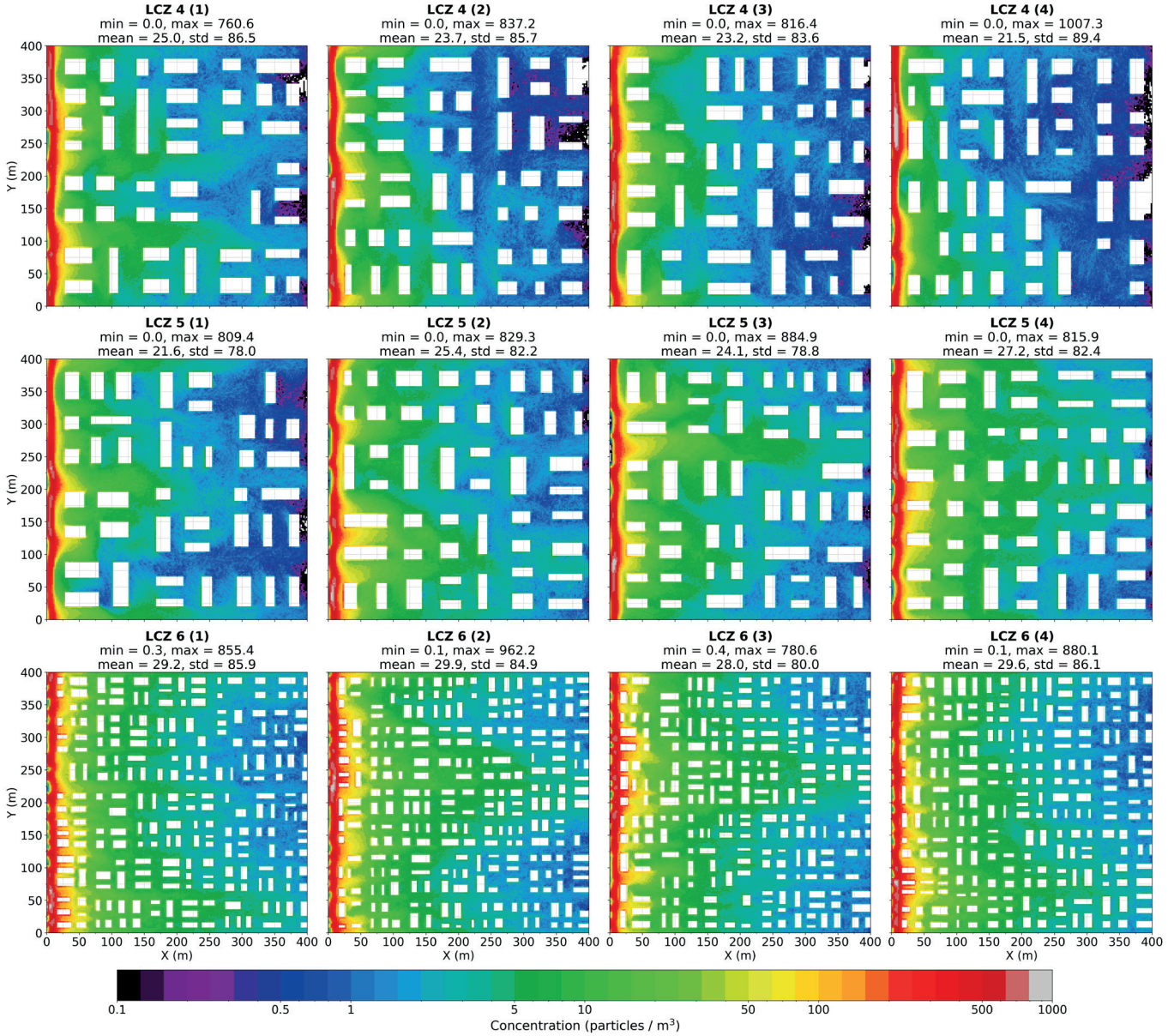

Fig. 5. Simulated surface (altitude 0-4 m) particle concentrations for randomized building configurations corresponding to Local Climate Zones LCZ 4, LCZ 5, LCZ 6

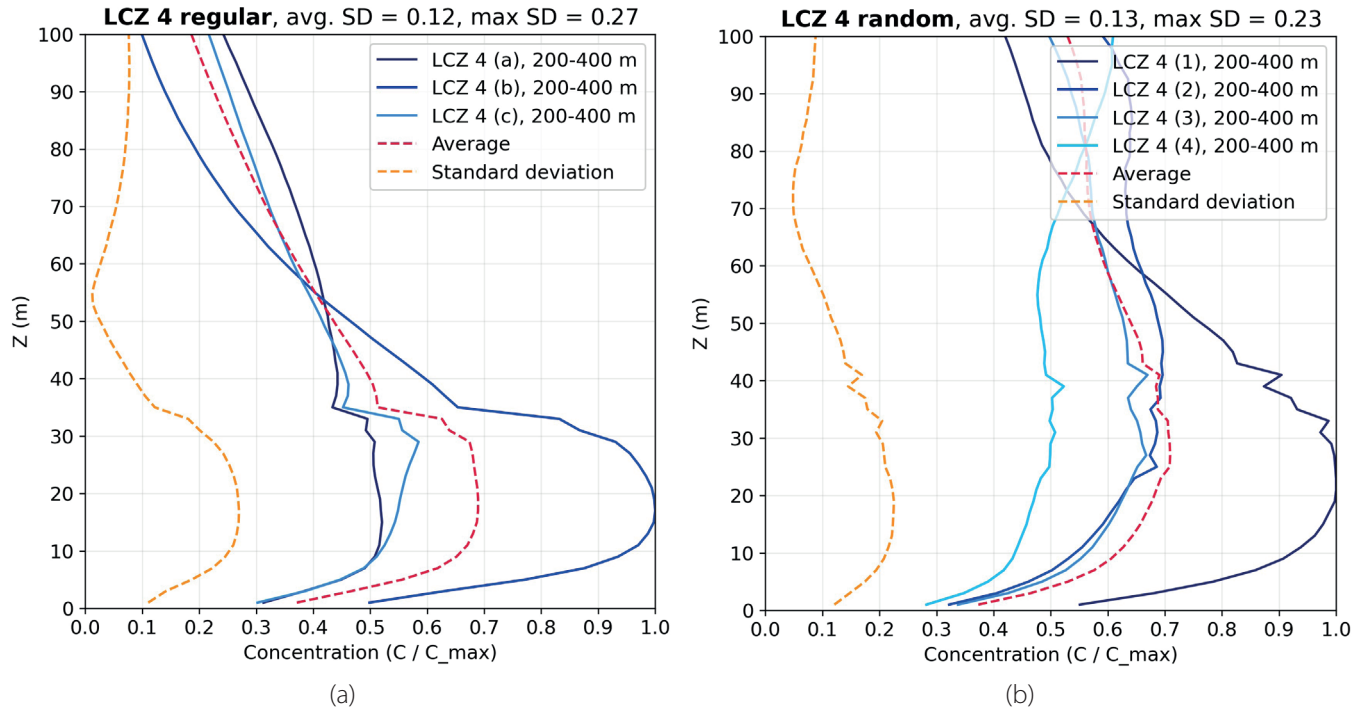

(a) (b)

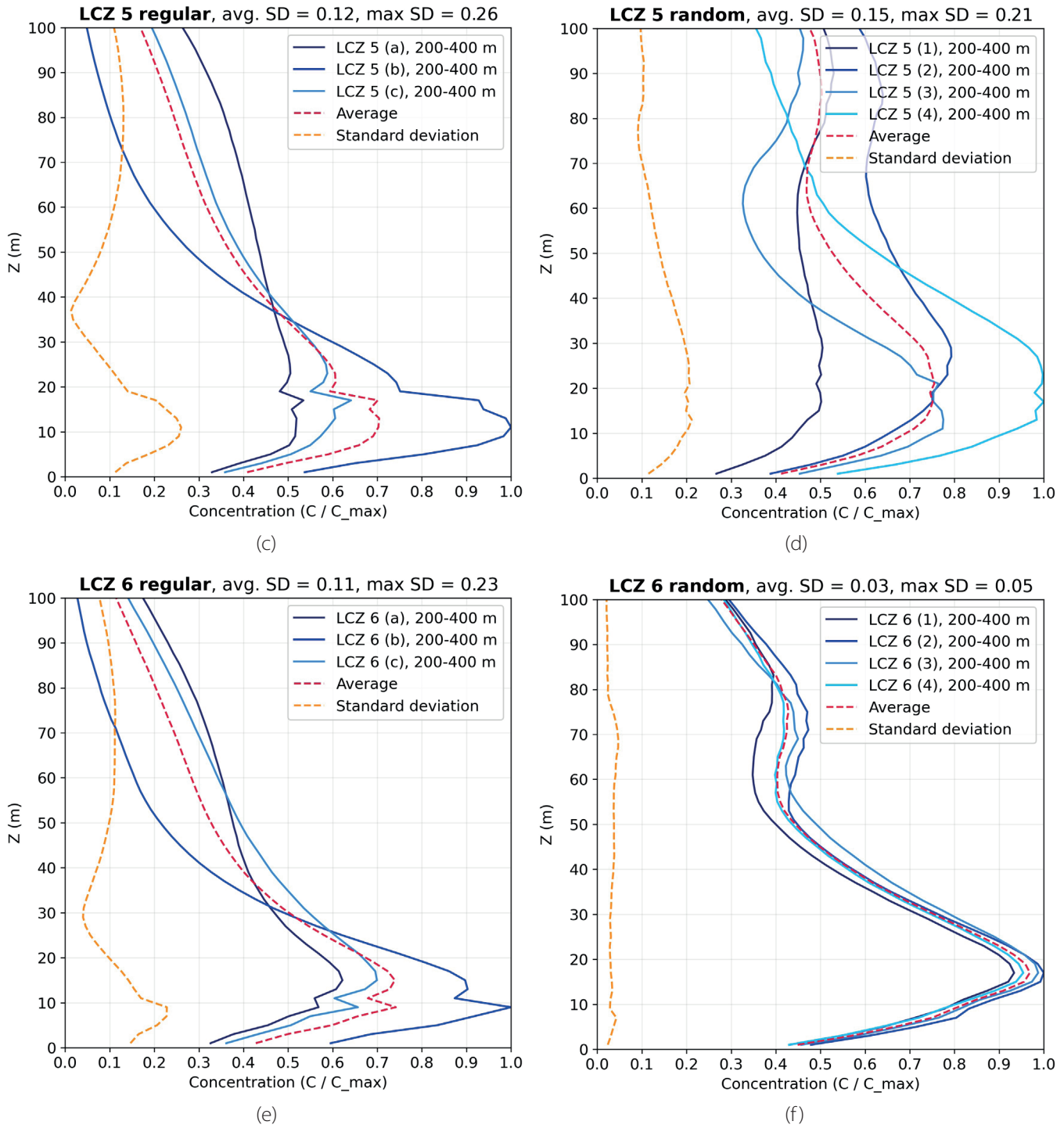

Fig. 6. Vertical particle concentration profiles, averaged over the eastern half of the region, for regular (a, c, e) and randomized (b, d, f) building configurations corresponding to Local Climate Zones LCZ 4 (a-b), LCZ 5 (c-d), LCZ 6 (e-f)

to the low height and small size of the buildings, unlike LCZ 6 regular configurations with longer and wider buildings, the geometry of buildings is more homogeneous and does not generate large disturbances in the wind flow.

Fig. 7 shows concentration profiles similar to Fig. 6, but averaged over all configurations of the same LCZ. In the case of regular geometries (Fig. 7a), the difference between different LCZ types is minimal at the surface and only significantly manifests itself at the roof level and in the layer above the buildings. The maximum standard deviation (0.2) turned out to be less than when comparing different geometry configurations within a single LCZ. Thus, for regular building configurations, the shape and orientation of buildings had a greater impact on the spread of aerosols than the different LCZ parameters: the height of the building and the aspect ratio of urban canyons.

For the randomized configurations (Fig. 7b), on the contrary, significant differences were found between the profiles for different LCZs. The maximum standard deviation values observed at heights of 15-20 m were approximately 1.5 times higher than the maximum standard deviation values for various configurations within the same LCZ. The average concentrations also vary significantly at the surface level – for LCZ 6, they were almost 2.5 times higher than for LCZ 4. The results for the randomized configurations demonstrate that in the absence of an ideal periodic structure of the city and the presence of heterogeneity in the size, shape, and height of buildings, the spread of aerosols in the urban environment is determined by the general morphometric parameters of the area much more strongly than the specific location of buildings and their orientation.

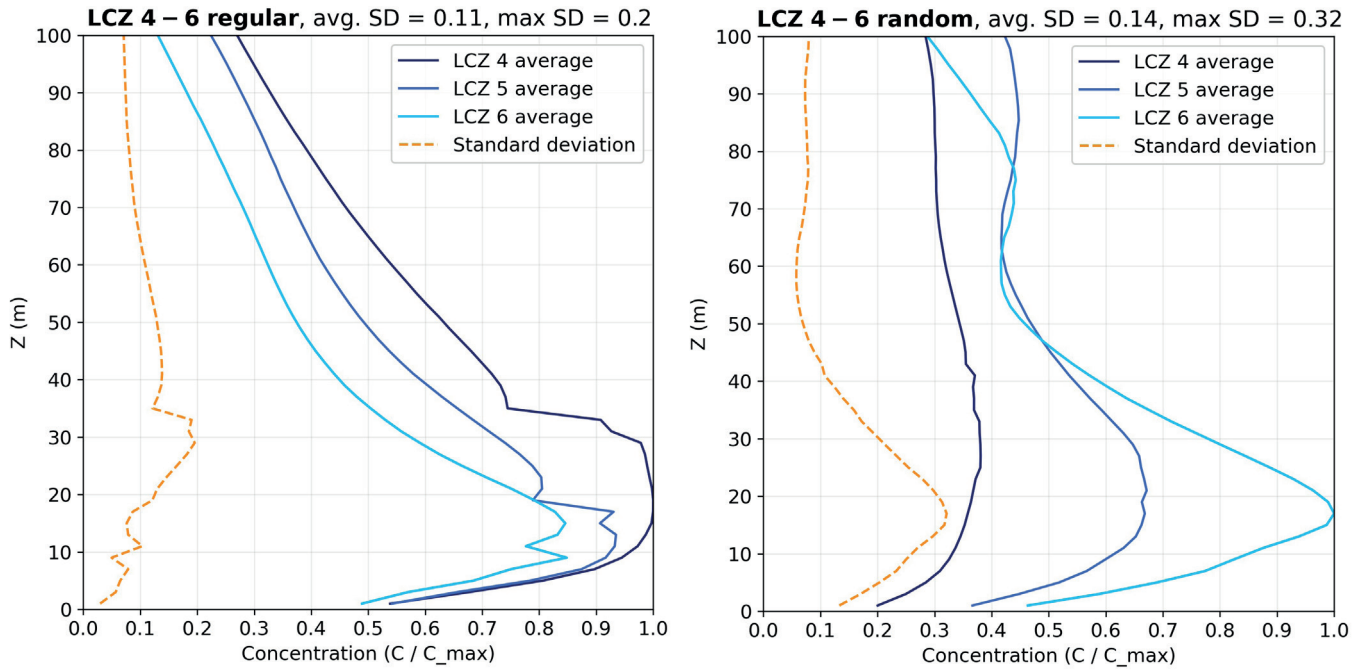

Fig. 7. Vertical particle concentration profiles in the eastern half of the region averaged over the implementations of each LCZ, for regular (a) and randomized (b) building configurations

CONCLUSIONS

In this paper, the analysis and comparison of aerosol particle dispersion within the city were carried out depending on the following parameters. Firstly, depending on the type of urban development based on the LCZ classification. Secondly, depending on the specifics of the geometry implementation for the selected LCZ type. Thirdly, depending on the randomization and periodicity of the geometry configuration. The results of numerical calculations using a large-eddy simulation model with a Lagrangian particle transport model allowed us to draw conclusions for a finely dispersed urban aerosol distribution under typical meteorological conditions: neutral stratification and low wind.

When generating regular geometry with identical buildings, the influence of the features of a particular configuration (primarily, the shape and orientation of buildings) turned out to be comparable, and in some cases more significant, than the influence of large-scale morphometric parameters of buildings, which are determined by LCZ types and characterize qualitatively different types of urban development. However, such LCZ implementations are highly idealized and have very few analogues in real cities, which motivates the creation of configurations with a limited range of building parameters and a random contribution to their location relative to each other.

Using the developed LCZ generator, building configurations were created taking into account the random contribution to the parameters and location of each building but corresponding to the large-scale morphometric characteristics of the selected LCZ types. Such configurations are more realistic, as they reflect the quasi-random nature of real urban development at the level of individual buildings but retain the typical scale of blocks and streets for most cities. Experiments with these configurations showed a significant variation in concentrations between specific implementations of a single LCZ for high-rise and medium-rise buildings (LCZ 4, LCZ 5) and a slight variation for low-rise buildings (LCZ 6), while for all LCZs the scale of variation between implementations was smaller than in the case of regular configurations. The differences between LCZs in this case turned out to be one and a half times greater than the maximum scale of differences between individual implementations of a single LCZ.

Thus, in urban areas, which are highly distinct from the single, regular, periodic structures, it is possible to describe the features of aerosol distribution by considering the aggregated type of urban development – for example, the LCZ type. This result opens up new prospects for the development of global and regional models of atmospheric dynamics and pollution dispersion by more accurately accounting for the urban underlying surface and its effect on the spread of aerosols.

Based on the results of this work, the following recommendations can be proposed for developers and urban planners. With low and medium building densities, one of the ways to increase air mixing and remove polluting aerosols from the surface level may be to increase the height spread of buildings and make their location and orientation more random, avoiding the construction of identical regular structures.

Further research on this topic is required to analyze the differences more accurately between all existing types of LCZ and to take into account a larger number of factors: atmospheric stratification, wind speed, aerosol size and composition, interaction of different LCZ types on the city scale, etc. Also, in further research, it is worth considering in more detail the influence of model parameters, especially spatial resolution.

REFERENCES

Aslam A. and Rana I.A. (2022). The use of local climate zones in the urban environment: A systematic review of data sources, methods, and themes. Urban Climate, 42, 101120. DOI: 10.1016/j.uclim.2022.101120

Baklanov A., Hänninen O., Slørdal L.H., Kukkonen J., Bjergene N., Fay B., Finardi S., Hoe S.C., Jantunen M., Karppinen A., Rasmussen A., Skouloudis A., Sokhi R.S., Sørensen J.H. and Ødegaard V. (2007). Integrated systems for forecasting urban meteorology, air pollution and population exposure. Atmospheric Chemistry and Physics, 7(3), 855–874. DOI: 10.5194/acp-7-855-2007

Baklanov Alexander and Zhang Y. (2020). Advances in air quality modeling and forecasting. Global Transitions, 2, 261–270. DOI: 10.1016/j.glt.2020.11.001

Berlyand M.E. (1991). Prediction and Regulation of Air Pollution. Springer Netherlands. DOI: 10.1007/978-94-011-3768-3

Blocken B., Janssen W.D. and van Hooff T. (2012). CFD simulation for pedestrian wind comfort and wind safety in urban areas: General decision framework and case study for the Eindhoven University campus. Environmental Modelling & Software, 30, 15–34. DOI: 10.1016/j.envsoft.2011.11.009

Blocken Bert. (2015). Computational Fluid Dynamics for urban physics: Importance, scales, possibilities, limitations and ten tips and tricks towards accurate and reliable simulations. Building and Environment, 91, 219–245. DOI: 10.1016/j.buildenv.2015.02.015

Britter R.E. and Hanna S.R. (2003). Better lowercase: Flow and dispersion in urban areas. Annual Review of Fluid Mechanics, 35(Volume 35, 2003), 469–496. DOI: 10.1146/annurev.fluid.35.101101.161147

Chatzidimitriou A. and Axarli K. (2017). Street Canyon Geometry Effects on Microclimate and Comfort; A Case Study in Thessaloniki. Procedia Environmental Sciences, 38, 643–650. DOI: 10.1016/j.proenv.2017.03.144

Cohen A.J., Brauer M., Burnett R., Anderson H.R., Frostad J., Estep K., Balakrishnan K., Brunekreef B., Dandona L., Dandona R., Feigin V., Freedman G., Hubbell B., Jobling A., Kan H., Knibbs L., Liu Y., Martin R., Morawska L., … Forouzanfar M.H. (2017). Estimates and 25-year trends of the global burden of disease attributable to ambient air pollution: an analysis of data from the Global Burden of Diseases Study 2015. The Lancet, 389(10082), 1907–1918. DOI: 10.1016/S0140-6736(17)30505-6

Debolskiy A.V., Mortikov E.V., Glazunov A.V. and Lüpkes C. (2023). Evaluation of Surface Layer Stability Functions and Their Extension to First Order Turbulent Closures for Weakly and Strongly Stratified Stable Boundary Layer. Boundary-Layer Meteorology, 187(1–2), 73–93. DOI: 10.1007/s10546-023-00784-3

Demuzere M., Kittner J., Martilli A., Mills G., Moede C., Stewart I.D., Van Vliet J. and Bechtel B. (2022). A global map of local climate zones to support earth system modelling and urban-scale environmental science. Earth System Science Data, 14(8), 3835–3873. DOI: 10.5194/essd-14-3835-2022

Engel B. (2022). The Concept of the Socialist City. International Planning History Society Proceedings, 663-678 Pages. DOI: 10.7480/IPHS.2022.1.6516

Germano M., Piomelli U., Moin P. and Cabot W.H. (1991). A dynamic subgrid-scale eddy viscosity model. Physics of Fluids A: Fluid Dynamics, 3(7), 1760–1765. DOI: 10.1063/1.857955

Glazunov A.V. (2018). Numerical simulation of turbulence and transport of fine particulate impurities in street canyons. Numerical Methods and Programming (Vychislitel'nye Metody i Programmirovanie), 1(55), 17–37. DOI: 10.26089/NumMet.v19r103

Grylls T., Le Cornec C.M.A., Salizzoni P., Soulhac L., Stettler M.E.J. and Van Reeuwijk M. (2019). Evaluation of an operational air quality model using large-eddy simulation. Atmospheric Environment: X, 3, 100041. DOI: 10.1016/j.aeaoa.2019.100041

Holmes N.S. and Morawska L. (2006). A review of dispersion modelling and its application to the dispersion of particles: An overview of different dispersion models available. Atmospheric Environment, 40(30), 5902–5928. DOI: 10.1016/j.atmosenv.2006.06.003

Jiang R., Xie C., Man Z., Afshari A. and Che S. (2023). LCZ method is more effective than traditional LUCC method in interpreting the relationship between urban landscape and atmospheric particles. Science of The Total Environment, 869, 161677. DOI: 10.1016/j.scitotenv.2023.161677

Kadantsev E., Mortikov E. and Zilitinkevich S. (2021). The resistance law for stably stratified atmospheric planetary boundary layers. Quarterly Journal of the Royal Meteorological Society, 147(737), 2233–2243. DOI: 10.1002/qj.4019

Kadaverugu R., Sharma A., Matli C. and Biniwale R. (2019). High Resolution Urban Air Quality Modeling by Coupling CFD and Mesoscale Models: a Review. Asia-Pacific Journal of Atmospheric Sciences, 55(4), 539–556. DOI: 10.1007/s13143-019-00110-3

Kampa M. and Castanas E. (2008). Human health effects of air pollution. Environmental Pollution, 151(2), 362–367. DOI: 10.1016/j.envpol.2007.06.012

Kasimov N., Chalov S., Chubarova N., Kosheleva N., Popovicheva O., Shartova N., Stepanenko V., Androsova E., Chichaeva M., Erina O., Kirsanov A., Kovach R., Revich B., Shinkareva G., Tereshina M., Varentsov M., Vasil'chuk J., Vlasov D., Denisova I. and Minkina T. (2024). Urban heat and pollution island in the Moscow megacity: Urban environmental compartments and their interactions. Urban Climate, 55, 101972. DOI: 10.1016/j.uclim.2024.101972

Kosheleva N.E., Vlasov D.V., Korlyakov I.D. and Kasimov N.S. (2018). Contamination of urban soils with heavy metals in Moscow as affected by building development. Science of The Total Environment, 636, 854–863. DOI: 10.1016/j.scitotenv.2018.04.308

Kurppa M., Hellsten A., Auvinen M., Raasch S., Vesala T. and Järvi L. (2018). Ventilation and Air Quality in City Blocks Using Large-Eddy Simulation—Urban Planning Perspective. Atmosphere, 9(2), 65. DOI: 10.3390/atmos9020065

Lee H. and Mayer H. (2018). Thermal comfort of pedestrians in an urban street canyon is affected by increasing albedo of building walls. International Journal of Biometeorology, 62(7), 1199–1209. DOI: 10.1007/s00484-018-1523-5

Lin Y., An X., Yuan J., Yuan J. and Chen B. (2024). The impact of the urban landscape on PM2.5 from LCZ perspective: A case study of Shenyang. Urban Climate, 57, 102107. DOI: 10.1016/j.uclim.2024.102107

Mortikov E.V., Glazunov A.V. and Lykosov V.N. (2019). Numerical study of plane Couette flow: turbulence statistics and the structure of pressure–strain correlations. Russian Journal of Numerical Analysis and Mathematical Modelling, 34(2), 119–132. DOI: 10.1515/rnam-2019-0010

Nourani S., Villalobos A.M. and Jorquera H. (2024). Indoor and outdoor PM2.5 in schools of Santiago, Chile: influence of local climate zone (LCZ) environment. Air Quality, Atmosphere & Health. DOI: 10.1007/s11869-024-01687-z

Oke T.R., Mills G., Christen A. and Voogt J.A. (2017). Urban Climates, 1st ed. Cambridge University Press. DOI: 10.1017/9781139016476

Pope III C.A. and Dockery D.W. (2006). Health Effects of Fine Particulate Air Pollution: Lines that Connect. Journal of the Air & Waste Management Association, 56(6), 709–742. DOI: 10.1080/10473289.2006.10464485

Reynolds A.M. and Cohen J.E. (2002). Stochastic simulation of heavy-particle trajectories in turbulent flows. Physics of Fluids, 14(1), 342–351. DOI: 10.1063/1.1426392

Shi Y., Ren C., Lau K.K.-L. and Ng E. (2019). Investigating the influence of urban land use and landscape pattern on PM2.5 spatial variation using mobile monitoring and WUDAPT. Landscape and Urban Planning, 189, 15–26. DOI: 10.1016/j.landurbplan.2019.04.004

Starchenko A.V., Danilkin E.A. and Leschinsky D.V. (2023). Numerical Simulation of the Distribution of Vehicle Emissions in a Street Canyon. Mathematical Models and Computer Simulations, 15(3), 427–435. DOI: 10.1134/S207004822303016X

Stewart I.D. and Oke T.R. (2012). Local Climate Zones for Urban Temperature Studies. DOI: 10.1175/BAMS-D-11-00019.1

Suiazova V.I., Debolskiy A.V. and Mortikov E.V. (2024). Study of Surface Layer Characteristics in the Presence of Suspended Snow Particles Using Observational Data and Large Eddy Simulation. Izvestiya, Atmospheric and Oceanic Physics, 60(2), 158–167. DOI: 10.1134/S000143382470021X

Sützl B.S., Rooney G.G. and Van Reeuwijk M. (2021). Drag Distribution in Idealized Heterogeneous Urban Environments. Boundary-Layer Meteorology, 178(2), 225–248. DOI: 10.1007/s10546-020-00567-0

Tarasova M.A., Debolskiy A.V., Mortikov E.V., Varentsov M.I., Glazunov A.V. and Stepanenko V.M. (2024). On the Parameterization of the Mean Wind Profile for Urban Canopy Models. Lobachevskii Journal of Mathematics, 45(7), 3198–3210. DOI: 10.1134/S1995080224603801

Thomson D.J. and Wilson J.D. (2012). History of Lagrangian Stochastic Models for Turbulent Dispersion. In: J. Lin, D. Brunner, C. Gerbig, A. Stohl, A. Luhar, and P. Webley eds., Lagrangian Modeling of the Atmosphere, 19–36. American Geophysical Union. DOI: 10.1029/2012GM001238

Tkachenko E.V., Debolskiy A.V., Mortikov E.V. and Glazunov A.V. (2022). Large-Eddy Simulation and Parameterization of Decaying Turbulence in the Evening Transition of the Atmospheric Boundary Layer. Izvestiya, Atmospheric and Oceanic Physics, 58(3), 219–236. DOI: 10.1134/S0001433822030112

Varentsov A.I., Imeev O.A., Glazunov A.V., Mortikov E.V. and Stepanenko V.M. (2023). Numerical Simulation of Particulate Matter Transport in the Atmospheric Urban Boundary Layer Using the Lagrangian Approach: Physical Problems and Parallel Implementation. Programming and Computer Software, 49(8), 894–905. DOI: 10.1134/S0361768823080248

Varentsov A.I., Stepanenko V.M., Mortikov E.V. and Konstantinov P.I. (2020). Numerical simulation of particle transport in the urban boundary layer with implications for SARS-CoV-2 virion distribution. IOP Conference Series: Earth and Environmental Science, 611(1), 012017. DOI: 10.1088/1755-1315/611/1/012017

Varentsov M., Konstantinov P., Repina I., Artamonov A., Pechkin A., Soromotin A., Esau I. and Baklanov A. (2023). Observations of the urban boundary layer in a cold climate city. Urban Climate, 47, 101351. DOI: 10.1016/j.uclim.2022.101351

Varentsov M., Samsonov T. and Demuzere M. (2020). Impact of Urban Canopy Parameters on a Megacity's Modelled Thermal Environment. Atmosphere, 11(12), 1349. DOI: 10.3390/atmos11121349

Venter Z.S., Hassani A., Stange E., Schneider P. and Castell N. (2024). Reassessing the role of urban green space in air pollution control. Proceedings of the National Academy of Sciences, 121(6), e2306200121. DOI: 10.1073/pnas.2306200121

Wu B. and Liu C. (2023). Impacts of Building Environment and Urban Green Space Features on Urban Air Quality: Focusing on Interaction Effects and Nonlinearity. Buildings, 13(12), 3111. DOI: 10.3390/buildings13123111

Zhang Y., Ye X., Wang S., He X., Dong L., Zhang N., Wang H., Wang Z., Ma Y., Wang L., Chi X., Ding A., Yao M., Li Y., Li Q., Zhang L. and Xiao Y. (2021). Large-eddy simulation of traffic-related air pollution at a very high resolution in a mega-city: evaluation against mobile sensors and insights for influencing factors. Atmospheric Chemistry and Physics, 21(4), 2917–2929. DOI: 10.5194/acp-21-2917-2021

Zheng X. and Yang J. (2021). CFD simulations of wind flow and pollutant dispersion in a street canyon with traffic flow: Comparison between RANS and LES. Sustainable Cities and Society, 75, 103307. DOI: 10.1016/j.scs.2021.103307

Zhou S., Wang Y., Jia W., Wang M., Wu Y., Qiao R. and Wu Z. (2023). Automatic responsive-generation of 3D urban morphology coupled with local climate zones using generative adversarial network. Building and Environment, 245, 110855. DOI: 10.1016/j.buildenv.2023.110855

Zwozdziak A., Gini M.I., Samek L., Rogula-Kozlowska W., Sowka I. and Eleftheriadis K. (2017). Implications of the aerosol size distribution modal structure of trace and major elements on human exposure, inhaled dose and relevance to the PM2.5 and PM10 metrics in a European pollution hotspot urban area. Journal of Aerosol Science, 103, 38–52. DOI: 10.1016/j.jaerosci.2016.10.004

RESEARCH PAPER

SELF-PURIFICATION CAPACITY AND PHYSICO-CHEMICAL ASSESSMENT ON A RIVER BASIN PRESSURED BY ANTHROPOGENIC INFLUENCES: EXAMPLE OF THE OSAM RIVER, BULGARIA

Kalin K. Seymenov[1*], Kristina M. Gartsiyanova[1], Atanas V. Kitev[2], Krasya P. Kolcheva[1]

[1]Bulgarian Academy of Sciences/National Institute of Geophysics, Geodesy, and Geography, Hydrology and Water Management Research Center, Acad. G. Bonchev Str., Sofia, 1113, Bulgaria

[2]Bulgarian Academy of Sciences/National Institute of Geophysics, Geodesy, and Geography, Department of Geography, Acad. G. Bonchev Str., Sofia, 1113, Bulgaria

***Corresponding author:** kalin.seimenov@abv.bg

Received: March 20th 2025 / Accepted: July 28th 2025 / Published: October 1st 2025

https://doi.org/10.24057/2071-9388-2025-3964

ABSTRACT. Various anthropogenic impacts alter the structure and functioning of natural components, and the process of self-recovery in a damaged environment is more relevant than ever. Water quality worsens due to pollution with organic and inorganic chemical substances, and understanding the ability of aquatic streams to self-purify is a key challenge facing the scientific community. This article, dedicated to the Osam River (Bulgaria), provides knowledge on how eight physico-chemical elements change their concentrations from upper to lower reaches and to what extent the river manages to self-purify of pollutants. The paper is based on information concerning the values of DO_2, $N\text{-}NH_4$, $N\text{-}NO_3$, $N\text{-}NO_2$, N-tot, $P\text{-}PO_4$, P-tot, and BOD_5, recorded at four sampling sites from 2015 until 2021. Water quality is classified into one of three classes of physico-chemical status (excellent, good, or moderate) following the guidelines in Regulation H-4/14.09.2012 for surface water characterization. The self-purification coefficient of Tumas (α) is computed to determine the extent to which the river is able to rid itself of pollutants. The results indicate that water quality changes from upstream to downstream due to the inflow of untreated wastewater discharged from various sources and the ongoing self-purification processes. In the upper section, the river fails to get rid of phosphate pollution caused by households and industry, while in the lower sector, nitrate loading from agriculture is most disturbing. The current research focuses on the ability of rivers to restore their natural conditions under various anthropogenic impacts and points to the need for more effective control of unregulated discharges.

KEYWORDS: self-purification ability, physico-chemical status, anthropogenic impact

CITATION: Seymenov K. K., Gartsiyanova K. M., Kitev A. V., Kolcheva K. P. (2025). Self-Purification Capacity And Physico-Chemical Assessment On A River Basin Pressured By Anthropogenic Influences: Example Of The Osam River, Bulgaria. Geography, Environment, Sustainability, 3 (18), 80-87

https://doi.org/10.24057/2071-9388-2025-3964

ACKNOWLEDGEMENTS: The authors are grateful to the Executive Environment Agency for the data provided.

Conflict of interests: The authors reported no potential conflict of interests.

INTRODUCTION

Water is one of the components of the environment that is most strongly and complexly subjected to a multivariate anthropogenic impact. The disruption of the normal aquatic ecosystem functioning is a consequence of water pollution, primarily resulting from anthropogenic pressures (Hishe et al. 2020; Sakke et al. 2023). The prolonged and continuous discharge of polluting substances is associated with a decrease in the water's self-purification ability, causing a hydro-ecological imbalance (Midyurova et al. 2021). The main sources of water loading with substances of various origins and compositions include agriculture, industry, the communal-household sector, transport, tourism, the character of land use, etc. (Zhang M et al. 2022), and rarely, some natural processes, such as erosion (Chalov et al. 2024).

According to the ecosystem approach, applied in the hydro-ecological practice, watercourses under certain conditions are able to restore their initial quality based on the ongoing biological, physical, chemical, and hydrodynamic processes. There are different definitions regarding the river water's self-purification. For example, it can be expressed as a partial or a complete restoration of the original state of water masses through natural processes (Benoit 1971). Another definition of self-purification states that it involves reduction in the content of pollutants entering in the water after a certain period or distance from the point of entry (Ignatova 1992) or that the aquatic environment responds to the entry of pollutants through a number of mechanisms aimed at restoring its original state (Vismara 1992). The process of self-purification consists of various complex phenomena,

involving numerous physical, chemical, and biological factors, acting and interacting more or less effectively. The scientific expression of the ability of river streams to self-purify (Bukaveckas 2007; Alexander et al. 2009), as well as the quantification of the water's self-purification capacity today is a relevant and complex research issue (Zhang X et al. 2022).

The review of the scientific publications addressing the problem of the rivers' self-restoration indicates the application of various methods, approaches, and techniques in determining their self-purification capacity. Vagnetti et al. (2003) found a significant reduction in the content of pollutants in water samples taken at the beginning and end of the Sile River in the Veneto Region, Italy, through statistical processing of existing data. The researchers draw conclusions about which elements show a significant reduction in values and formulate possible interpretations. Fisenko (2006) presents a model of a process for self-purifying river streams along the Mimico Creek in the Ontario Province, Canada, through a natural foam formation. To determine the self-purification capacity of river flows, Mala and Maly (2009) focus on assessing the toxic effect of heavy metals on biochemical oxygen demand (BOD_5) in surface waters of the Svratka River in the Brno District, Czech Republic. Self-purification of rivers occurs at a certain distance from the point where polluting substances enter and involves several processes (dilution, sedimentation, reaeration, adsorption, absorption, and both chemical and biological reactions). This complex mechanism of cleaning polluted water can be evaluated through various mathematical models. Menezes et al. (2015) and Salih et al. (2021), dealing with river basins at different spatial scales in Brazil and Iraq, use models that focus on the content of dissolved oxygen (DO_2), which is one of the crucial indicators for aquatic ecosystems and the water's self-purification processes. Hishe et al. (2020), applying the Streteer-Phelps model, assess the impact of point source pollutants from industry on the water's self-purification ability along the Abay River, Ethiopia. Zhang X et al. (2022), using the SWAT model, estimate the effect of non-point source pollutants on water's self-purification of the Yiluo River, China. Medupe and Letshwenyo (2025) leverage advanced predictive models and algorithms to offer real-time insights and future projections regarding self-purification for a tributary of the Limpopo River, Botswana. Gurjar and Tare (2019) and Xu et al. (2019), working with Bayesian Networks, evaluate the influence of land use and sewage outfalls on water's self-purification capabilities for tributaries of the Ganges River (India) and the Yangtze River (China), respectively. The surface water's self-purification by determining the distribution of nitrate (NO_3) and phosphate (PO_4) concentrations for natural and regulated stretches along the Nemunas River, Lithuania has been studied by Šaulys et al. (2020). The method proposed by the authors for comparing the amount of pollutants entering and leaving a certain section is, in practice, the most objective way to assess the self-purification capacity along the course of a given river.

Like a number of river systems in the Republic of Bulgaria, the catchment area of the Osam River is characterized by diverse natural conditions and the development of different socio-economic activities (agricultural, industrial, communal-household, etc.) (Gartsiyanova et al. 2023). The past studies (Gartsiyanova 2015; Gartsiyanova and Varbanov 2015) on the water quality of this river reported continuous pollution with chemical substances of various origins and compositions whose concentrations are changing from upstream to downstream (Seymenov 2022). This, in turn, implies variable self-purification ability along the river's course.

The present article builds on previous studies dealing with the water quality of the Osam River and is the first to focus on its capacity to dilute the entering pollutants. This paper aims to evaluate the Osam River's water self-purification ability by analyzing selected physico-chemical elements in three sections along its course for the period 2015–2021.

MATERIALS AND METHODS

Study area

The Osam River is the second longest tributary of the Danube River in the Republic of Bulgaria, with a total length of 314 km and a catchment area of 2824 km^2 (Hristova 2012) (see Fig. 1).

The main river is formed from the tributaries Beli Osam River (a left branch) and Cherni Osam River (a right branch), merging at the northern outskirts of the town of Troyan. The longer of them, the Cherni Osam River, has a total length of 36 km and takes its source on the western foothills of the Levski Peak (2166 m a.s.l), Central Balkan Mountains (Hristova 2012). In this part, the river runs north in a deep, narrow valley. Later, the river enters the Central Fore-Balkans, where between the towns of Lovech and Levski flows northeastern in a canyon-like valley through a karst terrain. Downstream after the town of Levski, the river crosses the Central Danube Plain in a northwesterly direction and forms an asymmetrical valley with flat left and steeper right slopes. The riverbed widens and, due to the low gradient, meanders in all directions. The Osam River empties into the Danube River not far from the village of Cherkovitsa at 22 m a.s.l. (Hristova 2012). The Osam River receives mostly short left- and right-bank tributaries, forming a narrow-shaped drainage basin with an expanded middle part (see Fig. 1).

The region is characterized by temperate-continental climatic conditions with a transition to mountainous with increasing altitude. The mean annual air temperature ranges from 9.0°C to 11.5°C. Winter temperatures are around -2.5°C, but decrease to -5.0°C toward the river's source, while summer temperatures reach 23°C. The annual sum of precipitation varies from 550–600 mm to 1000–1200 mm. The rainiest month is May or June, while the driest is February (Velev 2010). The Osam River has a mixed-type feed of snow, rain, and karst water (Hristova 2012). Snow and rain feed is prevalent in the Balkan Mountains, rain in the Danube Plain, and karst water in the Fore-Balkans. The average annual streamflow is increasing in a flowing direction, varying from 3.42 m^3/s (the Beli Osam River at Troyan) up to 14.10 m^3/s (the Osam River at Sanadinovo). The runoff regime is marked by a high water level in spring (April and May) and a low flow phase in late summer and autumn (September and October) (Hristova 2012). The water resources of the Osam River are utilized for irrigation, household, and industrial needs. There are also several small hydropower plants and balneological complexes. In the Balkan Mountains, the drainage basin is covered by deciduous forests, transitioning to low-stemmed woods and bushes in the Fore-Balkans and arable lands in the Danube Plain. The catchment area occupies parts of Lovech and Pleven Districts and concentrates a total of 88 settlements.

The combination of steep slopes, persistent snow cover, hydrothermal springs, and forest vegetation in the mountainous section, on the one hand, and flat relief with fertile soils in the plain sector, on the other hand,

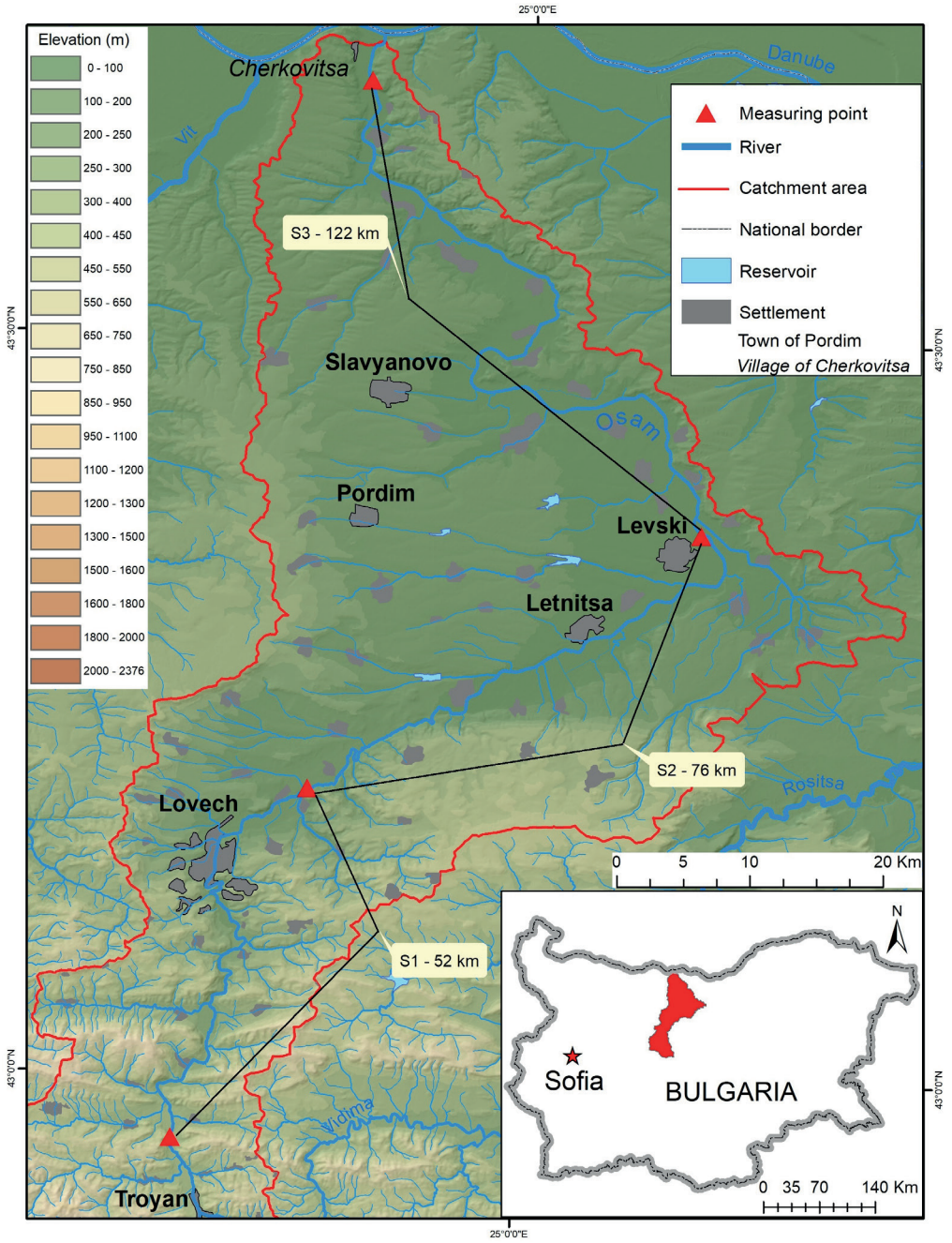

Fig. 1. Map of the Osam River Basin showing the location of settlements, water measuring points, and river stretches

is a prerequisite for the development of various socio-economic activities that are potential sources of surface water pollution (Gartsiyanova et al. 2023). The different natural conditions and anthropogenic practices in the upper and lower sections of the catchment area imply variable self-purification capacity for the river.

Data and Methodology

Water samples were collected according to the requirements of the Water Framework Directive 2000/60/EC and their equivalent criteria, transposed into Regulation H-4/14.09.2012 for surface water characterization. The concentrations of eight physico-chemical elements: dissolved oxygen (DO_2), ammonium nitrogen ($N\text{-}NH_4$), nitrate nitrogen ($N\text{-}NO_3$), nitrite nitrogen ($N\text{-}NO_2$), total nitrogen (N-tot), orthophosphates ($P\text{-}PO_4$), total phosphorus (P-tot), and biochemical oxygen demand (BOD_5) were used. The time-series data consists of 28 measurements taken from 2015 until 2021, with sampling four times per year or at least once per season. The output information was collected and published by the Executive Environment Agency (EEA) and processed using standard statistical procedures by the authors.

According to the mean annual values of each variable, water quality is assigned to one of the three classes of physico-chemical status following Regulation H-4/14.09.2012 for surface water characterization (see Table 1).

The observations were conducted at four water sampling sites (see Table 2). The measuring points, falling within surface water bodies of types R4 (Semi-mountainous streams in a Pontic province) and R7 (Large tributaries of the Danube River), were selected so that they cover parts of the upstream, midstream, and downstream of the examined river (see Fig. 1).

For an assessment of the self-purification ability, three stretches along the investigated river were distinguished (see Fig. 1, Table 3).

The water's self-purification coefficient of Tumas (2003), comparing the amount of pollutant entering and leaving a certain river section, and being in practice the most objective way to assess the self-restoration capacity along the course of a river, was applied in this study. The

Table 1. Status classification according to the physico-chemical elements as stated in Regulation H-4/14.09.2012 for surface water characterization

Water body types	Status	Physico-chemical elements							
		DO_2, mg/L^{-1}	N-NH_4, mg/L^{-1}	N-NO_3, mg/L^{-1}	N-NO_2, mg/L^{-1}	N-tot, mg/L^{-1}	P-PO_4, mg/L^{-1}	P-tot, mg/L^{-1}	BOD_5, mg/L^{-1}
R4	Excellent	>8.0	<0.04	<0.5	<0.01	<0.5	<0.02	<0.025	<1.2
	Good	8.0–6.0	0.04–0.4	0.5–1.5	0.01–0.03	0.5–1.5	0.02–0.04	0.025–0.075	1.2–3.0
	Moderate	<6.0	>0.4	>1.5	>0.03	>1.5	>0.04	>0.075	>3.0
R7	Excellent	>7.0	<0.1	<0.7	<0.03	<0.7	<0.07	<0.15	<2.0
	Good	7.0–6.0	0.1–0.3	0.7–2.0	0.03–0.06	0.7–2.5	0.07–0.15	0.15–0.3	2.0–4.0
	Moderate	<6.0	>0.3	>2.0	>0.06	>2.5	>0.15	>0.3	>4.0

Table 2. Information about water measuring points

Type of the water body	Number of the water body	Location of the measuring point		
		Description	Geographic coordinates	
			X (°E)	Y (°N)
R4	BG1OS700R1001	The Osam River after the town of Troyan	24.686	42.957
R4	BG1OS700R1001	The Osam River after the town of Lovech	24.804	43.195
R7	BG1OS700R1011	The Osam River after the town of Levski	25.163	43.371
R7	BG1OS130R1015	The Osam River at the village of Cherkovitsa	24.848	43.674

Table 3. Information about river stretches

River stretches	Altitude (m) of the river stretch		Slope (‰) of the river stretch	Length (km) of the river stretch
	At the beginning	At the end		
The Osam River after Troyan – the Osam River after Lovech	380	200	3.50	52
The Osam River after Lovech – the Osam River after Levski	200	50	2.00	76
The Osam River after Levski – the Osam River at Cherkovitsa	50	30	0.16	122

coefficient was calculated for each of the eight physico-chemical variables, using the Eq. 1:

$$\alpha = \ln\left(C_o C_L^{-1}\right) L^{-1} \quad (1)$$

where: C_0 – a concentration (mg/L^{-1}) of a physico-chemical element at the beginning of the river stretch; *CL* – a concentration (mg/L^{-1}) of a physico-chemical element at the end of the relevant stretch; *L* – length of the river stretch (km); *ln* – natural logarithm, and *α* – a self-purification coefficient.

This coefficient is preferred due to its simplicity of operation, sensitivity of parameters, and informative results. So far, it has been applied by Šaulys et al. (2020) to compare the water's self-purification capacity in terms of NO_3 and PO_4 for natural and regulated river stretches along the Nemunas River (Baltic Sea Basin, Lithuania). Montreuil et al. (2010) used a modified version of this coefficient to evaluate the impact of riparian wetlands on the values of NO_3 along the course of the Scorff River (Atlantic Ocean Basin, France). The authors concluded for which stretches the reduction in the monitored concentrations was significant and formulated possible interpretations. The coefficient has not been used in the Republic of Bulgaria until now.

A key point using this coefficient is the selection of river stretches, their beginning, end, and length. It is assumed that the length of the river stretch has a direct impact on the results obtained. In general, rivers need a certain distance to dilute pollutants, and selecting too short segments can lead to worse results (Tumas 2003). If conditions allow, the stretches should have approximately equal length. The slope gradients, soil types, topography, vegetation species and distribution, and anthropogenic practices could also influence the value of the self-purification coefficient (Tumas 2003). A higher value, for example, could be impacted by the adjacent permanent grasslands and forests. The dilution of polluted water with surface flow and groundwater can also affect it (Šaulys et al. 2020). On the other hand, a lower value typically indicates an uncontrolled discharge of untreated wastewater from industrial activities, which has a direct, often deleterious effect on water quality (Šaulys et al. 2020). If obtained ratings are less than zero, the stream fails to dilute the entering pollutants. Negative scores indicate that excessive amounts of chemical contaminants are disposed of in the river, so it is incapable of treating itself (Montreuil et al. 2010).

RESULTS and DISCUSSION

Statistical processing of monitoring data demonstrates spatial and temporal variations in the values of the physico-chemical elements along the Osam River (see Tables 4-5).

Table 4. verage multi-annual values of physico-chemical elements for 2015–2021 and status assessment according to Regulation H-4/14.09.2012 for surface water characterization

Measuring points	Physico-chemical elements							
	DO_2, mg/L^{-1}	N-NH_4, mg/L^{-1}	N-NO_3, mg/L^{-1}	N-NO_2 mg/L^{-1}	N-tot, mg/L^{-1}	P-PO_4, mg/L^{-1}	P-tot, mg/L^{-1}	BOD_5, mg/L^{-1}
The Osam River after Troyan	8.037	0.152	0.648	0.017	1.138	0.027	0.038	3.079
The Osam River after Lovech	8.150	0.146	0.970	0.015	1.524	0.088	0.105	3.463
The Osam River after Levski	8.512	0.223	2.258	0.042	3.110	0.054	0.069	4.102
The Osam River at Cherkovitsa	7.435	0.187	2.355	0.020	3.048	0.057	0.078	3.758

Note: Status of water: excellent (blue), good (green), and moderate (yellow)

The physico-chemical variables most often failing to meet the requirement of Regulation H-4/14.09.2012 for surface water bodies of type R4 are N-tot, P-PO_4, P-tot, and BOD_5 with average values falling within the numerical ranges for "moderate" status. Due to the increase/decrease in pollutant concentrations, as well as the more liberal reference standards, the failed variables for surface water bodies of type R7 include mostly N-NO_3 and N-tot (see Tables 4-5)[1].

The analysis of the temporal variability of the physico-chemical elements, as well as the review of past studies, shows that the Osam River's water fails to achieve "good" status for the last three decades. Gartsiyanova (2015) and Gartsiyanova and Varbanov (2015), exploring the water quality status at the measuring point after Lovech during the period 1990–2014, reported an elevated content of N-NH_4 and N-NO_3 from 1990 to 1993, N-NO_2 between 1994 and 2007, and P-PO4 from 1998 to 2009. The cited authors found continuous pollution with N-NH4 and P-PO_4 between 1996 and 2005 at the measuring sites after Levski and near Cherkovitsa, and stated that the highest observed concentrations of these elements exceeded from 10 to 25 times the reference norms for "good" status pointed in Regulation H-4/14.09.2012 for surface water characterization. The deteriorated water quality for the reported periods was mainly influenced by the unregulated discharge of untreated wastewater from households, industrial enterprises, and agricultural lands. The current results show another situation – the mean annual values of the failed variables for 2015–2021 exceed no more than three times the reference standards. This contradiction confirms the positive tendency in the water quality status, already established by Gartsiyanova (2015) and Seymenov (2022), and suggests that the Osam River's water continues to improve its physico-chemical conditions between 2015 and 2021. Recently, the study area has been strongly affected by the negative natural population growth, depopulation and emigration, the closure of industrial factories, and the crisis in agriculture. All of these adverse socio-economic processes contributed to reducing of the anthropogenic impact on water quality.

The analysis of spatial variations of the physico-chemical elements finds that the content of N-NO_3 and N-tot is increasing in a flowing direction, while the concentrations of the rest of the variables are increasing/decreasing from one measuring point to another (see Tables 4-5). This result partially confirms the study of Seymenov (2022), dealing with the spatial distribution of biogenic substances along the river.

As per the location of water measuring points, the river's course could be divided into three stretches (see Fig. 1, Table 3). The first sector is marked by increasing content of DO_2, N-NO_3, N-tot, P-tot, P-PO_4, and BOD_5 and declining values of N-NH_4 and N-NO_2. The second stretch has rising concentrations of all elements, excluding P-PO_4 and P-tot. The third sector is characterized by growing content of N-NO_3, P-PO_4, and P-tot and falling values of the rest of the variables (see Table 4).

The changes in the average concentrations, determined at the beginning and the end of the river stretches, as well as the computed self-purification coefficient values, show that the Osam River's water self-purifies better in the downstream section (see Fig. 2, Table 6).

In the upper part between Troyan and Lovech, almost all the time the river fails to dilute N-NO_3, N-tot, P-PO_4, and P-tot (see Fig. 2, Table 6). Although the entire river stretch is surrounded by permanent forests and natural grasslands covering steep mountainous terrain, i.e., the bank erosion is prevented, the flow rate is higher, and the detention of pollutants is lower, concentrations of polluting substances are gradually increasing. The untreated or partly treated domestic and industrial effluents released from settlements with incompletely developed sewage systems are the main factors deteriorating upstream water quality. In the mid-stretch between Lovech and Levski, the river manages to self-purify regarding P-PO_4 and P-tot but worsens its status as per N-NH_4, N-NO_3, N-NO_2, and N-tot (see Fig. 2, Table 6). In this part, the river enters flat terrain with arable lands, whereat it slows down its flow, which to some extent explains the growing values of nitrogenous compounds. In the lower unit between Levski and Cherkovitsa, the river self-purifies in terms of almost all elements, especially N-NH_4, N-NO_2, and BOD_5 (see Fig. 2, Table 6). Although the entire river stretch is abundant in meanders, i.e., the flow rate is lower and the detention of pollutants is higher, the river restores its water quality. Moreover, the surrounding farmlands release waste masses containing fertilizers and pesticides, but despite this, pollutant concentrations are decreasing. The higher rates of the self-purification coefficient can be explained by the dilution of wastewater with the surface flow and their connection with groundwater. It should be mentioned the relatively greater length of this stretch compared to the remaining two, but nevertheless, the river water's diluting ability is obvious.

The temporal analysis does not find a trend toward a decrease or increase in the water's self-purification capacity throughout the period. The upstream stretch is characterized by a worse ability to restore its condition in 2021, with the lowest coefficient ratings for three of the eight elements, and a better capacity to self-purify in 2016 and 2020, with positive scores for half of the indicators. Conversely, the mid-stretch achieved more negative results

[1]Such assessments were also reported in the second edition of the River Basin Management Plan (2016–2021), published by the Danube River Basin Directorate. Available from: www.bd-dunav.org/ (last accessed: 16.08.2025).

Table 5. Average annual values of physico-chemical elements and status assessment according to Regulation H-4/14.09.2012 for surface water characterization

Measuring points	Years	Physico-chemical elements							
		DO_2, mg/L^{-1}	N-NH_4, mg/L^{-1}	N-NO_3, mg/L^{-1}	N-NO_2, mg/L^{-1}	N-tot, mg/L^{-1}	P-PO_4, mg/L^{-1}	P-tot, mg/L^{-1}	BOD_5, mg/L^{-1}
The Osam River after Troyan	2015	9.800	0.088	0.675	0.012	1.115	0.044	0.051	3.475
	2016	10.100	0.090	0.570	0.006	0.680	0.037	0.044	2.100
	2017	7.066	0.086	0.381	0.022	0.669	0.016	0.028	3.600
	2018	7.338	0.120	0.906	0.012	1.219	0.022	0.030	2.650
	2019	6.500	0.226	0.546	0.025	1.607	0.032	0.041	2.766
	2020	6.630	0.247	0.790	0.020	1.308	0.021	0.046	4.500
	2021	10.750	0.227	0.465	0.015	1.000	0.015	0.021	1.185
The Osam River after Lovech	2015	10.675	0.070	0.907	0.014	1.965	0.082	0.090	5.900
	2016	7.200	0.060	0.670	0.012	0.750	0.031	0.040	3.200
	2017	7.433	0.087	0.693	0.008	0.937	0.095	0.108	2.160
	2018	7.527	0.097	1.587	0.010	1.985	0.073	0.092	2.025
	2019	6.333	0.246	0.733	0.012	1.830	0.092	0.105	3.100
	2020	6.966	0.289	1.206	0.013	1.790	0.012	0.016	5.430
	2021	9.275	0.147	0.698	0.034	1.215	0.095	0.106	1.916
The Osam River after Levski	2015	10.800	0.195	2.300	0.051	3.970	0.049	0.061	4.525
	2016	11.500	0.070	1.800	0.018	1.900	0.045	0.052	2.800
	2017	6.300	0.220	2.113	0.045	2.443	0.074	0.085	3.283
	2018	7.425	0.136	2.657	0.030	3.385	0.054	0.056	4.510
	2019	6.067	0.402	1.953	0.051	2.696	0.057	0.088	3.453
	2020	7.433	0.253	2.270	0.047	3.073	0.044	0.069	4.900
	2021	7.900	0.120	1.872	0.036	2.430	0.058	0.077	2.320
The Osam River at Cherkovitsa	2015	10.400	0.075	2.600	0.022	4.150	0.050	0.066	3.530
	2016	8.500	0.067	2.100	0.015	2.310	0.057	0.058	6.300
	2017	5.525	0.159	2.863	0.016	2.900	0.058	0.070	3.600
	2018	5.550	0.178	2.443	0.019	3.292	0.069	0.100	2.175
	2019	6.530	0.276	1.906	0.018	2.436	0.054	0.065	6.266
	2020	7.700	0.428	2.460	0.024	3.130	0.084	0.104	5.020
	2021	8.475	0.113	1.963	0.023	2.525	0.046	0.073	2.225

Note: Status of water: excellent (blue), good (green), and moderate (yellow)

in 2016 and positive ones in 2021. The downstream section generally demonstrates a higher ability to self-purify over the years (see Table 6). This variability confirms that river water's self-purification is a complex process involving multiple factors acting simultaneously and interacting more or less effectively.

CONCLUSIONS

The conducted research focused attention on a relatively poorly studied issue related to the capacity of rivers to restore their natural conditions under various anthropogenic pressures. The obtained results showed continuous pollution along the selected river, but with a general trend toward improvement in water quality. The applied self-purification coefficient was an informative and easy-to-use approach for assessing the ability of the watercourse to get rid of contaminants. The calculated ratings revealed that in the upper stretch the river is unable to self-purify, while in the lower section the streamflow and inflowing groundwater dilute the entering pollutants and thus contribute to the decrease in their concentrations.

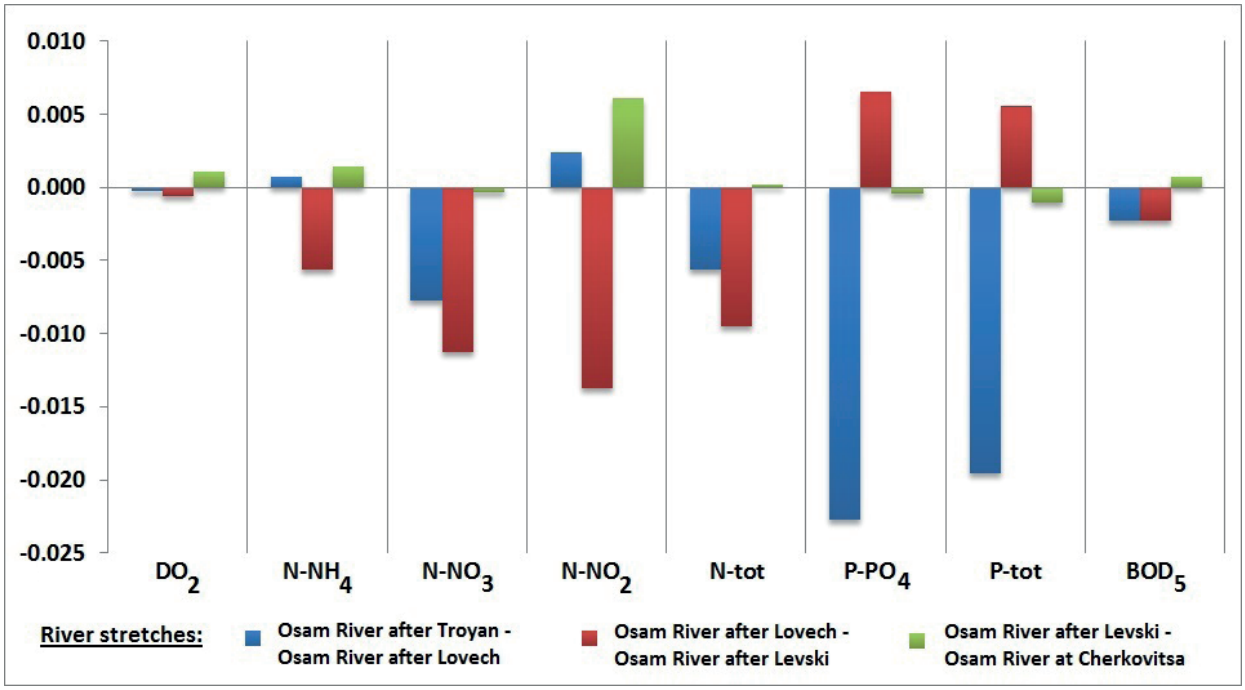

Fig. 2. Self-purification coefficient ratings based on the average multi-annual values of physico-chemical elements for 2015–2021

Table 6. Self-purification coefficient ratings based on the annual values of physico-chemical elements

River stretches	Years	Physico-chemical elements							
		DO_2	$N\text{-}NH_4$	$N\text{-}NO_3$	$N\text{-}NO_2$	N-tot	$P\text{-}PO_4$	P-tot	BOD_5
The Osam River after Troyan – the Osam River after Lovech	2015	-0.002	0.003	-0.006	-0.003	-0.011	-0.012	-0.011	-0.010
	2016	0.007	0.008	-0.003	-0.013	-0.002	0.003	0.002	-0.008
	2017	-0.001	0.000	-0.012	0.019	-0.006	-0.034	-0.026	0.010
	2018	0.000	0.004	-0.011	0.004	-0.009	-0.023	-0.022	0.005
	2019	0.001	-0.002	-0.006	0.014	-0.002	-0.020	-0.018	-0.002
	2020	-0.001	-0.003	-0.008	0.008	-0.006	0.011	0.020	-0.004
	2021	0.003	0.008	-0.008	-0.016	-0.004	-0.035	-0.031	-0.009
The Osam River after Lovech – the Osam River after Levski	2015	0.000	-0.013	-0.012	-0.017	-0.009	0.007	0.005	0.004
	2016	-0.006	-0.002	-0.013	-0.005	-0.012	-0.005	-0.003	0.002
	2017	0.002	-0.012	-0.015	-0.023	-0.013	0.003	0.003	-0.006
	2018	0.000	-0.005	-0.007	-0.015	-0.007	0.004	0.007	-0.011
	2019	0.001	-0.007	-0.013	-0.019	-0.005	0.006	0.002	-0.001
	2020	-0.005	0.002	-0.008	-0.017	-0.007	-0.018	-0.019	0.001
	2021	0.002	0.003	-0.013	-0.001	-0.009	0.007	0.004	-0.003
The Osam River after Levski – the Osam River at Cherkovitsa	2015	0.000	0.008	-0.001	0.007	0.000	0.000	-0.001	0.002
	2016	0.002	0.000	-0.001	0.001	-0.001	-0.002	-0.001	-0.007
	2017	0.001	0.003	-0.002	0.009	-0.001	0.002	0.002	-0.001
	2018	0.002	-0.002	0.001	0.004	0.000	-0.001	-0.005	0.006
	2019	-0.001	0.003	0.000	0.009	0.001	0.000	0.002	-0.005
	2020	0.002	-0.004	-0.001	0.006	0.000	-0.005	-0.003	0.000
	2021	-0.001	0.000	0.000	0.004	0.000	0.002	0.000	0.000

The study concludes that active actions are needed to prevent pollutants from entering the riverbed and to improve the self-purification capacity of surface water. The so-called soft naturalization measures are proposed. These include planting riparian protection zones along the riverbanks with connection to the surrounding wetlands in floodplains, maintaining well-aerated water by allowing woody vegetation to grow on river slopes, forming natural barriers and obstacles to water flow, etc. Stricter measures should be considered to limit the inflow of untreated wastewater into the river from agricultural, industrial, and residential sources.

This article evaluates the water quality status only in terms of averaged annual and multi-annual concentrations, but monthly and seasonal variations of physico-chemical elements are also significant factors that should be taken into account to fully assess the self-purification ability. This fact necessitates more frequent and regular monitoring of water quality elements. In the future, this work could be extended with additional indicators, such as river runoff, water temperature, etc., to obtain a comprehensive understanding of the self-purification mechanism.

REFERENCES

Alexander R., Bohlke J., Boyer E., David M., Harvey J., Mulholland P., Seitzinger S., Tobias C., Tonitto C., and Wollheim W. (2009). Dynamic modeling of nitrogen losses in river networks unravels the coupled effects of hydrological and biogeochemical processes. Biogeochemistry, 93(1), 91–116. DOI: 10.1007/s10533-008-9274-8

Benoit R. J. (1971). Self-purification in natural waters. Water Pollution Handbook, 1. Dekker, New York, USA.

Bukaveckas P. (2007). Effects of channel restoration on water velocity, transient storage, and nutrient uptake in a channelized stream. Environmental Science & Technology, 41(5), 1570–1576. DOI: 10.1021/es061618x

Chalov S. R., Moreido V., Urošev M., Golosov V., Zlatić M., Kasimov N. (2024). Advances in catchment and river erosion and pollutants' transport studies: from monitoring to modelling to management. GEOGRAPHY, ENVIRONMENT, SUSTAINABILITY, 17(4), 6–9. DOI: 10.24057/2071-9388-2024-0608

European Parliament and the Council of the European Union 2000. Directive 2000/60/EC of the European Parliament and of the Council of 23 October 2000 establishing a framework for Community action in the field of water policy. Official Journal of the European Communities L 327, 22.12.2000. 73 p.

Fisenko A. (2006). Natural purification of rivers and creeks through froth formation process. Research Journal Of Chemistry And Environment, 10(1), 24–29.

Gartsiyanova K. (2015). Anthropogenic influences on the water quality in the Osam River Basin. PhD Thesis, National Institute of Geophysics, Geodesy, and Geography, Sofia, Bulgaria.

Gartsiyanova K., and Varbanov M. (2015). Comparative assessment of the water quality in the river Osam. Science and technologies, Nautical and Environmental Studies, 6(2), 91–94.

Gartsiyanova K., Genchev S., and Kitev A. (2023). Evaluation of land cover, land use and water quality in the regions with various anthropogenic activities – a case study of the Osam River Basin, Bulgaria. European Journal of Materials Science and Engineering, 8(1), 3–10. DOI: 10.36868/ejmse.2023.08.01.003

Government of the Republic of Bulgaria (2012). Regulation H-4 from 14 September 2012 for surface water characterization. Available from: Naredba H-4.pdf.

Gurjar S. K., and Tare V. (2019). Spatial-temporal assessment of water quality and assimilative capacity of river Ramganga, a tributary of Ganga using multivariate analysis. Journal of Cleaner Production, 222, 550–564. DOI: 10.1016/j.jclepro.2019.03.064

Hishe T. G. (2020). Evaluation of point source pollutants impact on water quality and self-purification capacity of Abay River in Ethiopia. Civil Environment Research, 12(3), 1–8. DOI: 10.7176/CER/12-3-01.

Hristova N. (2012). Hydrology of Bulgaria. Tip-Top Press, Sofia.

Ignatova N. (1992). Conservation of water purity. Zemizdat, Sofia.

Mala J., and Maly J. (2009). Effect of heavy metals on self-purification processes in rivers. Applied Ecology and Environmental Research, 7(4), 333–340.

Medupe M., and Letshwenyo M. (2025). Investigation of self-purification and water quality index during dry and rainy seasons in the Khurumela Stream (Botswana). Journal of Ecohydraulics, 10(1), 1–18, DOI: 10.1080/24705357.2024.2363755

Menezes P., Bittencourt P., Farias S., Bello P., Oliveira L., and Fia R. (2015). Deoxygenation rate, reaeration and potential for self-purification of small tropical urban streams. Revista Ambiente & Água, 10(4), 748–757. DOI: 10.4136/ambi-agua.1599

Midyurova B., Belovski I., Dimova-Todorova M. (2021). Assessing the self-purification capacity of surface waters in Mladezhka River. Journal of Environmental Protection and Ecology, 22(1), 1–7.

Montreuil O., Merot P., and Marmonier P. (2010). Estimation of nitrate removal by riparian wetlands and streams in agricultural catchments: Effects of discharge and stream order. Freshwater Biology, 55, 2305–2318. DOI: 10.1111/J.1365-2427.2010.02439.X

Sakke N., Jafar A., Dollah R., Hair A., Asis B., Mapa M., Abas A. (2023). Water Quality Index (WQI) analysis as an indicator of ecosystem health in an urban river basin on Borneo Island. Water, 15(15):2717. DOI: 10. 3390/w15152717.

Salih S., Mohammad A., and Mohammed F. (2021). Study on the Self-purification of Tanjaro River. Tikrit Journal for Agricultural Sciences, 21(4), 54–62. DOI: 10.25130/tjas.21.4.7

Šaulys V., Survile O., and Stankeviciene R. (2020). An assessment of self-purification in streams. Water, 12(1):87. DOI: 10.3390/w12010087

Seymenov K. (2022). Assessment of water pollution with nitrogen and phosphorus along the course of a river: A case study from Northern Bulgaria. Journal of the Bulgarian Geographical Society, 47, 35–44. DOI: 10.3897/jbgs.e97971

Tumas R. (2003). Water Ecology. Naujasis Lankas, Kaunas.

Vagnetti R., Miana P., Fabris M., and Pavoni B. (2003). Self-purification ability of a resurgence stream. Chemosphere, 52, 1781–1795. DOI: 10.1016/S0045-6535(03)00445-4

Velev S. (2010). Climate of Bulgaria. Heron Press Publishing House, Sofia.

Vismara R. (1992). Applied Ecology. Hoepli U, Torino.

Xu J., Jin G., Tang H., Mo Y., Wang Y. G., and Li L. (2019). Response of water quality to land use and sewage outfalls in different seasons. Science of The Total Environment, 696. DOI: 10.1016/j.scitotenv.2019.134014

Zhang M., Wang L., Mu C., Huang X. (2022). Water quality change and pollution source accounting of Licun River under long-term governance. Scientific Reports, 12, 2779. DOI: 10.1038/s41598-022-06803-6.

Zhang X., Chen P., Han Y., Chang X., and Dai S. (2022). Quantitative analysis of self-purification capacity of non-point source pollutants in watersheds based on SWAT model. Ecological Indicators, 143. DOI: 10.1016/j.ecolind.2022.109425

RESEARCH PAPER

HOW DRONES AND LIDAR HELP IN COUNTING MANGROVE TREES: A PRACTICAL APPROACH

Muhammad Rizki Nandika[1*], Jeverson Renyaan[1], Bayu Prayudha[1], La Ode Alifatri[1], Herlambang Aulia Rachman[2], Yaya Ihya Ulumuddin[1], Turissa Pragunanti Ilyas[3], Dony Kushardono[3], Martiwi Diah Setiawati[1,4]

[1]Research Center for Oceanography, National Research and Innovation Agency, B. J. Habibie Science and Technology Area (KST), Serpong, South Tangerang, 15314, Indonesia

[2]Department of Marine Science, University of Trunojoyo, Jl. Raya Telang, Bangkalan, 69112, Indonesia

[3]Research Center for Geoinformatics, National Research and Innovation Agency, Jl. Cisitu, Bandung, 40135, Indonesia

[4]United Nations University – Institute for the Advanced Study of Sustainability (UNU-IAS), 5-53-70 Jingumae, Shibuya-ku, Tokyo, 150-8925, Japan

***Corresponding author:** rizki.nandika@gmail.com

Received: March 18th 2025 / Accepted: June 23rd 2025 / Published: October 1st 2025

https://doi.org/10.24057/2071-9388-2025-3958

ABSTRACT. Mangrove forests provide critical ecosystem services, including coastal protection, habitat for biodiversity, and carbon sequestration. Monitoring these ecosystems is essential for their conservation and sustainable management. This study was conducted on Pramuka Island, Indonesia, focusing on high-density Rhizophora stylosa vegetation. Data was collected using the DJI M300 RTK UAV equipped with the Zenmuse L1 LiDAR sensor, which generated a Canopy Height Model (CHM) and identified treetops. Various kernel sizes (3×3, 5×5, 9×9, 11×11, 21×21) and Local Maximum Filter (LMF) window sizes (0.5, 1, 3 meters) were applied to analyze mangrove tree density. The study found that the combination of a 3×3 kernel with a 0.5 meter window size yielded the best results, achieving the highest F-score and balancing precision and recall. However, despite the optimized settings, LiDAR still struggled to detect individual trees in dense mangrove stands, resulting in the underestimation of tree counts compared to field data. This highlights the challenges LiDAR faces in dense vegetation environments. The study emphasizes the need for optimized kernel and window size configurations for more accurate tree detection and calls for further development of LiDAR-based algorithms to improve detection in mangrove forests. Improved methodologies will enhance the effectiveness of mangrove forest conservation and management efforts.

KEYWORDS: mangrove, UAV, individual tree detection, LiDAR, kernel, window size

CITATION: Muhammad Rizki Nandika, Jeverson Renyaan, Bayu Prayudha, La Ode Alifatri, Herlambang Aulia Rachman, Yaya Ihya Ulumuddin, Turissa Pragunanti Ilyas, Dony Kushardono, Martiwi Diah Setiawati(2025). How Drones And Lidar Help In Counting Mangrove Trees: A Practical Approach. Geography, Environment, Sustainability, 3 (18), 88-98
https://doi.org/10.24057/2071-9388-2025-3958

ACKNOWLEDGEMENTS: The first author contributed to conceptualization, methodology, and writing of the original draft. The second author was responsible for data curation and writing—review and editing. The third author contributed to supervision and writing—review and editing. The fourth author handled data curation and writing—review and editing. The fifth author , sixth author, seventh author, eighth author, and ninth author all contributed to writing—review and editing, with the sixth author also providing supervision.

Conflict of interests: The authors reported no potential conflict of interests.

INTRODUCTION

Mangrove forests are vital coastal ecosystems that provide a wide range of ecological services. They play a crucial role in carbon sequestration, capturing CO_2 and storing it in their biomass and soil (Mumby et al. 2004; Himes-Cornell 2018; Sharifi 2022). These unique ecosystems act as natural barriers against storm surges and coastal erosion, safeguarding coastal communities and infrastructure (Sahu 2015; Giri et al. 2015; Carugati et al. 2018; Giri 2021; Sharifi 2022). Additionally, mangroves support many marine and terrestrial species, making them biodiversity hotspots (Mumby et al. 2004; Sahu 2015; Giri 2021). The role of mangroves in carbon sequestration is particularly vital in mitigating climate change, as they can store up to four times more carbon per unit area than terrestrial forests.

Monitoring mangrove forests is crucial for their conservation and sustainable management. Traditional methods of counting mangrove trees using ground surveys are labor-intensive, time-consuming, and expensive. These methods often require significant human resources, making them less feasible for large-scale monitoring (Tran et al. 2022). Moreover, the challenging muddy terrain and dangerous wildlife in mangrove ecosystems pose significant risks to researchers, further complicating ground surveys (Rajpar and Zakaria 2014; Saini et al. 2020).

Remote sensing techniques have been widely employed for mangrove monitoring, with satellite imagery

playing a prominent role. Early studies applied terrestrial vegetation indices to mangrove environments (Green et al. 1998), followed by advancements in mangrove classification (Lasalle et al., 2023), development of mangrove-specific indices (Gupta et al. 2018; Diniz et al. 2019; Prayudha et al. 2024), and carbon and biomass estimation from satellite data (Suardana et al. 2023). However, satellite-based methods face limitations in spatial resolution and temporal frequency, constraining their ability to provide detailed information at the scale of individual trees or small clusters. To address these limitations, advancements in remote sensing technologies such as unmanned aerial vehicles (UAVs) have enabled the collection of high-resolution imagery and data over targeted areas with greater efficiency and reduced cost (Jones et al. 2020; Tian et al. 2023; Yin et al. 2024). UAVs reduce the need for extensive ground surveys, minimizing risks and logistical challenges (Tamimi and Toth 2024), and provide access to areas difficult to survey on foot.

Among UAV-based technologies, Light Detection and Ranging (LiDAR) is particularly promising for mangrove monitoring. LiDAR employs laser pulses to measure distances between the sensor and objects on the Earth's surface, providing accurate and detailed data on forest structure[1]. The system calculates the time taken for the laser pulses to travel to the object and back, using this information to determine the distance with high precision. In mangrove forests, LiDAR can capture detailed images of canopy height, density, and tree distribution, which provide important information regarding the forest's health and composition (Wang et al. 2019; Yin and Wang 2019; Tian et al. 2023; Yin et al. 2024).

LiDAR technology has proven effective in various forest monitoring applications. For instance, studies that specifically utilize LiDAR for mangrove detection have been conducted by various researchers to observe, both to estimate the number of trees and tree height (Kasai et al. 2024; Yin et al. 2024) as well as to calculate mangrove biomass (Fatoyinbo et al. 2018; Qiu et al. 2019; Wang et al. 2019; Wang et al. 2022; Salum et al. 2020; Tian et al. 2021). However, the application of this technology still faces challenges in terms of accuracy and efficiency, particularly in areas with high vegetation density, where under-detection of trees occurs (Yin and Wang 2019).

The Seribu Islands, particularly Pramuka Island, serve as the focus of this study due to their characteristic mangrove plantations. The area consists primarily of a single species, *Rhizophora stylosa*, planted in clusters through community reforestation efforts[2]. This clustered planting results in high tree density, relatively short trees due to nutrient competition, and limited electromagnetic wave penetration, which complicates data acquisition and individual tree discrimination. These conditions provide a unique opportunity to evaluate and optimize the effectiveness of UAV-based LiDAR for individual tree detection in mangrove plantations.

Our research is expected to make a contribution to the conservation and sustainable management of mangrove forests by addressing the challenge of individual tree detection in dense mangrove plantations using UAV LiDAR data. Specifically, we investigate how the smoothing process and detection window size can affect the accuracy of individual tree detection in this challenging environment. By optimizing these parameters, we seek to enhance detection performance, providing more precise data on mangrove forest structure to support sustainability and environmental management.

MATERIALS AND METHODS

Study Area

The data was collected on Pramuka Island, a small island in the Seribu Islands, Indonesia (Fig. 1). The observed area covers approximately 0.6 ha (6,000 m^2), delineated using a rectangular boundary. It consists of a single mangrove species, *Rhizophora stylosa*, resulting from community planting efforts. The planting technique involved grouping seedlings in clusters, leading to a high-density stand of trees[3]. As a result, the trees are relatively short due to competition for nutrients. The density of the mangroves also causes low penetration of electromagnetic waves, resulting in limited information availability for ground data. Furthermore, the relatively homogeneous tree height across the plantation makes it difficult to discriminate between individual canopies. These circumstances are interesting to observe, as they provide an opportunity to test the effectiveness of the LiDAR sensor applied in the mangrove plantation community.

Data collection

Aerial imagery was acquired using the DJI M300 RTK UAV equipped with the Zenmuse L1 LiDAR sensor. The LiDAR sensor provides high-resolution point cloud data, which is crucial for accurately mapping and analyzing forest structures. The sensor is capable of a pulse repetition rate of up to 240,000 pulses per second, enabling high-density data recording. Additionally, the sensor integrates data with Global Navigation Satellite System (GNSS) and Inertial Measurement Unit (IMU) systems[4], providing very high georeferencing accuracy and resulting in highly detailed and accurate data. Table 1 presents the aircraft specifications and sensor used for the acquisition.

The data collection was conducted at 10:00 a.m. local time under clear sky conditions (minimal cloud cover) with a flying altitude of 80 meters. This acquisition process resulted in a total of 339,316 points, providing sufficient detail to capture the structural complexity of the mangrove canopy. Details of the flight settings are provided in Table 2.

Ground truth data were collected through a 10m^2 transect, encompassing measurements of tree density (including trees, saplings, and seedlings), diameter at breast height (DBH), average tree height, substrate type, and mangrove species composition. GPS was used solely to mark the transect location without recording the exact coordinates of individual trees. This limitation hindered the direct validation of LiDAR data. However, the ground truth data were utilized to estimate tree density and average height as a reference for evaluating the accuracy of individual tree detection (ITD) from the Canopy Height Model (CHM).

[1]Codex Y. (2023). Predicting Species Distributions using High-Resolution Remote Sensing Data: A Comprehensive Review and Assessment. Available at: https://codex.yubetsu.com/article/c004a755544b427a942af6ed2580f3f7 [Accessed 10 January 2025]
[2]Kementerian Lingkungan Hidup dan Kehutanan (KLHK) (2023). Penanaman mangrove dengan sistem rumpun berjarak di Kepulauan Seribu. Available at: https://itjen.menlhk.go.id/berita/penanaman-mangrove-dengan-sistem-rumpun-berjarak-di-kepulauan-seribu [Accessed 10 January 2025]
[3]Kementerian Lingkungan Hidup dan Kehutanan (KLHK) (2023). Penanaman mangrove dengan sistem rumpun berjarak di Kepulauan Seribu. Available at: https://itjen.menlhk.go.id/berita/penanaman-mangrove-dengan-sistem-rumpun-berjarak-di-kepulauan-seribu [Accessed 10 January 2025].
[4]DJI (2024). Zenmuse L1 specifications. Available at: https://enterprise.dji.com/zenmuse-l1/specs [Accessed: 6 August 2024].

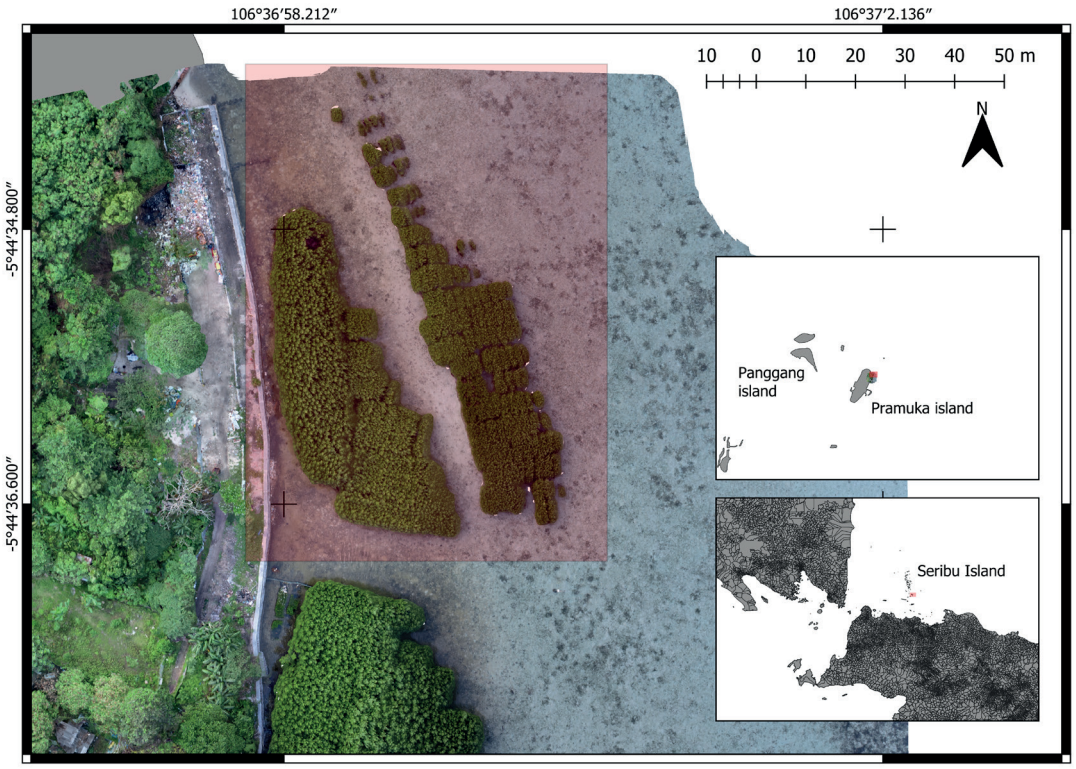

Fig. 1. The study site is located on Pramuka Island. The red box indicates the selected area for this study

Table 1. Aircraft and sensor specifications[1]

DJI M300 RTK (Aircraft)	DJI Zenmuse L1 (Camera)
RTK Positioning Accuracy RTK enabled and fixed: 1 cm + 1 ppm (horizontal) 1.5 cm + 1 ppm (vertical)	Point Rate Single return: 2,400,000 pts/s Multiple returns: 480,000 pts/s
Hovering Accuracy (P-mode with GPS) Vertical: ±0.1 m (Vision system enabled) ±0.5 m (GPS enabled) ±0.1 m (RTK enabled) Horizontal: ±0.3 m (Vision system enabled) ±1.5 m (GPS enabled) ±0.1 m (RTK enabled)	System Accuracy Horizontal: 10 cm @ 50 m Vertical: 5 cm @ 50 cm
Operating Frequency 2.4000 - 2.4835 GHz 5.725 - 5.850 GHz	Field of View (FOV) Repetitive line scan: 70.4° × 4.5° Non-repetitive line scan: 70.4° × 77.2°
Max Wind Resistance 12 m/s	Scan Modes Repetitive line scan mode Non-repetitive petal scan mode
GNSS GPS + GLONASS + BeiDou + Galileo	Maximum Return Supported: 3 Ranging Accuracy: 3 cm @ 100 m

Data pre-processing

Fig. 2 illustrates the entire process conducted in this study. The captured LiDAR data was initially processed using WebODM, an open-source photogrammetry and 3D reconstruction tool, to generate the 3D point cloud data (LAS file). Processing began with the lidR package (Roussel and Auty 2024) in an R environment[5].

The LAS file was first converted into a Digital Surface Model (DSM) using the Point-to-Raster (P2R) tool. This step involves transforming the LiDAR points into a 2D raster grid, where each cell (with a pixel size of 0.1 meter) represents the maximum elevation from the points within the cell. The resulting DSM captures the elevation, both terrain and all above-ground objects, such as vegetation and structures.

To generate a Digital Terrain Model (DTM) a more detailed workflow was applied. The original point cloud was then classified, separating bare earth from vegetation and other non-ground features. The ground-classified points were then interpolated using the Inverse Distance Weighting (IDW) method. This interpolation imparts more weight to nearby ground points, ensuring a smooth and accurate terrain surface (Mohan et al. 2021).

[5]R Core Team (2024). R: A language and environment for statistical computing. R Foundation for Statistical Computing, Vienna, Austria. Available at: https://www.R-project.org/. [Accessed: 10 August 2024]

Table 2. General flight setting

Parameters	Setting
Fly height	80 m
Drone speed (while recording)	8 m/s
Side overlap	50%

Following this, the CHM was produced by normalizing DSM with DTM, specifically by subtracting the DSM with DTM (Pertille et al. 2024). This process removes the ground elevation from the DSM, leaving only the height of vegetation or other objects above the ground. Once the basic data was prepared, the next step was to detect individual trees.

Individual tree detection

Filtering treatment

In tree detection using CHM data, the process typically involves an initial smoothing stage to reduce noise and minor irrelevant variations in the canopy height data. This reduction in noise results in more representative and accurate peak detection. Smoothing also clarifies treetops by diminishing minor variations, making the highest points that represent the treetops more prominent and distinct. Additionally, smoothing helps eliminate minor anomalies or outliers that may not be part of the tree structure, ensuring that irrelevant data does not disrupt peak detection (Pertille et al. 2024).

In this study, the Gaussian method was applied as a filtering treatment. The application of Gaussian filtering plays a crucial role in refining the CHM and improving the accuracy of individual tree detection. In this study, we tested a range of square-shaped kernel sizes, including unfiltered CHM and 3×3, 5×5, 9×9, 11×11, and 21×21 kernel sizes. These filters were used to smooth the CHM and remove noise while retaining critical information for detecting individual mangrove trees (Pertille et al. 2024).

Local maxima method and window size treatment

A relatively straightforward method for detecting individual trees on the LiDAR-derived CHM is the Local Maxima (LM) algorithm. The LM method assumes that local height maxima in the CHM represent treetops (Korpela 2006). This method is relatively simple and uses two main parameters: a smoothing parameter, often referred to as the smoothing window size (SWS), and a fixed window size (FWS) for tree detection (Silva et al. 2016). As the FWS increases, the number of detected trees decreases (Mohan et al. 2017). Applying smoothing filters helps eliminate invalid local maxima caused by significant, spreading tree branches, thereby reducing the number of detected local maxima and improving the algorithm's accuracy (Lindberg and Hollaus 2012).

In this study, we tested various combinations of CHM smoothing kernel sizes and LMF window sizes to evaluate their effect on individual tree detection performance. The smoothing kernel sizes included unfiltered, 3×3, 5×5, 9×9, 11×11, and 21×21, each applied with LMF window sizes of 0.5 m, 1 m, and 3 m.

F-score calculation

To evaluate the accuracy of individual tree detection, this study employed the F-score (F1) as a performance metric. The F-score is the harmonic mean of precision and recall, which balances the trade-off between detecting true positives (TP) while minimizing false positives (FP) and false negatives (FN) (Power 2011). This metric has also been widely adopted in similar studies related to UAV-based tree detection (Mohan et al. 2017; Ahmadi et al. 2022)

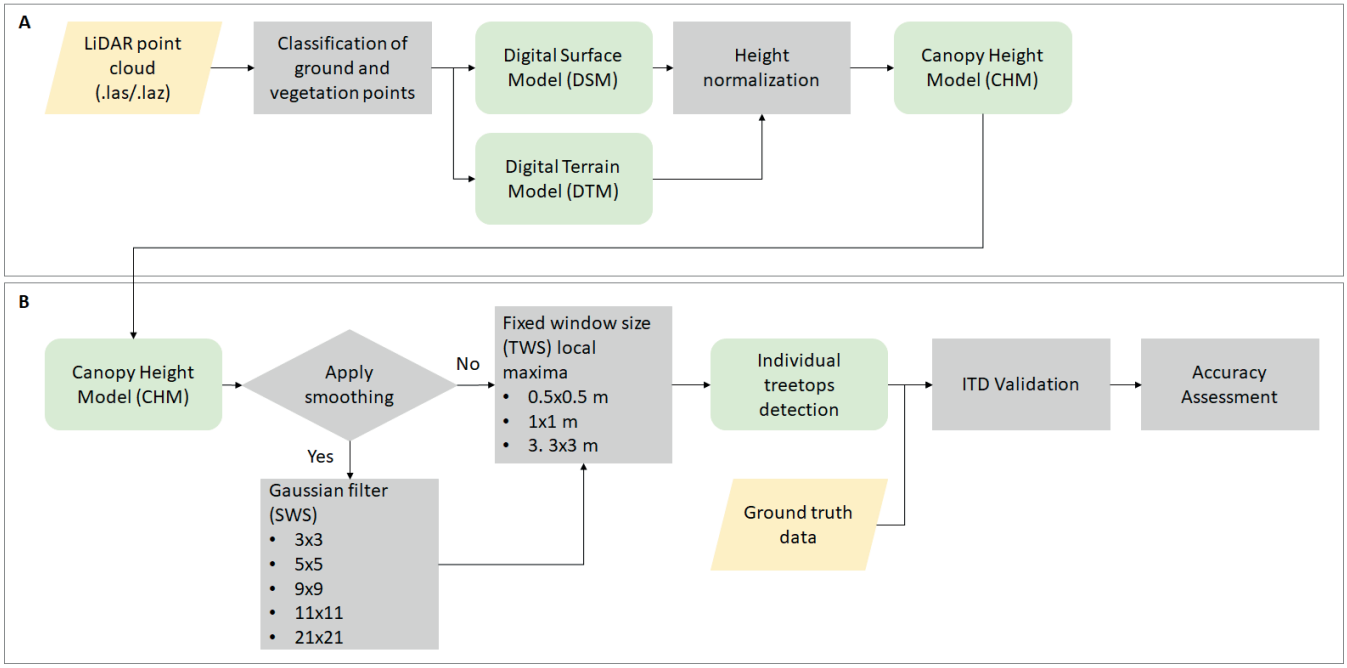

Fig. 2. Workflow of LiDAR data pre-processing and local-maxima-based individual tree detection (ITD) methodology. (A) LiDAR data pre-processing steps include filtering, normalization, point classification, noise removal, and data fusion to prepare the data for analysis. (B) Local-maxima-based individual tree detection involves the generation of the Canopy Height Model (CHM), followed by the detection of local maxima to identify tree tops and subsequent clustering to delineate individual trees

Given that UAV-based tree detection can result in both overestimation (FP > 0) and underestimation (FN < 0), this metric provides a comprehensive measure of detection effectiveness. The precision (P), recall (R), and F-score (F1) were calculated using the following Eqs. 1-3 (Power 2011):

$$Precision = \frac{TP}{TP + FP} \quad (1)$$

$$Recall = \frac{TP}{TP + FN} \quad (2)$$

$$F1 - score = 2x \frac{Precision \times Recall}{Precision + Recall} \quad (3)$$

True positives (TP) represent the number of trees detected by the UAV that match the expected tree count in the field. False negatives (FN) refer to trees that were present in the field but were not detected by the UAV. On the other hand, false positives (FP) indicate trees that were counted by the UAV but do not correspond to trees in the field. These definitions help evaluate the accuracy of the UAV-based tree detection system by assessing how well the detected trees align with the actual tree count in the field. Since ground-truth data on tree positions were unavailable, TP, FP, and FN were estimated based on the total number of trees recorded in the field rather than a tree-to-tree spatial validation. This is a clear limitation of the study, as the lack of spatial correspondence between UAV-detected trees and field-observed trees prevents the accurate matching of individual trees. As an alternative, TP, FP, and FN were approximated using total tree counts per plot. A detection was considered a true positive if it occurred within the plot area and the total number of UAV-detected trees did not exceed the field count. In underestimation cases (UAV count < field count), all detected trees were assumed to be true positives, and FP was set to zero. In contrast, if the UAV count exceeded the field count, the surplus detections were considered false positives. While this method does not allow spatially explicit matching between detected and actual trees, it does not replace precise spatial validation and should be interpreted accordingly.

RESULT

The UAV-acquired imagery was precisely cropped at the observation site to obtain more accurate and reliable data. This cropping process was designed to exclude non-target objects such as buildings, water bodies, or non-mangrove vegetation. By eliminating these elements, the precision of the CHM information was enhanced, resulting in cleaner data with minimal external interference. This process ensures that the analytical results have a high level of accuracy and are relatively free from errors, thereby improving the reliability of the data for this study. Fig. 3 shows the results of the 3D point cloud cropped specifically for the selected area.

CHM Normalization

The DSM showed elevation values ranging from 25.6 to 34.10 meters, capturing both ground and above-ground features such as vegetation and structures. In contrast, the DTM exhibited a narrower elevation range of 25.6 to 26.853 meters, indicating minimal elevation difference across the terrain. This relatively flat ground surface is consistent with typical mangrove habitats. However, in several areas, the DTM failed to fully represent the terrain due to limited ground returns. These gaps are not visually apparent in DTM figures but should be taken into account when interpreting the CHM result. Despite the limitation, the CHM was successfully generated by normalizing DSM with DTM (Gomroki et al. 2017), producing a height range from -0.24 to 7.59 meters. Fig. 4 illustrates the difference in height patterns before and after normalization.

Effects of Kernel and Window Size on Tree Detection Accuracy

The unfiltered CHM produced a noisy image with numerous local maxima that did not correspond to actual tree tops, primarily due to variations in the canopy structure, such as large branches or small gaps. This excessive noise compromised tree detection accuracy using the Local Maxima (LM) algorithm (Lisiewicz et al. 2022). In contrast, the 3×3 kernel applied a light smoothing filter, effectively reducing noise while preserving important canopy details. It eliminated minor irregularities and allowed for more accurate tree detection, especially in dense and uniform canopy structures. Visually, the CHM with a 3×3 kernel would show a more controlled and smoother image, with less color variation between areas, preserving the essential tree structures while softening the noise (Fig. 5).

As the kernel size increased to 5×5, 9×9, 11×11, 21×21, the CHM became progressively smoother. The 5×5 kernel removed additional noise and minor fluctuations, providing a balance between smoothing and preserving canopy details. However, larger kernel sizes like 9×9, 11×11, and 21×21 introduced excessive smoothing, which led to the merging of nearby treetops and a significant underestimation of the number of detected trees. The 21×21 kernel, in particular, overgeneralized the canopy, removing critical details about individual trees and rendering it unsuitable for dense mangrove forests (Tanhuanpaa et al. 2019; Quan et al. 2021).

Various combinations of kernel sizes (unfiltered, 3×3, 5×5, 9×9, 11×11, 21×21) and Local Maximum Filter (LMF) window sizes (0.5, 1, and 3 meters) were applied to analyze mangrove tree density (Fig. 6). The results indicate that smaller window sizes detect more trees due to their

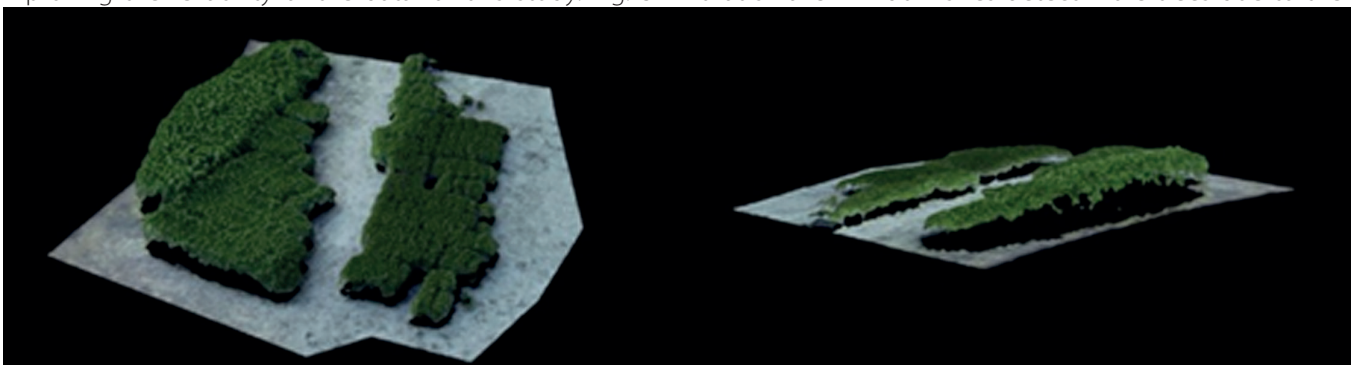

Fig. 3. 3D RGB LiDAR data of mangrove in Pramuka Island

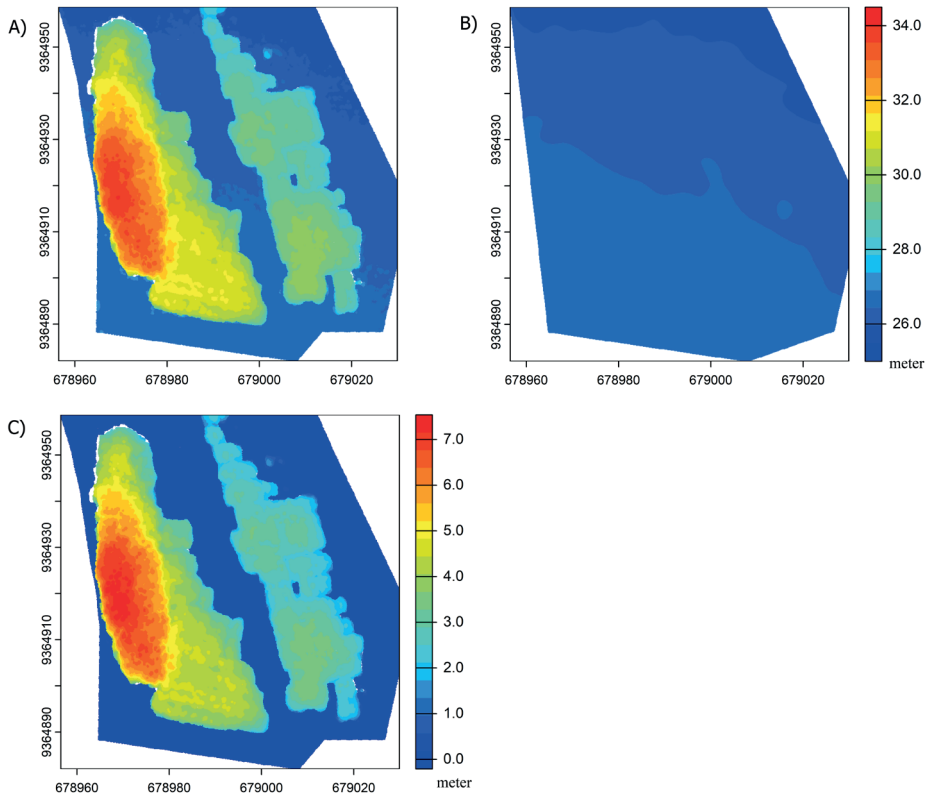

Fig. 4. Visualization of data at different stages: A) Digital Surface Model (DSM) before normalization; B) Digital Terrain Model (DTM); and C) Canopy Height Model (CHM) after normalization – in meter

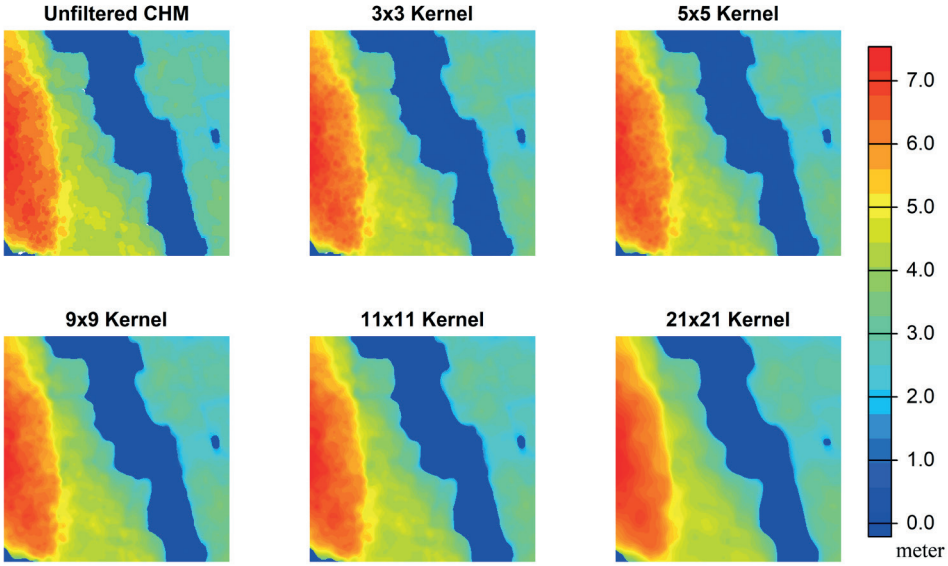

Fig. 5. Gaussian filtering for different pixel kernel – in meter

sensitivity to local variations. However, these findings may lead to overestimation in dense mangrove stands, where the algorithm may misidentify non-tree objects as treetops (Yan et al. 2024).

On the other hand, larger kernels and window sizes smooth out local variations, producing more refined estimates by reducing over-detection errors. While such practices may reduce the risk of excessive detection errors, using large kernels and window sizes can obscure important local details and lead to underestimating the number of trees (Balsi et al. 2018).

Given the limited field data obtained specifically from Pramuka Island, we attempted to broaden the scope of analysis by incorporating field data from several observation points on other islands within the Seribu Islands (Table 3). This approach is feasible due to the homogeneity of mangrove ecosystems across the Seribu Islands, where most of the mangroves are cultivated, predominantly consisting of *Rhizophora mucronata* and *Rhizophora stylosa*, and planted using a clustered spacing system[6]. This uniformity results in relatively similar structural patterns across the mangrove areas in the region.

The detection results show that using a window size of 0.5 meters, supported by kernels 3×3, 5×5, and 9×9, provides more accurate detection of mangroves, aligning with the average number of tree-phase mangroves found in the Seribu Islands (Fig. 7). This smaller window size is particularly effective in dense mangrove conditions, where

[6]Kementerian Lingkungan Hidup dan Kehutanan (KLHK) (2023). Penanaman mangrove dengan sistem rumpun berjarak di Kepulauan Seribu. Available at: https://itjen.menlhk.go.id/berita/penanaman-mangrove-dengan-sistem-rumpun-berjarak-di-kepulauan-seribu [Accessed 10 January 2025].

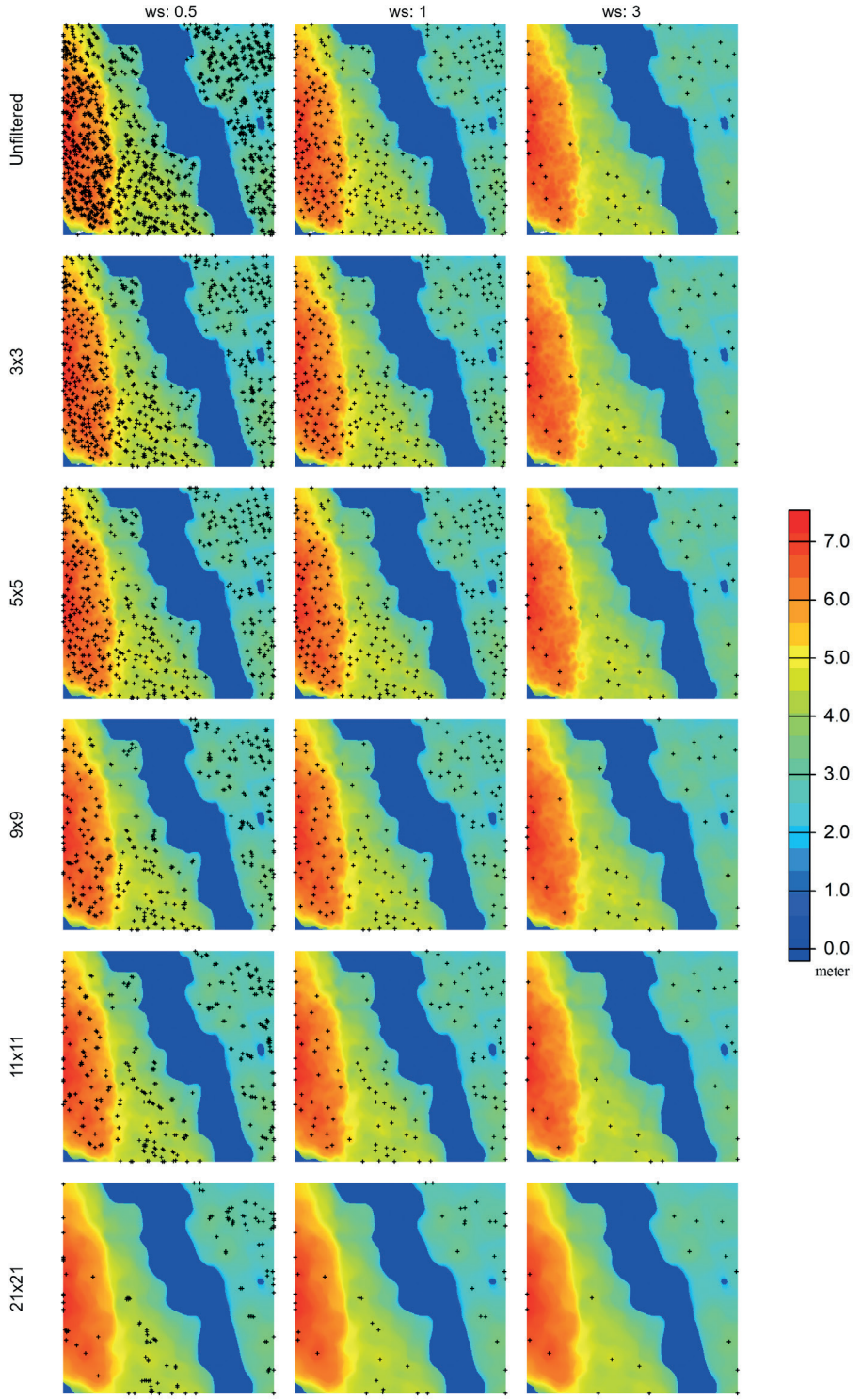

Fig. 6. Tree detection using the Local Maxima function with different window sizes for each kernel. In every kernel, a window size of 1 meter provides more detailed and numerous tree point information compared to larger window sizes (3 and 5 meters)

it can detect individual trees more accurately, especially in high-density areas (Kim et al., 2020). In contrast, using larger window sizes, such as 1 and 3 meters, tends to result in underestimates, except for the 1-meter window size combined with the 3×3 kernel, which aligns well with field data. Larger window sizes often lead to over smoothing, which hinders the detection of smaller or hidden trees beneath larger canopies (Balsi et al., 2018). Additionally, unfiltered data combined with a 0.5×0.5 meter window size leads to an overestimate, as unfiltered data does not distinguish well between mangrove trees and other objects, resulting in more trees being detected than are actually present. Despite these configurations yielding better results, all detection outcomes (except for the unfiltered configuration with kernel 0.5×0.5) are still underestimated compared to mangrove plots at specific locations on Pramuka Island. This highlights that LiDAR still struggles to distinguish individual mangrove trees with homogeneous heights, as this condition creates a bias where crowns overlap, making it difficult to clearly define the boundaries between individual trees (Galvincio & Popescu, 2016).

The analysis revealed that mangrove plots that had reached the tree growth stage—where tree-stage mangroves are the only ones detectable via drone imagery, unlike saplings and seedlings, which are often obscured by the tree canopy—contained between 19 and 63 individuals per 100 m^2. Additionally, the areas observed by drone

Table 3. Field Data of 10 mangrove plot points in the Seribu Islands, including substrate type, trees, saplings, and seedlings measurements

Plot Code	Lat (°)	Lon (°)	Substrate Type	Trees (ind./plot)	Saplings (ind./plot)	Seedlings (ind./plot)
Panggang 1	-5.74243	106.6041	Sandy mud	57	56	0
Panggang 2	-5.74196	106.6039	Sandy mud	21	96	4
Kelapa 1	-5.64895	106.5671	Sandy mud	0	390	0
Kelapa 2	-5.6568	106.5639	Sandy mud	25	216	0
Kelapa-Harapan	-5.65228	106.5743	Muddy sand	9	229	0
Harapan	-5.65379	106.5808	Muddy sand	9	243	0
Pari	-5.85288	106.6208	Sandy mud	43	4	10
Pramuka 1	-5.74391	106.6162	Sandy mud	63	65	2
Pramuka 2	-5.74527	106.615	Sandy mud	61	66	0
Pramuka 3	-5.74874	106.6116	Sandy mud	6	209	0

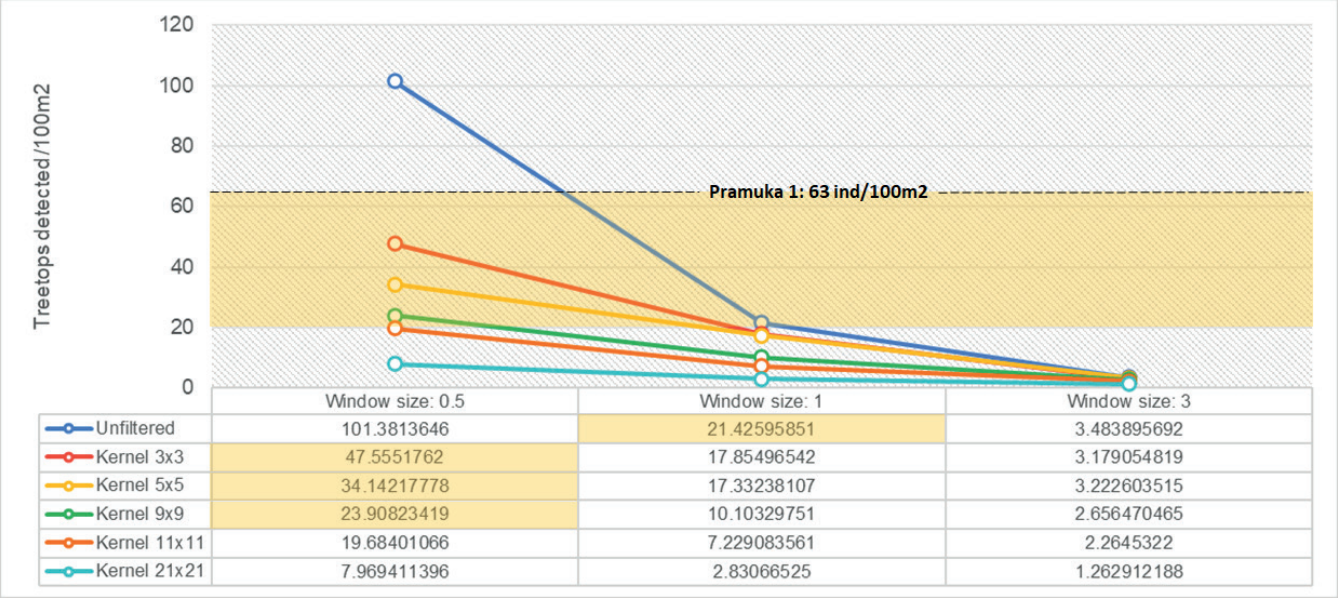

Fig. 7. Treetop Detection Density (ind./100m²) Across Different Kernel Sizes and Window Sizes Compared to Field Data (Pramuka 1: 63 ind/100m²)

specifically consisted of tree-stage mangroves, as this is the only stage where accurate observation and counting from aerial imagery are feasible, given the limitations of drone detection for saplings and seedlings (Hsu et al., 2020; Bakar et al., 2024).

Conversely, plots containing mangroves at the seedling stage exhibited much higher densities, with over 200 individuals per 100 m². This is due to the clustered spacing planting method[7], which supports mangrove growth up to the seedling stage.

Evaluation of F-score in UAV-based tree detection

This study applied various combinations of smoothing kernel sizes and local maxima filtering (LMF) window sizes to optimize individual tree detection from CHM (Table 4). The F-score was calculated for each combination to determine which method yielded the best balance between minimizing false positives (FP) and maximizing true positives (TP) while reducing false negatives (FN). A higher F-score indicates that the method correctly identifies trees and minimizes errors.

The highest F-score was achieved using the Kernel 3×3/WS 0.5 method (F1-score = 0.854), which provided the best trade-off between precision and recall. This method detected 47 of the 63 trees recorded in the field, resulting in a relatively high recall (0.746). This combination effectively minimized FN, making it the most balanced approach in the study. In contrast, methods with larger smoothing kernels and window sizes (e.g., Kernel 9×9/WS 3, Kernel 21×21/WS 3) had extremely low recall (0.031–0.047), leading to F-scores below 0.1. These methods failed to detect a significant portion of the trees due to excessive smoothing, which merged adjacent treetops and resulted in severe under detection.

DISCUSSION

This study aimed to detect and analyze individual mangrove trees using LiDAR-derived Canopy Height

[7]Kementerian Lingkungan Hidup dan Kehutanan (KLHK) (2023). Penanaman mangrove dengan sistem rumpun berjarak di Kepulauan Seribu. Available at: https://itjen.menlhk.go.id/berita/penanaman-mangrove-dengan-sistem-rumpun-berjarak-di-kepulauan-seribu [Accessed 10 January 2025].

Table 4. F1-score for all of the configuration

Method	UAV Count	TP	FP	FN	Precision	Recall	F1-Score
Kernel 3×3/WS 0.5	47	47	0	16	1	0.746	0.8545
Unfiltered/WS 0.5	101	63	38	0	0.6238	1	0.7683
Kernel 5×5/WS 0.5	34	34	0	29	1	0.54	0.701
Kernel 9x9/WS 0.5	23	23	0	40	1	0.365	0.5349
Unfiltered/WS 1	21	21	0	42	1	0.333	0.5
Kernel 11×11/WS 0.5	19	19	0	44	1	0.302	0.4634
Kernel 3×3/WS 1	17	17	0	46	1	0.27	0.425
Kernel 5×5/WS 1	17	17	0	46	1	0.27	0.425
Kernel 9×9/WS 1	10	10	0	53	1	0.159	0.2739
Kernel 11×11/WS 1	7	7	0	56	1	0.111	0.2
Kernel 21×21/WS 0.5	7	7	0	56	1	0.111	0.2
Unfiltered/WS 3	3	3	0	60	1	0.048	0.0909
Kernel 3×3/WS 3	3	3	0	60	1	0.048	0.0909
Kernel 5×5/WS 3	3	3	0	60	1	0.048	0.0909
Kernel 9×9/WS 3	2	2	0	61	1	0.032	0.0615
Kernel 11×11/WS 3	2	2	0	61	1	0.032	0.0615
Kernel 21×21/WS 1	2	2	0	61	1	0.032	0.0615
Kernel 21×21/WS 3	1	1	0	62	1	0.016	0.0313

Model (CHM) in a dense mangrove forest. The challenge of accurately extracting tree heights and positions in such complex environments is well-known due to structural variability and occlusions in the canopy. LiDAR data processing, including Digital Terrain Model (DTM) generation and smoothing of CHM data, plays a critical role in minimizing errors and improving tree detection accuracy.

One significant limitation encountered was the dense mangrove canopy, which likely obstructed the LiDAR sensor's ability to penetrate through to the ground, resulting in interpolation gaps and uneven terrain surfaces (Wannasiri et al. 2013; Balsi et al. 2018; Yin & Wang 2019; Li et al. 2023; Wijaya et al. 2023). This limited ground return coverage can affect the accuracy and reliability of the DTM, which in turn impacts the derived CHM and its interpretation. Although these interpolation gaps are not visually apparent in the DTM figures, they may lead to underestimation or spatial inconsistency in canopy height measurements. Future studies could consider integrating additional ground-based surveys or complementary remote sensing data to improve terrain representation in dense mangrove environments.

The unfiltered CHM's noise was mainly caused by structural variations in the canopy, such as large branches or small gaps, leading to numerous false local maxima and reduced tree detection accuracy with the Local Maxima algorithm (Lisiewicz et al. 2022). Applying a 3×3 Gaussian kernel offered light smoothing, which effectively reduced noise while preserving essential canopy features, thus improving detection in dense mangrove canopies.

Increasing kernel sizes progressively smoothed the CHM but introduced trade-offs. The 5×5 kernel balanced noise reduction and detail preservation, while larger kernels (9×9 and above) excessively smoothed the canopy, causing merging of adjacent treetops and underestimation of tree counts. The 21×21 kernel was particularly overgeneralizing, losing vital individual tree information and making it unsuitable for dense mangrove forests. This excessive smoothing reduces color and height variation, impairing the ability to distinguish individual trees in complex environments (Tanhuanpaa et al. 2019; Quan et al. 2021).

Choosing an appropriate kernel size is therefore critical to optimize the balance between noise suppression and canopy detail preservation in mangrove tree detection. These findings indicate a significant trade-off in selecting kernel and window sizes for optimal tree detection. Smaller LMF window sizes, while sensitive to minor variations, may not be appropriate in dense mangrove conditions, as they increase the likelihood of detecting false positives. Conversely, larger kernels and window sizes improve robustness against noise but risk underestimating true tree counts by merging individual tree signals and suppressing fine-scale canopy variation. While the 3×3 kernel and 0.5-meter window size yielded the best results in this study, this outcome should be interpreted with caution. The performance of these parameters is strongly influenced by the CHM pixel resolution (10 cm) and the relatively high density and structural uniformity of mangrove trees in the Seribu Islands. Parameter effectiveness may vary in different contexts, such as areas with lower tree density, heterogeneous canopy structures, or different CHM resolutions. Therefore, selecting kernel and window sizes should be context-specific, reflecting both the spatial resolution and vegetation characteristics of the study area.

Due to the lack of spatial ground-truth data containing exact tree positions, the F-score calculation in this study was based solely on the total number of detected trees rather than a one-to-one comparison of detected and actual trees. As a result, precision remained at 1.0 for all methods except Unfiltered/WS 0.5 since false positives (FP) were assumed to be zero in all underestimated cases. This means that every detected tree was considered correct despite the potential presence of undetected trees (false negatives, FN). Consequently, although precision appears perfect, recall remains significantly lower in most cases, leading to low F-scores for many methods. This highlights the limitations of relying solely on precision when evaluating detection performance in an underestimation scenario.

CONCLUSION

This study successfully demonstrated the potential of UAV LiDAR technology in monitoring mangrove forests. The optimum configuration, using a 3×3 kernel with a 0.5 meter window size, achieved the best balance between detection accuracy and noise reduction. These findings highlight that parameter tuning is critical to optimize detection performance, especially in complex and dense vegetation environments like mangroves. Despite its potential, LiDAR's limited ability to penetrate dense vegetation is a significant challenge. Thick foliage and branches obstruct the sensor's signal, making it difficult for the signal to reach the ground, which in turn limits the availability of accurate ground elevation. The selection of kernel and window sizes plays a key role in tree detection accuracy. Smaller window sizes tend to capture more trees by focusing on finer local details. However, smaller windows might lead to overcounting trees or misidentifying non-tree objects as treetops in areas with dense vegetation. On the other hand, using larger kernels and window sizes can reduce the level of detail and smooth the data, which may lead to a loss of local variations and a decrease in the accuracy of tree detection.

Future research should to refine measurement parameters to enhance tree detection in dense mangrove forests. It is also critical to develop more advanced algorithms that consider the specific conditions of the study area. By integrating LiDAR data with other monitoring methods, the overall quality and accuracy of the data can be improved, further supporting the conservation and management of mangrove forests.

REFERENCES

Ahmadi S. A., Ghorbanian A., Golparvar F., Mohammadzadeh A. and Jamali S. (2022). Individual tree detection from unmanned aerial vehicle (UAV) derived point cloud data in a mixed broadleaf forest using hierarchical graph approach. European Journal of Remote Sensing, 55(1), pp.520-539, DOI: 10.1080/22797254.2022.2129095

Bakar N.A.A., Jaafar W.S.W.M., Maulud K.N.A., Kamarulzaman A.M.M., Saad S.N.M., Mohan M. (2024). Monitoring mangrove-based blue carbon ecosystems using UAVs: a review. Geocarto International, 39:1, 2405123, DOI: 10.1080/10106049.2024.2405123.

Balsi M., Esposito S., Fallavollita P. and Nardinocchi C. (2018). Single-tree detection in high-density LiDAR data from UAV-based survey. European Journal of Remote Sensing, 51(1), pp.679-692, DOI: 10.1080/22797254.2018.1474722.

Carugati L., Gatto B., Rastelli E., Lo Martire M., Coral C., Greco S. and Danovaro R. (2018). Impact of mangrove forests degradation on biodiversity and ecosystem functioning. Scientific Reports, 8, 13298, DOI: 10.1038/s41598-018-31683-0.

Diniz C., Cortinhas L., Nerino G., Rodrigues J., Sadeck L., Adami M. and Souza-Filho P.W.M. (2019). Brazilian mangrove status: Three decades of satellite data analysis. Remote Sensing, 11(7), p.808, DOI: 10.3390/rs11070808

Fatoyinbo T., Feliciano E.A., Lagomasino D., Lee S.K. and Trettin C. (2018). Estimating mangrove aboveground biomass from airborne LiDAR data: a case study from the Zambezi River delta. Environmental Research Letters, 13(2), p.025012, DOI: 10.1088/1748-9326/aa9f03.

Galvincio J.D., and Popescu S.C. (2016). Measuring individual tree height and crown diameter for mangrove trees with airborne LiDAR data. International Journal of Advanced Engineering, Management & Science, 2(5), pp.431-443.

Giri C. (2021). Recent advancement in mangrove forests mapping and monitoring of the world using earth observation satellite data. Remote Sensing, 13(4), p.563, DOI: 10.3390/rs13040563.

Giri C., Long J., Abbas S., Murali R.M., Qamer F.M., Pengra B. and Thau D. (2015). Distribution and dynamics of mangrove forests of South Asia. Journal of Environmental Management, 148, pp.101-111, DOI: 10.1016/j.jenvman.2014.01.020.

Glotfelty J.E. (1999). Automatic selection of optimal window size and shape for texture analysis. West Virginia University.

Gomroki M., Jafari M., Sadeghian, S. and Azizi Z. (2017). Application of intelligent interpolation methods for DTM generation of forest areas based on LiDAR data. PFG–Journal of Photogrammetry, Remote Sensing and Geoinformation Science, 85, pp.227-241, DOI: 10.1007/s41064-017-0025-0.

Green E.P., Clark C.D., Mumby P.J., Edwards A.J. and Ellis A.C. (1998). Remote sensing techniques for mangrove mapping. International journal of remote sensing, 19(5), pp.935-956, DOI: 10.1080/014311698215801.

Gupta K., Mukhopadhyay A., Giri S., Chanda A., Majumdar S.D., Samanta S., Mitra D., Samal R.N., Pattnaik A.K. and Hazra S., 2018. An index for discrimination of mangroves from non-mangroves using LANDSAT 8 OLI imagery. MethodsX, 5, pp.1129-1139, DOI: 10.1016/j.mex.2018.09.011

Himes-Cornell A., Pendleton L. and Atiyah P. (2018). Valuing ecosystem services from blue forests: A systematic review of the valuation of salt marshes, sea grass beds and mangrove forests. Ecosystem Services, 30, pp.36-48, DOI: 10.1016/j.ecoser.2018.01.006.

Hsu A.J., Kumagai J., Favoretto F., Dorian J., Martinez B.G., Aburto-Oropeza O. (2020). Driven by drones: Improving mangrove extent maps using high-resolution remote sensing. Remote Sensing, 12(23), p.3986, DOI: 10.3390/rs12233986.

Jones A.R., Raja Segaran R., Clarke K.D., Waycott M., Goh W.S. and Gillanders B.M. (2020). Estimating mangrove tree biomass and carbon content: a comparison of forest inventory techniques and drone imagery. Frontiers in Marine Science, 6, p.784, DOI: 10.3389/fmars.2019.00784.

Kasai K., Yanagisawa H. and Goto K. (2024). Quantification of the spatial distribution of individual mangrove tree species derived from LiDAR point clouds. Progress in Earth and Planetary Science, 11(1), p.2, DOI: 10.1186/s40645-024-00626-x.

Kim J., Popescu S.C., Lopez R.R., Ben Wu X., Silvy N.J. (2020). Vegetation mapping of No Name Key, Florida using lidar and multispectral remote sensing. International Journal of Remote Sensing, 41(24), pp.9469-9506, DOI: 10.1080/01431161.2020.1800125.

Korpela I. (2006). Geometrically accurate time series of archived aerial images and airborne lidar data in a forest environment. Silva Fennica, 40(1), p.109, DOI: 10.14214/sf.355.

Lassalle G., Ferreira M.P., La Rosa L.E.C., Scafutto R.D.P.M. and de Souza Filho C.R. (2023). Advances in multi-and hyperspectral remote sensing of mangrove species: A synthesis and study case on airborne and multisource spaceborne imagery. ISPRS Journal of Photogrammetry and Remote Sensing, 195, pp.298-312, DOI: 10.1016/j.isprsjprs.2022.12.003.

Li Q., Wong F.K.K., Fung T., Brown L.A. and Dash J. (2023). Assessment of active LiDAR data and passive optical imagery for double-layered mangrove leaf area index estimation: a case study in Mai Po, Hong Kong. Remote Sensing, 15(10), p.2551, DOI: 10.3390/rs15102551.

Lindberg E. and Hollaus M. (2012). Comparison of methods for estimation of stem volume, stem number and basal area from airborne laser scanning data in a hemi-boreal forest. Remote Sensing, 4(4), pp.1004-1023, DOI: 10.3390/rs4041004.

Lisiewicz M., Kamin´ska A. and Steren´czak K. (2022). Recognition of specified errors of Individual Tree Detection methods based on Canopy Height Model. Remote Sensing Applications: Society and Environment, 25, p.100690, DOI: 10.1016/j.rsase.2021.100690.

Mohan M., Silva C.A., Klauberg C., Jat P., Catts G., Cardil A., Hudak A.T. and Dia M. (2017). Individual tree detection from unmanned aerial vehicle (UAV) derived canopy height model in an open canopy mixed conifer forest. Forests, 8(9), p.340, DOI: 10.3390/f8090340.

Mohan M., Leite R.V., Broadbent E.N., Wan Mohd Jaafar W.S., Srinivasan S., Bajaj S., Dalla Corte A.P., do Amaral C.H., Gopan G., Saad S.N.M. and Muhmad Kamarulzaman A.M. (2021). Individual tree detection using UAV-lidar and UAV-SfM data: A tutorial for beginners. Open Geosciences, 13(1), pp.1028-1039, DOI: 10.1515/geo-2020-0290.

Mumby P.J., Edwards A.J., Ernesto Arias-Gonz´alez J., Lindeman K.C., Blackwell P.G., Gall A., Gorczynska M.I., Harborne A.R., Pescod C.L., Renken H. and Wabnitz, C.C. (2004). Mangroves enhance the biomass of coral reef fish communities in the Caribbean. Nature, 427(6974), pp.533-536, DOI: 10.1038/nature02286.

Pertille C.T., Gomes K.M.A., Veras H.F.P., Mohan M., Sanquetta C.R., Behling A. and Dalla Corte A.P. (2024). Effects of flight and smoothing parameters of number of trees with aerial imagery in a native Brazilian atlantic forest remnant. CERNE, 30(1), DOI: 10.1590/01047760202330013338.

Powers D.M. (2011). Evaluation: from precision, recall and F-measure to ROC, informedness, markedness and correlation.

Prayudha B., Ulumuddin Y.I., Siregar V., Agus S.B., Prasetyo L.B., Avianto P. and Ramadhani M.R. (2024). Enhanced mangrove index: A spectral index for discrimination understorey, nypa, and mangrove trees. MethodsX, 12, p.102778, DOI: 10.1016/j.mex.2024.102778.

Qiu P., Wang D., Zou X., Yang X., Xie G., Xu S. and Zhong Z. (2019). Finer resolution estimation and mapping of mangrove biomass using UAV LiDAR and worldview-2 data. Forests, 10(10), p.871, DOI: 10.3390/f10100871.

Quan Y., Li M. and Wang B. (2021). Comparison and evaluation of different pit-filling methods for generating high-resolution canopy height model using UAV laser scanning data. Remote Sensing, 13, p.2239, DOI: 10.3390/rs13122239.

Rajpar M.N. and Zakaria M. (2014). Mangrove fauna of Asia. In: Mangrove ecosystems of Asia: Status, challenges and management strategies, pp.153-197, DOI: 10.1007/978-1-4614-8582-7 8.

Roussel J.R., Auty D., Coops N.C., Tompalski P., Goodbody T.R., Meador A.S., Bourdon J.F., De Boissieu F. and Achim A. (2020). lidR: An R package for analysis of Airborne Laser Scanning (ALS) data. Remote Sensing of Environment, 251, p.112061, DOI: 10.1016/j.rse.2020.112061.

Sahu S.C., Suresh H.S., Murthy I.K. and Ravindranath N.H. (2015). Mangrove area assessment in India: Implications of loss of mangroves. J. Earth Sci. Clim. Change, 6(5), p.280, DOI: 10.4172/2157-7617.1000280.

Saini O., Bhardwaj A. and Chatterjee R.S. (2020), November. The Potential of L-Band UAVSAR Data for the Extraction of Mangrove Land Cover Using Entropy and Anisotropy Based Classification. In Proceedings, 46(1), p.21, DOI: 10.3390/ecea-5-06673.

Salum R.B., Souza-Filho P.W.M., Simard M., Silva C.A., Fernandes M.E., Cougo M.F., do Nascimento Junior W. and Rogers K. (2020). Improving mangrove above-ground biomass estimates using LiDAR. Estuarine, Coastal and Shelf Science, 236, p.106585, DOI: 10.1016/j.ecss.2020.106585.

Sharifi A., Felegari S. and Tariq A. (2022). Mangrove forests mapping using Sentinel-1 and Sentinel-2 satellite images. Arabian Journal of Geosciences, 15(20), p.1593, DOI: 10.1007/s12517-022-10867-z.

Silva C.A., Hudak A.T., Vierling L.A., Loudermilk E.L., O'Brien J.J., Hiers J.K., Jack S.B., Gonzalez-Benecke C., Lee H., Falkowski M.J. and Khosravipour A. (2016). Imputation of individual longleaf pine (Pinus palustris Mill.) tree attributes from field and LiDAR data. Canadian Journal of Remote Sensing, 42(5), pp.554-573, DOI: 10.1080/07038992.2016.1196582.

Suardana A.M.A.P., Anggraini N., Nandika M.R., Aziz K., As-Syakur A.R., Ulfa A., Wijaya A.D., Prasetio W., Winarso G. and Dewanti R. (2023). Estimation and mapping above-ground mangrove carbon stock using sentinel-2 data derived vegetation indices in Benoa Bay of Bali Province, Indonesia. Forest and Society, 7(1), pp.116-134, DOI: 10.24259/fs.v7i1.22062.

Tamimi R. and Toth C. (2024). Accuracy Assessment of UAV LiDAR Compared to Traditional Total Station for Geospatial Data Collection in Land Surveying Contexts. The International Archives of the Photogrammetry, Remote Sensing and Spatial Information Sciences, 48, pp.421-426, DOI: 10.5194/isprs-archives-XLVIII-2-2024- 421-2024, 2024.

Tanhuanpaa T., Yu X., Luoma V., Saarinen N., Raisio J., Hyyppa J., Kumpula T. and Holopainen M. (2019). Effect of canopy structure on the performance of tree mapping methods in urban parks. Urban Forestry & Urban Greening, 44, p.126441, DOI: 10.1016/j.ufug.2019.126441.

Tian Y., Huang H., Zhou G., Zhang Q., Tao J., Zhang Y. and Lin J. (2021). Aboveground mangrove biomass estimation in Beibu Gulf using machine learning and UAV remote sensing. Science of the Total Environment, 781, p.146816, DOI: 10.1016/j.scitotenv.2021.146816.

Tian Y., Huang H., Zhou G., Zhang Q., Xie X., Ou J., Zhang Y., Tao J. and Lin J. (2023). Mangrove biodiversity assessment using UAV LiDAR and hyperspectral data in China's Pinglu canal estuary. Remote Sensing, 15(10), p.2622, DOI: 10.3390/rs15102622.

Tran T.V., Reef R. and Zhu X. (2022). A review of spectral indices for mangrove remote sensing. Remote Sensing, 14(19), p.4868, DOI: 10.3390/rs14194868.

Wannasiri W., Nagai M., Honda K., Santitamnont P. and Miphokasap P. (2013). Extraction of mangrove biophysical parameters using airborne LiDAR. Remote Sensing, 5(4), pp.1787-1808. DOI: 10.3390/rs5041787.

Wang D., Wan B., Qiu P., Zuo Z., Wang R. and Wu X. (2019). Mapping height and aboveground biomass of mangrove forests on Hainan Island using UAV-LiDAR sampling. Remote Sensing, 11(18), p.2156, DOI: 10.3390/rs11182156.

Wang D., Wan B., Qiu P., Tan X. and Zhang Q. (2022). Mapping mangrove species using combined UAV-LiDAR and Sentinel-2 data: Feature selection and point density effects. Advances in Space Research, 69(3), pp.1494-1512, DOI: 10.1016/j.asr.2021.11.020.

Wijaya M.S., Kamal M., Widayani P. and Arjasakusuma S. (2023). Classification of Mangrove Vegetation Structure using Airborne LiDAR in Ratai Bay, Lampung Province, Indonesia. Geoplanning: Journal of Geomatics and Planning, 10(2), pp.123-134, DOI: 10.14710/geoplanning.10.2.123-134.

Yan Y., Lei J., Jin J., Shi S. and Huang Y. (2024). Unmanned Aerial Vehicle Light Detection and Ranging-Based Individual Tree Segmentation. Eucalyptus spp. Forests: Performance and Sensitivity. Forests, 15(1), p.209, DOI: 10.3390/f15010209.

Yin D. and Wang L. (2019). Individual mangrove tree measurement using UAV-based LiDAR data: Possibilities and challenges. Remote Sensing of Environment, 223, pp.34-49, DOI: 10.1016/j.rse.2018.12.034.

Yin D., Wang L., Lu Y. and Shi C. (2024). Mangrove tree height growth monitoring from multi-temporal UAV-LiDAR. Remote Sensing of Environment, 303, p.114002, DOI: 10.1016/j.rse.2024.114002.

RESEARCH PAPER

KARST LANDFORMS OF THE SINYAYA RIVER VALLEY, PRILENSKOE PLATEAU

Nikolai V. Torgovkin[1*], Alexander I. Kizyakov[2], Anastasia A. Gavrilova[3], Julustan E. Sivtsev[1,2], Sebastian F.M. Breitenbach[4]

[1]Melnikov Permafrost Institute SB RAS, Laboratory of General Geocryology, Yakutsk, 677010, Russia
[2]Lomonosov Moscow State University, Cryolithology and Glaciology Department, Faculty of Geography, Moscow, 119991, Russia
[3]Institute of Precambrian Geology and Geochronology RAS, St.-Petersburg, 199034, Russia
4Department of Geography and Environmental Sciences, Northumbria University, Newcastle upon Tyne, NE77XA, UK
***Corresponding author:** TorgovkinNV@mpi.ysn.ru
Received: March 25th 2025 / Accepted: July 21st 2025 / Published: October 1st 2025
https://doi.org/10.24057/2071-9388-2025-3966

ABSTRACT. Unique karst evolution in Siberia is attributed to climatic factors and the presence of permafrost. Climatic fluctuations in Northern Eurasia had occurred during the Quaternary period and significantly influenced the processes of permafrost aggradation and degradation, as well as the karst activity. Despite their wide popularity and impressive manifestations, the karst landforms on the Prilenskoe Plateau still remain tenuously studied in terms of landform classification and obtaining their morphometric characteristics. The article presents the results of field studies of karst terrain in the Sinyaya River valley in Central Yakutia. Based on field observations and the analysis of the generated digital surface models, we have determined the median relative heights of different types of karst ridges in the Sinyaya River valley: "incipient ridges" - 34 m, "young ridges" - 42 m, "mature ridges" - 79 m and "old ridges" - 58 m. Most ridges that exceed 100 m are "mature and old". The highest ridges are located on the concave parts of river meanders and belong to the type of "mature ridges". In addition, our observations in the Sinyaya River valley have shown "old ridges" are the most common, accounting for over 58% of the overall ridge length. "Mature ridges" make up approximately 25%, "young ridges" 13%, and "incipient" ridges only 4% of the total. This distribution reflects the long history of topographic development in the valley and the significant influence of erosion processes on these features. The most prominent forms of this landscape include karst ridges, which present as rock pillars formed through physical and chemical weathering, with very active frost shattering, gravitational, and erosion processes. Using field surveys conducted with unmanned aerial vehicles (UAVs) and subsequent processing in a geographic information system (GIS), it was determined that the highest ridges are located in the lower reaches of the Sinyaya River, where it cuts through the axial, most elevated part of the Prilenskoe Plateau. The morphometric characteristics of the identified types of karst ridges and their spatial change along the river meanders are associated mainly with the activity of lateral river erosion, which ensures the removal of weathering material and slope deposits.

KEYWORDS: karst landforms, Siberia, Sinsky Pillars, Prilenskoe Plateau, karst ridges, weathering

CITATION: Torgovkin N. V., Kizyakov A. I., Gavrilova A. A., Sivtsev J. E., Breitenbach S. F. M. (2025). Karst Landforms Of The Sinyaya River Valley, Prilenskoe Plateau. Geography, Environment, Sustainability, 3 (18), 99-106
https://doi.org/10.24057/2071-9388-2025-3966

ACKNOWLEDGEMENTS: This research was supported by the Grant of the Republic of Sakha (Yakutia) for young scientists, specialists, and students, MPI SB RAS Project № 122011800064-9, and MSU Project № 121051100164-0.

Conflict of interests: The authors reported no potential conflict of interests.

INTRODUCTION

Modern karst study is conducted in a wide range of disciplines, including both the study of karst landform entanglement with lithology and tectonics and a set of environmental problems associated with karst development, land and soil degradation, changes in vegetation cover, and connections with water supply (Gillieson et al. 2022; Zhang et al. 2022; Saroli et al. 2022). Researchers use new methods to study karst topography, such as unmanned aerial vehicle (UAV) surveys for constructing digital elevation models and obtaining detailed karst landform characteristics (Silva et al. 2017; Doumit and Ghanem 2021; Kim and Hong 2024). The studies are mainly devoted to the tropical and subtropical karst or karst landforms in temperate climate. There is a lack of modern publications on karst in permafrost.

Sinsky Pillars within the Prilenskoe Plateau were inscribed on the List of UNESCO World Heritage[1] in 2016 as a part of National Park Lena Pillars. In the middle and lower reaches of the Sinyaya River, various karst forms are present, including high pillars (Fig. 1a). Karst ridges are confined to both sides of the meandering river (Fig. 1b, c). Sinsk Pillars are not directly related to the SDGs (Sustainable

[1]UNESCO World Heritage Convention (2012), https://whc.unesco.org/en/list/1299/documents/

Development Goals)[2] themselves. However, their significance as a UNESCO World Heritage Site, particularly for their geological and paleontological value, indirectly contributes to several SDGs, especially those related to environmental sustainability and knowledge, Sinsk Pillars connect to the SDGs. SDG 15 Life on Land serves as a prime example of geological formations and ecosystems that deserve protection and preservation. They showcase the planet's history and contribute to biodiversity conservation. SDG 13 Climate Action. The study of the Sinsk Pillars can offer new perspectives on past climate changes and the long-term impacts of environmental processes, aiding in understanding and mitigating current climate challenges. SDG 4 Quality Education - National Park Lena Pillars offers opportunities for educational and research initiatives, raising awareness about the importance of natural heritage and promoting scientific understanding. SDG 11 Sustainable Cities and Communities - National Park Lena Pillars supports ecotourism and sustainable development in local communities, providing economic opportunities while preserving the environment. SDG 17 Partnerships for the Goals - National Park Lena Pillars' inclusion on the UNESCO World Heritage List demonstrates the international collaboration needed to safeguard natural sites and promote sustainable practices (UN SDGs).

STUDY AREA

The distinctive characteristics of the Prilenskoe Plateau karst are attributable to its formation under permafrost conditions, with a thickness reaching up to 500 m (The Foundation… 2011). According to S.S. Korzhuev (1961), permafrost does not stop karst but only slows it down, and water moves freely in strongly fractured limestones and dolomites. In the middle reaches of the Lena River between the mouth of the Vitim River and the town of Pokrovsk, S.S. Korzhuev (1961) identified underground and surface forms of karst: 1) sinkholes, saucers, and baths; 2) caves, niches, canopies, and corridors; 3) disappearing streams and karst springs; 4) karst lakes; 5) ditches of slope subsidence; 6) spots of limestone scaling; 7) clay karst.

In Prilenskoe Plateau, the karst is developed in the Lower Cambrian limestones and dolomites 400-500 m thick (State geologic… 2022), covered by Quaternary deposits in the valleys and on the interfluve area of the Lena, Buotama, and Sinyaya Rivers (Fig. 2a, b). During the Middle Pleistocene ~400 ka Prilenskoe Plateau has been uplifted 150–300 m above the regional base level of erosion (Tolstikhin and Spektor 2004; Lena Pillars… 2012).

The climate of the region is strongly continental; as reported by the Pokrovsk meteorological station, there has

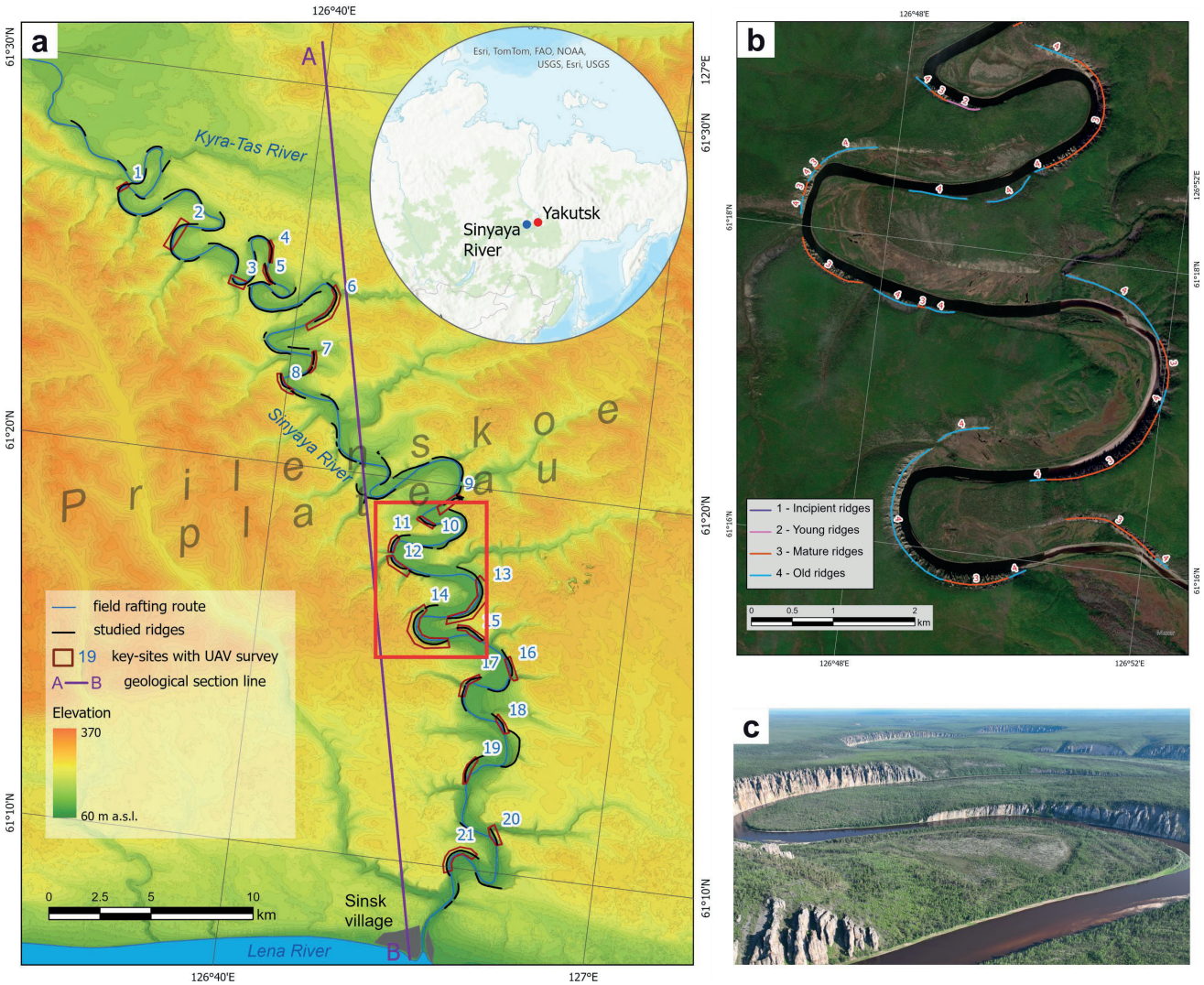

Fig. 1. Study area. a - the area of karst landform field studies in the Sinyaya River valley in 2023 and key sites with UAV surveys. ArcticDEM Mosaic (Porter, Claire et al., 2023) is used as elevation data, b - spatial distribution of ridges of various types along the Sinyaya River valley (a red rectangle on a). The map is based on ESRI Basemap World Imagery; c - areas of surface karst with ridge formation are confined to the areas of undercutting of the valley sides of the actively meandering Sinyaya River valley

[2]UN THE 17 GOALS, Sustainable Development, https://sdgs.un.org/goals

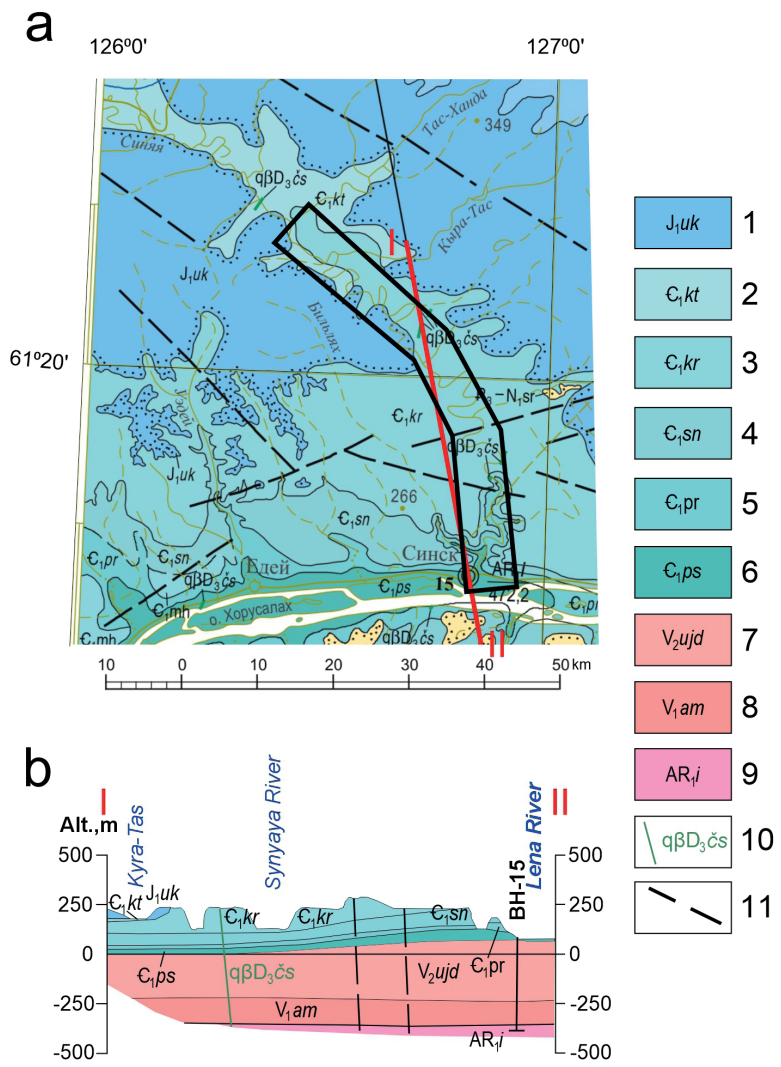

Fig. 2. Pre-Quaternary geology of the key site: a - fragment of the geological map scale 1:1 000 000; b - deposit cross-section. 1 Early Jurassic *Ukugut formation*; 2-6 Early Cambrian formations: *Keteme, Kutorgin, Sinsk, Perekhod, Pestrocvet*; 7-9 Precambrian formations: *Udoma, Amga, Iengra*; 10 Late Devonian diabase dykes; 11 Fault lines

been an increase in the average annual air temperature from -9.4 to -7.5°C between 2006 and 2023. The long-term average temperature of the coldest month, January, is -38.1°C, while the warmest month, July, has an average temperature of +19.2°C. The annual precipitation on average is 268 mm, with more than half of this amount falling during the warm season. The northern part of the Prilenskoe Plateau is distinguished by the presence of continuous permafrost, with a thickness of up to 400 m. In this region, the mean annual ground temperature is recorded to be -5°C. In contrast, the central part of the Prilenskoe Plateau exhibits a discontinuous permafrost, with a thickness ranging from 50 to 300 m. The mean annual ground temperature in this area varies from -1 to -4°C (Spektor et al. 2009).

For the Lena Pillars (and they are similar for Sinsky Pillars) M. Veress obtained 4 phases of development (Veress et al. 2014). Phase 1 – process of karstification occurred during a period of warmer climate conditions than are observed today, a time before the development of permafrost. Consequently, it was possible to form a karst water zone within the rock formation. The karst water level was situated close to the surface, with the karst surface exhibiting a height that was only marginally higher than the base level of erosion. The surface's altitude was therefore low, and the Lena had not yet undergone downcutting processes. Consequently, the development of caverns occurred in close proximity to the surface, with the formation of these caverns being driven by the presence of fractures. The process of karstification gave rise to a fracture-controlled phreatic network, which in turn gave rise to the formation of narrow, vertically developed corridor networks. These networks were characterized by the development of grikes on the surface, which were aligned perpendicular to the fracture systems. This resulted in the rock being dissected into clints, bordered by a grikes system. Phase 2 – the karst water table sank due to the uplift of the area. The deepening of the grikes resulted in the floors of some grikes reaching the caverns. The coalescence of the caverns and grikes occurred due to the caverns exceeding the water surface during this period. Consequently, the formation of giant grikes was initiated. The development of pinnacles from one part of the clints occurred during the dissolution of grike walls. Phase 3 – grikes were filled and buried. Phase 4 – the Lena River underwent a period of development, resulting in the destruction of some grikes and clints due to its downcutting activity. This process exposed the feature assemblage, leading to the partial destruction of the filling sediment in the remaining grikes. The walls of the exposed grikes exhibited potential for widening through frost weathering. The development of newer pinnacles was observed, indicating a transformation in the rock features of the pillars and the remaining karstic features. These features underwent destruction or transformation due to frost weathering, mass movements, sheet wash, and gully erosion. This ongoing process is a contemporary phenomenon.

The karst landforms in the Sinyaya River valley are concentrated in the part where it crosses the Prilenskoe Plateau. Various surface and underground karst features are prevalent along the Sinyaya River valley, including funnels, ponors, karst lakes, karren, karst niches, canopies, caves, sinkholes, and karst remnants (Trofimova 2012). Morphological classification of karst landforms of Lena Pillars was performed by E.V. Trofimova (2012, 2013, 2017, and 2018). She identified 4 types of karst ridges, using a description of their morphological features without numerical characteristics, which could be collected only on the basis of processing a significant number of sites. E.V. Trofimova noted that a comprehensive geomorphological survey and mapping of morphometric characteristics of karst features is still lacking (Trofimova 2012). In our research, we decided to rely on the classification proposed by E.V. Trofimova, since this is currently the most relevant classification developed specifically for the study area. It should be noted that Veress et al. (2014) conducted a morphological classification but for individual karst landforms - rock pillars.

The objective of this research is to provide a comprehensive description of the karst features found in the Sinaya River Valley, which exhibit various stages of development. The specific tasks include: 1) acquiring quantitative morphometric data regarding karst ridges; 2) validating the distinctions among the types identified by E.V. Trofimova based on this data; 3) identifying patterns in the spatial distribution of the different ridge types; and 4) characterizing the array of processes that influence the topography in karst regions.

MATERIALS AND METHODS

In June 2023, field route observations were conducted on the lower section of the Sinyaya River that passes through the Prilenskoe Plateau. (Fig. 1a). During the rafting expedition on the river, field descriptions and mapping of karst formations were conducted, along with photo documentation with GPS tracking and the capture of key sites using a UAV. The total length of the route was 126 km. The field studies utilize the approaches related to the stages of relief formation (Davis, 1899) and morphometric analysis of the relief (Simonov 1998; Simonov 1999). A UAV survey was undertaken at 21 key sites without ground control points. We captured high-resolution images of karst features using the DJI Mavic 3 drone with a 20 mpx Hasselblad 4/3 CMOS camera. Vertical and perspective shooting modes were used. UAV survey data were processed using Agisoft PhotoScan software based on Structure-from-Motion (SfM) photogrammetry. This way, point-cloud models, 3D and digital surface models (DSMs) were created with a spatial resolution of 0.1–0.2 m for each key site. The relative accuracy of the adjustment of the created point clouds, as reported by Agisoft for all key sites, is as follows: the root mean square (RMS) for reprojection errors ranges from 0.1 to 0.13 m, while the maximum errors range from 0.3 to 0.4 m. These DSMs were used to analyzed morphometric characteristics, such as the relative heights of ridges and rock pillars. Measurements of relative heights of karst ridges and rock pillars in our study were carried out with an accuracy of 1 m, ensured by the accuracy of the created point clouds and DSMs. To extract the heights from DSMs, the standard ArcGIS Pro Profile tool was used.

Through analysis of field data, including information from UAV surveys, photographs, and field descriptions, as well as very-high-resolution satellite imagery from the ESRI basemap (World Imagery), areas of rock ridges along the Sinyaya River Valley have been identified. Additionally, the segmentation of karst features by age, morphometric, and morphological characteristics has been carried out (Fig. 1). To characterize the topography of the area along the Sinyaya River valley, we used ArcticDEM Mosaic data with a spatial resolution of 2 m (Porter, Claire, et al., 2023). Ridge heights for the non-drone surveyed areas were measured using the Profile tool module in QGIS software. Elevation differences from the top of the ridge to the bottom of the slope were extracted from the profiles. Statistical analyses were performed in R (Samsonov 2024). The *tidyverse* package was used to determine the spatial distribution of ridges along the river. The *ggplot2* package was used to construct the graphs.

RESULTS

Following the classification introduced by E.V. Trofimova (2013), two distinct groups of karst features have been identified: surface and underground features. Surface features encompass positive forms like ridges, individual rock remnants, and pinnacles, along with negative forms such as cracks, corridors, and sinkholes. On the other hand, underground features include canopies, niches, caves, and tunnels. According to E.V. Trofimova (2013, 2017), positive landforms such as ridges can be classified based on their age, morphometric, and morphological characteristics. These categories include "incipient", "young", "mature", and "old" ridges (Fig. 3). Table 1 (Appendix) provides photographs that depict the distinct features and differences between these identified ridge types.

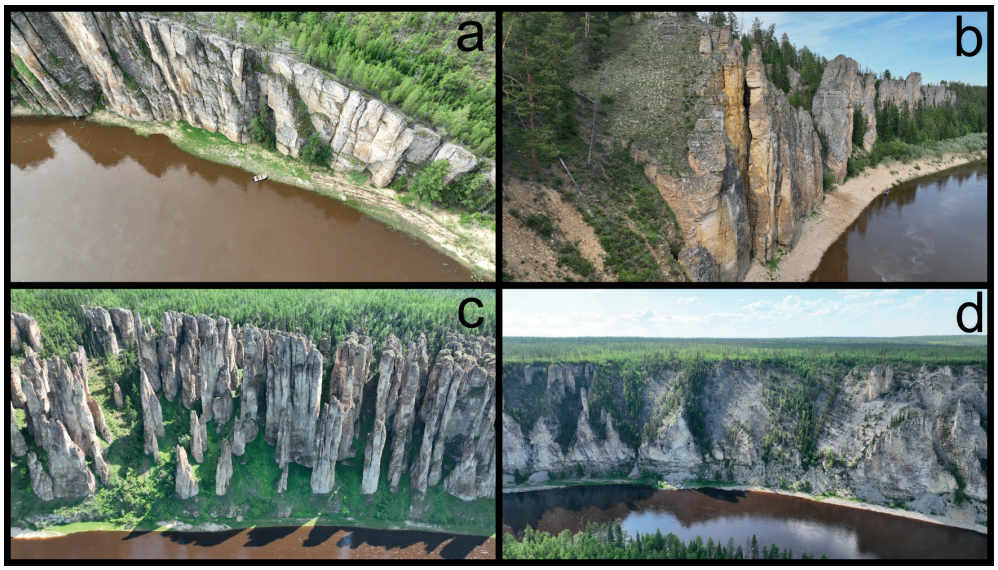

Fig. 3. Categories of ridges on the Sinyaya River Valley: a – incipient; b – young; c - mature; d – old

The "incipient ridges" are linear morphostructural elements that delineate the limestone cliffs. They are minimally cut by denudation and present nearly continuous cliffs with rare cracks. The altitude difference of "incipient ridges" between the summit and their base can reach 52 m with the rock's blocks from 15 to 28 m height. Primarily situated along the Sinyaya River banks, these ridges are located in places where the riverbed has arrived recently. "Incipient ridges" are directly cut by the river erosion, often resulting in the absence of a stable accumulative beach.

The "young ridges" are the next stage of the landform's transformation process due to denudation. These ridges mainly look like subvertical cliffs that are divided into blocks by cracks and erosion cuts. The height of" young ridges" can reach 113 m above the water, and the height of rock pillars can be up to 60 m. As well as "incipient", the "young ridges" are also located along the river bank.

"Mature ridges" mark the stage of significant separation of the limestone massif by karst and other denudation processes, which leads to the formation of a series of rock remnants. "Mature ridges" represent the most impressive positive karst landforms, including pronounced groups of banshee-shaped pinnacle pillars of various morphologies as needle-shaped, cylindrical, cone-shaped. They can be either standing alone or merged in the base, forming peculiar brushes or short ridges. Even within the same area, pinnacles differ in both morphology and height. In the studied areas, the relative heights of the pillars vary widely, from 20 to 124 m (the maximum heights of the "mature ridges" pillars are discovered within the key-site № 11).

For "old ridges", a characteristic feature is the presence of remnants or single pillars on the slopes, surrounded by a debris cover. "Old ridges" can be found either at a distance from the current position of the riverbed, such as on the periphery of meanders, or in areas where lateral erosion is not active now. Initially, "incipient ridges" are aligned along the meandering riverbed. Due to karst, slope, and erosion processes, these ridges divide into blocks that form short transverse micro-ridges perpendicular to the riverbed. Such a series of linear, elongated, halted ridges without mutual orientation can often be found within "old ridges" with an uphill gradient of up to 30-35°. Remnants can be represented by low cones and pillars. The relative height of pillars above the surface of the slopes, varies mainly depending on the age of the ridges, ranging from a few up to 92 m (the highest pillars of "old ridges" are discovered within the key-site № 14). It should be noted that local "rejuvenation" of ridges can occur in areas where the riverbed, as a result of meandering, begins to erode the base of an "old ridge" intensively, leading to the removal of the debris cover and the formation of a subvertical cliff of limestone at the base of the slope directly near the river.

In addition to the selected types of ridges, there are also intermediate states. Often, within the same extensive ridge, transitions between these selected types are observed, as well as alternating fragments. Several intermediate stages between "mature" and "old" ridges cover areas with varying degrees of erosion of limestone massif, their relative elevation above the surface of the slopes, and the proportion of areas of rock remnants compared to the debris covered slopes around them.

The median height for "mature ridges" is 79 m (the maximum is 134 m), and for "old ridges" - 58 m and 125 m, respectively. If for "mature ridges" these values characterize, among other things, the height of steep cliffs and pillars (which sometimes approach the full height of the ridge), then for "old ridges" this is the difference in height from the foot of the slopes (often covered with clastic material) to bedrock outcrops in the upper parts of the valley slopes. The heights of rock pillars within the "old ridges" are much lower and range from a few meters to a few tens of meters (Appendix).

"Incipient" and "young ridges" are lower than the other two types, which is reflected both in the maximum values (86 m and 104 m) and in fairly similar median heights (34 m and 42 m for "incipient" and "young ridges", respectively).

The "incipient ridges" are mainly localized in the middle part and the beginning of the second half of the observed part of the Sinaya River valley (Appendix), which corresponds to the most elevated part of the Prilenskoe Plateau. In this part, the river is intensively meandering, and along the bends, a long section of karst ridges is formed, which, according to morphological and morphometric characteristics, are segmented into several types. "Incipient ridges" with steep, weakly dissected cliffs mark the areas where the river channel has shifted relatively recently.

"Young ridges" are distributed along almost the entire length of the study part of the valley, mainly in the beginning and middle, the median value of appearance is located in the first half. Karst ridges of this type are beginning to appear in the upper part of the river. Closer to the mouth of the Sinyaya River, this type of ridges disappears; "mature" and "old ridges" prevail there. We assume that such a change in the occurrence of ridges of different types along the river is associated with a change in the intensity of lateral erosion and the restructuring of meanders due to the flattening of the longitudinal profile of the river as it approaches the mouth.

DISCUSSION

The methods we applied to obtain data on the morphometric characteristics of the landforms, using UAVs and GIS analysis, enabled us to gather information about both the height of karst ridges and rock pillars, as well as the spatial distribution of landforms and the relationship with a complex of relief-forming processes in the study area. The use of optical and LIDAR survey data from UAVs is widely used to study the topography, also in areas with karst landforms (Silva et al 2017; Kim and Hong 2024). Our study also fits into this context. Methods of morphometric data extraction and landform classification based on DSM are actively developing (Cao et al. 2023). A similar approach and automation of algorithms for remote sensing data processing and DSM analysis is a promising direction for further research.

The study area topography is the result of the joint development of relief-forming processes: 1) karst related to dissolution of carbonate rocks, 2) physical weathering, 3) fluvial processes, and 4) gravitational (slope) processes.

Karst activity is facilitated by fracturing limestones in the area of supra-permafrost groundwater. Deeper penetration of cracks contributes to the formation of vertical karst features because water dissolves minerals along the cracks and warms the permafrost. The cryogenic factor of physical weathering is most clearly manifested during cycles of systematic freezing and thawing. There are two main mechanisms of cryogenic weathering (Konishchev 1981) here: 1) frost weathering, when ice freezing in cracks splits frozen rocks into coarse fragments - blocks, rubble, debris; 2) cryohydration weathering, when the disjoining pressure of capillary water in microcracks when changing the phase state of water crushes and grinds the clastic material into small fractions of silty and fine sand grain sizes. Rock fragments disintegrated by physical weathering are thus prepared for further movement by other relief-forming processes.

Clastic rocks are moved on slopes under the influence of gravity in various forms and are transported by the action of flowing water in streams and rivers. Within the fragments of "old ridges", the slopes surrounding isolated rocky outcrops are covered with a stone coarse clastic cover. Various types of mass movements are observed. These debris fields creep like kurum stones due to the accumulation and melting of ice under the active layer. In sites where coarse clastic material is presented with finely dispersed loamy filler, in the case of local excessive water saturation, some types of landslides occur in the forms of translational landslides or debris avalanches (Fig. 4).

Among the fluvial processes determining morphological features of the karst landforms of the Sinyaya River valley, it is necessary to highlight the lateral erosion leading to the undercutting of carbonate rock outcrops on the concave parts of modern river meanders (Fig. 1c).

In some sites there is no beach, and a vertical rock cliff goes below the river's water level. In these cases, dissolution of limestone complements the activity of lateral erosion (Fig. 5). On the apex of the river meanders, significant karst landforms with rock pillars are located (Appendix, Table 1).

On the periphery of modern river meanders, along the sides of the valley with adjoining floodplain terraces, the absence of lateral erosion activity in the river leads to a decrease in the dissection of the terrain. More "mature" ridges are located here, the modern development of which is dominated by the role of karst proper, physical weathering of rock, gravitational processes which determine the movement of clastic material on slopes.

In spatial terms, ridges alternate on the left and right sides of the valley without a clearly expressed prevalence. The extent of ridge fragments is determined by the dimensions, primarily the radius, of the river meanders along which they are located. In the transverse profile of the Prilenskoe Plateau, the absolute elevations increase in the middle part, slightly closer to the Lena River valley. This pattern is also manifested in the relative heights of karst ridges. Within the study area, the highest karst ridge height, exceeding 100 m, are located in the second half of the Sinyaya River valley, closest to the mouth (Fig. 6a). Such significant heights are most typical for "mature" and some "old ridges" (Fig. 6b, c).

Within the studied area of the Sinyaya River valley, "old" ridges predominate, their length is 52.2 km, which is more than 58% of the total length of the studied ridges. The length of "mature" ridges is 21.9 km, which is about 25% of the length of all ridges; "young" ridges is 11.6 km (13%),

Fig. 4. Landslide (debris avalanche) of coarse clastic material in the section of the «old» ridge. The yellow line indicates the headscarp, the dashed yellow line - the transit zone, the red line - the accumulative landslide body borders

Fig. 5. Lateral river erosion expressed as niches on the base of limestone wall (at the «young ridge" site)

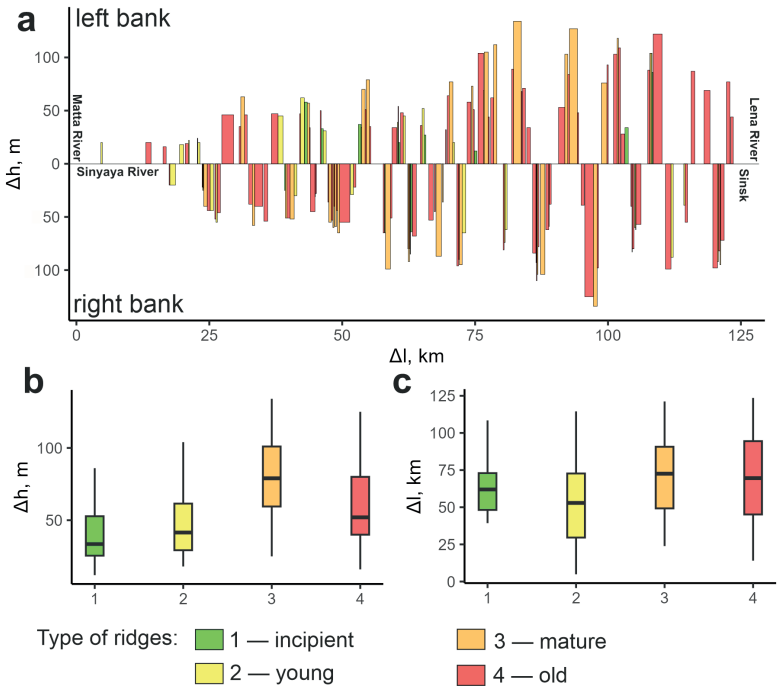

Fig. 6. Spatial analysis of ridge types according to E.V. Trofimova (2013) and their morphometric characteristics in the studied area from the mouth of the Matta River to the mouth of the Sinyaya River: a - location, length, and relative height of all ridge's types; b - height difference from the top level of the ridge to the foot of the slope; c - remoteness of the ridge in the downstream direction from the mouth of the Matta River to the Lena River. Check the Fig. 1 for the ridges' location

"incipient" ridges is 3.7 km (4%). Such distribution indicates a long history of the valley topography formation and a significant impact of denudation processes on the ridges.

There is a unity in the morphology of karst landforms and ridge types with the nearby Lena Pillars, which are included in one generalized region of karst development within permafrost (Spektor and Spektor 2009; Veress et al. 2014). The Lena Pillars region is also characterized by a significant diversity of karst landforms, and E.V. Trofimova (2013) identified ridge types similar to the Sinsky ones. The height of ridges, including rock remnants with vertical walls, reaches 200 m (Trofimova 2013), within which pinnacles up to 100 m high are located (Veress et al. 2014). Such karst landforms are quite rare for temperate latitudes. Alone-standing limestone towers (pillars or pinnacles) are most typical of tropical karst. In Guangxi Province, China, the Guilin karst is characterized by standing alone steep pillar towers up to 100 m high (Tang and Day 2000; Waltham 2008). These rock pillars are rising from an alluvial plain between Yangshuo and Fuli. On the Siberian platform, ancient buried karst is widespread; however, it lacks the striking positive landforms found in the Lena and Sinsky Pillars. On the Patom Plateau, the Proterozoic limestones are dominated by sinkholes, partly transformed into lakes. In the Aldan-Timpton interfluve and in the neighboring regions of southern Yakutia, where karst is developed in the carbonate rocks of the Cambrian, landforms of modern karst are widespread as sinkholes, depressions, funnels, and other negative landforms (Korzhuev 1961; Tolstikhin and Spektor 2004; Spektor and Spektor 2009; Veress et al. 2014; Trofimova 2018; Vaks et al. 2020).

CONCLUSIONS

The karst landforms in the Sinyaya River valley are the result of karst, river erosion, and slope processes paragenesis. These processes interact in a complex way to create a diverse range of landforms and to set their spatial distribution. Each process has varying degrees of influence on the formation of the terrain characteristics, leading to a unique landscape.

As a result of field observations and analysis of the created DSMs, morphometric characteristics of the previously identified types of karst ridges of the Sinyaya River valley were obtained: 1) "incipient ridges" with a median height of 34 m; 2) "young ridges" with a median height of 34 m, 3) "mature ridges" with a median height of 79 m; and 4) "old ridges" with a median height of 58 m. Most of the ridges with a height exceeding 100 m are of "mature" type. In spatial terms, the greatest heights of the ridges are observed where the valley cuts through the most elevated part of the Prilenskoe Plateau. Here, the highest single standing pinnacle pillars reaching 124 m are observed, located within the "mature ridges" (Appendix).

In the Sinyaya River valley "old" ridges are the most prevalent over 58% of the overall length of the examined ridges. "Mature" ridges represented approximately 25% of the total ridge length; "young" ridges 13%; while "incipient" ridges were 4%. This distribution reflects the extensive history of topographic development in the valley and highlights the significant influence of denudation processes on the ridges.

Within the river meander, a consistent change in the types of ridges is observed. "Incipient ridges" are located where the river channel came relatively recently. "Young" and "mature ridges" are located at the concave eroded river banks. "Old ridges" are usually located on the periphery of meanders where the river channel has gone or lateral erosion is not active.

The obtained data could be used in further studies on the stages of karst landform development in permafrost, as well as in regional studies on the terrain dynamics within the Prilenskoe Plateau, providing detailed morphometric characteristics of karst landforms.

REFERENCES

Cao H., Xiong L., Ma J., Wang H., Li S., Yu F. and Wang P. (2024) Karst landform classification considering surface flow characteristics derived from digital elevation models. Earth Surface Processes and Landforms, 49(1), P. 468–481, DOI: 10.1002/esp.5715

Davis W.M. (1899). The Geographical Cycle. Geographical Journal, Vol. 14, No. 5, 18, P. 481-504. doi:10.2307/1774538.

Doumit J. and Ghanem D. (2021). Using high-resolution Digital Surface Models and GIS-based geomorphometry to draw a karst landforms map. Mazedan Transactions on Engineering Systems Design, Vol-2, Issue-2, P. 1-4.

Gillieson D.S., Gunn J., Auler A., Bolger T. (editors) (2022). Guidelines for Cave and Karst Protection, 2nd Edition, Postojna, Slovenia: International Union of Speleology and Gland, Switzerland, IUCN. 112 p.

Kim J. and Hong I. (2024). Evaluation of the Usability of UAV LiDAR for Analysis of Karst (Doline) Terrain Morphology. Sensors, 24(21), 7062, DOI: 10.3390/s24217062

Konishchev V.N. Regularities of formation of rock composition in the cryolithozone (1981). (Zakonomernosti formirovaniya sostava porod v kriolitozone). Novosibirsk: Nauka. 218 p. (In Russian).

Korzhuev S.S. (1961). Merzlotnyi karst Srednego Prilen'ya i nekotorye osobennosti yego proyavleniya (The Middle-Lena frozen karst and its characteristics). Regionalnoe karstovedenie. Izdatelstvo AN SSSR, Moscow, P. 207-220. (In Russian).

Lena Pillars Nature Park (2012). Moscow: ANNIE, 56 p. (In Russian).

Porter C., Howat I., Noh M.-J., Husby E., Khuvis S., Danish E., Tomko K., Gardiner J., Negrete A., Yadav B., Klassen J., Kelleher C.; Cloutier M., Bakker J., Enos J., Arnold G., Bauer G. and Morin P. (2023). "ArcticDEM, Version 4.1", https://doi.org/10.7910/DVN/3VDC4W, Harvard Dataverse, V1, [Date Accessed 14 December 2023].

Samsonov T.E. (2024) Visualization and Analysis of Geographical Data in R. Moscow, Faculty of Geography Lomonosov MSU, (In Russian), DOI: 10.5281/zenodo.901911.

Saroli M., Albano M., Moro M., Falcucci E., Gori S., Galadini F. and Petitta M. (2022). Looking Into the Entanglement Between Karst Landforms and Fault Activity in Carbonate Ridges: The Fibreno Fault System (Central Italy). Front. Earth Sci., 10:891319. DOI: 10.3389/feart.2022.891319

Silva O.L., Bezerra F. H.R., Maia R.P. and Cazarin C.L. (2017). Karst landforms revealed at various scales using LiDAR and UAV in semi-arid Brazil: Consideration on karstification processes and methodological constraints. Geomorphology, 295, P. 611-630, DOI: 10.1016/j.geomorph.2017.07.025

Simonov Yu.G. (1998). Morfometricheskii analiz rel'efa (Geomorphometric analysis of terrain). Moscow–Smolensk: Izd-vo SGU (Publ.), 272 p. (in Russ.)

Simonov Yu.G. (1999). Ob"yasnitelnaya morfometriya rel'efa (Explanational geomorphometry). Moscow: GEOS (Publ.), 251 p. (in Russ.)

Spektor V.B. and Spektor V.V. (2009). Karst processes and phenomena in the frozen carbonate rocks of the Middle Lena River basin. Permafrost and Periglac. Process. (20): P. 71-78.

The Foundation of Geocryology, Part 4: Dynamic Geocryology (2001). Ed. by E. D. Ezhov, L. S. Garagulya, S. N. Buldovich, Moscow State Univ., Moscow (in Russian).

Tolstikhin O.N. and Spektor V.V. (2004). Lena Pillars. Science and Techniques in Yakutia, P. 101–106 (In Russian).

Trofimova E.V. (2012). Karst in the «Lena Pillars» Nature Park is a unique natural phenomenon. Izvestiya RGO, vol. 144, 3, P. 68-75. (In Russian).

Trofimova E.V. (2013). Morphology of the relief of the Lena Pillars (Lena River valley). Izvestiya RGO, vol. 145, 5, P. 19-28. (In Russian).

Trofimova E.V. (2017). Amazing karst in the valley of the Sinyaya River. Priroda, Vol. 1, P. 48-54. (In Russian).

Trofimova E.V. (2018). UNESCO world karst natural heritage sites: geographical and geological review. Geography, Environment, Sustainability. Vol. 11 (2): P. 63-72. https://doi.org/10.24057/2071-9388-2018-11-2-63-72.

Vaks A., Mason A.J., Breitenbach S.F.M., Kononov A.M., Osinzev A.V., Rosensaft M., Borshevsky A., Gutareva O.S. and Henderson G.M. (2020). Palaeoclimate evidence of vulnerable permafrost during times of low sea ice. Nature, 577, P. 221–225. https://doi.org/10.1038/s41586-019-1880-1.

Veress M., Zentai Z., Péntek K., Döbröntei L. and Kiprijanova L.D. (2014). The development of the pinnacles (Lena pillars) along Middle Lena (Sakha Republic, Siberia, Russia). Proc. Geol. Assoc. 125, 452–462.

Waltham T. (2008). Fengcong, fenglin, cone karst and tower karst. Cave and Karst Science, 35(3). P. 77-88.

Zhang L., Du H., Yang Z., Song T.; Zeng F., Peng W. and Huang G. (2022). Topography and Soil Properties Determine Biomass and Productivity Indirectly via Community Structural and Species Diversity in Karst Forest, Southwest China. Sustainability, 14, 7644, DOI: 10.3390/su14137644

RESEARCH PAPER

SUBMARINE PERMAFROST MAPS OF THE RUSSIAN ARCTIC. A REVIEW

Alexander A. Vasiliev, Gleb E. Oblogov, Nataliia G. Belova*
Earth Cryosphere Institute, Tyumen Scientific Centre SB RAS, Malygina St. 86, Tyumen, 625026, Russia
***Corresponding author:** belova.ng@gmail.com
Received: March 25th 2025 / Accepted: July 18th 2025 / Published: October 1st 2025
https://doi.org/10.24057/2071-9388-2025-3966

ABSTRACT. The article presents the results of digitizing the maps of submarine permafrost on the shelf of the Arctic seas of Russia. Submarine permafrost mapping relies heavily on expert knowledge because there is a lack of data regarding the structure and thickness of permafrost. Maps compiled by different authors vary significantly due to the use of different approaches, paleogeographic scenarios, ideas about the geological structure, evolution of shelf permafrost, sea level and climatic changes. The first maps were based on the analysis of shelf morphology and seawater temperature; they represent only the assumed boundaries of the submarine permafrost distribution. Later, the distribution of submarine permafrost was associated with neotectonic movements on the modern shelf. As the first drilling and seismoacoustic data were received, more detailed maps were compiled, and the discontinuous distribution of submarine permafrost was substantiated, especially in the Western Arctic. By now, a large amount of seismoacoustic and drilling data has been accumulated, which has made it possible to create new maps based on these data. In recent decades, methods of mathematical modeling the formation and evolution of submarine permafrost have been rapidly developed. Calculated maps of the distribution and depth of submarine permafrost top in the Russian Arctic have been compiled. For the first time, it has become possible to predict the rate of degradation of submarine permafrost under climate warming.

KEYWORDS: Russian Arctic, shelf, submarine permafrost, maps

CITATION: Vasiliev A. A., Oblogov G. E., Belova N. G. (2025). Submarine Permafrost Maps Of The Russian Arctic. A Review. Geography, Environment, Sustainability, 3 (18), 107-117
https://doi.org/10.24057/2071-9388-2025-3966

ACKNOWLEDGEMENTS: The research was carried out at the Earth Cryosphere Institute of the Tyumen Scientific Centre of the Siberian Branch of the Russian Academy of Sciences as part of the state assignment from the Ministry of Science and Higher Education of the Russian Federation (project № FWRZ-2021-0005).

Conflict of interests: The authors reported no potential conflict of interests.

INTRODUCTION

The study of submarine permafrost (SMP) is of interest in connection with the discovery of promising oil and gas fields on the shelf of the Russian Arctic and the development of the Northern Sea Route. Another important problem associated with SMP is the assessment of the role of permafrost in the formation of methane flows on the shelf of the Arctic seas (Bogoyavlensky et al. 2023a,b; Koshurnikov et al. 2020; Shakhova et al. 2015) and the overall impact of climate change on the Arctic environment.

Permafrost is formed when the shelf drains up during sea regression. During sea transgression, permafrost transitions to a subaqueous state, and its degradation occurs. New permafrost formation also occurs within currently developing marine accumulative forms (Grigoriev 1987).

The distribution and evolution of SMP in the Arctic have been the subject of many publications (Antipina et al. 1979; Zhigarev 1997; Kassens et al. 2000; Chen et al. 2022; Romanovskii et al. 1997; Romanovskii et al. 1999; Rokos et al. 2023 and many others).

Direct observations of the space distribution, thickness, state, and thermal regime of SMP are extremely limited. By 2024, only 17 boreholes had been drilled in the Barents and Kara Seas, which have exposed SMP. Drilling on the East Siberian Shelf commenced in 1953 (Grigoriev 1966) and has continued to the present day. Moreover, most of the boreholes are located in shallow coastal areas. At the same time, geophysical methods for studying SMP are increasingly advancing; among these, high-resolution seismic methods hold the greatest promise (Rekant and Vasiliev 2011; Kulikov et al. 2014; Overduin et al. 2015). Seismoacoustic profiling has become an almost mandatory task during marine expeditions. By now, a substantial number of seismoacoustic profiles have been completed in the Arctic seas. Methods of electrical exploration for the study of SMP are successfully developed by A.V. Koshurnikov (2023).

As our understanding of SMP evolves, attempts have been made to map its distribution, properties, and thickness. Due to limited data, most of the maps are based on expert assessments and reflect the authors' perspectives on the potential distribution and conditions of the occurrence of SMP. Currently, there are several maps illustrating the potential distribution of subaqueous permafrost on the shelf based on the analysis of bottom temperature, bathymetry, and sea level rise data. Until

recently, all these maps were available only in paper form. Some of these maps are currently unavailable for use, as they were only included in scientific and technical reports.

Recently, digital SMP maps compiled based on mathematical modeling of SMP formation and evolution have become increasingly widespread (Malakhova 2019; Smirnov et al. 2024; Nicolsky et al. 2012; Gavrilov et al. 2020; Malakhova and Eliseev 2020). The main drawback of such maps is an incomplete accounting of actual SMP data. The SMP parameters displayed on digital maps are calculated and can sometimes contradict even the limited factual information available. This issue is due to a lack of information, mainly on the boundary conditions used in mathematical models. Nonetheless, modeling the formation and evolution of SMP has resulted in a distinct and rapidly advancing field of SMP research.

This work is dedicated to the collection, processing, and analysis of approaches of published and archived maps of the SMP and the compilation of a GIS album, including SMP maps, some of which were previously inaccessible and unknown to researchers. Maps containing information about permafrost on the shelf of the Russian Arctic from published data, archives of the Institute of the Earth Cryosphere SB RAS, other institutes, and Rosgeolfond were processed. The purpose of the work is to ensure the availability of many published or unpublished (archived) maps of the SMP of the Russian Arctic.

MATERIALS AND METHODS

The QGIS geographic information system (GIS) was used. Today, it is among the most dynamically developing and functional desktop GIS applications. The main task was to digitize original paper maps. To work with GIS, it is essential to establish a correspondence between the internal coordinate system of the raster (graphic image) and the external (target) coordinate system used in the GIS project; in other words, it is necessary to perform raster referencing. Referencing consists of determining two pairs of coordinates for a certain number of points: coordinates in the internal coordinate system of the raster and coordinates in the target coordinate system. The reference points should be evenly distributed across the image (or at least the part used in the study) and not on the same line.

The Lambert Azimuthal Equal Area Projection (WGS 84/North Pole LAEA Russia) was selected as the coordinate system for the GIS project, as it is the most suitable for the cartographic representation of the Russian Arctic SMP. However, the created maps can easily be converted to any other projection. Additionally, one advantage of working in QGIS is the availability of base maps – coastline, hydrological network, and simplified topographic maps.

When digitizing the maps, we aimed to preserve the original legends as much as possible, as they reflect the authors' approaches to constructing the maps and their content. However, in some cases, the legend had to be modified.

Here we offer the visual representation of the maps; if needed, GIS projects can be obtained from the publication's authors.

RESULTS

By now, all available geocryological maps have been digitized. One of the first publications in 1972 was A.L. Chekhovsky's forecast scheme for the distribution of the subaqueous cryolithozone in the Asian sector of the Arctic (Chekhovsky 1972). In conditions of insufficient information, the author, in fact, displayed the spatial distribution of water temperature in the Arctic seas, considering the shelf relief. The scheme does not illustrate subaqueous permafrost but rather the cryolithozone, understood as sediments that presumably have a negative temperature (Fig. 1). It should be noted that, when applied to the western sector of the Russian Arctic, the boundaries of the cryolithozone and the distribution area of subaqueous permafrost containing ice differ significantly from the modern data. A.L. Chekhovsky identified two types of cryolithozone in the Arctic seas: shelf cryolithozone, extending to a depth of 200 m, and oceanic cryolithozone, found at depths greater than 200–800 m. Within the shelf cryolithozone, with ground temperatures ranging from 0 to –1.8°C, areas with positive summer temperatures have been identified in the estuaries of large rivers. The oceanic cryolithozone, located to the north of the shelf, has temperatures of –0.7°C in the Atlantic sector of the Arctic and –0.35°C in the Pacific.

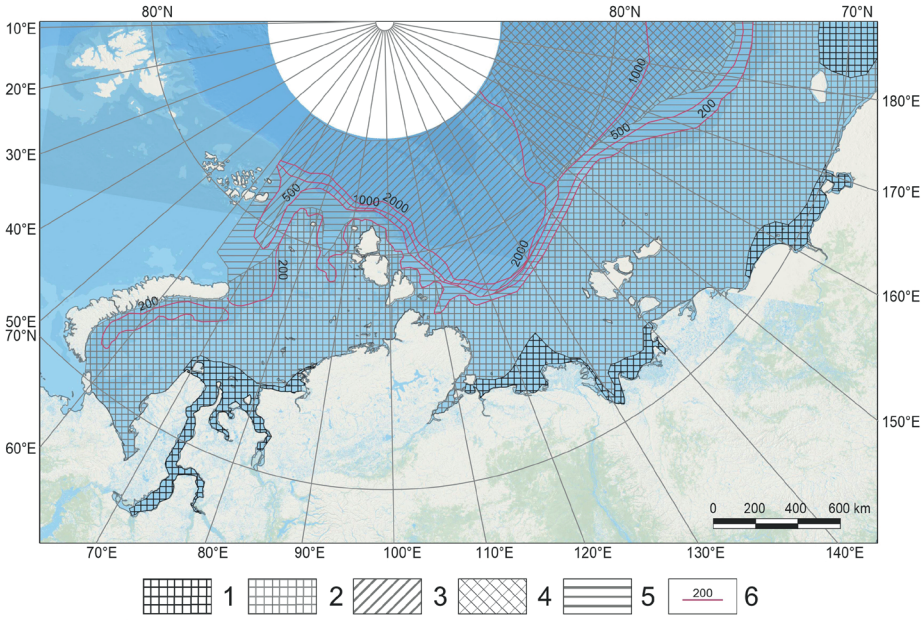

Fig. 1. Image of the forecast map of the distribution of cryolithozone in the Asian sector of the Arctic (Chekhovsky 1972). Legend: 1 – shelf cryolithozone, MAGT 0…-1°C with a positive summer water temperature; 2 – the same, but with a constant negative temperature; 3 – oceanic cryolithozone with MAGT -0.7°C; 4 – also with MAGT -0.35°C; 5 – unfrozen sediments with MAGT 0.6-2.0°C; 6 – isobaths, m

Later, the same approach to assessing the distribution of the shelf cryolithozone based on the spatial distribution of the temperature of the bottom water layer was used by L.A. Zhigarev in his monograph (1997). By the time the monograph was published, new data on seawater temperatures in the Arctic seas and, most importantly, the results of SMP studies in the coastal zones of the Laptev Sea, East Siberian Sea, and Chukchi Sea had been obtained. The monograph includes a schematic map of the cryolithozone in the Arctic seas of Russia. The map illustrates the boundaries of the distribution of alongshore permafrost (established and assumed), relict permafrost (established and assumed), seasonally frozen sediments (established), perennially and seasonally non-frozen sediments with temperatures below 0°C, cryotic sediments, and average annual isotherms (established and assumed). The author selected this classification of cryolithozone as a basis for identifying areas and regions that differ in the conditions of heat exchange between bottom sediments and seawater. The schematic map is created on a small scale, accompanied by an ineffective legend, making its practical use exceedingly challenging. The significant advantage of the schematic map was that it outlined the boundaries of the distribution of frozen rocks on the sea shelf of the Eastern Arctic. This schematic map has not been digitized.

In the 1950 and 1970s, the content was developed (Baranov 1960; 1972), and in 1977, the geocryological map of the USSR was published under the editorship of I. Ya. Baranov at a scale of 1:5,000,000. The map covers both the continental and shelf regions of the Russian Arctic. The construction of the marine part of the map was based on the concept of shelf drainage, freezing, and subsequent submersion and flooding of the shelf, along with the active involvement of tectonic movements (Fig. 2). The map for the first time reflected the boundaries of the SMP distribution in sufficient detail (Geocryo… 1977).

Surprisingly, the boundaries of the SMP distribution in the Kara Sea on this map align closely with modern ones derived from drilling and seismic acoustic data.

As ideas about the SMP's conditions, formation history, and evolution developed, more detailed maps began to be compiled using limited drilling data and high-resolution seismic data. One example is the map created by V.A. Soloviev for the Barents and Kara Seas (Fig. 3) (Soloviev et al. 1981).

For the first time, the map reflects different SMP types and their continuity and provides estimates of their thickness. The legend uses the concepts of cryolithozone and frozen zone. Apparently, the term "cryolithozone" is used to designate negative-temperature sediments without ice inclusions, and the term "frozen zone" refers to frozen sediments that contain ice. The non-continuous nature of the SMP distribution in the Barents and Kara Seas is substantiated for the first time. Later, the map was improved, and became more detailed, and the legend was slightly changed.

The ideas about the SMP distribution developed by Ya.V. Neizvestnov and V.A. Solovyov were implemented in compiling the well-known and accessible Geocryological Map of the USSR at a scale of 1:2,500,000 (1996). When it was created, drilling and seismoacoustic research data from the Arctic seas were considered. However, the map's legend in the part of the Arctic shelf turned out to be heavily overloaded and difficult to read. As a result, the practical utilization of the map for evaluating the distribution and conditions of SMP occurrence is quite challenging.

Later, the same authors tried to implement a qualitative assessment of the probability of the distribution of the SMP of different continuity – ranging from less probable to probable and then to more probable. When creating the map, in addition to considering the probability distribution of SMP, greater emphasis was placed on the morphology of the shelf and the temperature regime of the bottom layer of water. The map is characterized by a high level of spatial resolution, as the analysis of the distribution and conditions of occurrence of SMP was conducted for each sheet of the international sheet numbering on a scale of 1:1,000,000. Unfortunately, the map was not published and exists only in paper form in a report in the Rosgeolfond archive (Neizvestnov et al. 1991). The appearance of the map is shown in Fig. 4.

In creating a circumpolar map of Arctic permafrost and ground ice, developed by an international team of researchers (Broun et al. 2001), the Russian part of the map is based on the previously published Geocryological Map of the USSR at a scale of 1:2,500,000 (1996). The production of a comprehensive circumpolar map depicting the distribution and thickness of SMP was undertaken at the initiative of the IPA as part of the European project NUNATARYUK. For the shelf permafrost of the Russian Arctic seas, the boundaries of the SMP distribution were clarified, and the

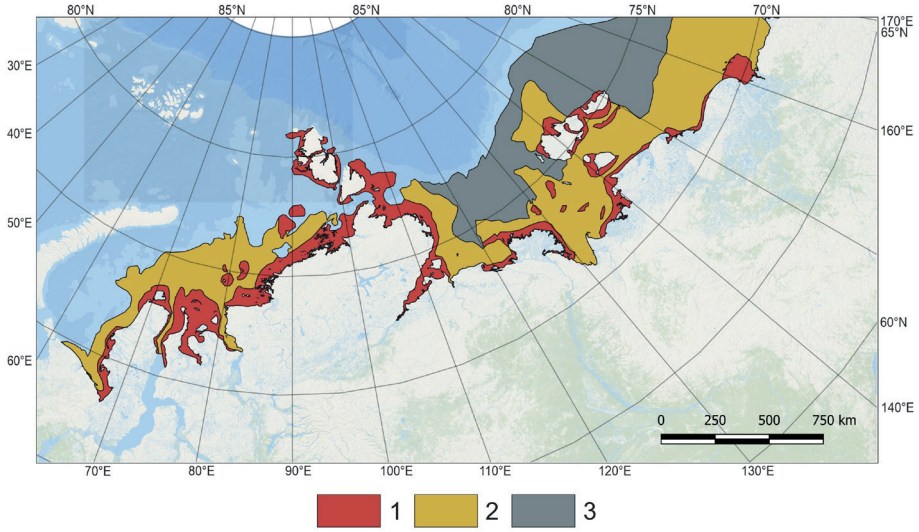

Fig. 2. Image of the marine part of the geocryological map of the USSR, edited by I. Baranov (1977). Legend: 1 – submarine permafrost in the inner part of the shelf, underlain by unfrozen saline sediments with a negative temperature; 2 – submarine permafrost in the outer part of the shelf partially thawed from above, underlain by unfrozen saline sediments with a negative temperature; 3 – unfrozen saline sediments with a negative temperature

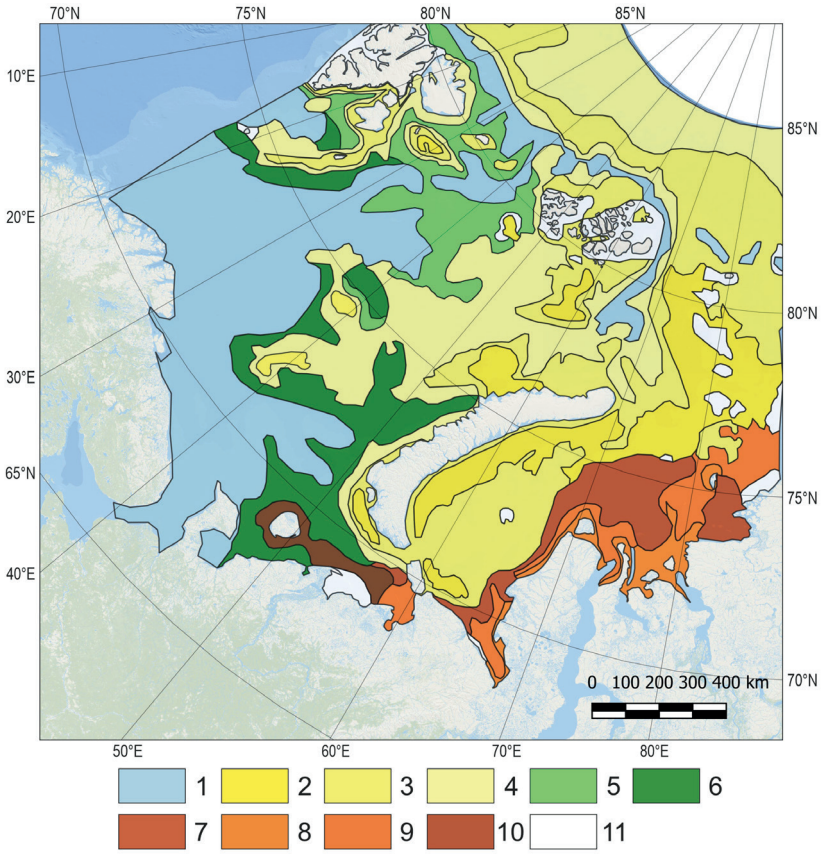

Fig. 3. Image of the SMP map of the Barents and Kara Seas (Soloviev et al. 1981). Legend: 1 – zone of positive temperatures; SMP: 2 –with a thickness of more than 50 m with cryopeg interlayers; 3 – with a thickness of 25-50 m with cryopeg interlayers; 4 – with a thickness of less than 25 m with cryopeg interlayers; 5 – seasonal submarine permafrost; 6 – episodically unfrozen area; 7 – area of sparse insular relict permafrost; 8 – insular relict permafrost with a thickness of less than 50 m; 9 – insular relict permafrost with a thickness of more than 100 m; 10 – insular relict permafrost beneath the episodically unfrozen zone; 11 – insular relict permafrost beneath the positive temperature zone

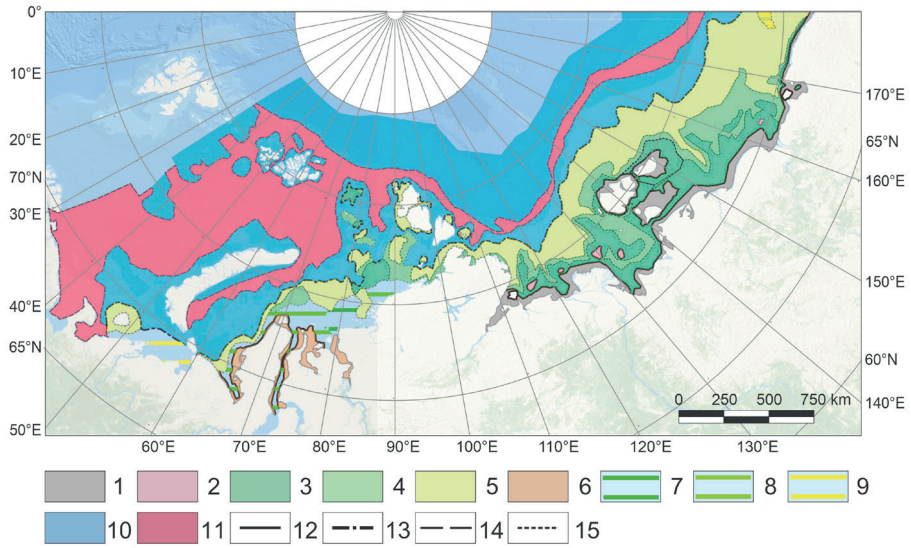

Fig. 4. Image of the forecast map of the cryolithozone of the shelf and islands of the Arctic seas of the USSR (Neizvestnov et al. 1991). Legend: 1 – continuous (newly formed) and relict permafrost zones turning into an island one; 2 – separate large massifs of frozen sediments within the island permafrost zone; 3 – island permafrost zone (more probabilistic distribution); 4 – island permafrost zone (probabilistic distribution); 5 – island permafrost zone (less probabilistic distribution); 6 – continuous relict permafrost zone under positive-temperature sediments; 7 – island relict permafrost zone under positive-temperature sediments (more probabilistic); 8 – island relict permafrost zone under positive-temperature sediments (probabilistic); 9 – island relict permafrost zone under positive-temperature sediments (less probabilistic); 10 – negative-temperature thawed non-frozen zone; 11 – positive-temperature zone; 12 – boundary of continuous permafrost, turning into an island permafrost; 13 – the boundary of the island permafrost; 14 – the boundary of the negative temperature thawed (not frozen) cryolithozone; 15 – the boundary of the intermediate island permafrost zone

map's legend and content were considerably simplified. This map illustrates the spatial distribution of the SMP along with the thickness estimations of the added SMP. It is available on the GRID-Arenda website (Fig. 5). It should be noted that the permafrost thickness was estimated based on the depth of the 0°C isotherm. For the eastern sector of the Arctic, the thickness estimates are generally satisfactory and correspond to other calculations (Romanovskii et al. 1997; Nicolsky et al. 2012; Koshurnikov et al. 2020), while for the western sector, the values of the SMP thickness are extremely overestimated. Quaternary deposits on the shelf of the western Arctic are represented by a thick stratum of saline sandy-clayey soils of predominantly marine origin. The onset temperature for freezing and thawing can vary from 0 to –1.5°C, depending on the salt content and lithological composition. In this case, the SMP permafrost occupies only the upper portion of the section with temperatures below the phase transition temperature; beneath, it is underlain by non-frozen sediments.

This same map was later used to model the submarine permafrost evolution from the Pleistocene to the Holocene. This was done to clarify the boundaries of the submarine permafrost's distribution and to calculate its thickness and ice content (Overduin et al. 2019; Angelopoulos et al. 2020; Chen et al. 2022). Both the original map and the model may not only overestimate the SMP thickness but also exaggerate the boundaries of its distribution. In particular, in the Barents Sea, the SMP is present north of Kolguev Island. However, according to seismoacoustic profiling data, the SMP was not detected in this area, and the SMP boundary is situated south of what is indicated on the map. In the same way, the SMP map in the Kara Sea indicates a large submarine permafrost massif to the west of the Severnaya Zemlya archipelago. Detailed seismoacoustic observations revealed a widespread distribution of Late Pleistocene marginal moraines framing the ice shelf here (Polyak et al. 2008). Thus, there were no conditions for the SMP formation (Gusev et al. 2012).

With the acquisition of new drilling and seismoacoustic profiling data in the Kara and Barents Seas, it became possible to utilize this information not only to interpret the geological structure of the Quaternary strata but also to analyze the distribution of SMP. All available seismoacoustic profiling and drilling data were gathered and reinterpreted to search for SMP manifestations (Rekant and Vasiliev 2011). Thus, a database of manifestations and occurrence depths of SMP in these seas was developed, and a GIS-oriented map of their distribution was constructed (Fig. 6).

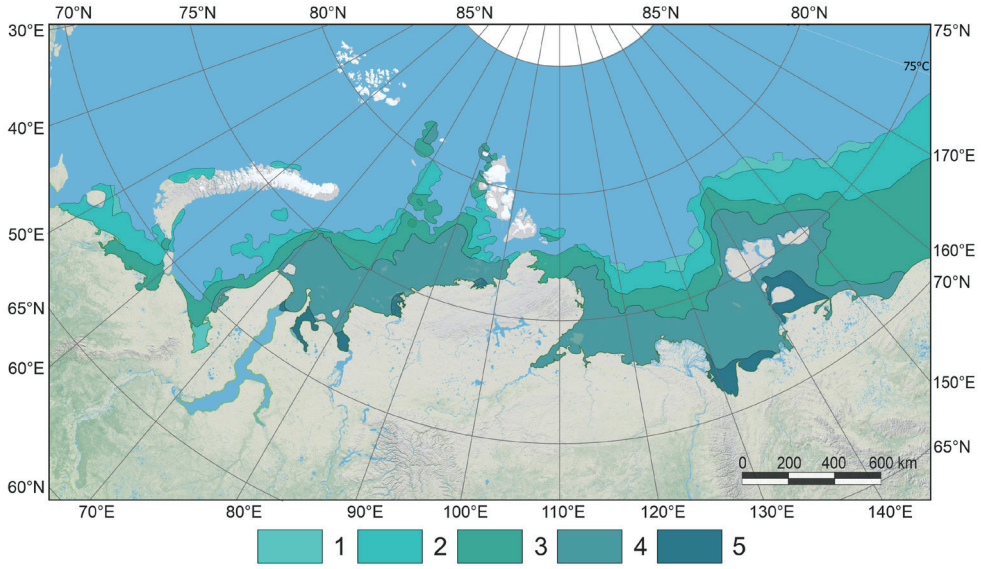

Fig. 5. Distribution and thickness of the submarine permafrost on the IPA map (Permafrost in the Northern Hemisphere 2020, based on Overduin et al. 2019). In the legend, the SMP thickness is as follows: 1 – 0-100 m; 2 – 100-300 m; 3 – 300-500 m; 4 – 500-700 m; 5 – 700-900 m

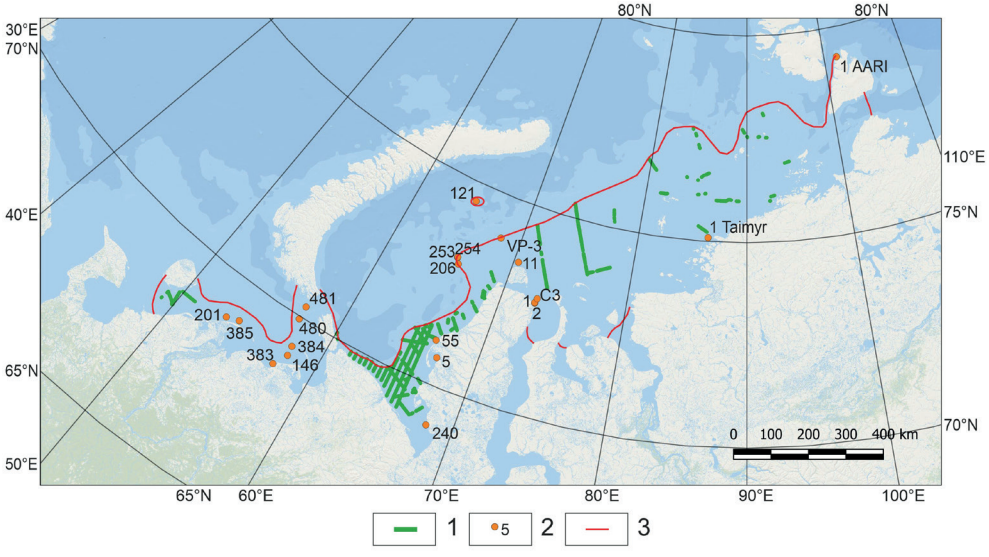

Fig. 6. Map of the distribution of submarine permafrost in the Barents and Kara Seas based on drilling and seismoacoustic profiling data (Rekant and Vasiliev 2011). Legend: 1 – seismoacoustic profiles; 2 – boreholes and their respective numbers; 3 – permafrost limit

The peculiarity of this map is the possibility of its continuous improvement and development as new seismoacoustic data become available and boreholes are drilled.

In 2025, V. Bogoyavlensky and co-authors published an article that provides a map of the SMP distribution in the Laptev Sea and the East Siberian Sea based on drilling data and, mainly, the results of deep seismic interpretation (Bogoyavlensky et al. 2025). The area of SMP distribution on this map is much smaller in the Laptev Sea, and SMP is completely absent in the East Siberian Sea. The authors explain these features of the SMP distribution through permafrost degradation, up to its complete thawing. This hypothesis contradicts all existing ideas about the distribution of SMP in the East Siberian seas. The Laptev and the East Siberian Seas shelves have a similar geological structure, a common paleogeographic history and a similar modern thermal regime of seawater. Therefore, the presence of permafrost in the Laptev Sea suggests that there are no reasons for it to completely thaw in the East Siberian Sea. Most likely, the source of the discrepancy is the incorrect interpretation of deep seismic data.

A detailed map of the distribution of SMP in the Russian Arctic was created at VNIIokeangeologiya (Shcherbakov et al. 2018). It considered all the drilling data and the results of our own seismoacoustic profiling in both the western and eastern sectors of the Arctic that were available at that time. The map reveals for the first time the spatial distribution of SMPs in various percentages of the permafrost area and offers more substantiated estimates of the thickness and temperature of frozen sediments than previous assessments. (Fig. 7). The water area of the Russian Arctic seas is divided into zones according to cryolithozone types. The boundaries of the SMP itself and non-frozen sediments are plotted. The VNIIokeangeologiya map illustrates the distribution of SMP in the seas of the Eastern Arctic with much greater detail. For the first time, potential new SMP formation areas are indicated on the shelf of the Arctic seas, based on the presence of bottom temperatures that fall below the phase transition temperature. However, according to direct observations (Dubrovin 2015; Rokos et al. 2023), a decrease in bottom temperatures only leads to the formation of frozen crusts with a thickness of no more than 0.2...0.5 m in the near-surface part of the section, which completely thaws during the summer season. Stable permafrost formation under current conditions is impossible in any area of the Arctic shelf.

In 2023, the Arctic Permafrost Atlas was published, which contains several maps characterizing the SMP (Westerveld et al. 2023). As an example, Fig. 8 shows a fragment of the distribution map of the Russian Arctic SMP based on modeling. In fact, the album repeats the maps (Fig. 5) given in the publications (Overduin et al. 2019; Angelopoulos et al. 2020). Contradictions regarding the distribution boundary of the SMP and its thickness remained unresolved when the atlas was published.

A promising method for studying the SMP using electrical exploration is being developed by A.V. Koshurnikov. Based on marine profiles in the Arctic seas of Russia, he showed that the specific electrical resistance of frozen strata and potential gas hydrates under permafrost are close to each other. The proximity does not allow them to be separated on the profiles. A map of the distribution of the SMP and the total thickness of SMP and gas hydrates has been developed (Koshurnikov, 2023). When digitizing the map, the legend was simplified (Fig. 9), and a different color scheme was used. The areas of distribution of the SMP and the total thickness of SMP and gas hydrates for the Barents and Kara Seas shown on the map differ greatly from other maps. The author explains these differences by the widespread development of saline Quaternary deposits on the shelf of the Western Arctic, which greatly complicates the interpretation of field observations.

Geoelectric surveys by magnetotelluric and transient electromagnetic methods have good prospects for subaqueous permafrost mapping (Yakovlev et al. 2018). The application of the method in the Khatanga Gulf has shown its effectiveness in determining the depth of the SMP top.

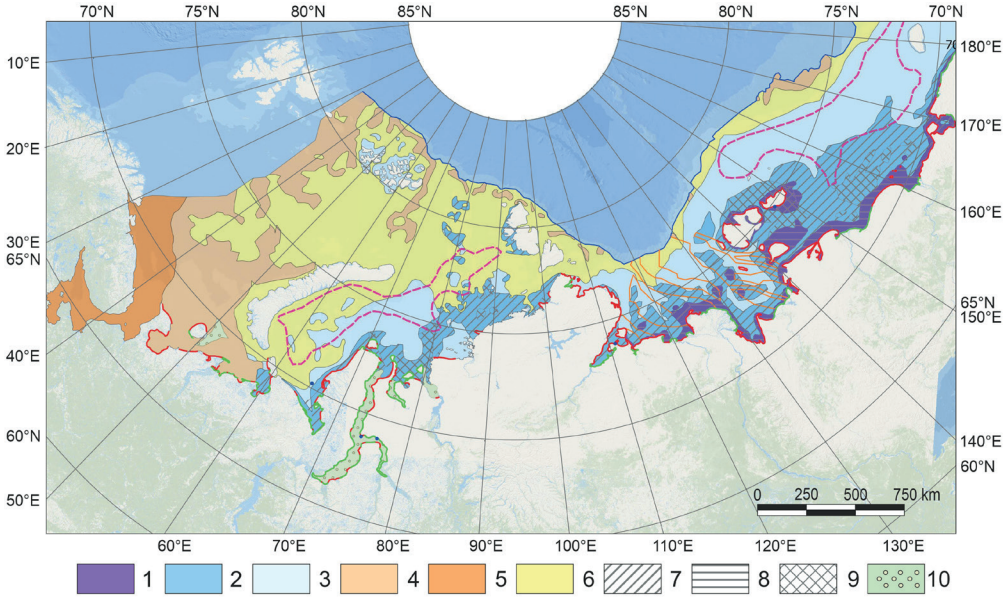

Fig. 7. An image of the SMP map of the Russian Arctic, VNIIokeangeologiya (Shcherbakov et al. 2018). Legend: 1 – relict and newly formed continuous, turning into an island, frozen submarine cryolithozone; 2 – island relict submarine frozen zone; 3 – rare island submarine frozen zone; 4 – negative-temperature frozen submarine cryolithozone with sediments temperature of 0…-1°C; 5 – positive-temperature zone; 6 – negative-temperature unfrozen submarine cryolithozone with sediment temperature of -1…-2°C; 7-9 –permafrost thickness: 7 – from 0 to 100 m, 8 – from 100 to 200 m, 9 – more than 200 m; 10 – submarine taliks; 11 – geocryological boundaries; 12 – zones of tectonic faults with endogenous through submarine taliks with the base of the permafrost layer raised by 100-200 m; 13 – supposed areas of modern permafrost formation; 14 – accumulative coasts; 15 – thermoerosional coasts; 16 – shelf boundary

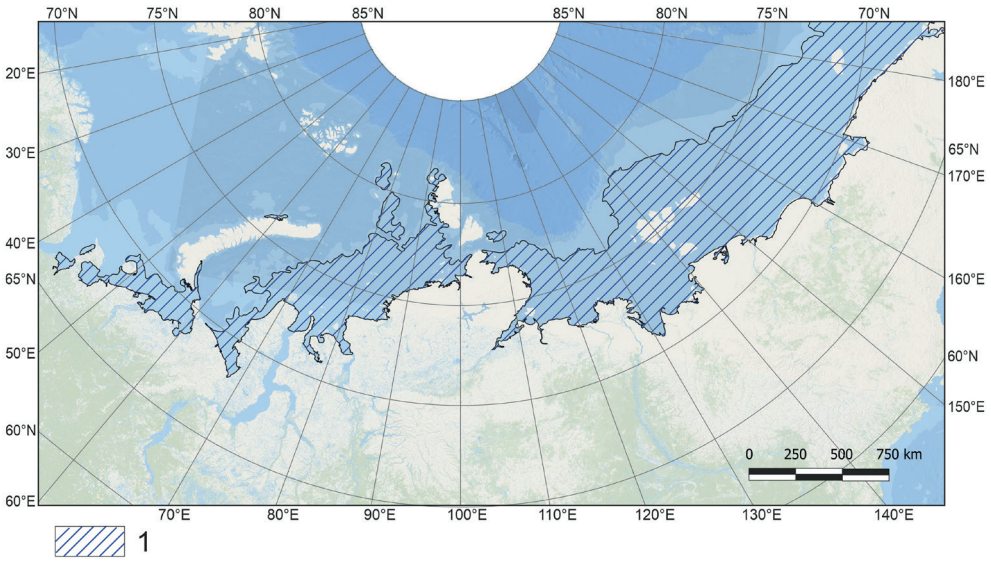

Fig. 8. Image of the Russian Arctic SMP distribution map according to (Westerveld et al. 2023). Legend: 1 – SMP distribution area

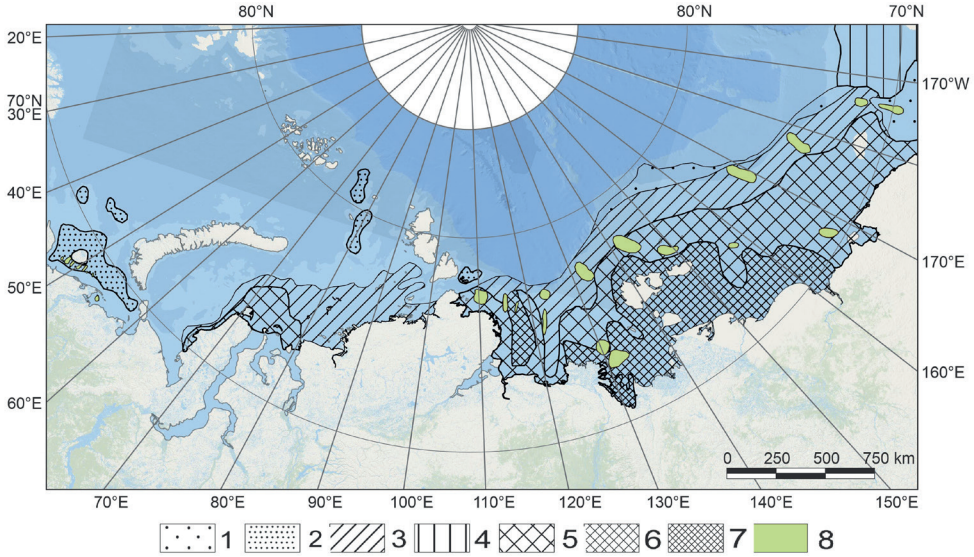

Fig. 9. An image of the SMP and gas hydrate distribution and total thickness in the Russian Arctic (Koshurnikov 2023). Legend: 1-7 – thickness of the cryogenic strata, m: 1 – 100-200, 2 – 200-300, 3 – 300-400, 4 – 400-500, 5 – 500-600, 6 – 800-900, 7 – more than 1000; 8 – high-temperature cryogenic strata

In recent decades, the construction of submarine permafrost maps based on mathematical modeling has been actively developing. Permafrost formation is considered a result of a long geological history of shelf development, with periodic stages of cooling and warming, transgressions, and regressions in the Arctic Ocean. As a rule, a heat exchange model based on the solution of the Stefan problem is used here. The primary issue with this modeling is to consider the characteristics of the geological structure of the Arctic shelf, as well as the composition, ice content, salinity, and temperature of phase transitions. The upper boundary conditions are established according to the chosen paleogeographic scenarios. In this case, specific paleotemperatures of the air are often assigned based on indirect data. The temperature on the Earth's surface is set equal to the air temperature. However, actual observations of modern air temperatures (MAAT) and permafrost temperatures (MAGT) show that the ratio of MAGT and MAAT ranges from 0.1 to 1.0 depending on the landscape conditions that determine the heat exchange at the surface. The average ratio between modern MAGT and MAAT for the western sector of the Russian Arctic is about 0.7 (Malkova et al. 2022).

An example of SMP maps constructed through mathematical modeling can be the map of the distribution and thickness of the SMP in the Kara Sea (Gavrilov et al. 2020) (Fig. 10).

When creating the map, the authors considered the 125 Kyr history of the Kara Sea shelf development. The model takes into account not only the change in sea level during the Late Pleistocene but also the eustatic uplift of the dried shelf surface during the postglacial transgression. Since the model contains several uncertainties in the properties of freezing bottom sediments, the temperature of the bottom water layer, paleoclimate, etc., the authors adopted broad ranges of the SMP thickness shown on the map in the legend. This enabled the identification of areas with sharply contrasting calculated thickness values. The map highlights a region with a SMP thickness of 100-300 m. However, A. Portnov showed that under the most severe climatic conditions of the Last Glacial Maximum in the Kara Sea, the submarine permafrost thickness cannot exceed 270 m (Portnov et al. 2014). Considering the SMP degradation from above and below, its maximum thickness cannot exceed 200-250 m. The area of SMP distribution in the southern part of the Kara Sea is underestimated when compared to seismoacoustic profiling data, whereas it is

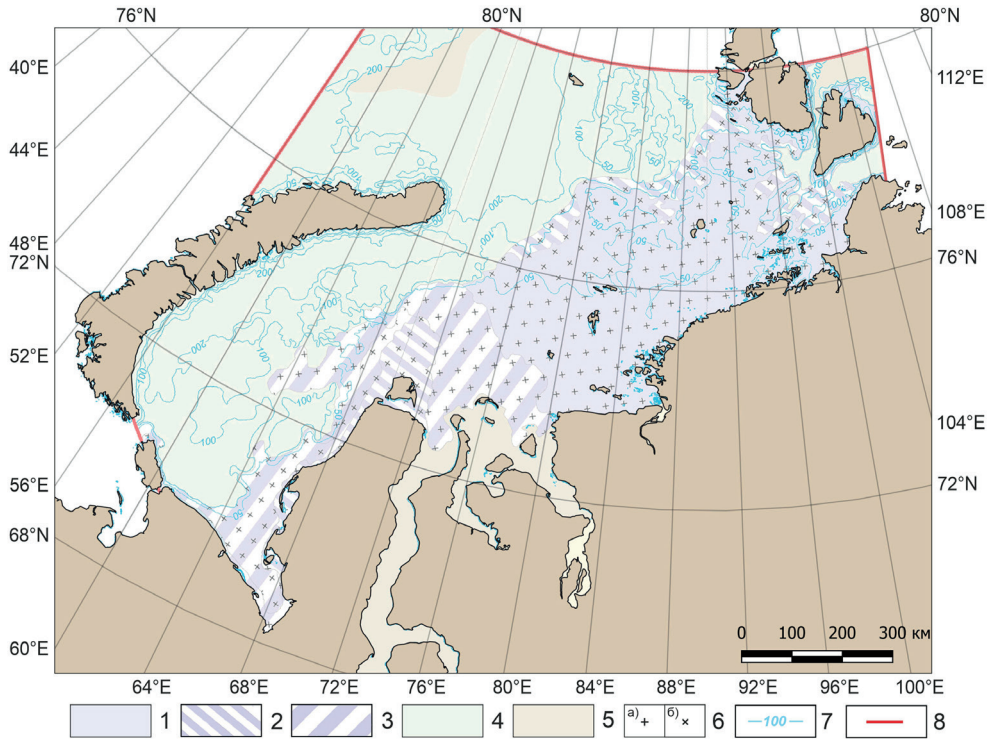

Fig. 10. Image of the submarine permafrost distribution and thickness map constructed based on mathematical modeling (Gavrilov et al. 2020). Legend: 1 – continuous SMP with a thickness of 100-300 m; 2 – discontinuous massive island and island SMP with a thickness of 0-100 m; 3 – island SMP with a thickness of 0-100 m; 4 – non-frozen cryotic sediments; 5 – thawed sediments; 6 – depth of the SMP top: a – 0-30 m, b – 25-50 m or more: 7 – isobaths; 8 – boundaries of the study area

overestimated in the central and northern parts of the sea. Later, an analogous map was compiled for the Laptev Sea (Gavrilov et al. 2024).

More efficient but also more complex modeling of the SMP is being developed in the Institute of Computational Mathematics and Mathematical Geophysics SB RAS (Malakhova 2019; Malakhova et al. 2020; Malakhova 2023; Malakhova and Eliseev 2023). This model uses both climate and heat exchange models in the Arctic Ocean. This approach allowed V. Malakhova, for the first time, to not only establish the modeled boundaries of the distribution of the SMP and its thickness (Fig. 11) but also to assess the current and projected trends of its degradation in the Russian Arctic. Under the RSP scenario of 8.5, the average rates of SMP degradation were 1-2 cm per year for 1950-2015, 5 cm per year for 2015-2100, and 10 cm per year for 2100-2300.

The map was not digitized due to its small scale.

Yu. Smirnov and co-authors (Smirnov et al. 2024) modeled the SMP, taking into account the climate zonality and spatial distribution of salinity in the seas of the Russian Arctic.

The boundaries of the distribution of the SMP on the map by Yu. Smirnov et al. for the central and southern Kara Sea demonstrate good agreement with those previously established based on seismoacoustic profiling and drilling data on the shelf (Rekant and Vasiliev 2011; Overduin et al. 2019), but for the Barents Sea, the area of the SMP distribution is clearly underestimated (see Fig. 6). Furthermore, in both seas, the depth of the SMP top is significantly underestimated. This is attributed to both the model's imperfections and the uncertainties regarding the characteristics of the soils on the shelf and the boundary conditions.

CONCLUSIONS

The conducted studies made it possible to ensure the availability of many published and unpublished (archive) maps of the Russian Arctic submarine permafrost. All maps were digitized and integrated into a single GIS format, enabling comparison. The review indicates that as the ideas about the distribution, conditions of occurrence, and thickness of the submarine permafrost developed, the content of the maps also changed.

The first maps were based on an analysis of the morphology of the Arctic shelf and seawater temperature. They only approximately reflected the boundaries of the spatial distribution of the sea and ocean cryolithozone, as well as the temperature of the bottom sediments.

I. Baranov developed ideas about the significant influence of neotectonics on the SMP's distribution and conditions of occurrence. A more or less detailed geocryological map of the continental zone and shelf of the Russian Arctic was compiled.

Since the early 1980s, the first factual data on SMP in the Barents and Kara Seas have been obtained based on offshore drilling and imperfect geophysical data. The concept of a predominantly discontinuous massive island and the island nature of SMP distribution in the Western Arctic has been established. In contrast, shallow drilling data from the Eastern Arctic shelf have provided a basis for the assumption of continuous, less frequently intermittent SMP in this region.

The development of methods and hardware for seismoacoustic profiling has become a powerful tool in SMP studying. Prognostic maps of SMP distribution were compiled to assess the probability of the occurrence of different types of continuity. The boundaries of SMP distribution were defined, and by the 1990s, estimates of its thickness appeared.

As seismoacoustic methods evolved and data on the manifestation of SMP was accumulated, including ongoing

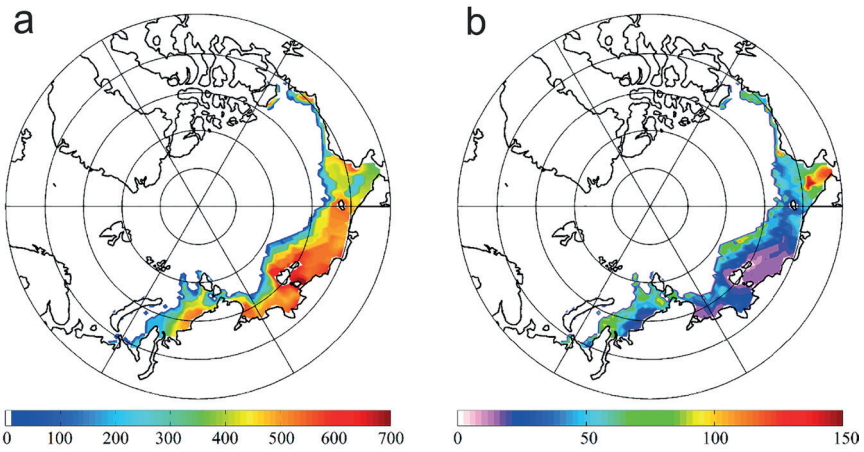

Fig. 11. Modeled submarine permafrost in the XX century. (a) The depth of the lower subsea permafrost boundary (in m). (b) The depth of the upper submarine permafrost boundary (in m) (Malakhova 2023)

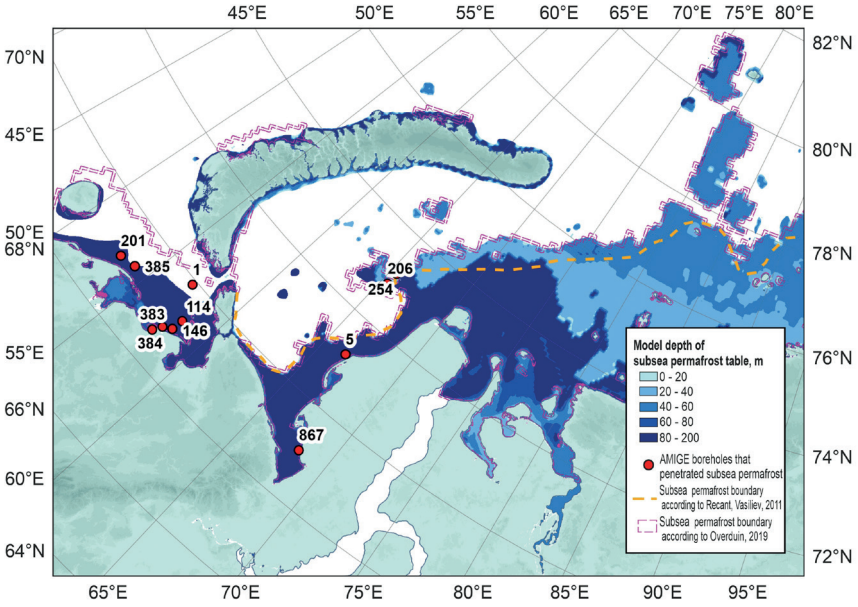

Fig. 12. Distribution and depth of the top of the submarine permafrost of the Kara and Barents Seas (Smirnov et al. 2024)

drilling, maps were constructed that substantiated the boundaries of SMP distribution and the depth of the top with factual data.

A major step in the study of shelf permafrost was the development of methods for mathematical modeling of the formation and evolution of SMP. Several maps were created reflecting the distribution and conditions of the SMP occurrence. These maps are detailed, but uncertainty in determining the properties of the sediments on the shelf and, most importantly, the boundary conditions leads to significant deviations in the estimates of the thickness and depth of the SMP top. Improvement of the models made it possible to develop methods for predicting the current and further degradation of the SMP under global warming and changes in the hydrology of the Arctic seas.

Digitization of the maps of SMP of the Russian Arctic shelf, which were created based on various approaches, and in different periods, and the formation of an album of GIS-oriented maps, can be used to compile more detailed maps of the cryolithozone of the shelf and for comparison of modeling results and actual data.

REFERENCES

Angelopoulos M., Overduin P.P., Miesner F., Grigoriev M.N., Vasiliev A.A. (2020). Recent advances in the study of Arctic submarine permafrost. Permafrost and Periglac.Process., 31, 442-453. DOI: 10.1002/ppp.2061.

Antipina Z.N., Are F.E., Voichenko V.V., Molochushkin E.N. (1979). Cryolithozone of the Arctic shelf of Asia. In: Late Quaternary history and sedimentogenesis of marginal and internal seas. Moscow, Russia: Nauka, pp. 183-189 (in Russian).

Baranov I.Ya. (1960). Geocryological map of the USSR at a scale of 1:10,000,000 (explanatory note). Moscow: Znanie, 48 p. (in Russian).

Baranov I.Ya. (1972). Geocryological (permafrost) map of the USSR at a scale of 1:5,000,000. Proceedings of the scientific All-Union conference on permafrost science. Moscow: Moscow State University Press, pp. 118-131 (in Russian).

Bogoyavlensky V., Kishankov A., Kazanin A. (2023a). Evidence of large-scale absence of frozen ground and gas hydrates in the northern part of the East Siberian Arctic shelf (Laptev and East Siberian seas). Marine and Petroleum Geology, 148, 106050, pp. 1-15.

Bogoyavlensky V.I., Kishankov A.V., Kazanin A.G. (2023b). Distribution of subaqueous permafrost in the Laptev Sea according to seismic exploration data using the refraction wave method. Arctic: ecology and economics, 13(4), pp. 501-515, DOI: 10.25283/2223-4594-2023-4-501-515. (in Russian).

Bogoyavlensky V. I., Kishankov A. V., Kazanin A. G. (2025). New information on subsea frozen ground in the Laptev and East Siberian seas based on seismic data. Doklady Earth Sciences, 521(11). DOI: 10.1134/S1028334X24605583.

Brown J., Ferrians O.J.J., Heginbottom J.A. and Melnikov E.S. (2001). Circum-Arctic map of permafrost and ground-ice conditions. Washington, DC: US Geological Survey in Cooperation with the Circum-Pacific Council for Energy and Mineral Resources. DOI: 10.3133/cp45.

Chekhovsky A.L. (1972). On the distribution of permafrost rocks under the shelf of the Kara Sea. Proceedings of the PNIIIS Gosstroy of the USSR. Moscow, vol. 18, pp. 100-110 (in Russian).

Chen Y., Li Q., Wen M., Wang Y., Duan W. (2022). Analytical and Numerical Analyzes on Vertical Site Responses of Submarine Permafrost in the Polar Ocean. Energies, 15, 5941. DOI: 10.3390/en15165941.

Dubrovin V.A. (2015). Results of drilling boreholes on the shelf of the Kara Sea in the area of the Marre-Sale geocryological station and the near future of its study. Proceedings of the International Conference "Arctic, Subarctic: mosaic, contrast, variability of the cryosphere", July 2–5, 2015, Tyumen: Epoch, pp. 109–111 (in Russian).

Gavrilov A.V., Malakhova V.V., Pizhankova E.I., Popova A.A., Buldovich S.N., Rolsklyakov A.G., Khilemonyuk V.Z. (2024). The state of the Arctic shelf cryolithozone and requirements for the necessary modern factual data for geocryological mapping. Proceedings of the VII International Geological and Geophysical Conference GeoEurasia 2024, vol. I, Tver: Poli Press LLC, pp. 372-378 (in Russian).

Gavrilov A., Pavlov V., Fridenberg A., Boldyrev M., Khilimonyuk V., Pizhankova E., Buldovich S., Kosevich N., Alyautdinov A., Ogienko M., Roslyakov A., Cherbunina M., and Ospennikov E. (2020). The current state and 125 kyr history of permafrost on the Kara Sea shelf: modeling constraints. The Cryosphere, 14, 1857–1873, DOI: 10.5194/tc-14-1857-2020.

Geocryological map of the USSR (1977). Edited by I.Ya. Baranov. Moscow, Main Directorate of Geodesy and Cartography under the Council of Ministers of the USSR.

Geocryological map of the USSR, scale 1:2,500,000 (1996). Edited by E.D. Ershov. Vinnitsa Cartographic Factory.

Grigoriev N.F. (1966). Permafrost of the Coastal zone of Yakutia. Moscow: Nauka, 180 p. (in Russian).

Grigoriev N.F. (1987). Cryolithozone of the coastal part of Western Yamal. Yakutsk: Publishing House of the Institute of the Sea of the Siberian Branch of the Russian Academy of Sciences, 111 p. (in Russian).

Gusev E.A., Kostin D.A., Markina N.V., Rekant P.V., Sharin V.V., Dorechkina D.E., Zarkhidze D.V. (2012). Problems of mapping and genetic interpretation of Quaternary deposits of the Arctic shelf of Russia (based on materials of GGK-1000/3). Regional Geology and Metallogeny, 50, pp. 5-14. (in Russian).

Kassens H. Bauch H., Drachev S., Gierlichs A., Niessen F., Taldenkova E., Roudoy A., Thiede J., Wessels M. (2000). The Transdrift VIII expedition to the Laptev Sea: the shelf drilling campaign of «Laptev Sea System 2000». Terra Nostra. No. 8, p. 39-40.

Koshurnikov A.V. (2023) Permafrost of the shelf of the Russian Arctic seas (based on geophysical research data). Abstract of Doctoral thesis. Moscow, Moscow University Press, 45 p.

Koshurnikov A.V., Tumskoy V.E., Skosar V.V., Efimov Ya.O., Kornishin K.A., Bekker A.T., Piskunov Yu.G., Tsimbelman N.Ya., Kosmach D.A. (2020). Submarine permafrost in the Laptev Sea. Intern. J. of Offshore and Polar Engineering, 30(1), pp. 86-93. DOI: 10.17736/ijope.2020.jc783.

Kulikov S.N., Rokos S.I., Tulapin A.V. (2014). On the criteria for identifying permafrost rock massifs in the Pechora Sea and southwestern Kara Sea on time sections of seismoacoustic profiling. Engineering Geophysics, 2014. Conference Proceedings. April 21-25, 2014. Gelendzhik, pp. 1-8. (in Russian).

Malakhova V. (2023). Modeling of the Arctic subsea permafrost thawing under possible climate warming. Proc. SPIE 12780, 29th International Symposium on Atmospheric and Ocean Optics: Atmospheric Physics, 127804U (17 October 2023). DOI: 10.1117/12.2688510.

Malakhova V.V. (2019). Subaqueous permafrost of the Arctic shelf: assessment of thickness and area of distribution. Proceedings of the XIII Siberian Conference and School of Young Scientists on Climate and Environmental Monitoring. October 15-19, 2019, Tomsk. (in Russian)

Malakhova V.V., Eliseev A.V. (2023). A Relationship between Changes of Surface Air and Sea Floor Temperatures at the Arctic Shelf from the Coupled Models Intercomparison Project, Phase 6 Data. Atmosphere, V. 14. P. 1024. DOI: 10.3390/atmos14061024.

Malakhova V.V., Eliseev V.A. (2020). Salt diffusion effect on the submarine permafrost state and distribution as well as on the stability zone of methane hydrates on the Laptev Sea shelf. Ice and Snow, 60, 533–546, (in Russian with English summary), DOI: 10.31857/S2076673420040058.

Malkova G., Drozdov D., Vasiliev A. et al. (2022). Spatial and Temporal Variability of Permafrost in the Western Part of the Russian Arctic. Energies, 15, 2311. DOI: 10.3390/en15072311.

Neizvestnov Ya.V., Soloviev V.A. et al. (1991). Forecast map of cryolithozone types of the shelf and islands of the Arctic seas of the USSR at a scale of 1:5,000,000. Scientific and technical report. Moscow, Rosgeolfond, No. 360606. (in Russian).

Nicolsky D.J., Romanovsky V.E., Romanovskii N.N., Kholodov A.L., Shakhova N.E., Semiletov I.P. (2012). Modeling Sub-Sea Permafrost in the East Siberian Arctic Shelf: The Laptev Sea Region. J. Geophys. Res. Earth Surf., 117, 1–22. DOI: 10.1029/2012JF002358.

Overduin P.P., Haberland C., Ryberg T., Kneier F., Jacobi T., Grigoriev M.N. and Ohrnberger M. (2015). Submarine permafrost depth from 385 ambient seismic noise. Geophysical Research Letters, 42, 7581–7588. DOI: 10.1002/2015GL065409.

Overduin P.P., Schneider von Deimling T., Miesner F., Grigoriev M.N., Ruppel C., Vasiliev A., Lantuit H., Juhls B. and Westermann S. (2019). Submarine permafrost map in the Arctic modeled using 1-D transient heat flux (SuPerMAP). Journal of Geophysical Research: Oceans, 124, 6, pp. 3490-3507. DOI: 10.1029/2018JC014675.

Permafrost in the Northern Hemisphere (2020). [online] Produced as a part of Nunataryuk research project. Cartographer: GRID-Arendal/ Nunataryuk. Available at: https://www.grida.no/resources/13519 [Accessed 25 Mar. 2025].

Polyak L., Niessen F., Gataullin V., Gainanov V. (2008). The eastern extent of the Barents–Kara ice sheet during the Last Glacial Maximum based on seismic-reflection data from the eastern Kara Sea. Polar Research, 27, pp. 162–174. DOI: 10.1111/j.1751-8369.2008.00061.

Portnov A., Mienert J., Serov P. (2014). Modeling the evolution of climate-sensitive Arctic subsea permafrost in regions of extensive gas expulsion at the West Yamal shelf. Journal of Geophysical Research: Biogeosciences, 119 (11), pp. 2082-2094. DOI: 10.1002/2014JG002685.

Rekant P.V. and Vasiliev A.A. (2011). Offshore permafrost in the Kara Sea. Earth's Cryosphere, 15(4), pp. 60-62.

Rokos S.I., Kostin D.A., Tulapin A.V., Kulikov S.N., Dlugach A.G. (2023). Frozen and cryotic soils in the Baydarata Bay area. Earth's Cryosphere, 27(5), pp. 3–13.

Romanovskii N.N., Gavrilov A.V., Pustovoit G.V., Kholodov A.L., et al. (1997). Off-shore permafrost distribution on the Laptev Sea shelf. Earth's Cryosphere, 1(3), pp. 9-18. (in Russian with English summary).

Romanovskii N.N., Kholodov A.L., Gavrilov A.V., Tumskoy V.E., Hubberten H.W., Kassens H. (1999) Ice-bonded permafrost thickness in the eastern part of the Laptev Sea shelf (results of computer modeling). Earth's Cryosphere, 3(2), pp. 22-32. (in Russian with English summary).

Shakhova N., Semiletov I., Sergienko V., Lobkovsky L., Yusupov V., Salyuk A., Salomatin A., Chernykh D., Kosmach D., Panteleev G., Nikolsky D., Samarkin V., Joye S., Charkin A., Dudarev O., Meluzov A., and Gustafsson O. (2015). The East Siberian Arctic Shelf: towards further assessment of permafrost-related methane fluxes and the role of sea ice. Phil. Trans. R. Soc. A., vol. 373, p. 2052. DOI: 10.1098/rsta.2014.0451.

Shcherbakov V.A., Ivanova V.V., Slinchenkov V.I. et al. (2018). Geocryological map of the marginal seas of the Arctic Ocean of the Arctic Zone of the Russian Federation at a scale of 1:5,000,000.. Explanatory note. St. Petersburg, FGBU «VNIIOkeangeologiya», 52 p. (in Russian).

Smirnov Yu.Yu., Matveeva T.V., Shchur N.A., Shchur A.A., Bochkarev A.V. (2024). Numerical modeling of subaqueous permafrost on the Eurasian Arctic shelf taking into account the zonality of the modern climate. Earth's Cryosphere, 28(5), pp. 38-59. DOI: 10.15372/kz20240504. (in Russian with English summary).

Soloviev V.A., Ginsburg G.D., Mikhalyuk Yu.N., Stanishcheva O.N., Telepnev E.V. (1981). Assessment of permafrost-geothermal conditions of the Barents-Kara shelf (report on topic 709). Leningrad, VNIIOkeangeologiya, 175 p., 12 graphs. appendix. (in Russian).

Westerveld L., Kurvits T., Schoolmeester T. et al. (2023) NUNATARYUK consortium. 2023. Arctic Permafrost Atlas. GRID- Arendal. DOI: 10.61523/KPJI4549.

Yakovlev D.V., Yakovlev A.G., Valyasina O.A. (2018). Permafrost study in the northern margin of the Siberian platform based on regional geoelectric survey data. Earth's Cryosphere, 22(5), pp. 67-84. DOI: 10.21782/EC2541-9994-2018-5(67-84)

Zhigarev L.A. (1997). Oceanic cryolithozone. Moscow: Moscow State University, 320 p. (in Russian).

RESEARCH PAPER

COUPLING THE TOWN ENERGY BALANCE (TEB) SCHEME WITH THE COSMO ATMOSPHERIC MODEL: EVALUATION AGAINST A BULK PARAMETERIZATION (TERRA_URB) FOR THE MOSCOW MEGACITY

Maria A. Tarasova[1,2,3,4,5]*, Mikhail I. Varentsov[1,2,3,4,5], Andrey V. Debolskiy[3,4,5], Victor M. Stepanenko[1,3]

[1]Faculty of Geography, Lomonosov Moscow State University, Leninskie Gory, 1, Moscow, 119991, Russia
[2]Hydrometeorological Research Center of Russia, B. Predtechenskiy Pereulok, 11-13, Moscow, 123242, Russia
[3]Research Computing Center, Lomonosov Moscow State University, Leninskie Gory, 1, bld.4, Moscow, 119991, Russia
[4]Moscow Center for Fundamental and Applied Mathematics, Leninskie Gory, 1, bld.4, Moscow, 119991, Russia
[5]A.M. Obukhov Institute of Atmospheric Physics, 3 Pyzhyovskiy Pereulok, Moscow, 119017, Russia
***Corresponding author:** mkolennikova@mail.ru
Received: March 30th 2024 / Accepted: July 18th 2025 / Published: October 1st 2025
https://doi.org/10.24057/2071-9388-2025-3975

ABSTRACT. Numerical weather prediction (NWP) models, coupled with urban parameterizations, play a crucial role in understanding and forecasting meteorological conditions within urban environments. In the mesoscale NWP model COSMO, only one urban parameterization, TERRA_URB, is available in the model's operational version. TERRA_URB describes the city as a flat surface with modified physical properties in accordance with the urban canyon geometry. In this study, we have coupled the latest version 6.0 of the COSMO atmospheric model with a more sophisticated urban canopy model, TEB (Town Energy Balance), which explicitly simulates the energy exchange between the facets of the urban canyon. Here, we present the coupling approach and assessment of the model's sensitivity to urban schemes of different complexity (TEB and TERRA_URB) over the Moscow region for August 2022. Despite using the same external parameters for both schemes, simulations demonstrate notable differences in modeled temperature, with TEB generally producing lower nighttime and morning temperatures. This leads to a greater underestimation of the urban heat island intensity in TEB when compared with the observations but improves the modeled diurnal cycle of the urban temperature. We attribute the observed temperature discrepancies to the different descriptions of heat conductivity and storage within urban surfaces. Although there are no clear advantages to using a more complex parameterization in terms of model air temperature errors, TEB offers more options to fine-tune input parameters and takes into account additional processes, in particular those associated with building heating and cooling, as well as with urban green infrastructure.

KEYWORDS: urban parameterizations, urban climate, atmospheric models, urban heat island, Moscow agglomeration, COSMO

CITATION: Tarasova M. A., Varentsov M. I., Debolskiy A. V., Stepanenko V. M. (2025). Coupling the Town Energy Balance (TEB) Scheme with the COSMO Atmospheric Model: Evaluation Against a Bulk Parameterization (TERRA_URB) for the Moscow Megacity. Geography, Environment, Sustainability, 3 (18), 118-134
https://doi.org/10.24057/2071-9388-2025-3975

ACKNOWLEDGEMENTS: Adaptation and testing of the TEB urban canopy model for conditions of Moscow was supported by the Russian Science Foundation № 24-17-00155. Coupling between TEB and COSMO was supported under the state assignment of Lomonosov Moscow State University. Preparation of the input parameters for urban canopy models was carried out with the financial support of the Russian Ministry of Science and Higher Education, agreement № 075-15-2019-1621. Supercomputer simulations and model evaluation were supported by the Federal Service for Hydrometeorology and Environmental Monitoring of Russia (topic № 125032004255-7).

Conflict of interests: The authors reported no potential conflict of interests.

INTRODUCTION

Modern numerical weather prediction (NWP) models, employed for forecasting and studying the atmospheric processes, operate at grid spacing down to 10 kilometers at the global scale and the first few kilometers at the regional scale, with pioneering high-resolution studies presenting hectometric grid spacing [Lean et al. 2024]. At such scales, it is not feasible to explicitly simulate the energy and momentum exchange between the atmosphere and specific elements of the urban environment, such as buildings. To address this issue, numerical models are coupled with urban parameterizations, also known as urban canopy models (UCMs). Most UCMs are based on the concept of the "urban canyon" [Nunez and Oke 1977], which assumes the description of the whole

urban geometry by two main representative parameters – the height of buildings and the width of the street between them. Urban parameterizations differ both in the complexity of describing physical processes and in approaches to coupling with atmospheric models. These include slab models or bulk parameterizations, single-layer urban canopy models (SLUCM) and multilayer urban canopy models (MLUCM) [Masson 2006; Grimmond et al. 2010; Garuma 2018; Tarasova et al. 2023].

Slab models, e.g., TERRA_URB [Wouters et al. 2016], one of the urban parameterizations available in the WRF atmospheric model as part of the Noah-LSM land surface model [Ek et al. 2003; Liu et al. 2006], and the JULES surface scheme [Best 2005], are incorporated into the land surface models, modifying their basic parameters, such as imperviousness, surface radiative, and soil thermal properties, taking into account the features of the urban environment.

Single-layer UCMs (SLUCMs), e.g., TEB (Town Energy Balance) [Masson 2000], SLUCM developed by [Kusaka 2001], MORUSES (Met Office–Reading Urban Surface Exchange Scheme) [Porson et al. 2010], explicitly simulate physical processes inside the urban canyon. These models reproduce the thermal heterogeneity of the urban environment by separately solving the energy balance for the roof, wall, and road surfaces. To calculate the surface temperature, SLUCMs simulate heat transfer within the roof, roads, and walls, dividing them into layers of certain thickness. They also simulate shortwave and longwave radiation balances of the mentioned surfaces, considering the effects of shading, reflection, and emission within the canyon. Heat and moisture turbulent fluxes are determined using the resistance approach and are proportional to the differences between surface and air temperatures/humidities, wind speed, and heat and moisture transfer coefficients. The urban canyon in the SLUCMs is assumed to be squeezed below the bottom surface of the atmospheric model. Therefore, SLUCMs provide lower boundary conditions that determine the interaction between the urban surface and the lower level of the atmospheric model.

Multilayer UCMs, e.g., BEP (Building Effect Parameterization) [Martilli et al. 2002], DCEP (Double-Canyon Effect Parameterization) [Schubert et al. 2012], TEB [Schoetter et al. 2020], represent the physical processes inside the urban canyon as well. However, unlike SLUCMs, these models divide the urban canopy into a number of horizontal layers that interact with the atmospheric model, assuming the canyon is immersed into the lowest levels of the atmospheric grid. Additional terms, which describe the contribution of the urban surface, are added to the prognostic equations of momentum, temperature, humidity, and turbulent kinetic energy at the model levels that are inside the urban canopy. These terms are calculated at a finer vertical resolution on the urban grid and then aggregated onto the grid of the atmospheric model.

Modern NWP models differ in the set of available UCMs: some provide an opportunity to choose between parameterizations of varying degree of complexity, while others only have a single option available. This study focuses on the COSMO (Consortium for Small-Scale Modeling) regional, non-hydrostatic atmospheric model developed and maintained by the COSMO consortium and COSMO-CLM community [Rockel et al. 2008]. Despite the experience of including various UCMs into this model, only the slab TERRA_URB scheme is available in its operational version [Garbero et al. 2021]. The COSMO model with TERRA_URB is used for operational weather forecasts, e.g., over the Moscow region [Rivin et al. 2019; 2020], and for research tasks. The latter include modeling of the urban heat island (UHI) [Varentsov et al. 2018; 2019], the urban impacts on severe convective events [Platonov et al. 2024], the assessment of ecosystem services of the urban green infrastructure [Varentsov et al. 2023], and the estimation of the anthropogenic heat flux contribution to the temperature and wind regime in the city [Ginzburg and Dokukin 2021].

Multilayer UCMs DCEP and BEP (version BEP-Tree) were incorporated into the COSMO model in the research mode under separate branches of the model [Schubert and Grossman-Clarke 2014; Mussetti et al. 2020] and have not been merged into the latter model updates. The single-layer UCM TEB was also implemented into the COSMO model by [Trusilova et al. 2013]. However, simulations of the Moscow heat island using two UCMs, TERRA_URB and TEB, within the COSMO model revealed that the coupling between COSMO and TEB was incorrectly implemented, leading to unrealistic results [Varentsov et al. 2017]. The spatial distribution of temperature anomalies demonstrated a highly variable field, with a strong signal in the urban cells with almost no effect transmitted to the neighboring cells without buildings (see Fig. 4 in [Varentsov et al. 2017]). Furthermore, the vertical structure of the thermal anomaly induced by the city when using the TEB scheme was inadequate; both the intensity and the vertical extent of the response were significantly lower compared to those simulated with TERRA_URB (see Fig. 5 in [Varentsov et al. 2017]). This suggests that the coupling of the TEB UCM with the COSMO atmospheric model may have been performed incorrectly, leading to a lack of transmission of the signal from the city surface to the atmosphere.

This study is devoted to the reimplementation of the TEB UCM into the latest operational version of the COSMO model and its comparison with the simpler TERRA_URB parameterization. Here we outline the technical details of the coupling approach, demonstrating the corresponding effects of the city's influence on the atmosphere. To analyze the sensitivity of COSMO to different UCMs, we compare simulations using the single-layer TEB UCM and the simpler slab scheme TERRA_URB with the same external city-descriptive parameters.

The article is organized as follows. The next section describes in detail the numerical weather forecast model COSMO, the urban canopy model TEB, and the elaborated coupling approach, as well as the setup of the numerical experiments. Section Results presents the results of the comparison of two UCMs and their assessment by the observations. Interpretation and discussion of the revealed differences in simulations between two UCMs are presented in the Discussion section, followed by conclusions in the last section.

MATERIALS AND METHODS

COSMO model

The COSMO model is a non-hydrostatic limited-area atmospheric model that has been vastly used both for operational and research applications. The model solves the hydro-thermodynamic equations for a compressible flow in a moist atmosphere in the advection form. The model uses the delta-two-stream method of the Ritter-Geleyn scheme for radiative transfer [Ritter and Geleyn 1992], the Tiedtke scheme to parameterize convection, which is not explicitly resolved [Tiedke 1989], and a prognostic turbulent kinetic energy closure at level 2.5 to

describe subgrid-scale turbulence [Doms et al. 2021]. The multi-layer land surface model TERRA is used to calculate the heat, moisture, and momentum exchange between the surface and the atmosphere [Heise et al. 2006; Schrodin and Heise 2001; Schulz and Vogel 2020].

To describe the interaction between the atmosphere and the urban surface, the TERRA model has been modified by integrating the TERRA_URB urban parameterization [Wouters et al., 2016]. For this purpose, a tile approach has been introduced into the COSMO model, assuming that the model grid cell can be represented partly by the natural and by the urban surface. The surface temperatures, heat and moisture fluxes, and other variables are calculated for each individual tile and then aggregated according to their areal fraction in the grid cell.

In this study, we use the latest version of the COSMO 6.0 model.

Town Energy Balance (TEB) urban canopy model

The TEB urban parameterization is a single-layer urban canopy model that can be used both as a standalone model and coupled to the numerical atmospheric models [Masson 2000; Masson 2013; Meyer et al. 2020] to simulate the impact of the urban surface on the atmospheric boundary layer. We used the TEB_open_source_v3_sfx8.1 version[1] to integrate it into the COSMO atmospheric model.

Like many other UCMs, TEB is based on the concept of the street canyon and calculates energy balance separately for its walls, roof, and road. To derive the surface temperature, TEB solves the thermal conduction equation with zero flux at the lower boundary for roads and building's internal temperature for roofs and walls. The model accounts for water reservoirs and snow cover on the horizontal surfaces. The radiation exchange considers reflections and shading effects inside the canyon. It can be modeled as an average over numerous canyons with an isotropic distribution of their azimuths, or for a specified road azimuth, taking into account the different shadings of two opposite walls [Lemonsu et al. 2012].

Turbulent sensible and latent heat fluxes are calculated according to the resistance approach (Fig. 1), where the transfer coefficients depend on wind speed and stability functions [Lemonsu et al. 2004]. Heat fluxes from industry and traffic can be added as constants, while anthropogenic heat flux associated with building heating and cooling is explicitly simulated at each time step using a simple model of building indoor temperature [Masson et al. 2002] or a more comprehensive Building Energy Model (BEM) [Bueno et al. 2012]. BEM calculates anthropogenic heat and moisture fluxes related to heating, ventilation, and air conditioning and due to the presence of people or electrical devices inside the buildings. It takes into account air supply through walls and natural ventilation, including windows, in the energy balance of walls. TEB has an ability to specify urban vegetation inside the canyon, implicitly represented as a flat surface [Lemonsu et al. 2012], along with an interface for the "green roof" module [de Munck et al. 2013]. The simulation of solar panels on roofs [Masson et al. 2014] and irrigation of roads, vegetation, and "green roofs" [de Munck et al. 2013] are also possible.

Coupling approach

The coupling approach in our study is based on the interface that was previously developed for the interaction between COSMO and TERRA_URB. This interface assumes that the land surface model TERRA is called twice for each COSMO's grid cell: once for the natural tile and once for the urban tile, with modified bulk parameters according to the urban geometry [Wouters et al. 2016]. Simulated fluxes are further aggregated over the two tiles. In the case of TEB, we call it instead of TERRA for the urban tile, but only for the grid cells with a non-zero urban fraction. TEB's output is saved to the model variables that are used by TERRA for the urban tile and is further passed to the procedure that performs the aggregation of fluxes and surface parameters over the two tiles, as it was proposed for TERRA_URB [Wouters et al. 2016].

COSMO provides TEB with input quantities at each time step. TEB requires the current date, latitude and longitude of the cell, the height of the lowest model level, external parameters describing the geometry of the urban surface and its thermal and radiative properties, as well as atmospheric forcing variables (Table 1). It should be noted that the TERRA_URB slab model uses albedo, emissivity, heat capacity, and conductivity parameters aggregated over roofs, roads, and walls, while TEB considers these parameters for each surface separately. We have implemented this feature into the model code. However, in this study, we use the aggregated values for all surfaces for a correct comparison between the two UCMs. Based on the input data, TEB calculates output parameters as averaged over the canyon and roofs and passes them to the COSMO model. The main variables transferred from TEB to COSMO are the effective urban albedo, emissivity, surface temperature, and surface specific humidity, as well as sensible and latent heat fluxes and heat and moisture transfer coefficients. These variables are listed in Table 1.

Below we present a detailed description of how the fluxes calculated by the TEB parameterization are transferred to the COSMO atmospheric model.

Radiation Fluxes

To estimate reflected shortwave radiation, the COSMO model uses the solar albedo aggregated over natural and urban tiles (Eq. 1):

$$a_{so} = \delta_{urb} a_{so,\,urb} + \left(1 - \delta_{urb}\right) a_{so,\,nat} \qquad (1)$$

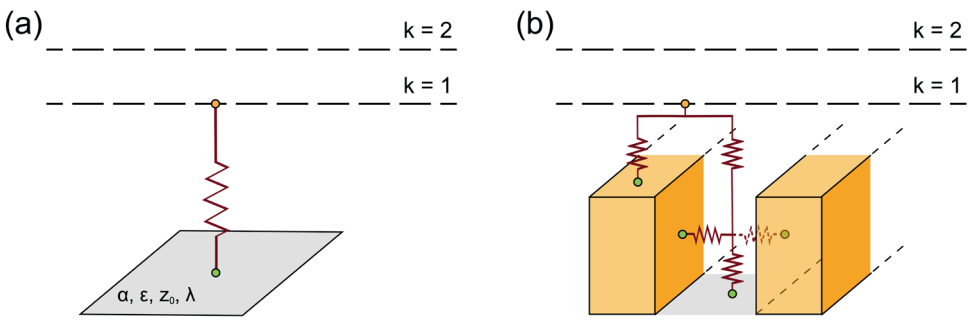

Fig. 1. Schematic representation of (a) TERRA_URB slab scheme and (b) TEB single-layer urban canopy model. Notation α, ε,z_0, and λ correspond to the albedo, emissivity, aerodynamic roughness, and thermal conductivity of the urban material. Dashed lines indicate levels of the atmospheric model. Modified after [Tarasova et al. 2023]

[1]https://opensource.umr-cnrm.fr/projects/teb/files

Table 1. Variables used in the coupling of TEB UCM into the COSMO model

Variable	Unit	Model variable
External static parameters for TEB		
Height of the lowest model level	m	hlev_teb*
Building areal fraction	–	urb_fr_bld
Building height	m	urb_h_bld
Canyon height-to-width ratio	–	urb_h2w
Volumetric heat capacity of urban materials**	$Jm^{-3}\ K^{-1}$	urb_hcap
Heat conductivity of urban materials**	$Wm^{-1}\ K^{-1}$	urb_hcon
Shortwave albedo of urban surfaces**	–	urb_alb_so
Emissivity of urban surfaces**	–	1 - urb_alb_th
Atmospheric forcing from COSMO to TEB		
Air temperature	K	t
Specific humidity	$kg\ kg^{-1}$	qv
Zonal component of wind velocity	$m\ s^{-1}$	u
Meridional component of wind velocity	$m\ s^{-1}$	v
Atmospheric pressure at the surface	Pa	ps
Rainfall rate	$kg\ m^{-2}\ s^{-1}$	prr_con + prr_gsp ***
Snowfall rate	$kg\ m^{-2}\ s^{-1}$	prs_con + prs_gsp (+ prg_gsp) ****
Downwelling direct shortwave radiation flux density	Wm^{-2}	swdir_s
Downwelling diffuse shortwave radiation flux density	Wm^{-2}	swdifd_s
Downwelling longwave radiation flux density	Wm^{-2}	lwd_s
TEB outputs for COSMO		
Urban surface albedo for shortwave radiation	–	teb_alb_so*
Urban surface emissivity	–	1 - teb_alb_th*
Urban surface temperature	K	teb_tstown_s*
Urban surface specific humidity	$kg\ kg^{-1}$	teb_qstown_s*
Heat and moisture transfer coefficient for urban surface	–	teb_tch_town*
Sensible heat flux for urban surface	Wm^{-2}	teb_shfl*
Latent heat flux for urban surface	Wm^{-2}	teb_lhfl*

* – New variables added to COSMO for its coupling with TEB. ** – Parameters can be set by the same value for all urban surfaces (roofs, walls, and roads) or separately for each surface. *** – The precipitation explicitly resolved by the atmospheric model and precipitation estimated by the convection parameterization are summed up. **** – The precipitation explicitly resolved by the atmospheric model and precipitation estimated by the convection parameterization are summed up. Grain is added to the solid precipitation if appropriate parameterization is used.

where a_{so} is the cell-averaged solar albedo, $a_{so,\ urb}$ is the solar albedo of the urban tile, $a_{so,\ nat}$ is the solar albedo of the natural tile.

As a result of shading and multiple reflections inside the urban canyon, the effective urban albedo is reduced compared to the albedo of individual building facets [Oke et al. 2017]. TEB UCM calculates the effective solar albedo at each time step, taking into account the incoming and reflected shortwave radiation by each canyon element (Eq. 2):

$$a_{so,\ urb} = \frac{S\uparrow_{urb}}{S\downarrow} \quad (2)$$

where $S\uparrow_{urb}$ is the outgoing shortwave radiation from the urban tile, including canyon and roof, $S\downarrow$ is the incoming shortwave radiation (forcing variable from the atmospheric model).

The reflection of shortwave radiation is considered isotropic and is approximated as an infinite number of efficient reflections between canyon elements [Masson 2000]. The outgoing shortwave radiation (direct and diffuse) is computed as the difference between the incoming shortwave radiation and the radiation absorbed by each of the canyon elements (Eq. 3):

$$S^{\uparrow}_{urb} = S^{\downarrow} - \sum_{i=1}^{N} \delta_i S_{net,\,i} \tag{3}$$

where $S_{net,i}$ is the net solar radiation at the i-th surface, δ_i is the ratio of the certain surface area to the area of the urban tile, i is the surface type identifier: road ("r"), wall ("w"), roof ("R").

The outgoing longwave radiation is calculated by COSMO based on the Stefan-Boltzmann law using surface temperature and emissivity aggregated over the tiles (Eqs. 4-5):

$$T_s = \sqrt[4]{\delta_{urb} T^4_{s,\,urb} + \left(1-\delta_{urb}\right) T^4_{s,\,nat}} \tag{4}$$

$$\varepsilon = \delta_{urb}\varepsilon_{urb} + \left(1-\delta_{urb}\right)\varepsilon_{nat} \tag{5}$$

where T_s and ε are the cell-averaged surface temperature and emissivity, $T_{s,urb}$ and ε_{urb} are the surface temperature and emissivity of the urban tile, $T_{s,\,nat}$ and ε_{nat} are the surface temperature and emissivity of the natural tile.

The effective surface temperature of the urban canyon is calculated through the outgoing longwave radiation according to the Stefan-Boltzmann law (Eq. 6):

$$T_{s,\,urb} = \sqrt[4]{\frac{L^{\uparrow}_{urb} - L^{\downarrow}\left(1-\varepsilon_{urb}\right)}{\sigma\varepsilon_{urb}}} \tag{6}$$

where $L^{\uparrow}_{urb}$ is the outgoing longwave radiation from the urban canyon, $L^{\downarrow}$ is the incoming longwave radiation (forcing variable from the atmospheric model), $L^{\downarrow}\left(1-\varepsilon_{urb}\right)$ is the reflected longwave radiation, σ is the Stefan-Boltzmann constant.

The outgoing longwave radiation is calculated as the difference between the incoming longwave radiation and the radiation absorbed by each of the canyon elements (Eq. 7):

$$L^{\uparrow}_{urb} = L^{\downarrow} - \sum_{i=1}^{N} \delta_i L_{net,\,i} \tag{7}$$

where $L_{net,i}$ is the net longwave radiation at the i-th surface, taking into account reflection and emission between canyon's surfaces.

Net longwave radiation at each canyon's surface consists of the atmospheric radiation coming directly from the sky and the radiation emitted or reflected from other canyon elements (road or walls). The reflection of longwave radiation assumes a single reflection of incident longwave radiation by the canyon surface.

Emissivity is calculated as a weighted average for each surface, taking into account the fraction of each canyon element and the sky view factor (Eq. 8):

$$\varepsilon_{urb} = \sum_{i=1}^{N} \delta_i \Psi_{i\to sky} \varepsilon_i \tag{8}$$

where $\Psi_{i\to sky}$ is the sky view factor for surface i, ε_i is the emissivity of surface i.

Turbulent Heat and Moisture Fluxes

To represent the turbulent heat and moisture exchange between the surface and the atmosphere, the sensible and latent heat fluxes are aggregated over the two tiles (Eqs. 9-10):

$$H = \delta_{urb} H_{urb} + \left(1-\delta_{urb}\right) H_{nat} \tag{9}$$

$$LE = \delta_{urb} LE_{urb} + \left(1-\delta_{urb}\right) LE_{nat} \tag{10}$$

where H, LE are the cell-averaged sensible and latent heat fluxes, H_{urb}, LE_{urb} are the sensible and latent heat fluxes of the urban tile, H_{nat}, LE_{nat} are the sensible and latent heat fluxes of the natural tile. To ensure consistency between the sensible and latent heat fluxes leaving the soil for individual tiles and those entering the atmosphere, additional technical adjustments are made (see Appendix).

TEB computes the turbulent fluxes from the urban canyon as weighted averages from each individual surface, with the addition of heat (and moisture) fluxes from traffic and industry (Eqs. 11-12):

$$H_{urb} = \sum_{i=1}^{N} \delta_i H_i + H_{traffic} + H_{industry} \tag{11}$$

$$LE_{urb} = \sum_{i=1}^{N} \delta_i LE_i + LE_{traffic} + LE_{industry} \tag{11}$$

where H_i, LE_i are the sensible and latent heat fluxes from the i-th surface, $H_{traffic}$, $LE_{traffic}$ are sensible and latent heat fluxes from traffic, $H_{industry}$, $LE_{industry}$ are sensible and latent heat fluxes from industry.

Fluxes from the roof, road, and walls are defined in accordance with the resistance approach, where the heat and moisture transfer coefficients are calculated by the Monin-Obukhov theory for horizontal surfaces and under empirical dependencies for vertical surfaces [Rowley et al. 1930; 1932]. Air temperature, humidity, and wind speed, which are required to calculate the fluxes, are taken from the atmospheric forcing level for the roof, and from the canyon's volume for the road and walls. The air temperature and humidity are assumed to be homogeneous inside the canyon. The wind speed for flux calculation from the road and walls is estimated at half the canyon height, assuming an exponential wind profile inside the urban canopy [Rotach 1995; Arya 1988]. Despite the recent study by [Tarasova et al. 2024] suggests using an alternative parameterization of the in-canopy wind profile; it is not included into the model version used in this study.

Momentum Fluxes

The calculation of momentum fluxes has been preserved using the same approach as in the TERRA_URB urban scheme. The urban tile is represented as a highly rough surface, with the aerodynamic roughness length defined proportionally to the average building height [Sarkar and De Ridder 2010]. The thermal roughness is described via the Reynolds roughness number, with refined coefficients derived from experiments with outdoor urban-scale models [Kanda et al. 2007].

Model Setup and External Data

We employ the new version of the COSMO model, coupled with the single-layer TEB UCM, to simulate the meteorological conditions of the Moscow agglomeration

with 1-km grid horizontal spacing. To evaluate the sensitivity of the model to the choice of the UCM, we also run identical simulations using the slab TERRA_URB scheme. Additionally, the noURB experiment was conducted with urban parameterizations switched off. The simulations cover the period of August 2022, which was characterized by an extremely high urban heat island in Moscow [Varentsov et al. 2023]. The monthly-averaged UHI intensity at the city center was 3.4°C, which is 1°C higher than the average value for the period 2000-2020 [Lokoshchenko et al. 2023].

We use two nested domains centered at the Moscow region. The ERA5 reanalysis data with 0.25°×0.25° grid spacing [Hersbach et al. 2020] is utilized to define boundary and initial conditions for the outermost domain with a 3-km grid spacing, covering an area of 720 × 720 km around Moscow (240 × 240 grid cells). Initial conditions for soil temperature and humidity are taken from the global operational analysis of the ICON model with a 13-km resolution. According to [Varentsov et al. 2023], using ICON initial data instead of ERA5 reanalysis allows for a more accurate simulation of near-surface temperature and humidity. Simulations for the outermost domain are further used to force simulations for the innermost domain with a horizontal grid spacing of 1 km, 240 × 240 grid cells, and activated urban schemes (excluding noURB simulation). The vertical resolution in COSMO is set to 50 atmospheric levels (up to a height of 22 km), of which 10 are located in the lower one-kilometer layer; 8 layers are set in soil. The time integration step for the inner domain is 15 seconds.

We use the same set of external city-descriptive parameters for both UCMs. These parameters are compiled from different data sources, including OpenStreetMap (OSM) cartographic data [Samsonov and Varentsov 2020; Frolkis et al. 2024], a map of Local Climate Zones (LCZ) [Stewart and Oke 2012] available for Moscow from [Varentsov et al. 2020], and new global land cover databases: WorldCover [Zanaga et al. 2021] and Copernicus Global Land Cover (CGLC) [Buchhorn et al. 2020]. The fraction of the urban tile in the model grid cells is assumed to be equal to the impervious area fraction. The latter is estimated based on two global land cover databases: WorldCover with a 10-meter resolution and CGLC with a 100-meter resolution. The need to use two databases is determined by different physical interpretations of their urban land cover classes. WorldCover treats urban areas as impervious artificial surfaces, while CGLC treats them as built-up areas including urban greenery but excluding impervious surfaces outside built-up zones (highways, airstrip, etc.). The urban tile is assumed to be simultaneously impervious and built-up by both UCMs, so we define its area fraction as the intersection of the built-up (CGLC) and impervious (WorldCover) areas. Hence, the urban tile is treated as a completely impervious surface that does not include any vegetation, such as alleys or lawns between buildings, and the urban greenery is considered part of the natural tile.

The OSM cartographic data is a valuable source for obtaining morphometric characteristics of cities that could be applied as external parameters in urban modeling or, e.g., to estimate the anthropogenic heat flux (AHF) [Frolkis et al. 2024]. Here, we use the OSM data to initially assess the fraction of buildings and their average height. Further, the LCZ map is used to restore information about buildings where they are missing in the OSM data (typically in suburbs and industrial zones) based on statistical relationships between the building area fraction and impervious and built-up area fractions for different LCZs [Varentsov et al. 2023]. The height-to-width ratio of street canyons is defined analytically based on the mean area of individual buildings, total building area in a grid cell, and built-up area fraction estimated according to CGLC, assuming a square building shape and their regular arrangement [Samsonov and Varentsov 2020]. Thermal and radiative properties of the urban surface, such as albedo, emissivity, heat capacity, and heat conductivity, are defined according to the LCZ map and look-up tables. The resulting set of external city-descriptive parameters is shown in Figs. 2 and 3. We additionally emphasize that we use the same thermal and radiative parameters aggregated over all canyon surfaces for both UCMs.

Another important external parameter is the anthropogenic heat flux. However, it is treated differently in the TEB and TERRA_URB schemes. TEB explicitly simulates AHF from building heating and cooling using a Building Energy Model (BEM) [Bueno et al. 2012] or a simpler scheme based on limiting building's indoor temperature within a given range, while AHF from traffic and industry are prescribed by the user as time-invariant 2D fields. In TERRA_URB, the total AHF is provided as an external parameter. To simplify mutual comparison between UCMs, we set all external AHF sources to zero in both cases.

RESULTS

Simulations with the COSMO model coupled with two different UCMs, TEB and TERRA_URB, were performed with a 1 km spatial resolution for August 2022 over the Moscow agglomeration. Both UCMs reproduce a pronounced warm temperature anomaly over Moscow, i.e., the UHI. To assess the quality of these simulations in terms of reproducing the UHI, we used 2-meter temperature observations at 14 synoptic weather stations in the Moscow region. Weather stations were classified into two samples to represent the rural and urban conditions. The UHI intensity was estimated as the temperature difference between stations within Moscow and the background (suburban) stations. The Balchug weather station, located in the center of Moscow, characterizes the temperature regime of the city center and is usually used to obtain the maximum UHI intensity [Lokoshchenko et al. 2023]. In addition, the mean UHI intensity was analyzed as the difference between mean urban temperature, averaged over 5 Moscow stations: Balchug, VDNKh, Moscow State University Meteorological Observatory (MSU MO), Mikhelson Observatory, and Tushino [Lokoshchenko et al. 2023]. Background conditions were assessed using observational data from Klin, Dmitrov, Alexandrov, Pavlovsky Posad, Kolomna, Serpukhov, Naro-Fominsk, Maloyaroslavets, and Novo-Jerusalem stations, as referenced in [Varentsov et al. 2023; Kuznetsova et al. 2024]. Observational data for these stations at 1-hourly intervals were obtained from the archives of the Hydrometeorological Research Center of Russia. In this study, we used the nearest grid point to the weather station when comparing with measurements.

The COSMO model nearly perfectly reproduces the monthly-mean diurnal temperature cycle in rural areas using both UCMs. (Fig. 4a). However, for urban stations, there is a notable shift in the diurnal cycle: the model's air temperature lags relative to the observations (Fig. 4b, d), especially in the morning hours, regardless of the urban sample. The observed UHI intensity increases at night, reaching up to 6°C at the city center (Fig. 4c) and up to 3.7°C when averaged over the five urban stations (Fig. 4e). The underestimation of the modeled air temperature in the city center is especially pronounced at night and in the morning – the maximum UHI intensity is underestimated by

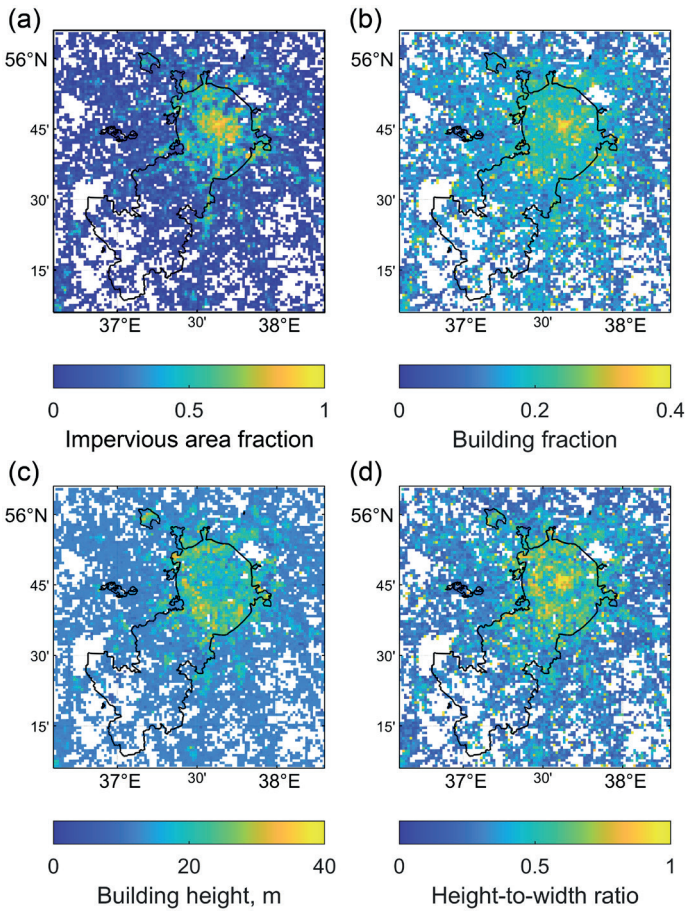

Fig. 2. City-descriptive parameters for the central part of the model's domain: (a) impervious area fraction, (b) building fraction, (c) building height, (d) canyon height-to-width ratio

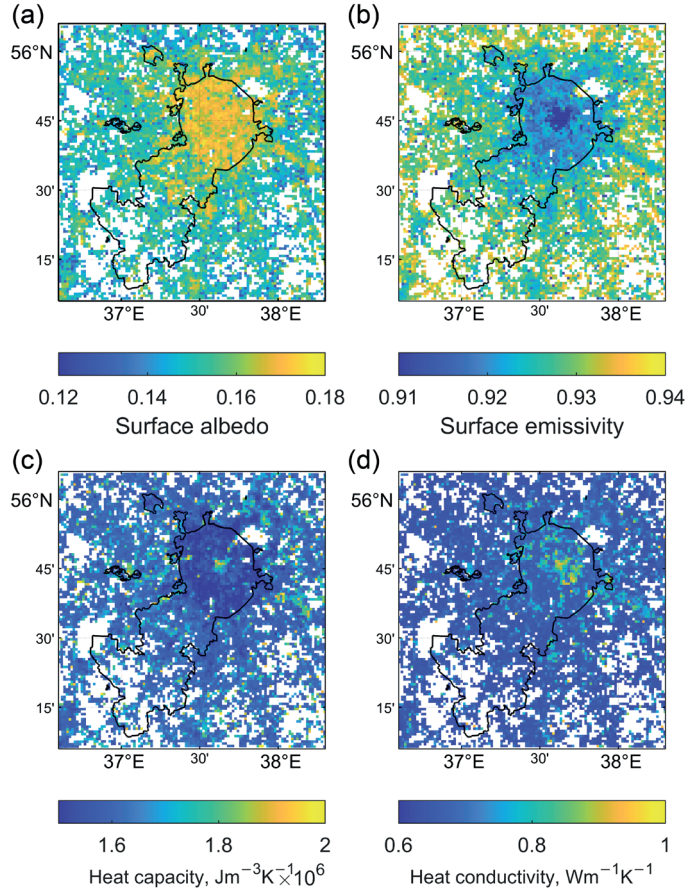

Fig. 3. Thermal and radiative parameters of the urban area for the central part of the model's domain: (a) surface albedo, (b) surface emissivity, (c) volumetric heat capacity, (d) heat conductivity

2°C. Differences between TEB and TERRA_URB are observed, with TEB showing lower nighttime air temperatures by up to 0.6°C. The mean errors (ME) of monthly-mean air temperature for the Balchug weather station are -1.18°C for TERRA_URB and -1.45°C for TEB, while for the average of five Moscow stations, these values are -0.66°C for TERRA_URB and -0.95°C for TEB. However, the root-mean-squared errors (RMSE) for the two UCMs are much closer, with RMSE values of 1.99°C (TERRA_URB) and 2.06°C (TEB) for Balchug, and 1.83°C (TERRA_URB) and 1.80°C (TEB) for the five urban stations.

The simulations were performed without anthropogenic heat flux, so agreement between observations and model data is not as good as in previous modeling studies for Moscow [Varentsov et al. 2020; Kuznetsova et al. 2024]. Despite the summer conditions, anthropogenic heat flux can be significant in forming the temperature regime, especially at nighttime [Salamanca et al. 2014].

Previous studies suggest that the vertical structure of the UHI in the lower troposphere is a key indicator of the correctness of coupling between UCM and the atmospheric model [Varentsov et al. 2017; 2018]. We analyze the vertical UHI extent as the temperature difference between simulations with TEB/TERRA_URB UCMs and the noURB run, in which urban effects are not taken into account, and the city is replaced by natural land cover types.

Fig. 5 presents vertical cross-sections of such a temperature difference through Moscow's center for two UCMs. Generally, results with the two UCMs are quite similar. The temperature anomaly is highest at the surface in the center of the urban area. The vertical extent of the daily average anomaly over the simulation period is observed up to 200-250 meters from the surface for both UCMs (Fig. 5a-c). In the daytime, UHI is much weaker but extends up to 1 km, with almost no difference in temperature anomaly between TEB and TERRA_URB (Fig. 5d-f). The differences between the UCMs become noticeable at night, when the model with TEB simulates weaker temperature anomalies (Fig. 5g-i). A pronounced nocturnal UHI exists within the 100-150 m layer, and above it changes to the opposite response, corresponding to a negative temperature anomaly of up to 0.1°C (Fig. 5g, h). This phenomenon, referred to the cross-over effect [Bornstein 1968] or cold lens [Khaikine et al. 2006], coincides with mast and radiosonde observations [Lokoshchenko et al. 2016] and previous simulations with the COSMO model for the Moscow region [Varentsov et al. 2017; 2018]. The presence of this cold layer may be attributed to more intense vertical mixing in the city center due to higher surface roughness and less stable stratification compared to rural areas, which, under stable stratification conditions, results in less intense surface inversions within the city.

Despite using the same external parameters, two UCMs reproduce the Moscow UHI with slight but noticeable differences. Our further analysis is aimed primarily at a deeper investigation and interpretation of the differences between simulations with TEB and TERRA_URB UCMs. Fig. 6a presents the differences in monthly mean 2-meter air temperature between the numerical experiments with TEB and TERRA_URB UCMs. The use of the TEB results in lower simulated air temperatures, with a maximum observed difference of 0.84°C between the UCMs. Furthermore, the differences in surface temperature are more pronounced than those in air temperature (Fig. 6c). The grid cells exhibiting the greatest differences in air temperature largely correspond to those showing significant surface temperature differences.

In order to find an explanation for the revealed temperature differences between TEB and TERRA_URB UCMs, we further analyze the components of the surface energy balance.

Differences between the two UCMs are observed in the effective surface albedo. The TERRA_URB model accounts for shading and reflections of solar radiation within urban canyons by parameterizing the effective albedo of the urban surface using an exponential function. This approach assumes that an increase in the height-to-width ratio of the canyon significantly reduces the effective albedo of the urban environment [Fortuniak 2007]. In contrast, the TEB model computes effective surface albedo at each time step based on the explicit account for multiple reflections of shortwave radiation between various canyon facets. Fig. 7 presents the cell-averaged surface albedo differences between TEB and TERRA_URB,

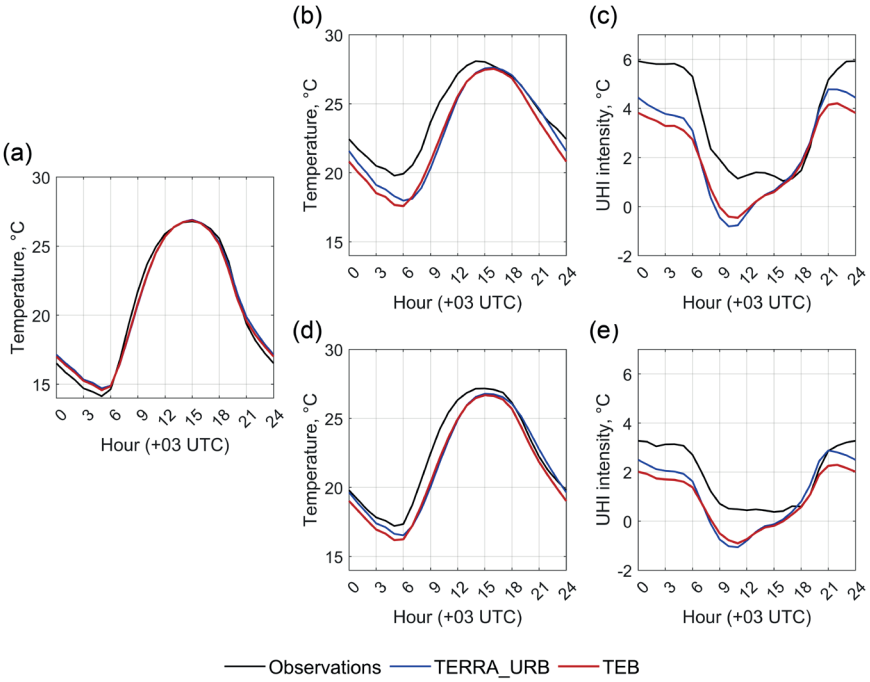

Fig. 4. The diurnal cycles of monthly mean (a) rural and (b) urban air (2-meter height) temperature at the Balchug weather station and (d) averaged over 5 Moscow weather stations, and (c, e) urban heat island (UHI) intensity during 1-31 August 2022 according to observations and simulation data

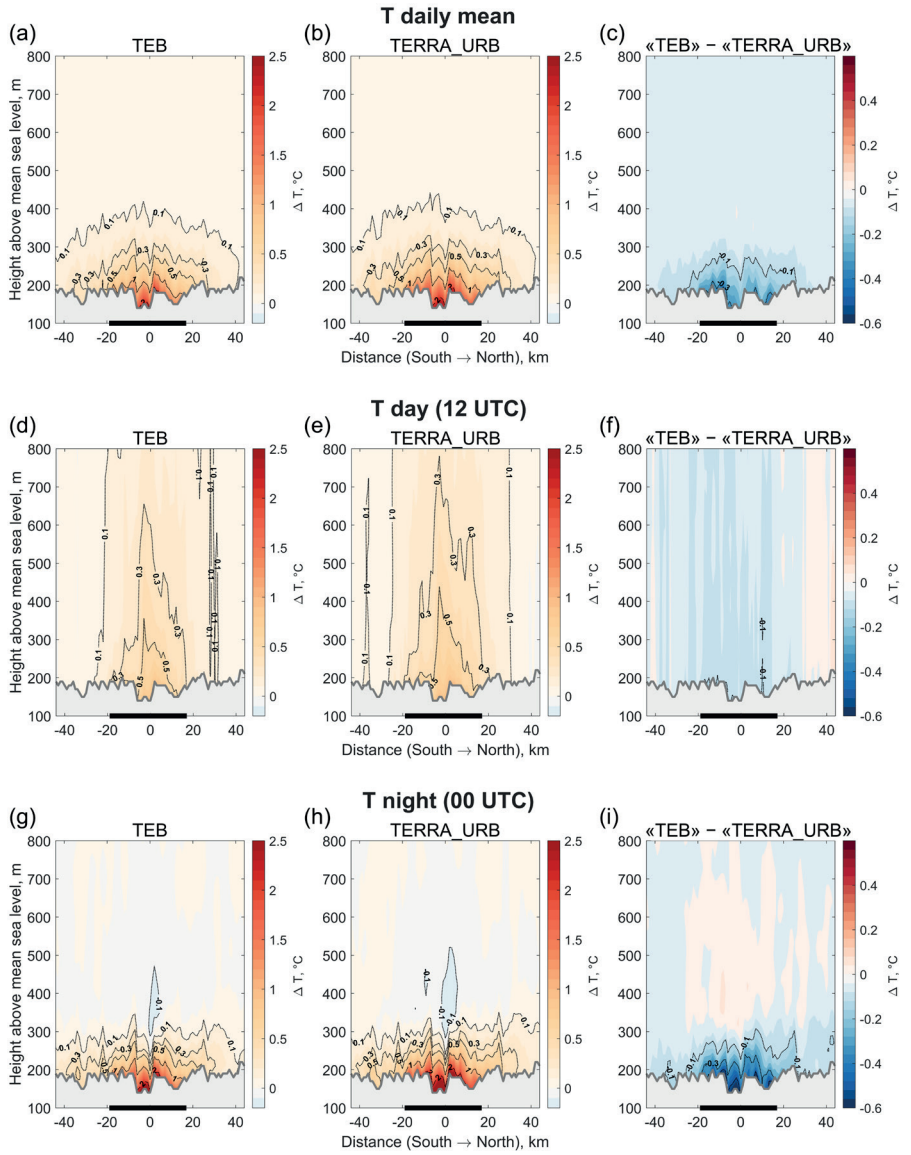

Fig. 5. Vertical sections through the center of Moscow from South to North, difference between (a-c) the daily average, (d-f) daytime average, and (g-i) nighttime average air temperature over the August of 2022 between experiments with switched-on and -off UCMs of the COSMO-CLM model with (a, d, g) the TEB scheme, (b, e, h) the TERRA-URB scheme, and (c, f, i) differences between them. The horizontal axis is directed from South to North; the location of the Balchug weather station corresponds to zero. The black solid line indicates the urban area

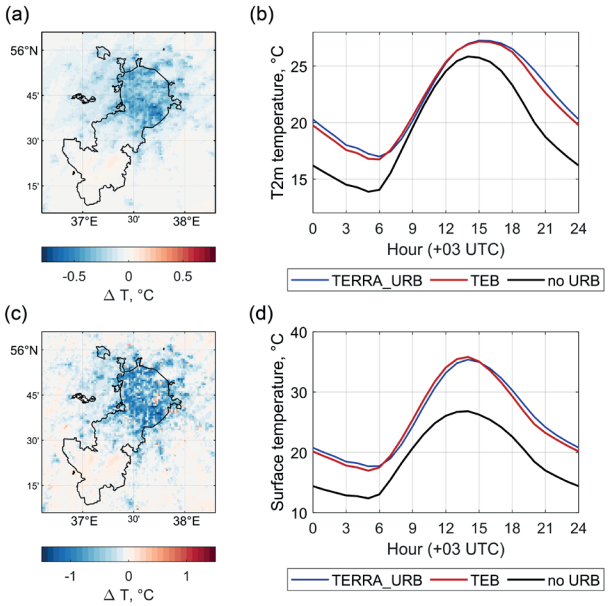

Fig. 6. Monthly mean (a) distribution of the air temperature (2-meter height) differences between the numerical experiments with COSMO+TEB and COSMO+TERRA_URB UCMs and (b) diurnal cycle of the air temperature for cells with urban fractions > 0.7 (183 cells). The same applies to the surface temperature (c) and (d)

along with the diurnal cycle of albedo observed in the two numerical experiments. The simulated surface albedo is consistently lower in TEB compared to TERRA_URB, with differences reaching up to 0.02. Additionally, TEB exhibits daily variations in albedo due to uneven illumination of different surfaces throughout the day, although these changes are relatively low (Fig. 7b). Roads typically possess a higher sky view factor than walls; therefore, as the sunlit area of the road increases, the effective albedo rises. This occurs because the surface albedo values for roads and walls are equal in our simulations. However, if roads had a significantly lower albedo, the opposite trend would be expected, with increased absorption leading to a decrease in a daytime effective albedo. The differences in surface albedo between the urban schemes are consistent with slightly higher maximum surface temperatures simulated with TEB (Fig. 6d); however, these findings cannot explain the lower daily mean and nocturnal air temperatures with respect to TERRA_URB.

The latent heat flux from the urban tile depends primarily on the amount of precipitation stored in the model over the impervious urban surface, such as water puddles. The maximum water content on the impervious surface in TERRA_URB is 1.31 mm, while the wet-surface fraction is parameterized, assuming its increase with increasing water content with an upper limit of 12% according to the measurements in Toulouse, France [Wouters et al. 2015]. TEB accumulates water on roofs and roads using the same approach as in TERRA_URB, with a difference in maximum water content (1 mm according to [Grimmond and Oke 1991]) and without an upper limit for the maximum wet-surface fraction. The excess water is assumed to form runoff to the sewer system. Fig. 8 presents the spatial distribution of average latent heat fluxes over August 2022 for TERRA_URB and TEB UCMs for urban tiles. The locations of areas with maximum latent heat flux are identified in both TEB and TERRA_URB models on the southern periphery of Moscow, whereas in the northern region, such spots are only noted in TERRA_URB simulations. Such differences can be explained by stochastic patterns of convective rainfall in the model and do not represent the differences between UCMs. The absolute values of latent heat flux for both urban models are relatively low. Additionally, there is a shift in the diurnal cycle, indicating increased evaporation during the morning hours for TEB, with a peak occurring between 9 AM and 12 PM MSK. In contrast, TERRA_URB shows its maximum later in the day, after noon. The cell-averaged values of latent heat flux are nearly identical between the experiments.

The distribution of sensible heat flux from urban tiles is presented in Fig. 9. The average sensible heat fluxes in TERRA_URB on the outskirts of Moscow are found to be higher than those in the city center (Fig. 9b). This phenomenon can be attributed to the significantly colder atmosphere in rural and suburban areas compared to central Moscow, resulting from a much lower urban fraction in these grid cells. Since turbulent heat flux is proportional to the difference between the surface and the air temperatures, the sensible heat flux is consequently lower in highly urbanized areas. In contrast, the TEB UCM exhibits an opposite distribution (Fig. 9a). In TEB, the effective sensible heat flux from the urban tile is aggregated across road, wall, and roof surfaces. The spatial distributions of sensible heat fluxes from these surfaces reveal the same pattern as for TERRA_URB, with higher values at the outskirts of the city (not shown). However, the pattern changes after the aggregation procedure, primarily due to the high wall fractions in the city center, where they exert a greater influence as an additional source of heat flux. In other words, for TEB, the highest surface-air temperature differences at the city's outskirts are compensated by a larger wall area in the central part of the city. The integral sensible heat fluxes from urban tiles differ between TEB and TERRA_URB, estimated as 79.6 W/m^2 and 92.6 W/m^2, respectively. As noted above, the primary differences between TEB and TERRA_URB are observed in the cells where the urban areal fraction is minimal. Consequently, these differences have a limited impact on the aggregated flux across the tiles. Thus, the integral cell-averaged quantities of sensible heat flux are almost equal and amount to 26.47 W/m^2 in TEB and 26.62 W/m^2 in TERRA_URB.

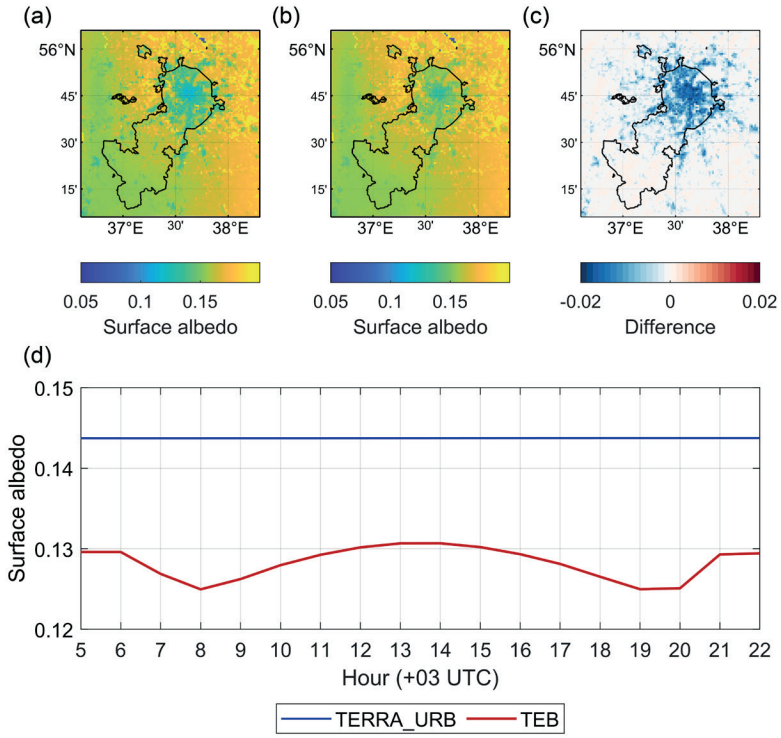

Fig. 7. The distribution of monthly mean cell-averaged surface albedo in (a) COSMO+TEB, (b) COSMO+TERRA_URB numerical experiments, and (c) differences between (a) and (b), (d) the monthly mean diurnal cycles of cell-averaged surface albedo for cells with urban fractions > 0.7 (183 cells)

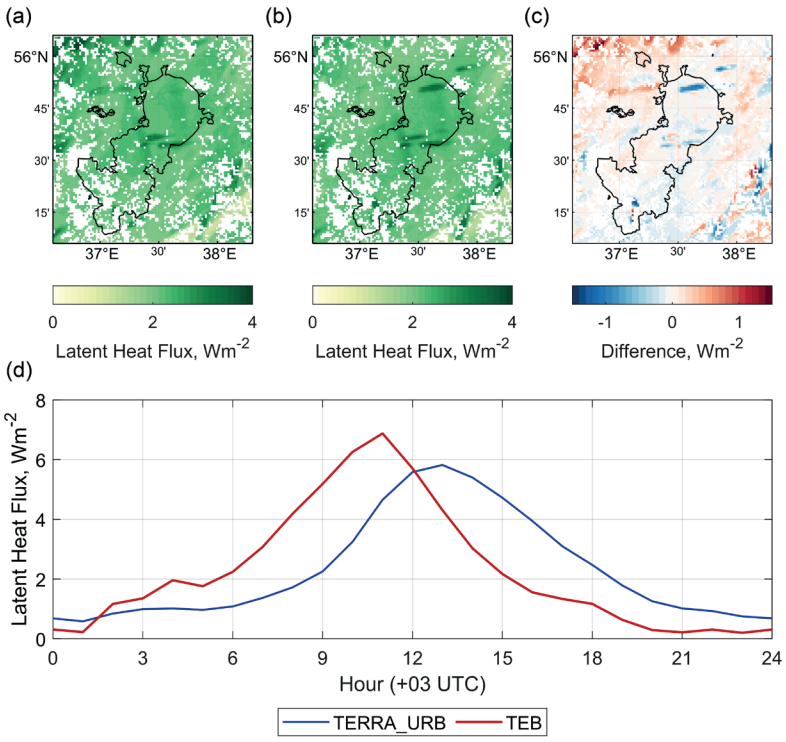

Fig. 8. The distribution of monthly mean latent heat flux for the urban tile in (a) COSMO+TEB, (b) COSMO+TERRA_URB numerical experiments, and (c) differences between (a) and (b), (d) the monthly mean diurnal cycles of cell-averaged latent heat fluxes for cells with urban fractions > 0.7 (183 cells)

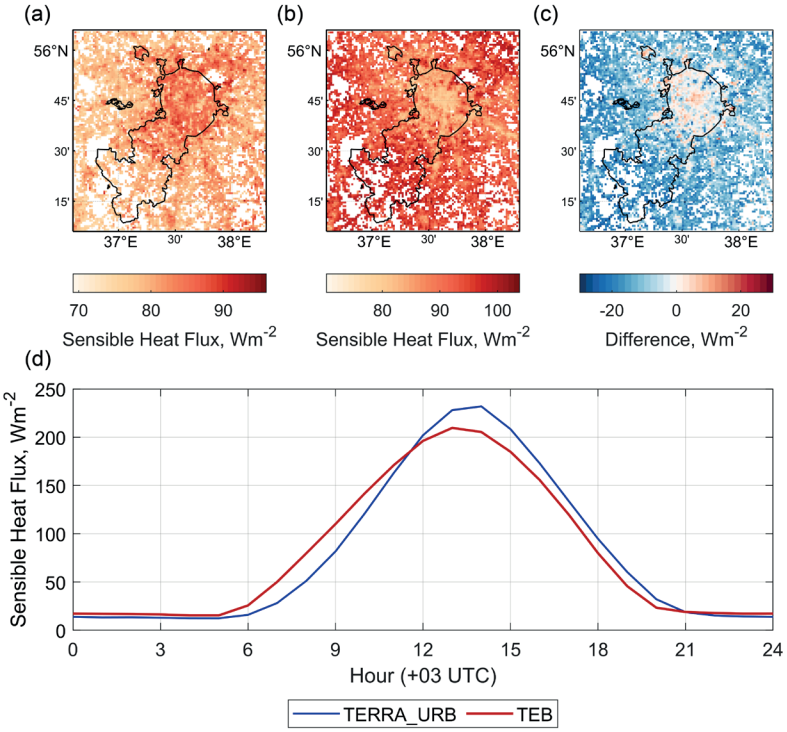

Fig. 9. The distribution of monthly-mean sensible heat flux for the urban tile in (a) COSMO+TEB and (b) COSMO+TERRA_URB numerical experiments, and (c) differences between (a) and (b), (d) the monthly mean diurnal cycles of cell-averaged sensible heat fluxes for cells with urban fractions > 0.7 (183 cells)

DISCUSSION

The presented results show differences between the slab model TERRA_URB and the single-layer urban canopy model TEB, which are primarily expressed in the lower air and surface temperatures simulated using TEB, with the most pronounced differences during nighttime and morning hours. The revealed temperature differences between the two urban schemes can be related to the different parameterizations representing surface albedo, turbulent heat and moisture fluxes, and heat storage within artificial surfaces in TEB and TERRA_URB. However, surface albedo is even lower in TEB and causes a slightly higher surface temperature at midday. Turbulent sensible and latent heat fluxes simulated by TEB and TERRA_URB differ in diurnal cycle and spatial patterns; however, there are only minor differences in their mean values over Moscow.

Another critical factor influencing surface temperature is heat conduction through the surface and its accumulation within urban materials. TERRA_URB uses the TERRA soil model with modified thermal properties. The values of heat capacity and heat conductivity for specific materials

(concrete, asphalt, etc.) are multiplied by the surface area index (SAI), which represents the total area of the road, two walls, and the roof divided by the plan area [Wouters et al. 2016]. This approach accounts for heat flux not solely over the horizontal surface but over an enlarged urban canyon surface. SAI values used in our simulations locally exceed 3.0, resulting in a triple increase of the mentioned thermal parameters, thereby enhancing surface heat conductivity and changing the rate of heat transfer to the ground [Wouters et al. 2016]. In contrast, TEB utilizes thermal parameters for artificial materials directly for roads, walls, and roofs, without applying multiplication by SAI, as the heat fluxes through these surfaces are simulated explicitly.

To assess the effect of the described SAI-based parameterization in TERRA_URB, we conducted an additional numerical experiment without modifying the materials' thermal parameters by SAI (TERRA_URB_noSAI). When these parameters are not multiplied by SAI, the model simulates significantly lower monthly average air temperatures. The mean differences between the basic TERRA_URB configuration and TERRA_URB_noSAI can reach up to 1°C (Fig. 10a). Significantly smaller, yet still noticeable, differences are observed when compared with TEB, with the most pronounced discrepancies occurring in central Moscow (Fig. 10b). Therefore, differences between the two UCMs in heat conduction processes at the surface-atmosphere interface are likely a key factor responsible for the observed differences in simulated temperatures. However, more specific quantification of these factors requires further investigation.

Our results indicate that the COSMO model is sensitive to the UCMs of different complexity, with the response primarily revealed in the air and surface temperature. Both the TEB and TERRA_URB UCMs successfully simulated the UHI effect. One might expect that the more advanced TEB UCM would enhance the accuracy of UHI simulation; however, the current results do not support this hypothesized improvement but also do not indicate a significant deterioration in the results. It is important to note that we used TEB in a simplified configuration, which did not account for building heating and cooling via the BEM model, nor urban greening, etc. The inclusion and optimization of these components are expected to yield improved outcomes in future simulations.

Furthermore, TEB suggests a finer analysis of model outputs due to the presence of more diagnostic variables, such as the temperature of different canyon surfaces (Fig. 11), along with temperature, specific humidity, and wind speed inside the urban canyon. These enhancements not only improve analytical capabilities but also enable more accurate validation against weather station data located within urban areas. The current methodology assumes comparing observations with the 2-meter height temperature provided by the NWP model as a diagnostic variable calculated according to the Monin-Obukhov theory above the urban canopy. The possibility to incorporate green spaces inside the urban canyon could replace the traditional tile approach, allowing for the use of canyon temperatures calculated by the UCM for verification purposes. In addition, the new output parameters provided by TEB enable the enhancement of the accuracy of thermal comfort index calculations by considering the urban canyon geometry.

In 2018, the Consortium for Small-scale Modeling announced the transition from the limited-area COSMO model to the global ICON model as the future operational model. The last version of COSMO was released in 2021, and after this, the model was not maintained and developed officially any more. However, the COSMO-CLM version remains in demand for long-term climate studies. The implementation of TEB into the COSMO model, along with sensitivity tests to UCMs of different complexity, could be useful for ICON as well, since these NWP models share the same land surface model.

CONCLUSIONS

The official version of the COSMO NWP model includes only one urban scheme, TERRA_URB, which represents the simplest class of bulk or slab urban canopy models. In this study, we propose and describe the coupling approach between the COSMO model and the more detailed single-layer urban canopy model TEB. Both UCMs are supposed to be squeezed into the model surface and provide the NWP model with lower boundary conditions. The TERRA_URB scheme modifies surface thermodynamic properties, taking into account the features of urban geometry, while TEB explicitly simulates the radiation and turbulent fluxes

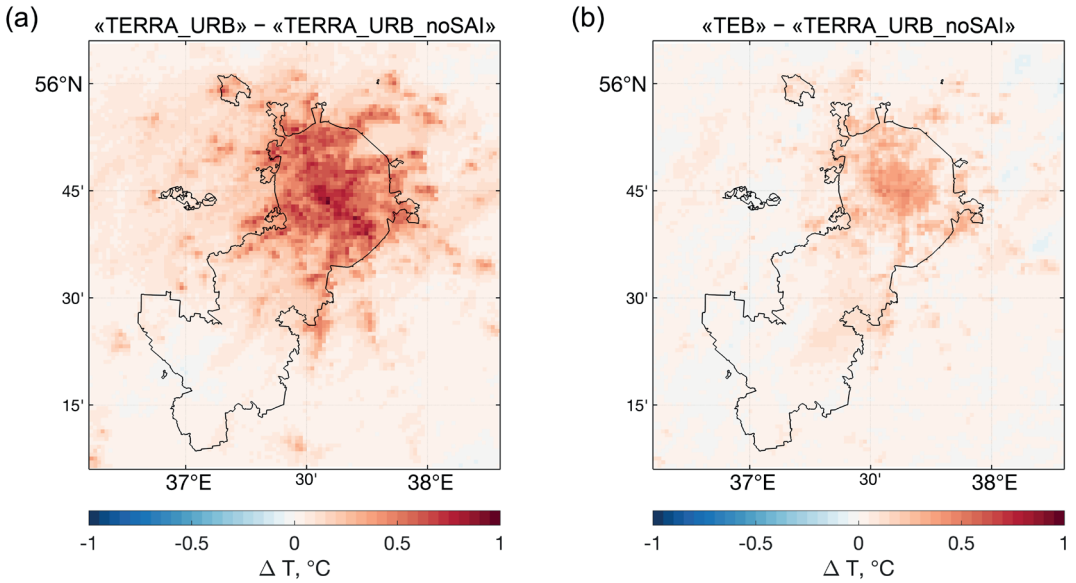

Fig. 10. The distribution of monthly mean air (2-meter height) temperature differences between the numerical experiments with (a) COSMO+TERRA_URB and COSMO+TERRA_URB_noSAI and (b) COSMO+TEB and COSMO+TERRA_URB_noSAI

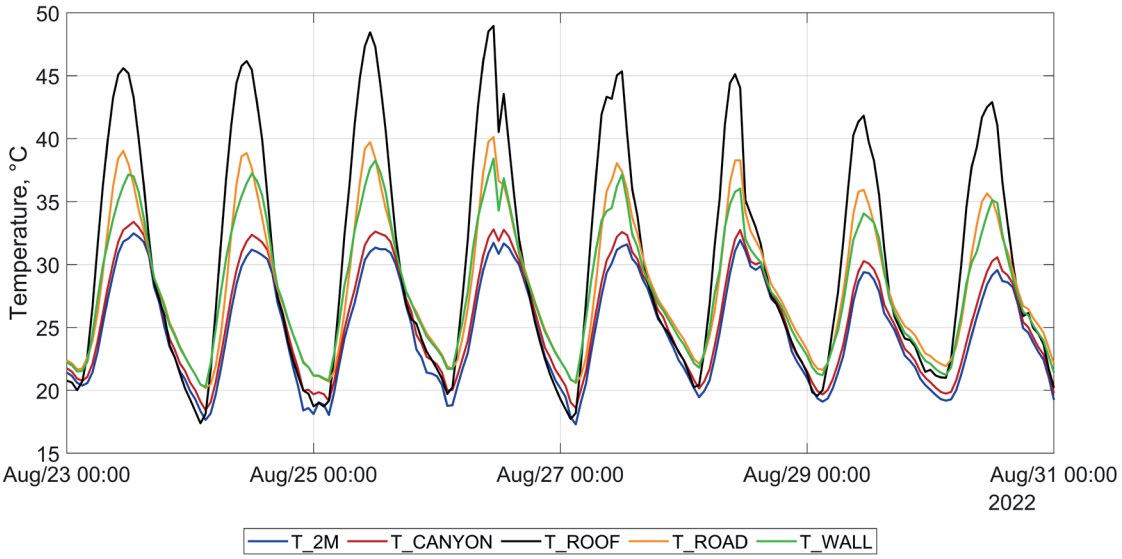

Fig. 11. Model simulations of COSMO+TEB for 2-meter height (T_2M), air canyon (T_CANYON), roof surface (T_ROOF), road surface (T_ROAD), and wall surface (T_WALL) temperature during the week of 23-31 August 2022 for the nearest to the Balchug weather station grid cell

inside the urban canyon and heat conduction and storage within its walls, road, and roof. The model's sensitivity to urban schemes of different complexity, TERRA_URB and TEB, was assessed over the Moscow agglomeration for August 2022. In such a comparison, we utilized TEB in a simplified configuration with the same external parameters as TERRA_URB and switched off anthropogenic heating in the UCMs.

Both UCMs allowed COSMO to reproduce the observed urban heat island of Moscow. In particular, simulations with two UCMs almost agree in terms of the vertical extent and intensity of the urban temperature anomaly in the atmospheric boundary layer. When compared with observations, both simulations demonstrate an underestimation of nighttime and morning temperatures in the city, which is not surprising due to the absence of anthropogenic heat flux in the model. Additionally, the modeled diurnal cycle of urban temperature lags with respect to observations.

We found slight but noticeable differences in urban air temperature between the simulations using TEB and TERRA_URB. The COSMO model with TEB simulates slightly lower 2-meter air temperatures compared to TERRA_URB, with a monthly mean difference of up to 0.84°C, resulting in a stronger underestimation of the observed UHI intensity. Meanwhile, the use of TEB improves the accuracy in reproducing the diurnal cycle of urban air temperatures, reducing the model's lag relative to observations.

A more detailed comparison between energy balance components simulated by TEB and TERRA_URB revealed several insights into the factors responsible for the temperature differences. Due to the explicit calculation of radiative fluxes within the urban canyon, the effective urban albedo in TEB was lower than the parameterized values in TERRA_URB, resulting in greater solar energy absorption and higher surface temperatures during the day. This difference in albedo contrasts with the revealed lower nocturnal and daily mean temperatures simulated with TEB. For sensible and latent heat fluxes, we obtained noticable differences between the UCMs in spatial patterns and diurnal cycle of fluxes from urban tile, yet with almost similar cell-average values. The primary factor contributing to the revealed temperature differences between the UCMs appears to be related to their different approaches to describing the heat conductivity and storage within urban surfaces.

Although the implementation of the TEB UCM in the COSMO model did not result in a substantial increase in the model quality metrics, it does open up broad opportunities for further improvements of the model accuracy. This can be achieved by activating and fine-tuning the components of the TEB, such as the BEM or street vegetation module "garden", refining the input parameters for these modules, and improving the parameterizations of specific processes like the wind profile [Tarasova et al. 2024]. Moreover, TEB greatly expands the capabilities of the COSMO model as a tool for evaluating urban planning and adaptation strategies, allowing for consideration of scenarios associated with changes in urban green infrastructure, building materials, energy management, and more.

The presented results were obtained for the warm period of August 2022. However, we expect other differences between the two UCMs in the cold season, since the UCMs use different snow models, as well as different treatments for anthropogenic heat flux, which is a key driver of the UHI in winter [Varentsov et al. 2020]. Simulation of the temperature regime for cold weather conditions in Moscow with TEB and TERRA_URB UCMs is planned to be analyzed in future studies.

The code of the coupled COSMO-TEB model is available upon request.

REFERENCES

Arya S.P. (1988). Introduction to Micrometeorology, Academic, New York.

Best M. J. (2005). Representing urban areas within operational numerical weather predictionmodels. Bound.-Layer Meteor., 114, 91–109.

Bornstein R.D. (1968). Observations of the Urban Heat Island Effect in New York City. J. Appl. Meteorol., 7, 575–582.

Buchhorn M., Lesiv M., Tsendbazar N.E., Herold M., Bertels L., and Smets B. (2020). Copernicus global land cover layers-collection 2. Remote Sens., 12, 1–14, DOI: 10.3390/rs12061044.

Bueno B., Pigeon G., Norford L. K., Zibouche K., and Marchadier C. (2012). Development and evaluation of a building energy model integrated in the TEB scheme. Geoscientific Model Development, 5(2), 433–448, DOI: 10.5194/gmd-5-433-2012.

de Munck C., Lemonsu A., Bouzouidja R., Masson, V., and Claverie R. (2013). The GREENROOF module (v7.3) for modelling green roof hydrological and energetic performances within TEB. Geoscientific Model Development Discussions, 6, DOI: 10.5194/gmdd-6-1127-2013.

Doms G. et al. (2021). A description of the Nonhydrostatic Regional COSMO-Model. Part II: physical parameterizations. Deutscher Wetterdienst Publisher, 171 pp.

Ek M. B., Mitchell K. E., Lin Y., Rogers E., Grunmann P., Koren V., Gayno G., and Tarpley J. D. (2003). Implementation of Noah land surface model advances in the National Centers for Environmental Prediction operational mesoscale Eta model. Journal of Geophysical Research, 108(D22), 8851, DOI: 10.1029/2002JD003296.

Fortuniak K. (2007). Numerical estimation of the effective albedo of an urban canyon. Theor. Appl. Climatol., 91, 245–258, DOI: 10.1007/s00704-007-0312-6.

Frolkis V.A., Evsikov I.A., Ginzburg, A.S. (2024). Modeling Anthropogenic Heat Flux during the Heating Season in Large Cities of the Russian Federation. Izv. Atmos. Ocean. Phys., 60, 407–420, DOI: 10.1134/S0001433824700361.

Garbero V., Milelli M., Bucchignani E., Mercogliano P., Varentsov M., Rozinkina I., Rivin G., Blinov D., Wouters H., Schulz J.–P., Schättler U., Bassani F., Demuzere M., and Repola F. (2021). Evaluating the urban canopy scheme TERRA_URB in the COSMO model for selected European cities. Atmosphere, 12(2), DOI: 10.3390/atmos12020237.

Garuma G. (2018). Review of urban surface parameterizations for numerical climate models. Urban Climate, 24, 830–851, DOI: 10.1016/j.uclim.2017.10.006.

Ginzburg A.S., Dokukin S.A. (2021). Influence of Thermal Air Pollution on the Urban Climate (Estimates Using the COSMO-CLM Model). Izv. Atmos. Ocean. Phys., 57, 47–59, DOI: 10.1134/S0001433821010059.

Grimmond C. S. B. and Oke T. (1991). An Evapotranspiration–Interception Model for Urban Areas. Water Resour. Res., 27, 1739–1755, DOI: 10.1029/91WR00557.

Grimmond C.S.B., Blackett M., Best M., Barlow J., Baik J.–J., Belcher S., Bohnenstengel S.I., Calmet I., Chen F., Dandou A., Fortuniak K., Gouvea M.L., Hamdi R., Hendry M., Kondo H., Krayenhoff S., Lee S.–H., Loridan T., Martilli A., Masson V., Miao S., Oleson K., Pigeon G., Porson A., Salamanca F., Shashua–Bar L., Steeneveld G.–J., Tombrou M., Voogt J., and Zhang N. (2010). The international urban energy balance models comparison project: First results from Phase 1. Journal of Applied Meteorology and Climatology, 49, 1268–1292, DOI: 10.1175/2010JAMC2354.1.

Heise E., Ritter B., and Schrodin R. (2006). Operational implementation of the multilayer soil model. COSMO Technical Reports No. 9, Consortium for Small-Scale Modelling, 19pp.

Hersbach H., Bell B., Berrisford P., Hirahara S., Horányi A., Muñoz-Sabater J., et al. (2020). The ERA5 global reanalysis. Q. J. R. Meteorol. Soc., 146. 1999–2049, DOI: 10.1002/qj.3803.

Kanda M., Kanega M., Kawai T., Moriwaki R., and Sugawara H. (2007). Roughness lengths for momentum and heat derived from outdoor urban scale models. J. Appl. Meteorol. Climatol., 46(7), 1067–1079, DOI: 10.1175/JAM2500.1.

Khaikine M.N. Kuznetsova I.N. Kadygrov E.N. Miller E.A. (2006). Investigation of temporal-spatial parameters of an urban heat island on the basis of passive microwave remote sensing. Theor. Appl. Climatol., 84, 161–169.

Kusaka H., Kondo H., Kikegawa Y., and Kimura F. (2001). A simple single–layer urban canopy model for atmospheric models: Comparison with multi–layer and slab models. Boundary–Layer Meteorology, 101(3), 329–358, DOI: 10.1023/A:1019207923078.

Kuznetsova I. N., Semutnikova E. G., Lezina E. A., Zakharova P. V., Tkacheva Yu. V., Varentsov M. I., Tarasova M. A., Rivin G. S., and Khrykina E. A. (2024). Characteristics of the Moscow Heat Island and Quality of Its Simulation with the COSMO-Ru1-MSK Model Based on the Mosecomonitoring Observations. Russ. Meteorol. Hydrol., 49(9), 795–810.

Lean H. W., Theeuwes N. E., Baldauf M., Barkmeijer J., Bessardon G., Blunn L., et al. (2024). The hectometric modelling challenge: Gaps in the current state of the art and ways forward towards the implementation of 100-m scale weather and climate models. Quarterly Journal of the Royal Meteorological Society, 150(765), 4671–4708. DOI: 10.1002/QJ.4858.

Lemonsu A., Grimmond C. S. B., and Masson V. (2004). Modeling the Surface Energy Balance of the Core of an Old Mediterranean City: Marseille. J. Appl. Meteorol., 43, 312–327, DOI: 10.1175/1520-0450(2004)043<0312:MTSEBO>2.0.CO;2.

Lemonsu A., Masson V., Shashua–Bar L., Erell E., and Pearlmutter D. (2012). Inclusion of vegetation in the Town Energy Balance model for modelling urban green areas. Geosci. Model Dev., 5, 1377–1393, DOI: 10.5194/gmd–5–1377–2012.

Liu Y., Chen F., Warner T., and Basara J. (2006). Verification of a mesoscale data assimilation and forecasting system for the Oklahoma city area during the joint urban 2003 field project. J. Appl. Meteorol., 45, 912–929.

Lokoshchenko M.A., Korneva I.A., Kochin A.V., Dubovetsky A.Z., Novitsky M.A., and Razin P.Ye. (2016). Vertical extension of the urban heat island above Moscow. Dokl. Earth Sc., 466, 70–74, DOI: 10.1134/S1028334X16010128.

Lokoshchenko M. A., Enukova E. A., Alekseeva L. I. (2023). Modern changes of the urban heat island in Moscow. Doklady Earth Sciences, 511(2), 716–725.

Martilli A., Clappier A., and Rotach M. W. (2002). An Urban Surface Exchange Parameterisation for Mesoscale Models. Bound.–Lay. Meteorol., 104, 261–304, DOI: 10.1023/A:1016099921195.

Masson V. A (2000). Physically–Based Scheme For The Urban Energy Budget In Atmospheric Models. Bound.–Lay. Meteorol., 94, 357–397, DOI: 10.1023/A:1002463829265.

Masson V., Grimmond C. S. B., and Oke T. R. (2002). Evaluation of the Town Energy Balance (TEB) Scheme with Direct Measurements from Dry Districts in Two Cities. J. Appl. Meteorol., 41, 1011– 1026, DOI: 10.1175/1520-0450(2002)041<1011:EOTTEB>2.0.CO;2.

Masson, V. (2006). Urban surface modeling and the meso–scale impact of cities. Theor. Appl. Climatol., 84, 35–45, DOI: 10.1007/s00704-005-0142-3.

Masson V., Le Moigne P., Martin E., Faroux S., Alias A., Alkama R., Belamari S., Barbu A., Boone A., Bouyssel F., Brousseau P., Brun E., Calvet J.–C., Carrer D., Decharme B., Delire C., Donier S., Essaouini K., Gibelin A.–L., Giordani H., Habets F., Jidane M., Kerdraon G., Kourzeneva E., Lafaysse M., Lafont S., Lebeaupin Brossier C., Lemonsu A., Mahfouf J.–F., Marguinaud P., Mokhtari M., Morin S., Pigeon G., Salgado R., Seity Y., Taillefer F., Tanguy G., Tulet P., Vincendon B., Vionnet V., and Voldoire A. (2013). The SURFEXv7.2 land and ocean surface platform for coupled or offline simulation of earth surface variables and fluxes. Geoscientific Model Development, 6, 929–960, DOI: 10.5194/gmd–6–929–2013.

Masson V., Bonhomme M., Salagnac J.-L., Briottet X., and Lemonsu A. (2014). Solar panels reduce both global warming and urban heat island. Frontiers in Environmental Science, 2, DOI: 10.3389/fenvs.2014.00014.

Meyer D., Schoetter R., Riechert M., Verrelle A., Tewari M., Dudhia J., Masson V., van Reeuwijk M., and Grimmond S. (2020). WRF-TEB: Implementation and evaluation of the coupled Weather Research and Forecasting (WRF) and Town Energy Balance (TEB) model. Journal of Advances in Modeling Earth Systems, 12, e2019MS001961, DOI: 10.1029/2019MS001961.

Mussetti G., Brunner D., Henne S., Allegrini J., Krayenhoff E., Schubert S., Feigenwinter, C., Vogt R., Wicki A., and Carmeliet J. (2020). COSMO–BEP–Tree v1.0: a coupled urban climate model with explicit representation of street trees. Geoscientific Model Development, 13(3), 1685–1710, DOI: 10.5194/gmd-13-1685-2020.

Nunez M. and Oke T. R. (1977). The Energy Balance of an Urban Canyon. Journal of Applied Meteorology, 16, 11–19, DOI: 10.1175/1520-0450(1977)016<0011:TEBOAU>2.0.CO;2.

Oke T., Mills G., Christen A., and Voogt J. (2017). Urban Climates. Cambridge: Cambridge University Press., 548 p. DOI: 10.1017/9781139016476.

Platonov V.S., Varentsov M.I., Yarinich Y.I., Shikhov A.N., and Chernokulsky A.V. (2024). A large mid-latitude city intensifies severe convective events: Evidence from long-term high-resolution simulations. Urban Climate, 54, DOI: 10.1016/j.uclim.2024.101837.

Porson A., Clark P. A., Harman I. N., Best, M. J., and Belcher, S. E. (2010). Implementation of a new urban energy budget scheme in the MetUM. Part I: Description and idealized simulations. Quarterly Journal of the Royal Meteorological Society, 136(651), 1514–1529, DOI: 10.1002/qj.668.

Ritter B. and Geleyn J. (1992). A Comprehensive Radiation Scheme for Numerical Weather Prediction Models with Potential Applications in Climate Simulations. Mon. Wea. Rev., 120, 303–325, DOI: 10.1175/1520-0493(1992)120<0303:ACRSFN>2.0.CO;2.

Rivin G.S., Vil'fand R.M., Kiktev D.B., Rozinkina I.A., Tudriy K.O., Blinov D.V., Varentsov M.I., Samsonov T.E., Bundel' A.Y., Kirsanov A.A., and Zakharchenko D.I. (2019). The system for numerical prediction of weather events (including severe ones) for Moscow megacity: The prototype development. Russian Meteorology and Hydrology, 44(11), 33–45, DOI: 10.3103/S1068373919110025.

Rivin G.S., Rozinkina I.A., Vil'fand R.M., Kiktev D.B., Tudrii K.O., Blinov D.V., Varentsov M.I., Zakharchenko D.I., Samsonov T.E., Repina I.A., and Artamonov A. Yu. (2020). Development of the High–Resolution Operational System for Numerical Prediction of Weather and Severe Weather Events for The Moscow Region. Russ. Meteorol. Hydrol., 45, 455–465, DOI: 10.3103/s1068373920070018.

Rockel B., Will A., and Hense A. (2008). The regional climate model COSMO-CLM (CCLM). Meteorol. Z., 17, 347–348, DOI: 10.1127/0941-2948/2008/0309.

Rotach M. (1995). Profiles of turbulence statistics in and above an urban street canyon. Atmos. Environ., 29, 1473–1486.

Rowley F.B., Algren A.B., and Blackshaw J.L. (1930). Surface Conductances as Affected by Air Velocity, Temperature and Character of Surface. ASHRAE Trans., 36, 429–446.

Rowley F.B., and Eckley W. (1932). A. Surface Coefficients as Affected by Wind Direction. ASHRAE Trans., 38, 33–46.

Salamanca F., Georgescu M., Mahalov A., Moustaoui M., and Wang M. (2014). Anthropogenic heating of the urban environment due to air conditioning. J. Geophys. Res. Atmos., 119, 5949–5965, DOI:10.1002/2013JD021225.

Samsonov T.E., and Varentsov M.I. (2020). Computation of City-descriptive parameters for high-resolution numerical weather prediction in Moscow megacity in the framework of the COSMO model. Russ. Meteorol. Hydrol., 45, 515–521, DOI: 10.3103/S1068373920070079.

Sarkar A. and De Ridder K. (2010). The Urban Heat Island Intensity of Paris: A Case Study Based on a Simple Urban Surface Parametrization. Bound.-Lay. Meteorol., 138, 511–520, DOI: 10.1007/s10546-010-9568-y.

Schoetter R., Kwok Y., de Munck C., Lau K., Wong W., and Masson V. (2020). Multi–layer coupling between SURFEX–TEB–V9.0 and Meso–NH–v5.3 for modelling the urban climate of high–rise cities. Geoscientific Model Development, 13(11), 5609–5643, DOI: 10.5194/gmd-13-5609-2020.

Schubert S., Grossman–Clarke S., and Martilli A. (2012). A Double–Canyon Radiation Scheme for Multi–Layer Urban Canopy Models. Boundary–Layer Meteorology, 145(3), 439–468, DOI: 10.1007/s10546-012-9728-3.

Schubert S. and Grossman–Clarke S. (2014). Evaluation of the coupled COSMO–CLM/DCEP model with observations from BUBBLE. Q. J. R. Meteorol Soc., 140(685), 2465–2483, DOI: 10.1002/qj.2311.

Schrodin R. and Heise E. (2001). The Multi-Layer Version of the DWD Soil Model TERRA LM. Tech. Rep. 2, Consortium for Small-Scale Modelling, 1–16.

Schulz J. and Vogel G. (2020). Improving the Processes in the Land Surface Scheme TERRA: Bare Soil Evaporation and Skin Temperature. Atmosphere, 11, 513, DOI: 10.3390/atmos11050513.

Stewart I.D. and Oke T.R. (2012). Local climate zones for urban temperature studies. Bull. Am. Meteorol. Soc., 93, 1879–1900, DOI: 10.1175/BAMS-D-11-00019.1.

Tarasova M. A., Varentsov M. I., and Stepanenko V. M. (2023). Parameterization of the interaction between the atmosphere and the urban surface: Current state and prospects. Izvestiya - Atmospheric and Oceanic Physics, 59(2), 127–148, DOI: 10.1134/S0001433823020068.

Tarasova M.A., Debolskiy A.V., Mortikov E.V., Varentsov M.I., Glazunov A.V., Stepanenko V.M. (2024). On the Parameterization of the Mean Wind Profile for Urban Canopy Models. Lobachevskii Journal of Mathematics, 45(7), 3198–3210.

Tiedke M. (1989). A comprehensive mass flux scheme for cumulus parameterization in large-scale models. Mon. Weath. Rev., 117, 1779–1800, DOI: 10.1175/1520-0493(1989)117<1779:ACMFSF>2.0.CO;2.

Trusilova K., Früh B., Brienen S., Walter A., Masson V., Pigeon G., and Becker P. (2013). Implementation of an Urban Parameterization Scheme into the Regional Climate Model COSMO–CLM. Journal of Applied Meteorology and Climatology, 52(10), 2296–2311, DOI: 10.1175/JAMC-D-12-0209.1.

Varentsov M.I., Samsonov T.E., Kislov A.V., and Konstantinov P.I. (2017). Simulations of Moscow agglomeration heat island within the framework of the regional climate model COSMO-CLM. Moscow University Vestnik. Series 5. Geography, 6, 25-37 (in Russian with English summary).

Varentsov M., Wouters H., Platonov V., and Konstantinov P. (2018). Megacity–Induced Mesoclimatic Effects in the Lower Atmosphere: A Modeling Study for Multiple Summers over Moscow, Russia. Atmosphere, 9(2), 50, DOI: 10.3390/atmos9020050.

Varentsov M. I., Grishchenko M. Y., and Wouters H. (2019). Simultaneous assessment of the summer urban heat island in Moscow megacity based on in situ observations, thermal satellite images and mesoscale modeling. GEOGRAPHY, ENVIRONMENT, SUSTAINABILITY, 12(4), 74–95, DOI: 10.24057/2071-9388-2019-10.

Varentsov M., Samsonov T., and Demuzere M. (2020). Impact of urban canopy parameters on a megacity's modelled thermal environment. Atmosphere, 11(2), 1349, DOI: 10.3390/atmos11121349.

Varentsov M., Vasenev V., Dvornikov Y., Samsonov T., and Klimanova O. (2023) Does size matter? Modelling the cooling effect of green infrastructures in a megacity during a heat wave. Science of The Total Environment, 902, 165966, DOI: 10.1016/j.scitotenv.2023.165966.

Wouters H., Demuzere M., De Ridder K., and van Lipzig N.P. (2015). The impact of impervious water–storage parametrization on urban climate modeling. Urban Climate, 11, 24–50, DOI: 10.1016/j.uclim.2014.11.005.

Wouters H., Demuzere M., Blahak U., Fortuniak K., Maiheu B., Camps J., Tielemans D., and van Lipzig N.P. (2016). The efficient urban canopy dependency parametrization (SURY) v1.0 for atmospheric modeling: description and application with the COSMO–CLM model for a Belgian summer. Geoscientific Model Development, 9(9), 3027–3054, DOI: 10.5194/gmd-9-3027-2016.

Zanaga D., Van De Kerchove R., De Keersmaecker W., Souverijns N., Brockmann C., Quast R., Wevers J., Grosu A., Paccini A., Vergnaud S., Cartus O., Santoro M., Fritz S., Georgieva I., Lesiv M., Carter S., Herold M., Li Linlin, Tsendbazar N.E., Ramoino F., and Arino O. (2012). ESA WorldCover 10 m 2020 v100. DOI: 10.5281/zenodo.5571936.

APPENDICES

The basic aggregation algorithm of sensible and latent heat fluxes assumes weighting each of the land–atmosphere fluxes according to the fractions of the urban and natural tiles by the land surface model. However, in the latest version of COSMO, the fluxes are further re-calculated in the model's dynamic core based on the cell-averaged variables: surface temperature, surface specific humidity and heat transfer coefficient. These recalculated fluxes are assigned to tile 0 (cell-averaged) and are actually used in temperature and humidity evolution in the atmospheric model. As expected, their values are not equal to the weighted sum of fluxes from tiles; the difference may reach up to 100 W/m^2 in our tests (note that these tests were performed without AHF).

In the original version of the tile approach proposed by [Wouters et al. 2016] for TERRA_URB in COSMO-CLM 5.0, the fluxes aggregation scheme was a bit different: the heat transfer coefficient and surface specific humidity were calculated in a specific way to ensure equality of heat fluxes calculated in the dynamical core to the weighted sum of the fluxes from individual tiles. However, since COSMO version 5.05, these tricks have been removed.

To avoid discrepancy in fluxes, we have adopted the tricks from COSMO-CLM 5.0 back to version 6.0. The weighted average of the heat transfer coefficient is redefined through the weighted sensible heat flux from individual tiles (Eq. A1):

$$C_{H\ cell} = \frac{H_{cell}}{\rho \times c_{pd} \times u \times \left(T_{g\ cell} - T_a \right)} \quad \text{(A1)}$$

where $C_{H\ cell}$ is the redefined weighted heat transfer coefficient, H_{cell} is the weighted sensible heat flux from individual tiles, ρ is air density, c_{pd} is specific heat capacity of dry air at constant pressure, u is wind speed, $T_{g\ cell}$ is weighted surface temperature, T_a is air temperature.

For the latent heat flux, a correction is made for the surface specific humidity (Eq. A2):

$$qv_{cell} = qv_a - \frac{LE_{cell}}{\rho \times L_v \times u \times C_{H\ cell}} \quad \text{(A2)}$$

where qv_{cell} is the redefined weighted surface specific humidity, qv_a is air specific humidity, LE_{cell} is the weighted latent heat flux from individual tiles, L_v is latent heat of vaporization.

Initially, the adaptation of these tricks led to the appearance of errors during the model run, so we proposed additional limitations for $C_{H\ cell}$ and qv_{cell} (Eqs. A3-A4):

$$C_{H\ cell} = min\left(C_{H\ cell},\ 1 \right) \quad \text{(A3)}$$

$$qv_{cell} = min\left(qv_{cell},\ max\left(qv_{nat},\ qv_{urb} \right) \times 10 \right) \quad \text{(A4)}$$

where qv_{nat}, qv_{urb} are surface specific humidity from natural and urban tiles.

Our tests have indicated that the proposed solution decreases the discrepancy in fluxes by an order of magnitude. The changes in the resulting surface-atmosphere flux sufficiently impact the simulation results, particularly for the grid cells with a significant fraction of both tiles.

RESEARCH PAPER

MAPPING GHG EMISSION VULNERABILITY USING CONVOLUTIONAL AUTOENCODER AND MULTI-SENSOR SATELLITE IN BALI, INDONESIA

Moh Saifulloh[1,2*], I Gusti Ngurah Santosa[3], I Nyoman Sunarta[4], I Gusti Agung Ayu Ambarawati[3], I Made Sudarma[5], Abd. Rahman As-syakur[5]

[1]Faculty of Marine Sciences and Fisheries, Udayana University, Badung, 80361, Indonesia
[2]Spatial Data Infrastructure Development Center (PPIDS) Denpasar City, 80225, Indonesia
[3]Faculty of Agriculture, Udayana University, Denpasar, 80225, Indonesia
[4]Doctoral Program of Tourism Sciences, Udayana University, 80225, Denpasar, Indonesia
[5]Research Center for Environmental (PPLH) of Udayana University, Denpasar, 80225, Indonesia
***Corresponding author:** m.saifulloh@unud.ac.id
Received: April 15th 2025 / Accepted: August 7th 2025 / Published: October 1st 2025
https://doi.org/10.24057/2071-9388-2025-4005

ABSTRACT. Global warming, driven by the rising concentration of greenhouse gases (GHGs), demands innovative, data-driven approaches to assess emission vulnerability at regional scales. This study developed a novel framework utilizing an unsupervised Convolutional Autoencoder (CAE) deep learning model combined with multi-sensor satellite data to map GHG emission vulnerability. The framework integrated nine environmental indicators, including tropospheric gases, land surface temperature, vegetation cover, anthropogenic proxies, and elevation, all sourced from freely accessible remote sensing platforms. The CAE model effectively captured complex spatial patterns and reduced high-dimensional inputs into 128 latent features, enabling vulnerability assessment without requiring labeled training data. Results indicated that southern coastal regions, particularly Denpasar and Badung, exhibited the highest vulnerability due to dense urbanization and tourism-related activities. Based on zonal statistics, 11.31% of local administrative zones were identified as having high to very high vulnerability, while 18.72% were classified as moderate, and 69.97% as low to very low. The most vulnerable areas were concentrated along the southern coastline, known as a hub for tourism and economic activity, with additional pockets of vulnerability found in several northern coastal zones. These findings demonstrate the capacity of unsupervised deep learning to detect emission hotspots and spatial variability, particularly in data-limited environments. The integration of scalable algorithms with open-access satellite data allows for rapid, cost-efficient assessments to inform evidence-based climate planning and mitigation strategies. This study introduces a practical and transferable approach for spatial quantification of GHG vulnerability, offering actionable insights for advancing global climate policy and supporting the Sustainable Development Goals.

KEYWORDS: greenhouse gas, vulnerability mapping, convolutional autoencoder, remote sensing, deep learning, spatial modeling, climate change

CITATION: Moh Saifulloh, I Gusti Ngurah Santosa, I Nyoman Sunarta, I Gusti Agung Ayu Ambarawati, I Made Sudarma, Abd. Rahman As-syakur (2025). Mapping Ghg Emission Vulnerability Using Convolutional Autoencoder And Multi-Sensor Satellite In Bali, Indonesia. Geography, Environment, Sustainability, 3 (18), 135-144
https://doi.org/10.24057/2071-9388-2025-4005

ACKNOWLEDGEMENTS: This research was conducted without financial support from any funding agency or institution. The authors gratefully acknowledge the developers of the Google Earth Engine (GEE) platform for providing open-access satellite data and tools that enabled advanced geospatial analysis. Appreciation is also extended to the open-source Python community for the development of powerful libraries used in this study. We sincerely thank the anonymous reviewers for their valuable insights and constructive feedback, which significantly improved the quality of this manuscript.

Conflict of interests: The authors reported no potential conflict of interests.

INTRODUCTION

Global climate change is widely recognized as one of the most urgent environmental challenges of the 21st century, with far-reaching implications for ecological sustainability, human health, and socio-economic development (Scafetta 2024). The primary cause of this phenomenon is the rising concentration of greenhouse gases (GHGs) in the atmosphere, which intensifies the natural greenhouse effect and contributes significantly to global warming (Yang et al., 2022). GHGs such as carbon dioxide (CO_2), methane (CH_4), nitrogen dioxide (NO_2), and sulfur dioxide (SO_2) trap outgoing longwave radiation (Bhatti et al., 2024), thereby leading to an increase in Earth's surface temperatures (Rahaman et al., 2022). The accumulation of these gases is associated with a wide range of adverse effects, including more frequent extreme weather events, declining air quality, and disrupted

regional climate systems (Edo et al., 2024). These impacts present substantial obstacles to the achievement of the United Nations Sustainable Development Goals (SDGs), particularly Goal 13 on climate action.

Climate change, beyond its atmospheric implications, also affects the structural integrity of ecosystems and the functionality of biomes. The warming of Earth's climate alters species distributions, hydrological cycles, and ecosystem services that support agriculture, forestry, and coastal livelihoods (Dar et al., 2020; Grimm et al., 2013; Pecl et al., 2017). The majority of GHG emissions are anthropogenic, stemming from sectors such as energy, industry, transportation, agriculture, land-use change, and waste management (Priyadarshini et al., 2025). Urbanization exacerbates these emissions, with dense population centers contributing disproportionately through increased infrastructure, vehicular activity, and energy consumption. Over time, these patterns of emission become spatially correlated with zones of intense human activity and temporally aligned with rapid economic expansion (Yu et al., 2024). To address these spatial and systemic complexities, remote sensing and Geographic Information Systems (GIS) have emerged as indispensable tools for environmental analysis. Remote sensing enables continuous monitoring of Earth's surface parameters, while GIS allows for spatially explicit modeling of environmental indicators and anthropogenic pressures. These tools provide a basis for multi-scale climate vulnerability assessments, from local urban settings to regional and global contexts. For example, Valjarević et al. (2022) utilized satellite and GIS-based approaches to update global climate classification, revealing nuanced climate dynamics and spatial vulnerabilities.

Bali Province, Indonesia, a globally recognized tourism hotspot, is experiencing substantial environmental stress due to accelerated land-use transformation (Saifulloh et al., 2025). Recent research indicates that surface temperatures in Bali have been increasing at an average rate of 0.01°C per year (Sunarta et al., 2022). This trend is closely associated with the widespread conversion of natural landscapes into built environments, including hotels, resorts, restaurants, and urban settlements (Andyana et al., 2023; Diara et al., 2024; Sunarta and Saifulloh, 2022a). The loss of vegetative cover resulting from urban expansion significantly reduces the landscape's capacity for carbon sequestration (Sudarma et al., 2024; Susila et al., 2024; Trigunasih and Saifulloh, 2022), while emissions from transportation, hospitality operations, solid waste, and agricultural practices continue to intensify. Despite the significance of these transformations, there remains a lack of spatially explicit data and systematic assessments of GHG emission vulnerability for the region. This data gap highlights the need for robust geospatial methodologies to inform mitigation strategies and policy interventions.

Although various studies have sought to analyze GHG vulnerability, most have been constrained by limited spatial, temporal, or variable coverage. For instance, (Hassaan et al., 2023) assessed CO and PM2.5 exposure using discrete point-source data, lacking spatial continuity. Sakti et al. (2023) employed Sentinel-5P to monitor gaseous pollutants such as CO, NO_2, and SO_2, yet failed to incorporate critical environmental metrics such as vegetation and temperature (Pan et al., 2024). While meteorological influences have been examined in studies by (Ayyamperumal et al., 2024; Z. Feng et al., 2023), few efforts have systematically integrated these variables within spatially scalable frameworks. In the region of Bali Province, NO_2 concentrations have been examined for the year 2020 (Sunarta and Saifulloh, 2022b), though such assessments were not embedded within a broader vulnerability framework. Meanwhile, spatial machine learning models such as fuzzy geographically weighted clustering (Grekousis et al., 2024) have incorporated static demographic indicators but still fall short of accounting for dynamic spatiotemporal GHG variability.

To overcome these limitations, the present study introduces a comprehensive approach for mapping GHG vulnerability through unsupervised deep learning. The framework employs a convolutional autoencoder (CAE), a class of neural networks capable of learning latent feature representations without requiring labeled data (Azarang et al., 2019; Cui et al., 2018). All input variables are derived from freely available multi-sensor satellite datasets, retrieved via the Google Earth Engine (GEE) platform (Gorelick et al., 2017). These include primary GHG indicators (NO_2, CO, SO_2, and Aerosol Optical Depth), environmental variables (temperature and vegetation indices), human activity proxies (population density and nighttime lights), and topographic data.

This method enables detailed spatial and temporal characterization of emission vulnerability, eliminating the need for resource-intensive field data collection. By forgoing reliance on labeled training data, the CAE model supports rapid, cost-effective, and reproducible assessments of environmental vulnerability. The innovation of this research lies in the fusion of multi-source satellite data with unsupervised deep learning to detect spatial patterns of vulnerability, particularly in data-limited regions such as Bali. Ultimately, this research advances both the scientific understanding and practical management of GHG emissions, contributing meaningfully to global climate resilience and sustainability agendas.

MATERIALS AND METHODS

Study area

The study was conducted in Bali Province, Indonesia, an island located in Southeast Asia with significant ecological sensitivity and economic reliance on tourism. Geographically, Bali lies around 8°00'S latitude and 115°40'E longitude, covering a land area of 5,593.60 km^2 (Fig. 1). Administratively, the province consists of nine regencies and one city: Denpasar, Badung, Gianyar, Buleleng, Tabanan, Jembrana, Klungkung, Bangli, and Karangasem, encompassing 57 subdistricts and 716 villages. According to the 2025 provincial census (BPS Bali, 2025), Bali has a population of approximately 4.46 million, with an average density of 798 people/km^2. Denpasar City has the highest population density (6,058 people/km^2), followed by Gianyar (1,447 people/km^2) and Badung (1,426 people/km^2), which are the primary centers of tourism and urban development (BPS Provinsi Bali, 2025).

In terms of long-term climatic conditions, Bali experiences a tropical monsoon climate with a distinct wet and dry season. Based on historical records, average temperatures have ranged between 22.5 and 27.5°C, while projections suggest future increases to 25.5–29.5°C. Northern Bali in particular is projected to face temperature anomalies ranging from 1.6 to 2.9°C, coupled with declining humidity levels, especially in the north. In contrast, southern areas may experience slight increases in humidity. Under the representative concentration pathways (RCP) 4.5 climate scenario, Bali is predicted to lose areas with comfortable climate zones (20–26°C), giving way to predominately hot and dry conditions (Toersilowati

et al., 2022). Similarly, long-term projections suggest rainfall will fluctuate annually but remain within a relatively stable range of 2,066–2,170 mm, with both maximum and minimum temperatures continuing to rise by up to 2°C (Puspitasari and Wu, 2025). These climatic shifts pose significant implications for urban planning, agriculture, and environmental resilience in Bali, underscoring the urgent need for spatially explicit assessments of greenhouse gas vulnerability.

Workflow framework and data sources

To assess greenhouse gas (GHG) emission vulnerability spatially, a systematic methodological framework was developed, integrating multi-sensor satellite observations with unsupervised deep learning. The methodological workflow (Fig. 2) comprises three core phases: (1) data acquisition and preprocessing using Google Earth Engine (GEE), (2) deep learning modeling using a convolutional autoencoder (CAE), and (3) postprocessing and interpretation using zonal statistics.

In Phase I, remotely sensed variables were selected to reflect GHG emission sources, environmental sensitivity, and anthropogenic exposure. Table 1 outlines the nine indicators used: NO2, CO, SO2 (Sentinel-5P), NDVI, LST, AOD (MODIS), population density (WorldPop), nighttime lights (VIIRS), and elevation (SRTM). All datasets were resampled to 1 km^2 and reprojected to WGS 1984 UTM Zone 50S.

The open-source remote sensing data utilized in this study originated from multiple sensors with native spatial resolutions ranging from 30 meters to approximately 1,000 meters. Most of the datasets representing sources of greenhouse gas emissions, particularly from atmospheric sensors, are provided at a coarser resolution of around 1 km. Therefore, for consistency and compatibility within the modeling process, all variables were resampled to a uniform spatial resolution of 1 km^2. This harmonization of spatial resolution is essential for feeding standardized input into the unsupervised deep learning model, ensuring that data dimensions are consistent (Y. Han et al., 2024; Li et al., 2024). To maintain temporal consistency across datasets, pollutant-related variables and other emission source indicators (such as NO_2, CO, SO_2, AOD, NDVI, and LST) were accessed using mean values coded over the 2022–2024 period via GEE. In contrast, datasets lacking temporal resolution, such as SRTM elevation and WorldPop population data, used the most recent available data. Given that this is a preliminary study conducted at a regional mapping scale, a 1 km^2 resolution is appropriate and consistent with similar studies implemented in other parts of the world (Garajeh et al., 2023; Maurya et al., 2022; Xiong et al., 2021).

Data preprocessing and tensor construction

Each raster file was imported using the rasterio library and converted to 32-bit floating-point arrays. Missing values were replaced with zero, particularly for elevation data beyond the study boundary. After spatial alignment, each dataset was normalized using min-max scaling to standardize feature ranges to [0, 1], following Eq. 1:

$$x'_{ik} = \frac{x_{ik} - min\left(x_k\right)}{max\left(x_k\right) - min\left(x_k\right)} \quad (1)$$

where x'_{ik} denotes the normalized value of variable k at pixel i, while min (x_k) and max (x_k) represent the minimum and maximum values observed across the entire raster for variable kk. This ensures comparability among different datasets during model training.

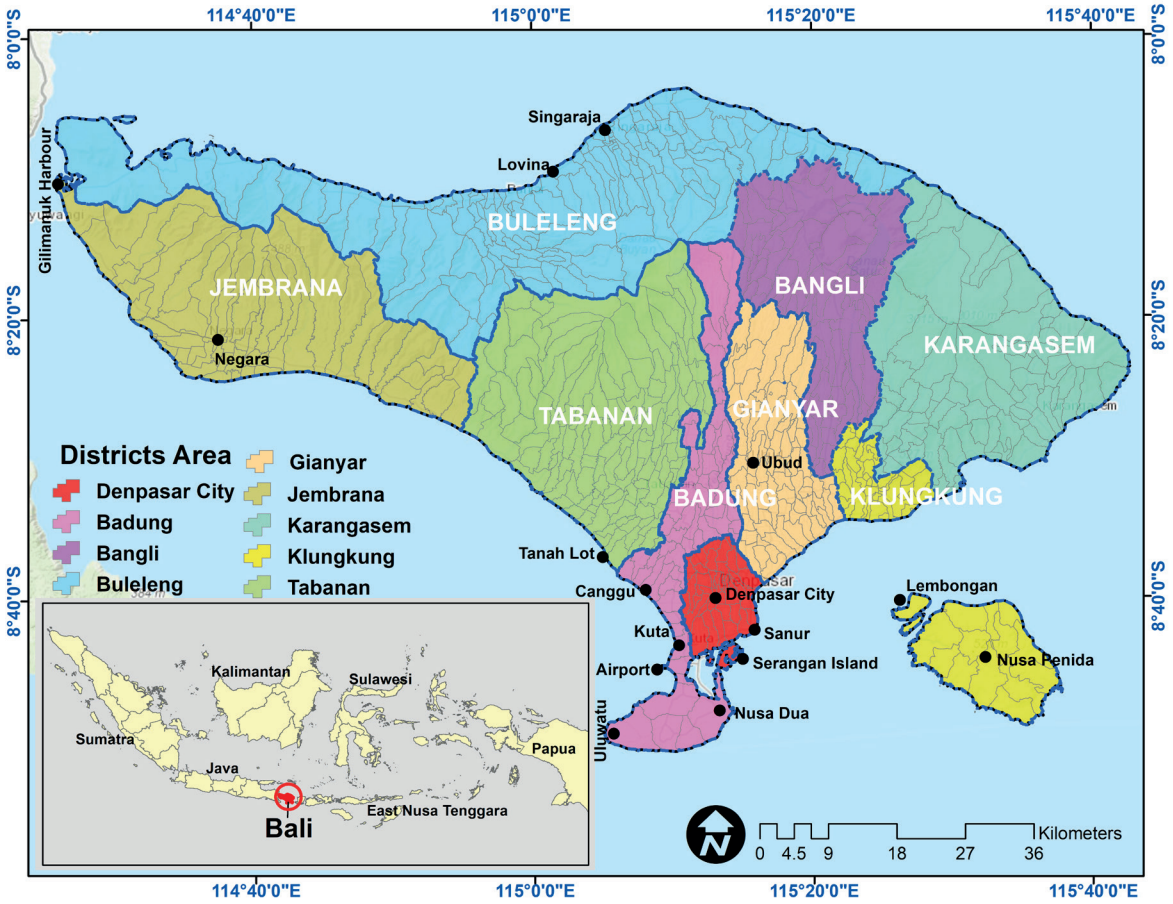

Fig. 1. Research location in Bali Province, Indonesia

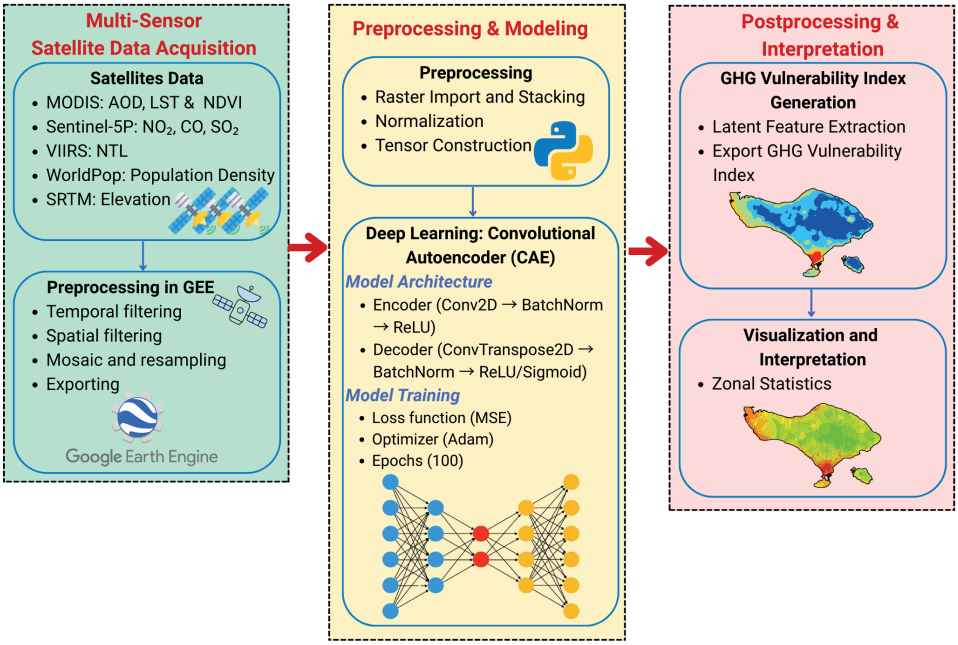

Fig. 2. Workflow Framework of the Research

Table 1. Multi-Sensor Satellite Data and Functional Roles in Regional GHG Vulnerability Modeling

№	Data source (GEE)	Extracted variable	Spatial & temporal resolution	Functional role in the model
1	Sentinel-5P TROPOMI (COPERNICUS/S5P/OFFL/ L3_NO2)	Tropospheric NO_2 (mol/m²)	• Pixel Size: 1113.2 meters • Revisit Interval: 2 Days	Proxy for traffic and industrial emissions; indicates nitrogen-based pollution intensity
2	Sentinel-5P TROPOMI (COPERNICUS/S5P/OFFL/ L3_CO)	Tropospheric CO (mol/m²)	• Pixel Size: 1113.2 meters • Revisit Interval: 2 Days	Represents incomplete combustion from fossil fuel and biomass burning
3	Sentinel-5P TROPOMI (COPERNICUS/S5P/OFFL/ L3_SO2)	Tropospheric SO_2 (mol/m²)	• Pixel Size: 1113.2 meters • Revisit Interval: 2 Days	Emission from power plants, volcanic activity, and smelting industries
4	MODIS MCD19A2 (MODIS/061/MCD19A2_ GRANULES)	Aerosol Optical Depth (unitless)	• Pixel Size: 1000 meters • Revisit Interval: Daily	Indicator of atmospheric particulate concentration; linked to PM2.5 exposure
5	MODIS Terra MOD13Q1 (MODIS/061/MOD13Q1)	NDVI (unitless)	• Pixel Size: 250 meters • Revisit Interval: 16 Days	Vegetative cover and greenness; indicator of carbon sequestration capacity
6	MODIS Terra MOD11A2 (MODIS/061/MOD11A2)	Land Surface Temperature (°C)	• Pixel Size: 1000 meters • Revisit Interval: 8 Days	Surface heat intensity; associated with urbanization and land energy balance
7	WorldPop 100m (WorldPop/ GP/100m/pop)	Population Density (people/ km2)	• Pixel Size: 92.77 meters • Revisit Interval: -	Proxy for population exposure to emissions; measures human concentration in space
8	VIIRS Nighttime Lights (NOAA/ VIIRS/DNB/MONTHLY_V1/ VCMCFG)	Nighttime Light Radiance (nW/ cm2/sr)	• Pixel Size: 463.83 meters • Revisit Interval: Monthly	Indicator of anthropogenic energy use and urban footprint
9	SRTM DEM (USGS/ SRTMGL1_003)	Elevation (meters)	• Pixel Size: 30 meters • Revisit Interval: -	Terrain factor affecting air flow and pollutant accumulation in lowland areas

The normalized raster stack was reshaped into a 3D tensor $\mathcal{D} \in R^{CxHxW}$, where C is the number of channels (or features), and H and W are the spatial dimensions of the input. This tensor was further converted into a 4D tensor $X \in R^{1xCxHxW}$ to match the input format required by the convolutional autoencoder.

Convolutional autoencoder (CAE) modeling

The CAE model was implemented using the PyTorch library (Costa et al., 2024; Subramanian, 2018). It consisted of an encoder that extracted feature representations and a decoder that reconstructed the input. The architecture was as follows.

Encoder Layers:

- Conv2D (9 → 32) → BatchNorm → ReLU
- Conv2D (32 → 64) → BatchNorm → ReLU
- Conv2D (64 → 128) → BatchNorm → ReLU

Decoder Layers:

- ConvTranspose2D (128 → 64) → BatchNorm → ReLU
- ConvTranspose2D (64 → 32) → BatchNorm → ReLU
- ConvTranspose2D (32 → 9) → Sigmoid

The model was trained using the Mean Squared Error (MSE) loss function, defined by Eq. 2:

$$\mathcal{L}_{MSE} = \frac{1}{n}\sum_{i=1}^{n}\left(x_i - \hat{x}_i\right)^2 \quad (2)$$

where x_i denotes the original input tensor value at index i, and $\hat{x}_i$ is the corresponding reconstructed output. The loss function penalizes reconstruction errors, thereby guiding the encoder to learn compact yet informative representations. The Adam optimizer was employed with a learning rate of 0.001 over 100 training epochs.

GHG vulnerability index

Upon convergence, the encoder output was extracted as a latent tensor $Z \in R^{128xHxW}$, where 128 is the number of abstract feature channels. To collapse this multidimensional feature space into a single-band vulnerability index, mean pooling was applied across all channels (Eq. 3):

$$GHG_{index} = \frac{1}{128}\sum_{c=1}^{128} Z_c \quad (3)$$

where GHG_{index} is the final greenhouse gas emission vulnerability index, and Z_c is the activation of the c^{th} feature channel. The resulting index was again normalized to the range [0, 1] to facilitate interpretation. Higher index values indicate areas with a greater confluence of emission-related stressors and limited ecological buffering.

For policy-oriented interpretation, the vulnerability index raster was intersected with Bali's district-level administrative boundaries. The average vulnerability score for each administrative unit mm was calculated as Eq. 4:

$$V_m = \frac{1}{|Z_m|}\sum_{i \in Z_m} v_i \quad (4)$$

where V_m represents the mean vulnerability index of zone m, calculated by summing all pixel-level vulnerability values v_i within the set of spatial units Z_m, and dividing the result by the total number of pixels $|Z_m|$ within that zone. This procedure translated fine-resolution pixel values into actionable administrative-level metrics that can guide localized climate mitigation planning, land use policy, and emission reduction initiatives.

RESULTS

Dataset from Multi-Sensor Satellite

This study utilized nine environmental variables derived from freely available multi-sensor satellite products. These included tropospheric gases (NO_2, CO, SO_2), Aerosol Optical Depth (AOD), Land Surface Temperature (LST), vegetation indices (NDVI), anthropogenic proxies (Nighttime Light Radiance and Population Density), and Elevation (Fig. 3). All raster datasets were resampled to a uniform spatial resolution of 1 km2 and aligned to the WGS 1984 UTM Zone 50S coordinate system. Each variable was normalized to a [0,1] scale to ensure consistent input for the convolutional model.

Elevated values of NO_2, CO, SO_2, and AOD were predominantly observed in lowland urban regions. These concentrations reflect intense combustion activity and atmospheric pollutant accumulation from transportation and industrial sources. Such hotspots were spatially clustered in urban centers and along coastal corridors characterized by dense infrastructure and minimal vegetative cover. Other variables, such as LST, NDVI, population density, and nighttime lights, mirrored patterns of urban expansion. Built-up zones displayed higher land surface temperatures and lower vegetation greenness. Population and light radiance levels further emphasized anthropogenic pressure, while elevation helped determine pollutant dispersion across terrain gradients.

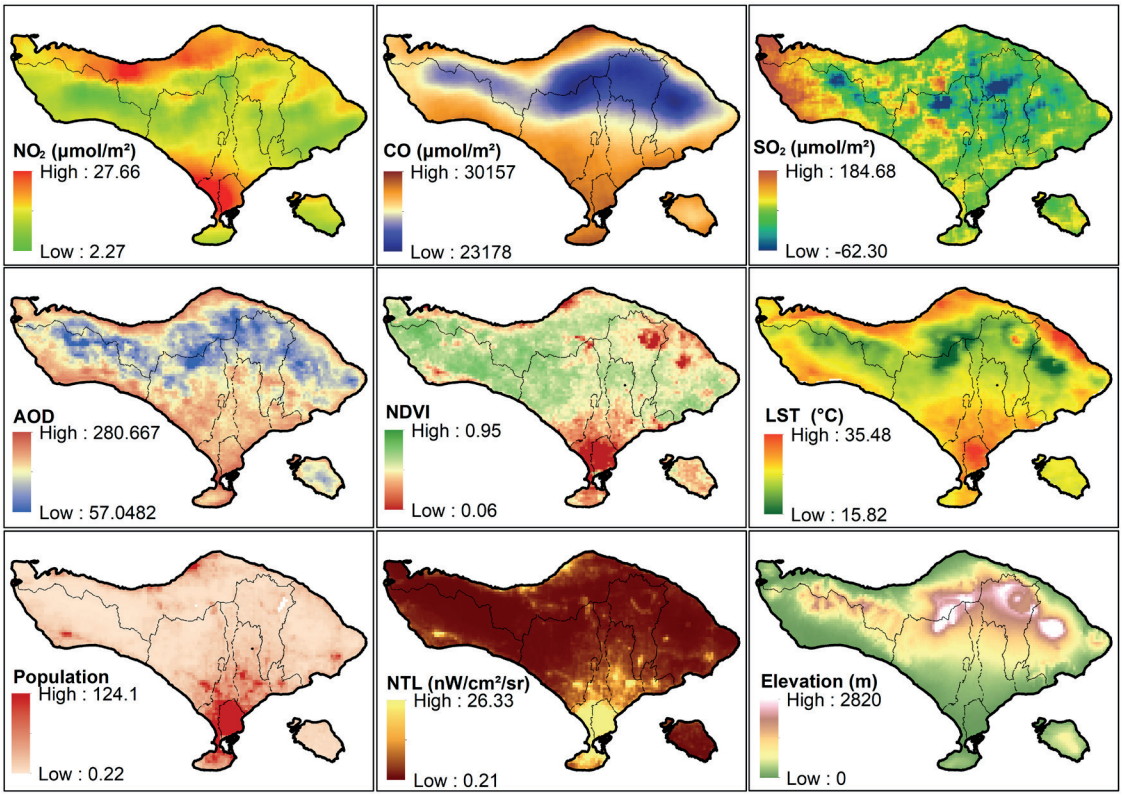

Fig. 3. Environmental variables derived from multi-sensor satellite datasets used in greenhouse gas emission vulnerability modeling

Multivariate Relationships and Feature Space Analysis

The correlation matrix (Fig. 4) identified strong associations among several variables. AOD exhibited high correlation with CO (r = 0.98), NDVI (r = 0.93), and LST (r = 0.92), indicating that areas with higher particulate concentrations often coincide with vegetation decline and thermal stress. NO_2 also showed strong correlations with CO (r = 0.92) and LST (r = 0.88). Additionally, nighttime light radiance and population density were closely linked (r = 0.89), reinforcing their combined role as indicators of urbanization intensity.

Autoencoder Training and Latent Representation

The convolutional autoencoder was trained for 100 epochs using the Adam optimizer with a learning rate of 0.001. Training loss, calculated using mean squared error (MSE), decreased from 0.195 to 0.0021 (Fig. 5), confirming effective convergence. The encoder architecture featured three convolutional layers integrated with batch normalization and ReLU activations, compressing the nine-band input into 128 latent features. The decoder then reconstructed the input using transposed convolutional layers and activation functions.

The latent feature space effectively captured non-linear dependencies among input variables, enabling the model to identify complex spatial patterns of vulnerability. For example, locations with elevated LST, high NO2, and low NDVI were consistently abstracted into high-risk zones. The low reconstruction error confirmed the model's capability to retain meaningful spatial representations. A single-band vulnerability index was generated via mean pooling across all latent feature channels.

The GHG vulnerability index was classified using the Jenks Natural Breaks method, which separates values into statistically distinct classes by minimizing within-class variance and maximizing variance between classes. This method is widely recognized for its suitability in environmental vulnerability assessments (Hou et al., 2022; Ke et al., 2023; Rzasa and Ciski, 2021). The spatial distribution (Fig. 6) showed that very high vulnerability zones were concentrated in southern Bali, particularly in Denpasar and coastal Badung, where index values exceeded 0.66. These areas exhibited characteristics such as dense urbanization, extensive infrastructure, low vegetation cover, and intensified human activity. High vulnerability also appeared in segments of southern Gianyar and Klungkung. Moderate vulnerability values were observed in transitional inland regions, while low to very low vulnerability was dominant in upland and northern areas with greater ecological stability.

Further analysis of administrative-level units revealed that 11.31% were categorized as high or very high vulnerability, 18.72% as moderate, and 69.97% as low to very low (Fig. 7). These village-level areas represent local jurisdictions responsible for implementing environmental policy. The highest vulnerability scores were recorded in Denpasar, southern Badung, Gilimanuk (Jembrana), and Singaraja (Buleleng), all of which are recognized for concentrated tourism and urban development.

DISCUSSION

This study presents a significant advancement in spatial modeling of greenhouse gas (GHG) emission vulnerability by integrating a convolutional autoencoder (CAE) deep learning approach with multi-sensor satellite

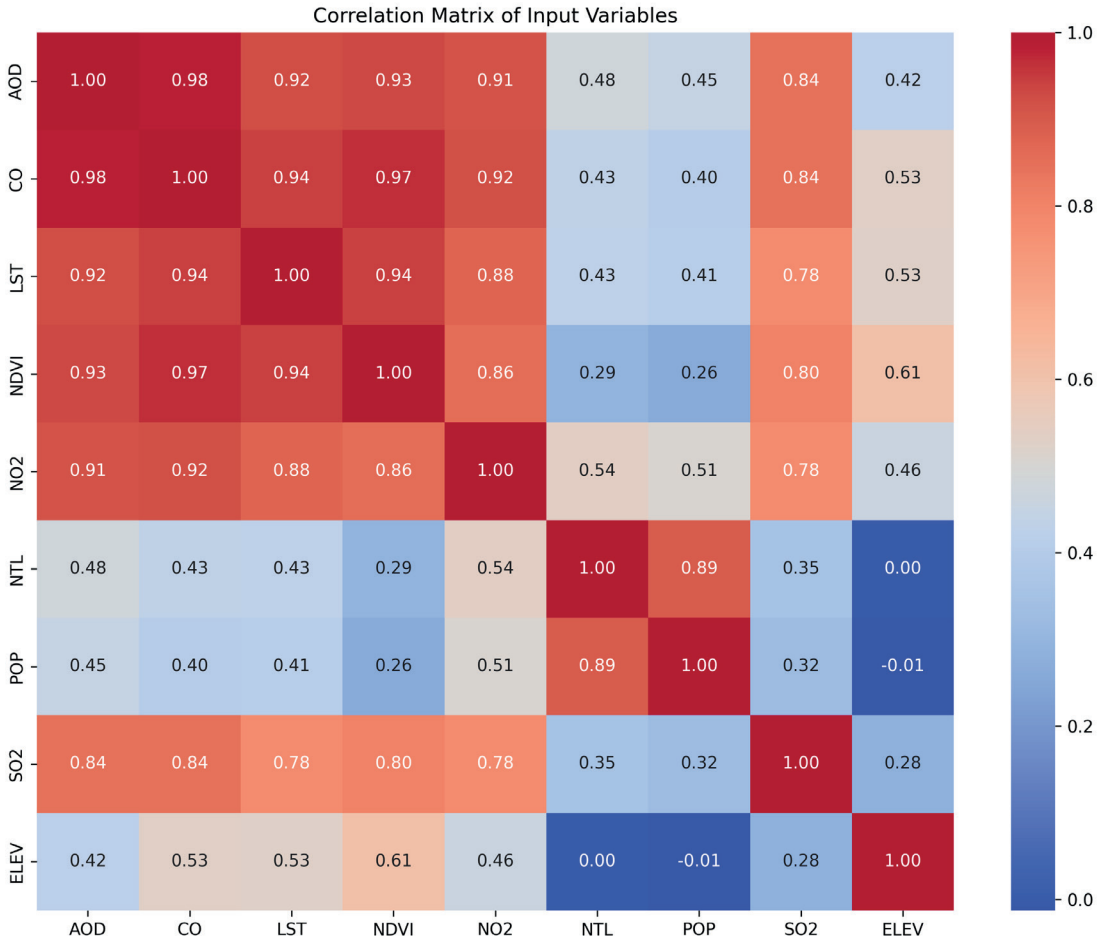

Fig. 4. Correlation matrix of environmental variables used in GHG vulnerability modeling

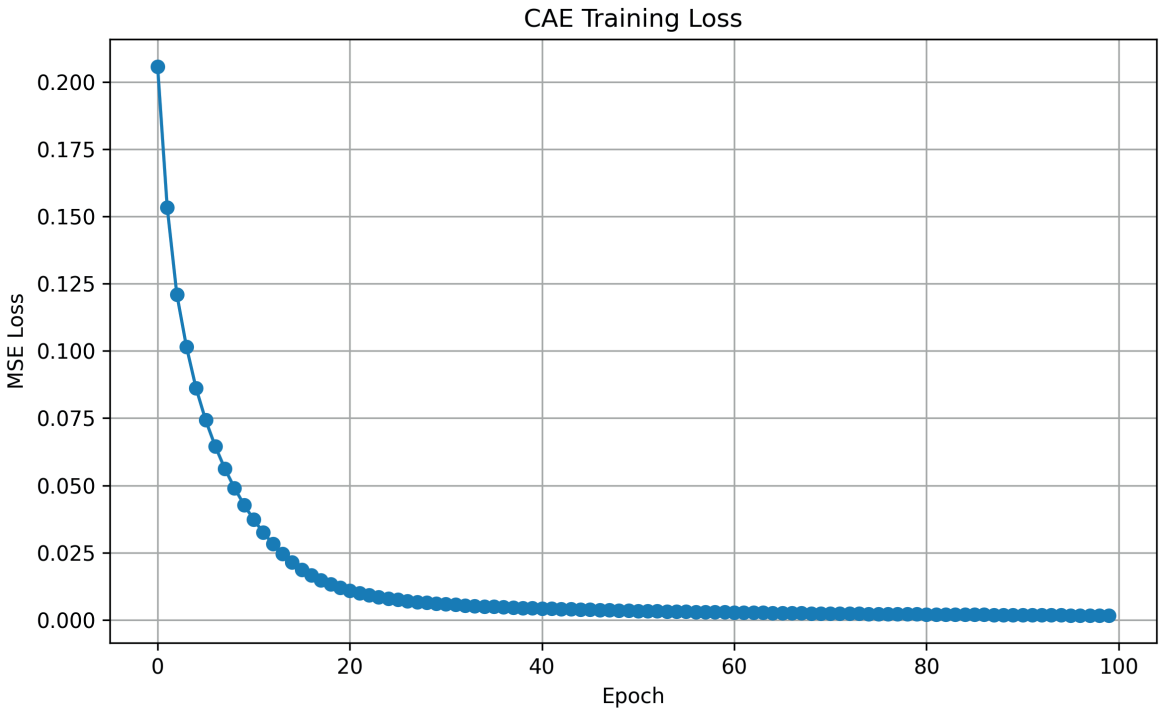

Fig. 5. Convergence of training loss in convolutional autoencoder over 100 epochs

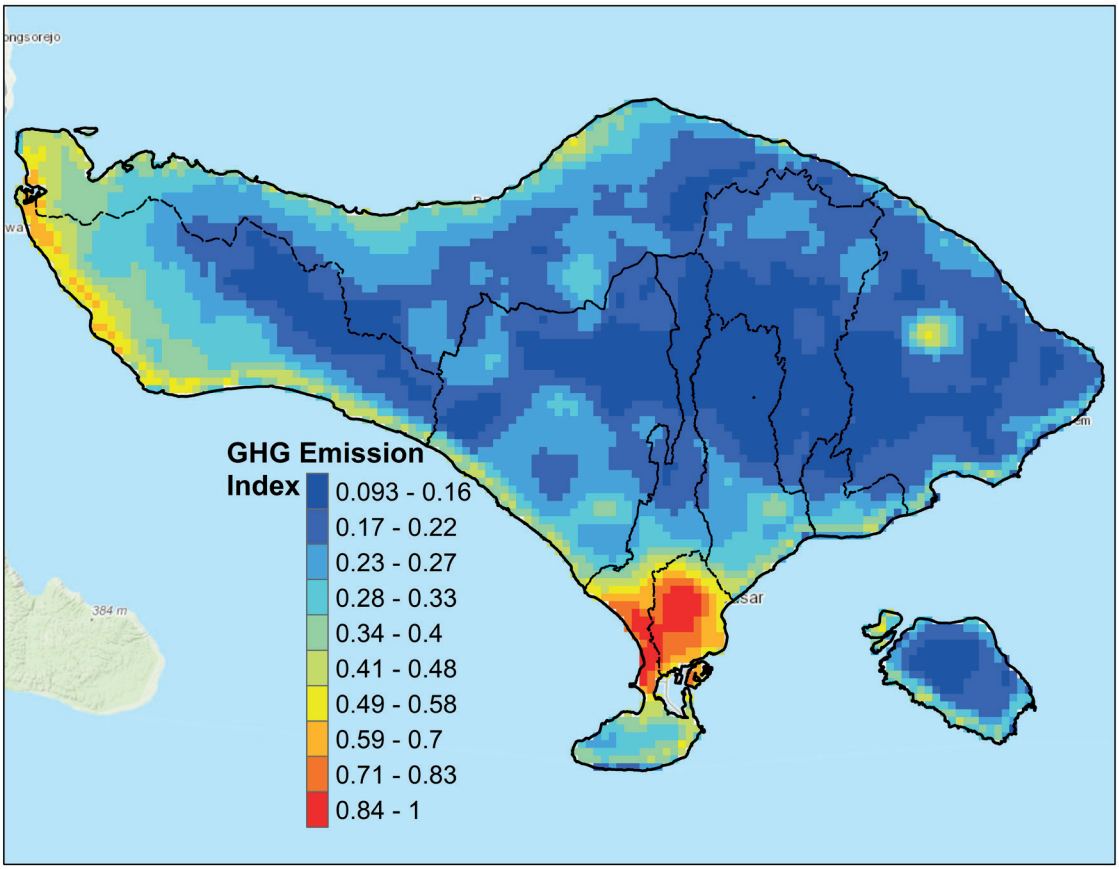

Fig. 6. Spatial distribution and proportional area of GHG emission vulnerability in Bali Province

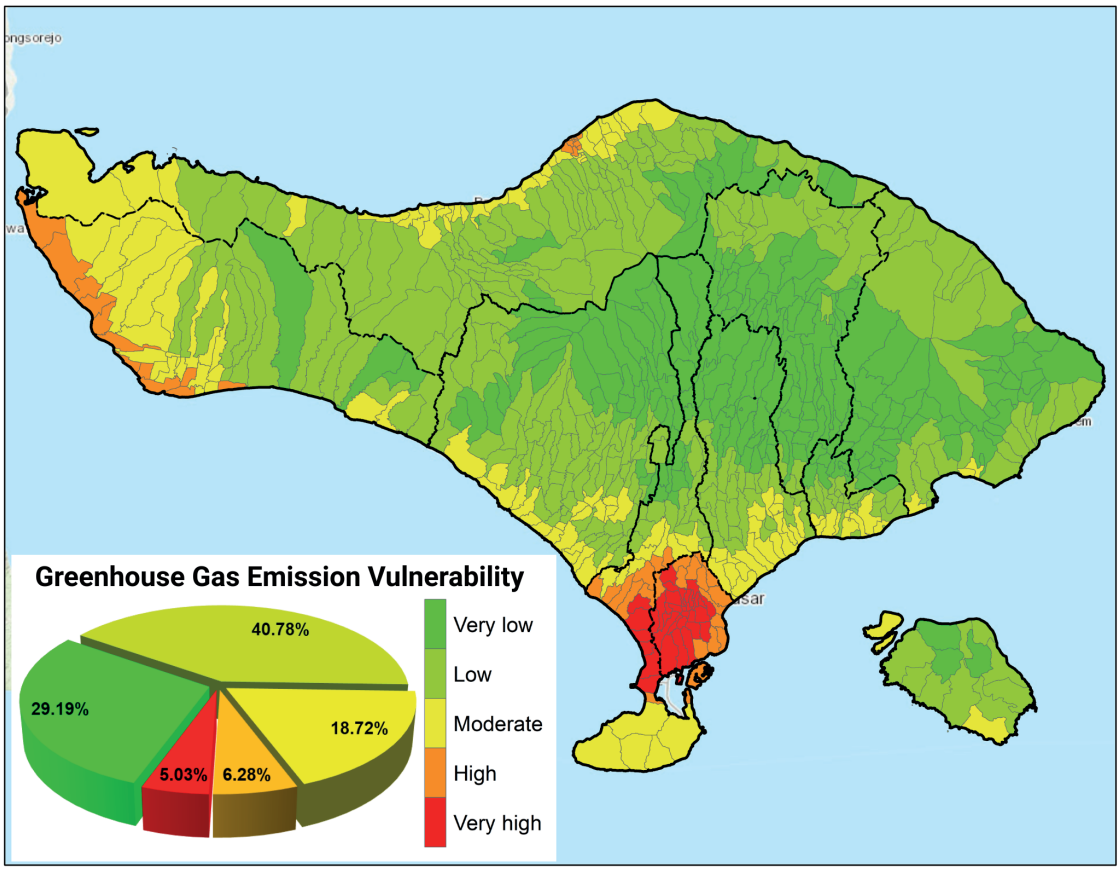

Fig. 7. Spatial alignment of GHG vulnerability with administrative boundaries

data. The unsupervised CAE model eliminated the need for labeled training data, addressing a persistent challenge in regional-scale environmental assessments where ground-based measurements are often unavailable. Previous research has demonstrated that autoencoders are effective for extracting latent features and reconstructing complex geospatial patterns in remote sensing applications (X. Han et al., 2017; Pintelas et al., 2021). In this study, the model achieved rapid convergence and low reconstruction loss, affirming its ability to process and learn from high-dimensional environmental inputs.

The resulting vulnerability index revealed distinct spatial gradients, with high-risk zones concentrated in southern coastal areas, such as Denpasar and southern Badung. These regions are associated with dense urbanization, tourism-related development, and intensive energy use. These findings align with global studies showing that atmospheric pollutants like NO_2, CO, and AOD are often concentrated in urban-industrial zones (Fioletov et al., 2025; Wang et al., 2025). The integration of land surface temperature, NDVI, nighttime lights, and population density further substantiated the mapping of anthropogenic stressors and ecological degradation (Liu et al., 2015; McRoberts et al., 2020).

A key innovation of this research is its use of openly accessible satellite data and an unsupervised deep learning approach to generate a replicable and cost-effective GHG vulnerability mapping framework. Designed to be compatible with Google Earth Engine and other open-source platforms, this methodology can be scaled to other regions lacking the technical capacity or financial means for traditional emissions monitoring. This approach complements previous efforts in urban classification and land use mapping, where autoencoder-based models have demonstrated effective generalization across geographic contexts (Jiang, 2018). The framework provides critical support for environmental planning and is aligned with the objectives of SDG 13 on climate action.

This study also acknowledges certain methodological constraints. The use of 1 km^2 spatial resolution, while adequate for regional-scale visualization, may not capture the fine-scale variability needed for local urban or zoning applications. Additionally, while MODIS and Sentinel-5P data offer global consistency, they may lack sensitivity to site-specific emission patterns or infrastructure dynamics. To enhance spatial detail and accuracy, future research should incorporate higher-resolution datasets such as Sentinel-1 and Sentinel-2 imagery. Furthermore, integrating thematic variables like road networks, industrial zones, localized greenhouse gas emissions inventories, and spatially distributed land use categories would provide a more comprehensive picture of emissions at finer scales (Q. Feng et al., 2021). Additional consideration should be given to incorporating landscape circulatory factors and pollutant dispersion mechanisms using digital elevation models and meteorological data that capture prevailing wind directions. The findings validate the effectiveness of combining unsupervised deep learning with multi-sensor remote sensing for emission vulnerability mapping. The proposed framework is transferable, cost-efficient, and capable of identifying high-risk areas, particularly in urbanizing regions. This method serves as a valuable tool for supporting spatially informed climate mitigation strategies and advancing global climate governance.

CONCLUSIONS

This study demonstrated a rapid and cost-effective approach to mapping greenhouse gas (GHG) emission vulnerability by integrating multi-sensor satellite data with an unsupervised convolutional autoencoder (CAE) deep learning model. The framework avoided the need for field-based training data and extracted 128 latent features from a range of environmental indicators, enabling robust spatial characterization of emission risks. The vulnerability

index showed distinct spatial gradients, with the highest values concentrated in southern coastal areas experiencing dense anthropogenic activity, particularly from tourism and urbanization. These results confirm the effectiveness of unsupervised deep learning in identifying emission hotspots and spatial variability in data-limited settings. Utilizing open-access datasets and scalable computational methods, the framework offers a replicable solution for other regions, especially in developing countries where financial and technical constraints hinder regular monitoring. It presents a practical tool to support emission analysis and planning aligned with climate mitigation strategies. To enhance precision, future improvements should incorporate high-resolution imagery through data fusion techniques, such as integrating Sentinel-2 or commercial satellite data. This advancement would allow for more detailed mapping suitable for urban-scale planning and targeted mitigation. This research contributes a transferable, efficient methodology for spatial quantification of GHG emission vulnerability, offering actionable insights to support climate policy and advance the Sustainable Development Goals (SDGs).

REFERENCES

Andyana I.W.S., As-Syakur A.R., Sunarta I.N., Suyarto R., Diara I.W., Susila K.D., Saifulloh M., Kusmiyarti T.B. and Wiyanti W. (2023). Urban tourism expansion monitoring by remote sensing and random forest. IOP Conference Series: Earth and Environmental Science, 1180(1). DOI: 10.1088/1755-1315/1180/1/012046

Ayyamperumal R., Banerjee A., Zhang Z., Nazir N., Li F., Zhang C. and Huang X. (2024). Quantifying climate variation and associated regional air pollution in southern India using Google Earth Engine. Science of the Total Environment, 909. DOI: 10.1016/j.scitotenv.2023.168470

Azarang A., Manoochehri H.E. and Kehtarnavaz N. (2019). Convolutional Autoencoder-Based Multispectral Image Fusion. IEEE Access, 7. DOI: 10.1109/ACCESS.2019.2905511

Bhatti U.A., Bhatti M.A., Tang H., Syam M.S., Awwad E.M., Sharaf M. and Ghadi Y.Y. (2024). Global production patterns: Understanding the relationship between greenhouse gas emissions, agriculture greening and climate variability. Environmental Research, 245. DOI: 10.1016/j.envres.2023.118049

Costa N., Pérez L. and Sánchez L. (2024). Rapidae: A python library for creation, experimentation, and benchmarking of autoencoder models. 2024 IEEE International Conference on Fuzzy Systems (FUZZ-IEEE), 1–8.

Cui W., Zhou Q. and Zheng Z. (2018). Application of a Hybrid model based on a convolutional auto-encoder and convolutional neural network in object-oriented remote sensing classification. Algorithms, 11(1). DOI: 10.3390/a11010009

Dar J.A., Subashree K., Bhat N.A., Sundarapandian S., Xu M., Saikia P., Kumar A., Kumar A., Khare P.K. and Khan M.L. (2020). Role of major forest biomes in climate change mitigation: An eco-biological perspective. In: Environmental Science and Engineering. DOI: 10.1007/978-3-030-32463-6_24

Diara I.W., Susila K.D., Wiyanti W., Sunarta I.N., Kusmiyarti T.B. and Saifulloh M. (2024). Exploring the Influence of Various Land Use Land Cover on Land Surface Temperature of Coastal Tourism Areas in Bali Using Landsat 9. Environmental Research, Engineering and Management, 80(2), 118–132.

Edo G.I., Itoje-akpokiniovo L.O., Obasohan P., Ikpekoro V.O., Samuel P.O., Jikah A.N., Nosu L.C., Ekokotu H.A., Ugbune U. and Oghroro E.E.A. (2024). Impact of environmental pollution from human activities on water, air quality and climate change. Ecological Frontiers.

Feng Q., Niu B., Chen B., Ren Y., Zhu D., Yang J., Liu J., Ou C. and Li B. (2021). Mapping of plastic greenhouses and mulching films from very high resolution remote sensing imagery based on a dilated and non-local convolutional neural network. International Journal of Applied Earth Observation and Geoinformation, 102. DOI: 10.1016/j.jag.2021.102441

Feng Z., Wang X., Yuan J., Zhang Y. and Yu M. (2023). Changes in air pollution, land surface temperature, and urban heat islands during the COVID-19 lockdown in three Chinese urban agglomerations. Science of the Total Environment, 892. DOI: 10.1016/j.scitotenv.2023.164496

Fioletov V., McLinden C.A., Griffin D., Zhao X. and Eskes H. (2025). Global seasonal urban, industrial, and background NO2 estimated from TROPOMI satellite observations. Atmospheric Chemistry and Physics, 25(1), 575–596.

Garajeh K.M., Laneve G., Rezaei H., Sadeghnejad M., Mohamadzadeh N. and Salmani B. (2023). Monitoring Trends of CO, NO_2, SO_2, and O3 Pollutants Using Time-Series Sentinel-5 Images Based on Google Earth Engine. Pollutants, 3(2). DOI: 10.3390/pollutants3020019

Gorelick N., Hancher M., Dixon M., Ilyushchenko S., Thau D. and Moore R. (2017). Google Earth Engine: Planetary-scale geospatial analysis for everyone. Remote Sensing of Environment, 202. DOI: 10.1016/j.rse.2017.06.031

Grekousis G., Sunarta I.N. and Stratoulias D. (2024). Tracing vulnerable communities to ambient air pollution exposure: A geodemographic and remote sensing approach. Environmental Research, 258, 119491.

Grimm N.B., Chapin F.S., Bierwagen B., Gonzalez P., Groffman P.M., Luo Y., Melton F., Nadelhoffer K., Pairis A., Raymond P.A., Schimel J. and Williamson C.E. (2013). The impacts of climate change on ecosystem structure and function. In: Frontiers in Ecology and the Environment , Vol. 11, Issue 9. DOI: 10.1890/120282

Han X., Zhong Y. and Zhang L. (2017). Spatial-spectral unsupervised convolutional sparse auto-encoder classifier for hyperspectral imagery. Photogrammetric Engineering and Remote Sensing, 83(3). DOI: 10.14358/PERS.83.3.195

Han Y., Chi H., Huang J., Gao X., Zhang Z. and Ling F. (2024). TemPanSharpening: A multi-temporal Pansharpening solution based on deep learning and edge extraction. ISPRS Journal of Photogrammetry and Remote Sensing, 211, 406–424.

Hassaan M.A., Abdallah S.M., Shalaby E.S.A. and Ibrahim A.A. (2023). Assessing vulnerability of densely populated areas to air pollution using Sentinel-5P imageries: a case study of the Nile Delta, Egypt. Scientific Reports, 13(1). DOI: 10.1038/s41598-023-44186-4

Hou C., Xie Y. and Zhang Z. (2022). An improved convolutional neural network based indoor localization by using Jenks natural breaks algorithm. China Communications, 19(4). DOI: 10.23919/JCC.2022.04.021

Jiang W. (2018). Object-based deep convolutional autoencoders for high-resolution remote sensing image classification. Journal of Applied Remote Sensing, 12(03). DOI: 10.1117/1.jrs.12.035002

Ke C., He S. and Qin Y. (2023). Comparison of natural breaks method and frequency ratio dividing attribute intervals for landslide susceptibility mapping. Bulletin of Engineering Geology and the Environment, 82(10). DOI: 10.1007/s10064-023-03392-0

Li Z., Chen B., Wu S., Su M., Chen J.M. and Xu B. (2024). Deep learning for urban land use category classification: A review and experimental assessment. Remote Sensing of Environment, 311, 114290.

Liu Y., Wang Y., Peng J., Du Y., Liu X., Li S. and Zhang D. (2015). Correlations between urbanization and vegetation degradation across the world's metropolises using DMSP/OLS nighttime light data. Remote Sensing, 7(2), 2067–2088.

Maurya N.K., Pandey P.C., Sarkar S., Kumar R. and Srivastava P.K. (2022). Spatio-Temporal Monitoring of Atmospheric Pollutants Using Earth Observation Sentinel 5P TROPOMI Data: Impact of Stubble Burning a Case Study. ISPRS International Journal of Geo-Information, 11(5). DOI: 10.3390/ijgi11050301

McRoberts R.E., Næsset E., Sannier C., Stehman S. V. and Tomppo E.O. (2020). Remote sensing support for the gain-loss approach for greenhouse gas inventories. In: Remote Sensing , Vol. 12, Issue 11. DOI: 10.3390/rs12111891

Pan Y., Wu J., Liu G., Liu W. and Ma L. (2024). Differential responses of temperature sensitivity of greenhouse gases emission to seasonal variations in plateau riparian zones. Environmental Pollution, 353, 124190.

Pecl G.T., Araújo M.B., Bell J.D., Blanchard J., Bonebrake T.C., Chen I.C., Clark T.D., Colwell R.K., Danielsen F., Evengård B., Falconi L., Ferrier S., Frusher S., Garcia R.A., Griffis R.B., Hobday A.J., Janion-Scheepers C., Jarzyna M.A., Jennings S., … Williams S.E. (2017). Biodiversity redistribution under climate change: Impacts on ecosystems and human well-being. In: Science , Vol. 355, Issue 6332. DOI: 10.1126/science.aai9214

Pintelas E., Livieris I.E. and Pintelas P.E. (2021). A convolutional autoencoder topology for classification in high-dimensional noisy image datasets. Sensors, 21(22). DOI: 10.3390/s21227731

Priyadarshini S.L.A., Kaushik V. and Kataria R. (2025). The Role of Anthropogenic Activities, Energy Demand, and Global Climate Change. In: The Intersection of Global Energy Politics and Climate Change: A Comprehensive Analysis of Energy Markets and Economics , 35–61. Springer.

Puspitasari S.A. and Wu C.-F. (2025). Assessing future climate change with a weather generator: A case study in Bali, Indonesia. BIO Web of Conferences, 155, 3003.

Rahaman Z.A., Kafy A. Al, Saha M., Rahim A.A., Almulhim A.I., Rahaman S.N., Fattah M.A., Rahman M.T., S K., Faisal A. Al and Al Rakib A. (2022). Assessing the impacts of vegetation cover loss on surface temperature, urban heat island and carbon emission in Penang city, Malaysia. Building and Environment, 222. DOI: 10.1016/j.buildenv.2022.109335

Rzasa K. and Ciski M. (2021). Determination of the level of sustainable development of the cities - A proposal for a method of classifying Objects based on natural breaks. Acta Scientiarum Polonorum, Administratio Locorum, 20(3). DOI: 10.31648/aspal.6701

Sakti A.D., Anggraini T.S., Ihsan K.T.N., Misra P., Trang N.T.Q., Pradhan B., Wenten I.G., Hadi P.O. and Wikantika K. (2023). Multi-air pollution risk assessment in Southeast Asia region using integrated remote sensing and socio-economic data products. Science of the Total Environment, 854. DOI: 10.1016/j.scitotenv.2022.158825

Saifulloh, M., Sunarta, I. N., Baiquni, M., Trigunasih, N. M., Adikampana, I. M. (2025). Linking annual land subsidence to built-up density across coastal tourism zones via Sentinel-1 differential interferometric synthetic aperture radar. Ecological Engineering & Environmental Technology, 26(9), 325-335.

Scafetta N. (2024). Impacts and risks of "realistic" global warming projections for the 21st century. Geoscience Frontiers, 15(2). DOI: 10.1016/j.gsf.2023.101774

Subramanian V. (2018). Deep Learning with PyTorch: A practical approach to building neural network models using PyTorch. In: O'Reilly Media.

Sudarma I., Saifulloh M., Diara I.W. and As-Syakur A. (2024). Carbon Stocks Dynamics of Urban Green Space Ecosystems Using Time-Series Vegetation Indices. Ecological Engineering & Environmental Technology (EEET), 25(9).

Sunarta I.N. and Saifulloh M. (2022a). Coastal tourism: impact for built-up area growth and correlation to vegetation and water indices derived from Sentinel-2 remote sensing imagery. Geojournal of Tourism and Geosites , 41(2). DOI: 10.30892/gtg.41223-857

Sunarta I.N. and Saifulloh M. (2022b). Spatial variation of NO2 levels during the Covid-19 pandemic in the Bali tourism area. Geographia technica, 17(1). DOI: 10.21163/GT_2022.171.11

Sunarta I.N., Suyarto R., Saifulloh M., Wiyanti W., Susila K.D. and Kusumadewi L.G.L. (2022). Surface urban heat island (SUHI) phenomenon in Bali and Lombok tourism areas based on remote sensing. Journal of Southwest Jiaotong University, 57(4). DOI: 10.35741/issn.0258-2724.57.4.44

Susila K.D., Trigunasih N.M. and Saifulloh M. (2024). Monitoring Agricultural Drought in Savanna Ecosystems Using the Vegetation Health Index--Implications of Climate Change. Ecological Engineering & Environmental Technology (EEET), 25(9).

Toersilowati L., Siswanto B., Maryadi E., Susanti I., Suhermat M., Witono A., Sipayung S.B., Rahayu S.A., Aminuddin J. and Lubis R.F. (2022). The Projections of Climate Change using Conformal Cubic Atmospheric Model (CCAM) in Bali-Indonesia. IOP Conference Series: Earth and Environmental Science, 1047(1), 12033.

Trigunasih N.M. and Saifulloh M. (2022). The Investigating Water Infiltration Conditions Caused by Annual Urban Flooding Using Integrated Remote Sensing and Geographic Information Systems. Journal of Environmental Management & Tourism, 13(5), 1467–1480.

Valjarević A., Milanović M., Gultepe I., Filipović D. and Lukić T. (2022). Updated Trewartha climate classification with four climate change scenarios. Geographical Journal, 188(4). DOI: 10.1111/geoj.12458

Wang S., Cohen J.B., Guan L., Lu L., Tiwari P. and Qin K. (2025). Observationally constrained global NOx and CO emissions variability reveals sources which contribute significantly to CO2 emissions. Npj Climate and Atmospheric Science, 8(1), 87.

Xiong X., Liu J., Chen L., Ju W. and Moshary F. (2021). Special issue "remote sensing of greenhouse gases and air pollution." In: Remote Sensing , Vol. 13, Issue 11. DOI: 10.3390/rs13112057

Yang L., Muhammad I., Chi Y.X., Liu Y.X., Wang G.Y., Wang Y. and Zhou X.B. (2022). Straw return and nitrogen fertilization regulate soil greenhouse gas emissions and global warming potential in dual maize cropping system. Science of the Total Environment, 853. DOI: 10.1016/j.scitotenv.2022.158370

Yu Q., Li S. and Chen N. (2024). Urbanization and greenhouse gas emissions from municipal wastewater in coastal provinces of China: Spatiotemporal patterns, driving factors, and mitigation strategies. Environmental Research, 259, 119398.

ges.rgo.ru/jour/

ISSN 2542-1565 (Online)